https://doi.org/10.15388/vu.thesis.363
https://orcid.org/0000-0001-7662-2998

VILNIUS UNIVERSITY
CENTER FOR PHYSICAL SCIENCES AND TECHNOLOGY

Marek Kolenda

Fabrication, investigation, and application of III-nitride semiconductor structures in devices of a specific spectral range

DOCTORAL DISSERTATION

Technological Sciences,
Materials Engineering (T 008)

VILNIUS 2022

This dissertation was written between 2017 and 2021 at the Institute of Photonics and Nanotechnology of Vilnius University.

Academic supervisor:
prof. dr. Roland Tomašiūnas (Vilnius University, Technological Sciences, Materials Engineering – T 008)

Dissertation Defense Panel:

Chairman – dr. Šarūnas Meškinis (Kaunas University of Technology, Technological Sciences, Materials Engineering – T 008)

Members:
dr. Paweł Prystawko (Institute of High Pressure Physics of the Polish Academy of Sciences, TopGaN Ltd., Natural Sciences, Physics – N 002)
dr. Pranciškus Vitta (Vilnius University, Technological Sciences, Materials Engineering – T 008)
dr. Vaidas Pačebutas (Center for Physical Sciences and Technology, Technological Sciences, Materials Engineering – T 008)
dr. Virgilijus Vaičaitis (Vilnius University, Natural Sciences, Physics – N 002)

The dissertation shall be defended at a public meeting of the Dissertation Defense Panel at 13:00 on the 20th of September, 2022, in Room A101 of the Center for Physical Sciences and Technology.
Address: Saulėtekio av. 3, Vilnius, LT-10257, Lithuania.
Tel. +370 264 9211; e-mail: office@ftmc.lt

The text of this dissertation can be accessed at the Vilnius University Library, as well as on the website of Vilnius University:
www.vu.lt/naujienos/ivykiu-kalendorius

https://doi.org/10.15388/vu.thesis.363
https://orcid.org/0000-0001-7662-2998

VILNIAUS UNIVERSITETAS
FIZINIŲ IR TECHNOLOGIJOS MOKSLŲ CENTRAS

Marek Kolenda

III-grupės nitridinių puslaidininkinių darinių kūrimas, tyrimas ir taikymas specifinio spektro ruožų prietaisuose

DAKTARO DISERTACIJA

Technologijos mokslai,
Medžiagų inžinerija (T 008)

VILNIUS 2022

Disertacija rengta 2017–2021 metais Vilniaus universiteto Fotonikos ir nanotechnologijų institute.

Mokslinis vadovas:
prof. dr. Roland Tomašiūnas (Vilniaus universitetas, technologijos mokslai, medžiagų inžinerija – T 008)

Gynimo taryba:

Pirmininkas – dr. Šarūnas Meškinis (Kauno technologijos universitetas, technologijos mokslai, medžiagų inžinerija – T 008)

Nariai:
dr. Paweł Prystawko (Lenkijos mokslų akademijos aukštųjų slėgių institutas, TopGaN, gamtos mokslai, fizika – N 002)
dr. Pranciškus Vitta (Vilniaus universitetas, technologijos mokslai, medžiagų inžinerija – T 008)
dr. Vaidas Pačebutas (Fizinių ir technologijos mokslų centras, technologijos mokslai, medžiagų inžinerija – T 008)
dr. Virgilijus Vaičaitis (Vilniaus universitetas, gamtos mokslai, fizika – N 002)

Disertacija ginama viešame gynimo tarybos posėdyje 2022 m. rugsėjo mėn. 20 d. 13:00 val. Nacionaliniame fizinių ir technologijos mokslų centre A101 auditorijoje. Adresas: Saulėtekio al. 3, Vilnius, LT-10257, Lietuva.
Tel. +370 264 9211; el. paštas: office@ftmc.lt

Disertaciją galima peržiūrėti Vilniaus universiteto bibliotekoje ir VU interneto svetainėje adresu: www.vu.lt/naujienos/ivykiu-kalendorius

CONTENTS

CONTENTS 5
LIST OF ABBREVIATIONS 7
INTRODUCTION 9
LIST OF PUBLICATIONS 15
1 GROUP-III NITRIDES SEMICONDUCTORS (LITERATURE OVERVIEW) 20
1.1 Material Properties 20
1.1.1 Crystalline structure 22
1.1.2 Polarization and polarity (face) of group-III nitride semiconductors 24
1.2 Group-III nitrides optical properties for second harmonic generation (SHG) 26
2 INTRODUCTION INTO SECOND HARMONIC GENERATION (LITERATURE OVERVIEW) 29
2.1 A brief introduction into nonlinear optics 29
2.2 Second harmonic generation (SHG) 31
2.3 Optical Waveguiding principles 34
2.4 Modal dispersion phase matching (MDPM) in group-III nitrides . 38
2.5 Quasi-phase matching (QPM) in group-III nitrides 40
3 MOVPE TECHNOLOGY (LITERATURE OVERVIEW) 44
3.1 MOVPE Reactor 44
3.2 MOVPE growth process 44
3.3 Epitaxy of Ga-polarity and N-polarity GaN 49
4 CHARACTERIZATION METHODS 56
4.1 *In-situ* growth rate control by reflectometry 56
4.2 *Ex-situ* surface characterization methods 57
4.2.1 Scanning electron microscopy (SEM) 57
4.2.2 Atomic force microscopy (AFM) 58
4.3 *Ex-situ* structural characterization methods 60
4.3.1 X-ray diffraction (XRD) 60
4.3.2 Transmission electron microscopy (TEM) 62
4.4 Electron-beam induced current (EBIC) 63
4.5 Polarity determination by KOH etching 64
4.6 External quantum efficiency (EQE) measurement 66
5 FABRICATION OF GaN/AlGaN PLANAR WAVEGUIDE 68
5.1 Modeling results 68
5.2 Growth of GaN/AlGaN structure 75
5.2.1 Growth of the Al-polarity AlGaN as optical cladding layer . . . 76

5.2.2 Growth of the Ga-polarity GaN layer on the AlGaN 81
5.2.3 ALD-Al_2O_3 as polarity inversion layer 84
5.2.4 Growth of the N-polarity GaN layer on the ALD-Al_2O_3 86
6 CHARACTERIZATION OF N-POLARITY GaN 88
6.1 N-polarity GaN growth experiments – finding core growth process 88
6.2 N-polarity GaN on the different thickness ALD-Al_2O_3 layers . . . 91
6.3 Smoothing the surface of N-polarity GaN 100
6.4 Nucleation layer influence on the N-polarity GaN 103
6.5 Smoothing N-polarity GaN surface on the 0.3° sapphire substrates 117
7 A NOVEL PULSED MOVPE GROWTH METHOD FOR THE InN LAYERS 121
7.1 InN band gap mystery 121
7.2 Overview on the InN MOVPE growth 124
7.3 Pulsed MOVPE growth of the InN and InN/p-GaN junction . . . 129
7.4 Characterization of the InN/p-GaN junction 136
CONCLUSIONS 145
SANTRAUKA LIETUVIŲ KALBA 147
BIBLIOGRAPHY 165
CURRICULUM VITAE 182

LIST OF ABBREVIATIONS

μ-PL	Microphotoluminescence
AFM	Atomic force microscopy
ALD	Atomic layer deposition
AlGaN	Aluminum gallium nitride
AlN	Aluminum nitride
CBED	Convergent beam electron diffraction
CL	Cathodoluminescence
CM	Charge multiplication
DUT	Device under test
EBIC	Electron beam induced current
EM	Electromagnetic
EQE	External quantum efficiency
FFT	Fast Fourier transformation
FWHM	Full width at half maximum
GaN	Gallium nitride
H_2 or H	Hydrogen
HT	High-temperature
IDB	Inversion domain boundary
InN	Indium nitride
IQE	Internal quantum efficiency
LTB	Low-temperature buffer
KOH	Potassium hydroxide
MDPM	Modal-phase-matching
MOCVD	Metalorganic chemical vapor deposition
MOVPE	Metalorganic vapor phase epitaxy
N_2 or N	Nitrogen
NH_3	Ammonia
NIR	Near infrared
OM	Optical microscope
PL	Photoluminescence
QPM	Quasi-phase-matching
SEM	Scanning electron microscopy
SH	Second harmonic
SHG	Second harmonic generation
SR	Spectral response
T	Temperature
TE	Transverse electric
TEM	Transmission electron microscopy
TM	Transverse magnetic
TMAl	Trimethylaluminum
TMGa	Trimethylgallium
TMIn	Trimethylindium
UV	Ultraviolet
VIS	Visible

WZ	Wurtzite
XRC	X-ray rocking curve
XRD	X-ray diffraction

INTRODUCTION

The modern world can't be imagined without the high-end nanotechnologies. The nanotechnologies with every year cover more and more aspects of the human lives, starting from the agricultural and food technologies [1–3], electronics used in the portable devices (the Apple A14 Bionic processor with 5 nm chipset with 11.8 billion transistors) [4], nanoelectronics [5], and ending with medicine technologies [6, 7]. Especially as the modern world would like to work at micro- and nano-scale dimensions, the devices that give feedback about the micro- and nano-world must also be miniaturized. Moreover, the modern world more and more switches from the classical electronic circuits to the more sophisticated photonic systems. The information carriers vectors in photonics can be photons, solitons or plasmons [8]. The advantages of the photons over the electrons as information carriers are the possibility to transmit information at any distance and with higher frequency (about 100 THz) and the ability to confine light in very small dimension objects. Lasers are the optical equivalent of the electrical generators, optical waveguides and fibers act as the transport cables and optical detectors or optical transistors are the equivalents of the electrical switches and electronic transistors. Integration of these separate devices on the one wafer and making a lab-on-chip where the electrical and optical parts work in synergy would be an enormous leap for humankind toward the nano-world characterization.

The candidates for a such future technology for NIR-VIS-UV (near infrared-visible-ultraviolet) spectrum part are group-III nitrides semiconductors. These semiconductors can be fabricated into light generators, transistors, diodes and detectors, thus covering all the devices that the modern world uses. The GaN and AlN wide band gap [9] (3.39 eV (365 nm) and 6.2 eV (200 nm)) and relatively high refractive index contrast (2.3330 [10] and 2.1297 [11]) and wide transparency window [10] give an ability to implement them in the waveguide structures that could operate in the NIR-VIS spectrum. Their chemical and structural stability allows them to work also in harsh environments. On the other hand InN, one of the most mysterious and "delicate" group-III nitrides semiconductors, exhibits a narrow band gap energy of $0.65 \div 0.75$ eV ($1907 \div 1653$ nm) [12, 13], which has found its application in the NIR spectrum region. Moreover, by combining InN, GaN and AlN, the whole visible spectrum can be covered, thus giving the ability to generate, transmit and detect photons of different wavelengths.

Although the group-III nitride technology is not new, a considerable amount of research has been focused on the GaN and AlN as novel materials for non-linear optics and photonics. Optical harmonic generation is one of the challenges [14–17]. During an epitaxial growth of the group-III nitride semiconductors, they all crystallize in a wurtzite phase with non-zero second-order nonlinear properties due to their noncentrosymmetric crystalline structure. However, the GaN and AlN dispersion curves do not allow for reaching classical birefringent phase-matching conditions to achieve second harmonic generation. Thus several techniques must be implemented in order to fulfill the conditions for the second harmonic generation. Two of the most popular methods to satisfy the phase-matching condition are the quasi-phase-matching (QPM) [17] and modal-dispersion-phase-matching (MDPM) [14, 18] techniques. The first one is based on the growth of periodically polar oriented GaN and AlN structures, where the second-order optical susceptibility changes its sign periodically along the light propagation direction. As group-III nitrides semiconductors are the polar materials, the condition can be easily achieved by inverting their polarity from Ga, Al and In face to N face. The second one is based on the dispersion of the particular optical modes in the GaN and AlN waveguide structures that can be phase-matched. Our calculations and the results in the literature [14] prove that by implementing different GaN polarities into a waveguide, the conversion efficiency of the second harmonic generation increases. But here is one difficulty related to the N-polarity GaN layers. Due to different growth mechanisms, N-polarity GaN layers' surface morphology compared to Ga-polarity GaN layers is more rougher when grown on the standard, low off-cut angles sapphire substrates [19, 20]. The surface roughness increases the optical scattering, which results in additional optical losses [14]. Thus, controlling the surface morphology for the N-polarity GaN layers waveguide becomes crucial in maintaining low optical losses. As a result, the surface roughness of the N-polarity GaN layers is influenced by the nitridation process and nucleation layer. Hite *et al.* [21] presented that deposited Al_2O_3 by the ALD method is eligible for the polarity inversion, but this was implemented only in the periodically poled GaN structure. Nevertheless, a proper nitridation process for the recrystallization of the ALD-Al_2O_3 and surface preparation for the N-polarity GaN layer must be performed. Next, the optimization of the nucleation layer on the nitrided ALD-Al_2O_3 must be performed in order to acquire high crystalline quality, smooth and pure N-polarity GaN layers.

As mentioned earlier due InN low band gap energy and combining it with the GaN semiconductor a possibility to cover the NIR-VIS spectrum can be achieved. Moreover, high electron mobility values can be achieved. Theoretically, it was calculated that electron mobility could reach as high as 4400 $cm^2V^{-1}s^{-1}$ at room temperature [22]. But nowhere such value practically was reported. The values presented in the literature are between 500 $\div$ 900 $cm^2V^{-1}s^{-1}$ [23–25]. Nevertheless, it is a very attractive material for detectors and even solar cell technologies [26]. The non-toxicity of the primary elements offers opportunities for future "green" technologies. However, the realization of the high crystalline quality InN layers remains a challenge [23, 27]. Due to the low dissociation temperature of the InN and high equilibrium nitrogen pressure, InN must be grown at lower temperatures. Due to low temperatures, MOVPE growth is restricted by the low decomposition of NH_3, resulting in poor crystalline quality of the InN and formation of metallic In droplets. The reduction of the unintentional n-type doping due to indium or nitrogen and oxygen-related defects is one of the goals for the narrow band gap energy InN layer [28]. The solution to these problems is a pulsed MOVPE method implemented in this work. However, to date, the best results were obtained through growth by the MBE method. From the point of view of optoelectronic device production, MOVPE is more suitable.

The objective of the thesis

The work is divided into two parts where the growth of different group-III nitride semiconductors was investigated targeting the fabrication of different heterostructure devices. The first part is dedicated to the growth and characterization of AlGaN and GaN with different polarities. The second part is dedicated to the growth, characterization and device application of the InN, a narrow band gap nitride semiconductor. Thus the main task of the work was to develop the MOVPE growth method for different III-group nitride semiconductor heterostructures with a potential for the photonic, optoelectronic and photovoltaic devices in the specific spectral ranges.

The main tasks of the thesis

- Determine the GaN/AlGaN heterostructure capable of generating second harmonic wave.
- Optimize the growth parameters for the Al-polarity AlN and AlGaN optical cladding layers.
- Find the core recipe for the N-polarity GaN layers on the 2° sapphire substrates and implement them on the ALD-Al_2O_3 layers.
- Optimize the parameters for the N-polarity GaN layers on the ALD-Al_2O_3 to complete a waveguiding structure.
- By employing the pulsed MOVPE method acquire high-quality InN layer on the p-type GaN for an efficient p-n heterojunction.

Practical and scientific novelty

- Although Hite *et al.* [21] presented the possibility of polarity inversion in the GaN layers by implementing the ALD-Al_2O_3 interlayer, they present it only in the periodically oriented structure on the GaN substrate. In the literature, has not been demonstrated a planar structure where the GaN polarity inversion would be done by the insertion of the ALD-Al_2O_3 in the AlGaN/GaN waveguiding platform grown on the sapphire substrate.

- The literature also does not have any reports on the extended characterization of the N-polarity GaN layers as a composite of the complex N-polarity GaN/ALD-Al_2O_3/Ga- polarity GaN/AlGaN waveguiding platform. By implementing different characterization techniques, this work presents a study of nitridation time and the influence of the nucleation layer on the resulting N-polarity GaN layer.

- Original pulsed MOVPE growth method was developed to grow high crystalline quality InN layers. Outstanding low electron concentration, reaching 10^{18} cm^{-3} and high electron mobility reaching 980 cm^{2}V^{-1}s^{-1} was acquired. The use of the p-GaN/InN p-n heterojunction in an optoelectronic device working under avalanche regime is original and new.

Statements to defend

1. ALD-Al_2O_3 is suitable for the polarity inversion in a complex waveguiding structure N-polarity GaN/ALD-Al_2O_3/Ga-polarity GaN/AlGaN/AlN/sapphire. The threshold thickness for the GaN polarity inversion is 20 nm.

2. Reduction in the V/III ratio and TMGa flow as well as using the optimized nitridation duration enhance the Ga atoms migration, thus letting to achieve high-quality N-polarity GaN layers eligible for the complex optical waveguides structures.

3. InN grown by the pulsed MOVPE method on the GaN templates exhibits a single wurtzite crystalline phase, however, by adding p-type GaN, the crystalline quality of InN improves. A photoelectric response in the NIR spectral range due to InN absorption in the p-GaN/InN heterojunction can be observed.

Layout of the dissertation

The main focus of the dissertation is made on the development of different group-III nitrides (GaN, AlN, AlGaN, InN) semiconductor structures by MOVPE growth. By using these layers and heterostructures, an approach to device implementation was presented.

The first chapter of the dissertation briefly introduces and presents the group-III nitrides semiconductors' physical properties. The focus is mainly on the GaN and AlN semiconductors due to the ability to implement them in the waveguiding structures, which can be used as a platform for the second harmonic generation.

The second chapter briefly introduces the nonlinear optic phenomenon. Explains the second harmonic generation. Next, it introduces the waveguiding optics. The chapter presents the problems of the second harmonic generation in the complex structures consisting of the AlN, GaN and their alloys.

The third chapter introduces the MOVPE technology itself. Explains the processes that occur during the growth. Presents the difficulties and the ways how to overcome them. Explains the difference between Ga- and N-polarity GaN layers'.

The fourth chapter briefly explains the characterization methods used in the work.

The fifth chapter presents the modeling results of the different waveguiding structures using GaN/AlGaN platform. It also presents the exact structures with every consecutive layer thickness. Shows the way of improving the efficiency of the second harmonic generation. Lastly, it presents the waveguiding structure's parameters used for the "classic" Nd:YAG laser wavelength (1064 nm). After the modeling results, the chapter presents a growth process of the Al-polarity AlN and AlGaN layers as optical cladding layers for the waveguide structure. Then follows the Ga-polarity GaN growth process and optimization on the AlGaN layer. Lastly, an explanation about the ALD-Al_2O_3 layer, as the polarity inversion layer, is given.

The sixth chapter presents the different thicknesses of LTB-GaN (nucleation layer) layers' influence on the overall N-polarity GaN layer quality and surface morphology. Presents the characterization and etching results. Lastly, for a comparison the surface smoothening of the N-polarity GaN layers is presented on the conventional sapphire substrates.

The seventh chapter is dedicated to the growth and application of InN layer. The chapter starts with an overview on the InN band gap energy and growth problems. Next, the pulsed MOVPE growth approach for the growth of a high-quality InN layer is presented. After the growth optimization, a growth process of the heterostructure consisting of p-type GaN and InN is presented. Lastly, the modeling of the heterostructure and electrical, optoelectrical characterization results are presented.

Contribution of the author

All the growth experiments presented in the dissertation were performed by the author. The author performed by himself or in part assisted in the SEM/EDX/EBIC, AFM experiments, and all the surface morphology analysis. The etching experiments to determine the GaN layers' polarity and the Hall measurements were performed by the author. The author also did the XRD data analysis and the PL data analysis. The author performed also the p-GaN/InN junction calculations with the Nextnano3 software.

The author would like to thank Edvinas Radiunas for the help with acquiring AFM data and dr. Martynas Skapas for the TEM measurements. Also, dr. Tadas Malinauskas for the XRD measurements and data acquisition. For the PL measurement data, the author would like to thank dr. Darius Dobrovolskas. The author is very thankful dr. Riina Ritasalo (Picosun, Finland) for the fast work and good quality ALD-Al_2O_3 layers. The author also would like to thank Darius Kezys for the second harmonic modeling results (dispersion curves, conversion efficiencies, layer thicknesses) and dr. Vladimir Svrcek (AIST, Tsukuba, Japan) for the EQE measurements and photovoltaic response in the p-GaN/InN heterojunction with the solar simulator. The most important, the author is grateful for the supervisor dr. Roland Tomašiūnas for the guidance through the PhD study and dr. Arūnas Kadys, and dr. Tomas Grinys for the constructive discussion.

The articles [**A1**] and [**A2**] were written by the author (Marek Kolenda) and dr. Roland Tomašiūnas. Article [**A3**] was written in cooperate with dr. Vladimir Svrcek (AIST, Tsukuba, Japan) and by the author, and dr. Roland Tomašiūnas.

LIST OF PUBLICATIONS

On the dissertation topic

[A1] **M. Kolenda**, D. Kezys, I. Reklaitis, E. Radiunas, R. Ritasalo, A. Kadys, T. Grinys, T. Malinauskas, S. Stanionytė, M. Skapas, R. Petruškevičius, R. Tomašiūnas, Development of polarity inversion in a GaN waveguide structure for modal phase matching, J. Mater. Sci. **55**, 12008–12021 (2020).

[A2] **M. Kolenda**, A. Kadys, T. Malinauskas, E. Radiunas, R. Ritasalo, R. Tomašiūnas, The importance of nucleation layer for the GaN N-face purity on the annealed Al_2O_3 layers deposited by atomic layer deposition, Mater. Sci. Eng. B, **284**, 115850 (2022).

[A3] V. Svrcek, **M. Kolenda**, A. Kadys, I. Reklaitis, D. Dobrovolskas, T. Malinauskas, M. Lozach, D. Mariotti, M. Strassburg, R. Tomašiūnas, Significant carrier extraction enhancement at the interface of an InN/p-GaN heterojunction under reverse bias voltage, Nanomaterials **8**, 1039 (2018).

Other publications

[B1] A. Kadys, J. Mickevičius, T. Malinauskas, J. Jurkevičius, **M. Kolenda**, S. Stanionytė, G. Tamulaitis, Optical and structural properties of BGaN layers grown on different substrates, J. Phys. D:Appl. Phys **48**, 465307 (2015).

[B2] J. Jurkevičius, J. Mickevičius, A. Kadys, **M. Kolenda**, G. Tamulaitis, Photoluminescence efficiency of BGaN epitaxial layers with high boron content, Phys. B: Condens. Matter **492**, 23–26 (2016).

[B3] J. Jurkevičius, D. Dobrovolskas, T. Steponavičius, T. Malinauskas, **M. Kolenda**, A. Kadys, G. Tamulaitis, Engineering of InN epilayers by repeated deposition of ultrathin layers in pulsed MOCVD growth, Appl. Surf. Sci. **427**, 1027–1032 (2018).

[B4] R. Aleksiejūnas, Ž. Podlipskas, S. Nargelas, A. Kadys, **M. Kolenda**, K. Nomeika, J. Mickevičius, G. Tamulaitis, Direct Auger recombination and density-dependent hole diffusion in InN, Sci. Rep. **8**, 4621 (2018).

[B5] Ž. Podlipskas, J. Jurkevičius, A. Kadys, **M. Kolenda**, V. Kovalevskij, D. Dobrovolskas, R. Aleksiejūnas, G. Tamulaitis, Extreme radiation resistance in InN, J. Alloys Compd. **8**, 4621 (2018).

[B6] J. Jurkevičius, D. Dobrovolskas, T. Malinauskas, **M. Kolenda**, A. Kadys, G. Tamulaitis, Improvement of luminescence properties of InN by optimization of multi-step deposition on sapphire, Thin Solid Films **680**, 89–93 (2019).

[B7] R. Norkus, R. Aleksiejūnas, A. Kadys, **M. Kolenda**, G. Tamulaitis, A. Krotkus, Spectral dependence of THz emission from InN and InGaN layers, Sci. Rep. **9**, 7077 (2019).

[B8] P. Ščajev, R. Aleksiejūnas, P. Baronas, D. Litvinas, **M. Kolenda**, C. Qin, T. Fujihara, T. Matsushima, C. Adachi, S. Juršėnas, Carrier recombination and diffusion in wet-cast Tin Iodide Perovskite layers under high intensity photoexcitation, J. Phys. Chem. C **123**, 32, 19275–19281 (2019).

[B9] A. Mekys, J. Jurkevičius, A. Kadys, **M. Kolenda**, V. Kovalevskij, Influence of proton irradiation on carrier mobility in InN epitaxial layers, Thin Solid Films **692**, 137619 (2019).

Conference presentations during PhD studies

[C1] **M. Kolenda**, V. Svrcek, A. Kadys, I. Reklaitis D. Dobrovolskas, T. Malinauskas, R. Tomašiūnas, Carrier extraction enhancement at InN/p-GaN interface heterojunction under reverse bias voltage, 20th International Conference-School “Advanced Materials and Technologies”, Palanga, Lithuania, 2018.

[C2] D. Dobrovolskas, Ž. Podlipskas, J. Jurkevičius, A. Kadys, **M. Kolenda**, V. Kovalevskij, R. Aleksiejūnas, G. Tamulaitis. Origin of extreme radiation resistance of InN. International Workshop on Nitride Semiconductors, Kanazawa, Japan, 2018.

[C3] J. Mickevičius, D. Dobrovolskas, T. Malinauskas, **M. Kolenda**, A. Kadys, G. Tamulaitis. Transformation of photoluminescence spatial distribution with thickness in pulsed-MOCVD-grown InN epilayers. International Workshop on Nitride Semiconductors, Kanazawa, Japan, 2018.

[C4] [1]**M. Kolenda**, V. Svrcek, A. Kadys, I. Reklaitis, D. Dobrovolskas, T. Malinauskas, R. Tomašiūnas, Carrier extraction enhancement at InN/p-GaN interface heterojunction under reverse bias voltage, International Workshop on Nitride Semiconductors, Kanazawa, Japan, 2018.

[C5] [1]**M. Kolenda**, D. Kezys, A. Kadys, T. Malinauskas, R. Petruškevičius, R. Tomašiūnas, Growth of GaN/AlGaN planar waveguides for second harmonic generation adapted for the pump range of $(1 \div 1.5)$ μm, The 18th European Workshop on Metal-Organic Vapour Phase Epitaxy, Vilnius, Lithuania, 2019.

[C6] [1]**M. Kolenda**, Second harmonic generation in GaN, 1st PhD and ECI meeting (eCOST), Ljubljana, Slovenia, 2019.

[C7] **M. Kolenda**, D. Kezys, A. Kadys, T. Malinauskas, R. Petruškevičius, R. Tomašiūnas, Development of AlGaN cladding layer for GaN second harmonic generation structure, Lithuania-Poland Workshop on Physics and Technology, Vilnius, Lithuania, 2019.

[C8] R. Petruškevičius, D. Kezys, T. Malinauskas, **M. Kolenda**, R. Tomašiūnas, Quasi-Phase-Matching method based on coupling compensation for second harmonic generation in GaN waveguides, 21st International Conference on Transparent Optical Networks, Angers, France, 2019.

[C9] **M. Kolenda**, A. Kadys, T. Malinauskas, E. Radiunas, R. Ritasalo, T. Grinys, M. Skapas, R. Tomašiūnas, GaN Polarity Inversion using

---

[1] Presented at the international conference.

ALD-Al_2O_3 Interlayer, 23rd International Conference-School "Advanced Materials and Technologies", Palanga, Lithuania, 2021.

[C10] **M. Kolenda**, A. Kadys, T. Malinauskas, E. Radiunas, R. Ritasalo, T. Grinys, M. Skapas, S. Stanionytė, R. Tomašiūnas, Growth and investigation of polarity inversed GaN layers on ALD-Al_2O_3, 44-oji Lietuvos Nacionalinė Fizikos konferencija, Vilnius, Lithuania, 2021.

[C11] [1]**M. Kolenda**, A. Kadys, T. Malinauskas, D. Kezys, E. Radiunas, R. Ritasalo, T. Grinys, M. Skapas, R. Tomašiūnas, Growth and investigation of polarity inversed GaN layers and N-face GaN purity on ALD-Al_2O_3, The 20th International Conference on Metal Organic Vapor Phase Epitaxy (ICMOVPE XX), Stuttgart, Germany, 2022.

Other conference presentations

[C12] **M. Kolenda**, T. Malinauskas, J. Mickevičius, D. Dobrovolskas, A. Kadys, AlN and AlGaN growth by MOCVD and characterization, Open Readings 2015, Vilnius, Lithuania, 2015.

[C13] **M. Kolenda**, T. Malinauskas, J. Mickevičius, D. Dobrovolskas, A. Kadys, AlN and AlGaN growth by MOCVD and characterization, 41-oji Lietuvos Nacionalinė Fizikos konferencija, Vilnius, Lithuania, 2015.

[C14] **M. Kolenda**, T. Malinauskas, J. Mickevičius, J. Jurkevičius, D. Dobrovolskas, A. Kadys, BGaN growth on 6H-SiC and AlN by MOVPE and characterization, Open Readings 2016, Vilnius, Lithuania, 2016.

[C15] **M. Kolenda**, T. Malinauskas, D. Dobrovolskas, A. Kadys, InN growth on GaN and sapphire by MOVPE and characterization, Open Readings 2017, Vilnius, Lithuania, 2017.

[C16] J. Jurkevičius, D. Dobrovolskas, Ž. Podlipskas, K. Nomeika, **M. Kolenda**, A. Kadys, T. Malinauskas, J. Mickevičius, R. Aleksiejūnas, G. Tamulaitis, Growth of InN epilayers by pulsed MOCVD, 42-oji Lietuvos Nacionalinė Fizikos konferencija, Vilnius, Lithuania, 2017.

[C17] J. Mickevičius, D. Dobrovolskas, **M. Kolenda**, M. Dmukauskas, T. Girnys, A. Kadys, T. Malinauskas, K. Nomeika, R. Aleksiejūnas, G. Tamulaitis, Variation of localizing potential in InGaN QW structures, 42-oji Lietuvos Nacionalinė Fizikos konferencija, Vilnius, Lithuania, 2017.

[C18] M. Dmukauskas, **M. Kolenda**, A. Kadys, T. Malinauskas, M. Skapas, J. Mickevičius, R. Tomašiūnas, All-optical research of In segregation suppression in InGaN QWs grown by MOVPE using metal precursor mul-

---

[1] Presented at the international conference.

tiple flow interruptions, The 17th European Workshop on Metalorganic Vapour Phase Epitaxy, Grenoble, France, 2017.

1. GROUP-III NITRIDES SEMICONDUCTORS (LITERATURE OVERVIEW)

1.1. Material properties

Gallium nitride (GaN) based compounds have found their niche mainly in solid state lighting and high power/high frequency electronics. The aluminum (Al), gallium (Ga), indium (In) –N nitrides materials system covers the entire visible range, with the band gap energy varying from 0.77 eV (InN), through 3.4 eV (GaN) to 6.2 eV (AlN) [9]. (Al, In, Ga)-N based compounds band gap and lattice parameter relation is presented in Figure 1.1. More importantly, the band gap of nitrides based system from InN through GaN to AlN transition stays direct. This main feature makes this material attractive in solid state lighting applications.

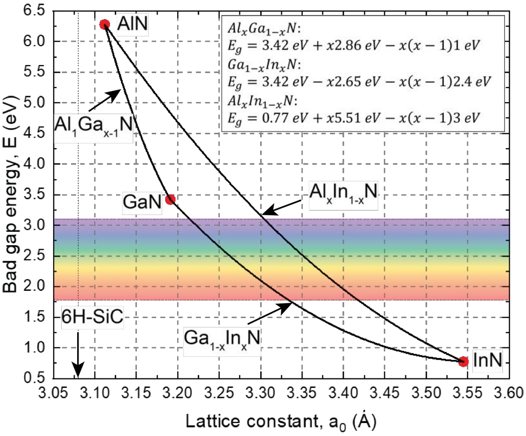

Figure 1.1: Band gap and lattice constant for the nitrides semiconductors. Adapted from [9].

GaN, AlN and InN energy band structure schematically looks the same for these materials and are presented in Figure 1.2 (a). The conduction band energy minimum and the valence band energy maximum are located at the Γ point of the center of the Brillouin zone, where $k = 0$ [29]. The first Brillouin zone of III-nitrides semiconductors is presented in Figure 1.2 (b). In addition to this, the second energy valley M-L valley and the third energy valley A are also found in the energy band. Due to interaction between the crystal field and the spin-orbit coupling, the valence band splits into a heavy hole band, a light hole band and a spin-coupled split band. E_{SO} is the spin-coupled splitting energy, and E_{cr} is the splitting energy of the crystal field [29].

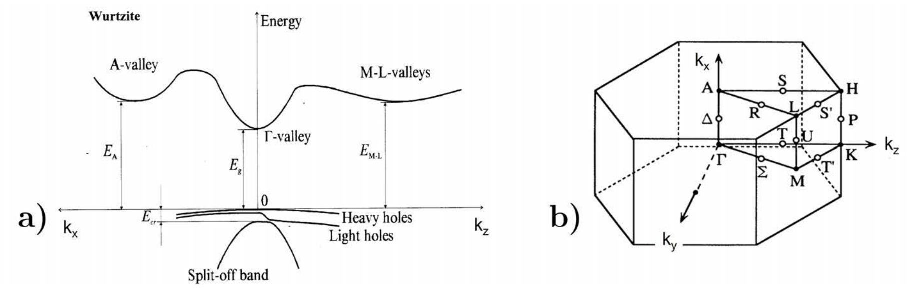

Figure 1.2: (a) Schematic view of band energy structure for group-III nitrides semiconductors. (b) The first Brillouin zone of the wurtzite crystal. Adapted from [30].

GaN and AlN exhibit outstanding thermal stability. Their melting temperature is 3200°C and 2500°C for AlN and GaN, respectively. This is due to strong Ga–N and Al–N bond energy, which equal 2.24 eV and 2.88 eV, respectively [34]. In contrast, In–N bond energy is 1.93 eV. Therefore, InN starts to sublimate at temperatures above 550°C and its melting temperature is 1100°C. Secondly, III-group nitrides exhibits large conduction band offset at the interfaces. These factors make them (especially GaN and AlN heterostructures) suitable for high-power and high-frequency as well as for high temperature electronic applications such as high electron mobility transistors (HEMT).

Additionally, III-polarity GaN and AlN semiconductors exhibit remarkable chemical stability. They are resistant to the chemical wet etching used in semiconductor processing and fabrication. They can be only etched in the high concentration or pure, hot, or melted alkali solutions (NaOH or KOH) and hot acid solutions (H_3PO_4 or H_2SO_4). On the contrary, N-polarity nitrides semiconductors' wet etching process is slightly different due to their bond configuration, which is explained in more detail later in this work. Significant physical properties of GaN, AlN and InN are presented in Table 1.1.

Table 1.1: Relevant physical parameters of III-group nitrides semiconductors [29,31–33].

	Units	InN	GaN	AlN
Density	g/cm^3	6.81	6.15	3.23
Thermal conductivity	W/cmK	0.45	1.3	2.85
Bulk modulus	GPa	140	210	210
Vickers hardness*	GPa	11.2	12	14
Band gap energy	eV	0.77	3.39	6.2
Bond energy	eV	1.93	2.24	2.88
Melting temperature	°C	1100 sublimation 550	2530	3000
Electron mobility	cm^2/Vs	3980	900 2000**	426
Hole mobility	cm^2/Vs	< 80	< 200	14
Static dielectric constant		8.5	8.9	15.3
Effective mass of electron	$m_0\times$	0.11	0.2	0.48
Breakdown field	MV/cm	1.2***	3.3	8.4

*Vickers hardness for sapphire 19.4 ÷ 22 GPa, diamond – 115 GPa.

** 2D electron gas (2DEG).

***Breakdown field of InN is not well investigated due to the high trap concentrations and the new findings for the fundamental band gap.

1.1.1. Crystalline structure

Group-III nitrides can be found in three crystal structures: the wurtzite (WZ), zincblende (ZB) and rocksalt structures [34,35]. The rocksalt structure is impossible to produce by any epitaxial growth. It is possible to form only under high pressure. The ZB structure for GaN and InN can be formed by epitaxial growth of the thin films on the (001) crystal planes of the cubic substrates as Si and GaAs.

In this work, every grown group-III nitride structure exhibited WZ like structure. Thus crystalline structure of WZ GaN (AlN and InN) will be presented in this subsection. WZ form of bulk GaN, AlN and InN is a thermodynamically stable phase under ambient conditions. A schematic view of the group-III nitrides WZ structure is presented in Figure 1.3. The space grouping for the WZ structure is $P6_3mc$ in the Hermann-Mauguin notation. The structure's Bravais lattice is hexagonal, thus resulting in two lattice constants, axial lattice constant c and basal plane lattice constant a (see Figure 1.3). It contains six atoms of each type and whole WZ structure consists of two interpenetrating hexagonal close-packed (hcp) sublattices, each with one kind of atom offset along the c-axis by 5/8 of the cell height (5c/8). One sublattice is made up of cations (group-III metal atoms) and the other is occupied by anions (nitrogen). Each group-III atom is tetrahedrally bonded with four nitrogen atoms and vice versa. The interatomic distance in the basic unit is described by the

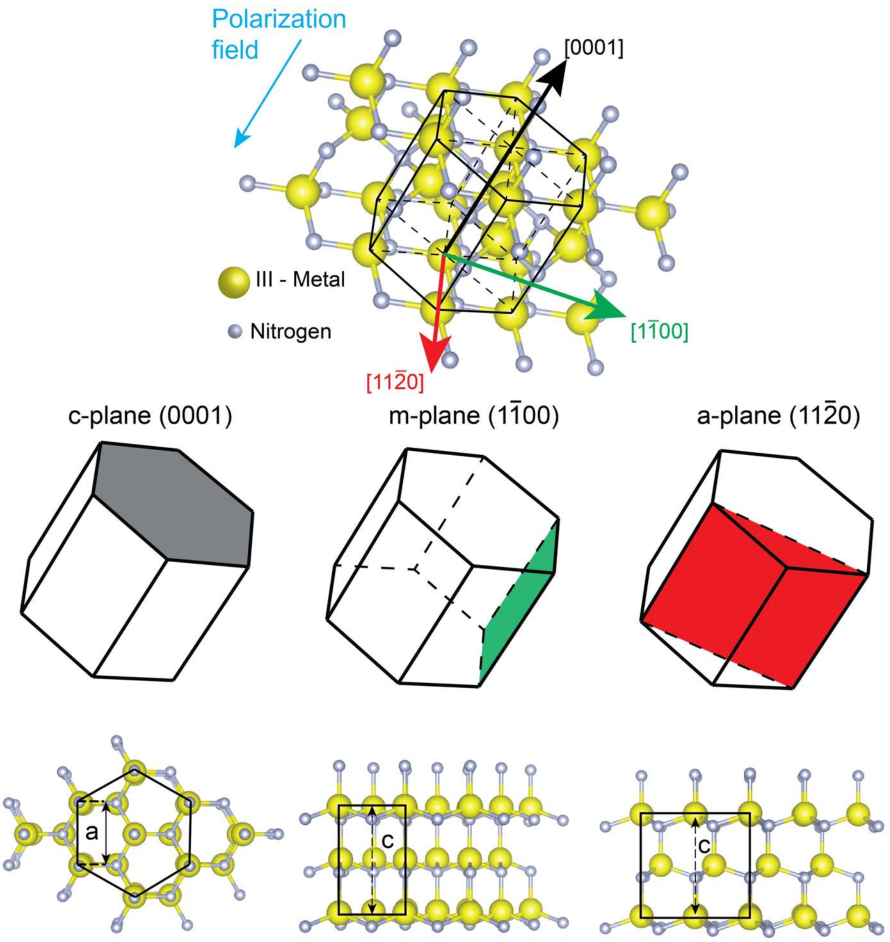

Figure 1.3: Schematic view of the group-III nitrides wurtzite structure, where the basal plane (c-plane), m-plane and a-plane are highlighted and their projections.

internal parameter u. It is defined as the ratio between bond length (length between the two nearest neighbors atoms along the c-axis) and the c axial lattice constant [36]. In an ideal WZ structure, the values of the axial ratio and the internal parameter are $c/a = \sqrt{8/3} = 1.633$ and $u = 3/8 = 0.375$Å, respectively. However, the experimental values of c/a and u for III-group nitrides deviate from the ideal ones due to strain, partial relaxation of strain and a high concentration of structural defects [34]. Moreover, parameter u correlates with the electronegativity of the respective atoms as well as the spontaneous polarization field. Table 1.2 gives group-III nitride semiconductors lattice parameter values and compares them for ideal tetrahedral atom configuration. From Table 1.2, it is clearly seen that parameter u gets longer and the c/a

ratio gets smaller from GaN through InN to AlN. GaN is the closest to the ideal value of mentioned parameters for the WZ structure, while AlN exhibits the largest deviation from the ideal values. Such deviation in the nonideality of the structure determines the polarization strength of the WZ group-III nitride materials [36].

Table 1.2: Lattice parameters for group-III nitride semiconductors [29, 31–34, 37].

	InN	GaN	AlN	Ideal tetrahedral
Lattice constant a (Å)	3.538 – 3.544	3.189	3.112	
Lattice constant c (Å)	5.703	5.186	4.982	
c/a	1.608	1.626	1.601	1.633
u (Å)	0.377	0.376	0.382	0.375

1.1.2. Polarization and polarity (face) of group-III nitride semiconductors

The WZ structure group-III nitride crystals exhibit a highly pronounced polarization field, called spontaneous polarization field, along [0001] direction (c-direction) due to a lack of center of inversion symmetry and strong ionicity between nitrogen and group-III metal atoms. These two factor causes a misalignment between positive and negative charge cloud centers leading to strong electric fields of 3 MV/cm [33]. This polarization strength and direction are only dependent on the material nature. Calculated spontaneous polarization and piezoelectric constants for metal-polarity group-III nitrides are given in Table 1.3. Polarization is dependent on the polarity of the crystal. In other words, whether the bonds along the c-direction are from cation sites to anion (group-III metal – N) or visa versa [34, 38]. In general, the [0001] axis points out from the N-plane to group-III-metal-plane (Ga, Al, In) and marks the positive c-direction. If the bonds along the c-direction (single vertical bond) are from the cation to anion atoms, then the layer's polarity is said to be (Ga, Al, In)-polarity. In the N-polarity layers, the bonds along the c-direction are from anion to cation atoms. This can be seen clearly in a ball-and-stick diagram of a tetrahedral bond between (Ga, Al or In) and N in different polarities configurations presented in Figure 1.4. The figure also presents spontaneous polarization direction P in different polarities of group-III nitride materials (see Figure 1.4 (a), (b)) and the cause of this spontaneous polarization (see Figure 1.4 (c), (d)). AlN has the largest spontaneous polarization and GaN – the smallest, which corresponds well with the nonideality factor for AlN and GaN (see Table 1.2 (c/a)).

Group-III nitride materials also exhibit piezoelectric effects when they are strained along c-direction. Latter effect has two components. One is due to

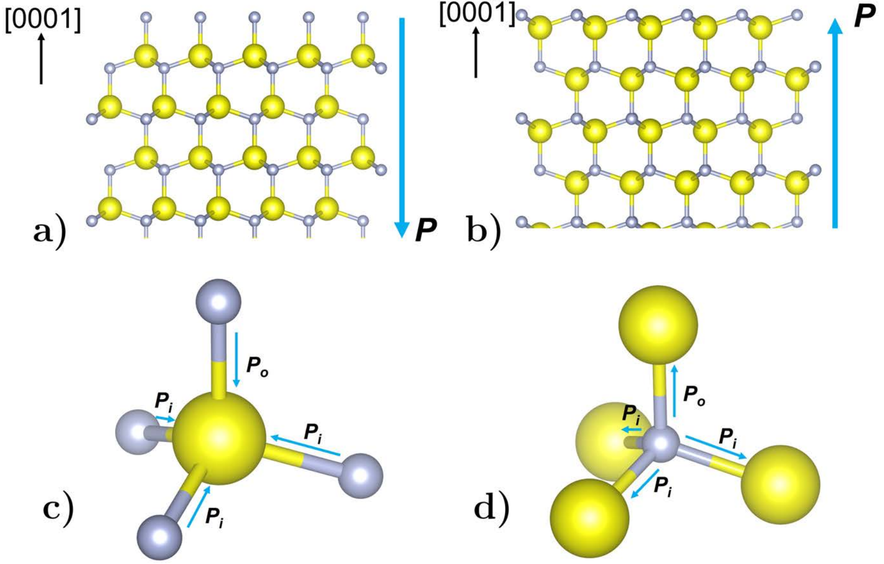

Figure 1.4: Schematic view of atom arrangement of group-III nitrides structure in *a*-plane for (a) group-III metal polarity and (b) N-polarity layers. Configuration of a group-III nitride tetrahedron for (c) group-III metal polarity and (d) N-polarity with polarization vectors for each bond. Yellow balls stand for group-III metal atoms and grey ones - for nitrogen atoms. P_i stands for in-plane dipole, P_o – out-of-plane dipole.

lattice mismatch strain, while the other is due to thermal strain caused by different thermal expansion coefficients between the substrate and the epitaxial layer [34]. The total polarization of the material is the sum of spontaneous and piezoelectric polarizations. Unlike spontaneous polarization, the magnitude of the piezoelectric polarization depends on a strain induced in the epitaxial layer. For the compressive strain, the tetrahedral unit is stretched along the c-axis resulting in a c/a factor increase. Due to this elongated form, the projections of in-plane dipole components P_i (see Figure 1.4 (c) or (d)) onto the c-axis increase as well. Consequently, it partially cancels spontaneous polarization, thus resulting in a total polarization strength decrease. In the tensile strain case, the lattice tends to shrink along the c-axis, increasing the total polarization strength. Unlike spontaneous polarization, piezoelectric polarization can exhibit both induced polarization directions in the same polarity material.

Table 1.3: Calculated spontaneous polarization and piezoelectric constants for metal-polarity group-III nitrides [34, 36].

	Symbol	Units	InN	GaN	AlN
Spontaneous polarization	P_{SP}	C/m^2	-0.032	-0.029	-0.081
Piezoelectric constant in out-of-plane direction	e_{33}	C/m^2	0.97	0.73	1.46
Piezoelectric constant in in-plane direction	e_{31}	C/m^2	-0.57	-0.49	-0.6

1.2. Group-III nitrides optical properties for second harmonic generation (SHG)

Although InN is one of the member of group-III nitride semiconductor family there is no or scarce information about this material application in the second harmonic generation. This could be due to two factors mainly. Firstly, due to a very narrow band gap (0.77 eV) – secondly, difficulties in the InN growth process. Recently Zahedi *et al.* have calculated a third-order susceptibility of InGaN/InN double quantum well structure for efficient third harmonic generation and optimized the structure for 8610 nm and ~10500 nm fundamental wavelengths. [39].

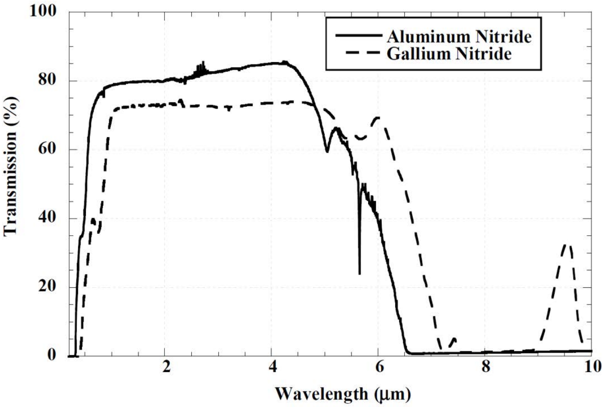

Figure 1.5: Room temperature transmission of bulk nitride crystals. Adapted from [10, 40].

GaN and AlN are both uniaxial birefringent crystals with their optical axis along the c-direction. Both materials exhibit a broad transparency window. The much larger band gap of AlN (6.2 eV) provides the potential for deep ultraviolet (UV) transmission, while lower phonon energies in GaN provide longer midwave transmission [40, 41]. The transparency window for GaN and AlN at room temperature is presented in Figure 1.5. By employing a two-pole Sellmeier equation (Equation (1.1)) and parameters given in Table 1.4, ordinary (o) and extraordinary (e) refractive indices can be obtained.

$$n_i^2 = 1 + \frac{a\lambda^2}{\lambda^2 - \lambda_a^2} + \frac{b\lambda^2}{\lambda^2 - \lambda_b^2}, \tag{1.1}$$

where λ stands for wavelength in μm. Their refractive indices suggest that both materials are positive uniaxial with the higher extraordinary polarization index parallel to the *c*-axis. AlN exhibit significantly higher birefringence than GaN [40]. It is worth noting that both materials exhibit weak temperature dependence on their birefringence, meaning that frequency conversion would be relatively insensitive to temperature fluctuations.

Table 1.4: Parameters for Equation (1.1) enabling to calculate refractive indices for AlN and GaN. Based on [40].

Material	n_i	a (μm^{-2})	λ_a (μm)	b (μm^{-2})	λ_b (μm)
AlN	n_o	3.167	0.1364	1.01	8
AlN	n_e	3.339	0.1433	1.02	8
GaN	n_o	4.166	0.1857	0.64	13
GaN	n_e	4.314	0.1897	0.76	13

The origin of nonlinear optical properties comes from the asymmetric part of the charge distribution of chemical bonding. WZ group-III nitride materials are believed to be related to the excess charge in the bonding region between group-III and nitrogen atoms [34]. The nonlinear polarizability appears when a strong external (incident) electric field causes perturbation on the linear susceptibility. Since AlN and GaN are hexagonal crystals, they have the same form of second-order susceptibility tensor, which is presented in 1.2.

$$\chi_{ij}^{(2)} = \begin{bmatrix} 0 & 0 & 0 & 0 & \chi_{31}^{(2)} & 0 \\ 0 & 0 & 0 & \chi_{31}^{(2)} & 0 & 0 \\ \chi_{31}^{(2)} & \chi_{31}^{(2)} & \chi_{33}^{(2)} & 0 & 0 & 0 \end{bmatrix}. \tag{1.2}$$

Calculating 1.2 tensor, an assumption of negligible absorption is made so that dispersion of the susceptibility can be neglected and Kleinman symmetry can be applied [34,40,42]. After this assumption, WZ group-III nitride crystals have five nonvanishing second-order nonlinear susceptibility tensor elements. In the ideal WZ crystal these elements have a relation given in Equation (1.3). The units of nonlinear susceptibilities are pm/V. In many reports, the second-order nonlinear coefficient is referred to as $d_{ikl} = d_{xyz} = (\chi_{ikl}^{(2)})/2$.

$$\chi_{31}^{(2)} = \frac{-\chi_{33}^{(2)}}{2}. \tag{1.3}$$

In spite of similarity in the crystal structure, GaN and AlN exhibit quite different nonlinear optical behavior. Typical birefringent nonlinear material such as lithium niobate ($LiNbO_3$) ($\chi^{(2)}_{33} = 50 \div 54$ pm/V [43, 44]) employs conventional phase-matching to generate a second harmonic wave, but birefringent-phase-matching in the deep UV region is not reachable. $LiNbO_3$ transparency window is 350 nm $\div$ 5 μm and is comparable with GaN in the shorter wavelength region. GaN, due to its wider transparency window in the longer wavelength region, has an ability to generate wavelength in either the far-infrared or near-UV by sum or difference frequency generation [34]. AlN would have an advantage in the deep UV region. The published values of the second-order nonlinear optical coefficients of AlN range between 1 $\div$ 8 pm/V ($\chi^{(2)}_{33}$) and 0.4 $\div$ 1.6 ($\chi^{(2)}_{31}$). Respectively, measured values for GaN vary between -11.52 $\div$ -7.4 pm/V ($\chi^{(2)}_{33}$) and 4.8 $\div$ 6.9 ($\chi^{(2)}_{31}$) [14,18,34,40,42,43,45,46,46,47].The discrepancies in the values could come from the different GaN and AlN growth results and methods, crystalline quality, different fabrication methods and parameters of the waveguides, and lastly different laser wavelengths used to characterize prepared samples. Calculation results show that second-order nonlinear susceptibility exhibits its dispersion. For the group-III nitrides semiconductors, the value of this coefficient rises as the fundamental wavelength shifts toward shorter wavelengths [43]. Unfortunately, there is quite difficult to achieve SHG via angle-tuned birefringence phase-matching in GaN and AlN due to insufficient birefringence. However, phase-matching can be achieved by either modal-dispersion-phase-matching (MDPM) or quasi-phase-matching (QPM) methods. MDPM method plays on the fact that the waveguide modes of different orders have different effective refractive index dispersion where phase-matching can occur [14, 18]. The QPM method is possible if the sign of the material second-order nonlinear susceptibility is periodically modulated at regular intervals to reset the phase mismatch between fundamental and second harmonic waves without matching the phase velocities [17, 48]. These two methods will be presented more in detail in Chapter 2.

2. INTRODUCTION INTO SECOND HARMONIC GENERATION (LITERATURE OVERVIEW)

2.1. A brief introduction into nonlinear optics

Nonlinear optical phenomena in the sense that they start to play an important role when the response of a material to an applied external electric field depends in a nonlinear manner on the strength of the field. [49] Let's consider how polarization (dipole moment per unit volume) $P(t)$ of a material depends on the strength $E(t)$ of an applied external electric field. In the case of linear optics, the induced polarization depends linearly on the applied electric field. This relation can be described by the relationship

$$P(t) = \varepsilon_0 \chi^{(1)} E(t), \tag{2.1}$$

where ε_0 is the vacuum permittivity and $\chi^{(1)}$ – linear material susceptibility. In nonlinear optics, the material response can be described by generalizing Equation (2.1), where $P(t)$ is expressed as a power series of the external field strength $E(t)$

$$\begin{aligned} P(t) &= \varepsilon_0[\chi^{(1)} E(t) + \chi^{(2)} E^2(t) + \chi^{(3)} E^3(t) + \cdots] \\ &\equiv P^{(1)}(t) + [P^{(2)}(t) + P^{(3)}(t) + \cdots] = \\ &= P^L(t) + P^{NL}(t). \end{aligned} \tag{2.2}$$

The quantities $\chi^{(i)}$, where $i = 1, 2, 3, ...$ in Equation (2.2) are known as the i-th order nonlinear optical susceptibilities. $P(t)$ and $E(t)$ presented in Equation (2.1) and Equation (2.2) can be treated as scalar quantities when the assumption that the medium responds instantaneously is made. In other words, the medium is lossless and dispersionless. $P^{(L)}(t) \equiv P^{(1)}(t)$ in Equation (2.2) is the linear electric polarization term, which is responsible for linear optical phenomena such as refraction, dispersion and refraction. $P^{(NL)}(t) \equiv P^{(2)}(t) + P^{(3)}(t) + \cdots$ in Equation (2.2) refers to the second-order nonlinear polarization, which is responsible for second harmonic generation, Kerr comb generation and other nonlinear optical phenomena. Second-order nonlinear optical phenomena can only occur in noncentrosymmetric crystals, which do not exhibit inversion symmetry. It is worth noting that third-order nonlinear optical phenomena can occur in both centrosymmetric and noncentrosymmetric materials.

By assuming that nonlinearity is only electronic in origin a simple order of-magnitude estimation of $\chi^{(2)}$ can be made [49,50]. By using this estimation, the lowest-order nonlinear term $P^{(2)}(t)$ should be comparable to the linear term of $P^{(1)}(t)$ when the applied external electric field strength is comparable to atomic electric field strength expressed as

$$E_{at} = \frac{e}{4\pi\varepsilon_0 a_0^2}, \tag{2.3}$$

where e is the charge of the electron and $a_0 = 4\pi\varepsilon_0\hbar^2/m_e e^2$ is the Bohr radius of the hydrogen atom. Form these calculations, E_{at} is found to be about $E_{at} \approx 5 \cdot 10^{10}$ V/m. Under non-resonant excitation, $\chi^{(2)}$ should be of the order of $\chi^{(1)}/E_{at}$, whereas for solid materials $\chi^{(1)}$ is of the order of unity. Thus $\chi^{(2)}$ can be expected of around $\chi^{(2)} \approx 1.9$ pm/V.

For more general case, where optical waves in material exhibit dispersion and losses, nonlinear susceptibility turns out to be a complex quantity relating to the complex amplitudes of the external electric field and polarization. Let express electric field of the incident optical wave as the sum of a number of frequency components as ("prime" denotes a summation over positive frequency components)

$$\vec{E}(\vec{r},t) = \sum_n{}' \vec{E}_n(\vec{r},t), \tag{2.4}$$

where

$$\vec{E}_n(\vec{r},t) = \vec{E}_n(\vec{r})e^{-i\omega_n t} + CC. \tag{2.5}$$

CC stands for complex conjugate. Summation in Equation (2.4) is taken over only for positive frequencies. There is worth to define a slowly varying amplitude of the optical wave electric field. It is defined as

$$\vec{E}_n(\vec{r}) = \vec{A}_n e^{-i\vec{k}_n\cdot\vec{r}} + CC, \tag{2.6}$$

and Equation (2.5) can be rewritten as

$$\vec{E}(\vec{r},t) = \sum_n{}' \vec{A}_n e^{i(\vec{k}_n\cdot\vec{r}-\omega_n t)} + CC. \tag{2.7}$$

In Equation (2.7) optical electric field $\vec{E}(\vec{r},t)$ is represented in the form of monochromatic plane wave. To simplify Equation (2.7) new notation of external field amplitudes should be used. These new notations are presented in Equation (2.8) and Equation (2.9).

$$\vec{E}_n = \vec{E}(\omega_n) \;\; and \;\; \vec{A}_n = \vec{A}(\omega_n), \tag{2.8}$$

where

$$\vec{E}(-\omega_n) = \vec{E}(\omega_n)^* \quad and \quad \vec{A}(-\omega_n) = \vec{A}(\omega_n)^*. \tag{2.9}$$

Using this new notation total external field can be rewritten in more compact form

$$\begin{aligned}\vec{E}(\vec{r},t) &= \sum_n \vec{E}(\omega_n)e^{-i\omega_n t} \\ &= \sum_n \vec{A}(\omega_n)e^{i(\vec{k}_n\cdot\vec{r}-\omega_n t)}.\end{aligned} \tag{2.10}$$

Here in Equation (2.10) summation is done over all frequencies. Using similar form to that as in Equation (2.11), nonlinear polarization can also be expressed as the sum of a number of frequency components.

$$\vec{P}(\vec{r},t) = \sum_n \vec{P}(\omega_n)e^{-i\omega_n t}. \tag{2.11}$$

The components of the second-order susceptibility tensor $\chi^{(2)}_{ijk}(\omega_n + \omega_m, \omega_n, \omega_m)$ can be defined by expanding the electric polarization vector in terms of its components

$$P_i(\omega_n+\omega_m) = \varepsilon_0 \sum_{jk}\sum_{(nm)} \chi^{(2)}_{ijk}(\omega_n+\omega_m,\omega_n,\omega_m)E_j(\omega_n)E_k(\omega_m). \tag{2.12}$$

Here indices *i, j, k* are the Cartesian *x, y, z* components of the fields. Notation (mn) indicates the summation over n and m. The sum $\omega_n + \omega_m$ is fixed, while separate components ω_n and ω_m can vary. Since the amplitudes $E(\omega_n)$ and $E(\omega_m)$ are time-dependent, hence the product of these amplitudes contributes to the nonlinear polarization oscillating at frequency $\omega_n + \omega_m$:

$$E(\omega_n)E(\omega_m) \sim exp(-i\omega_n t)exp(-i\omega_m t) \Rightarrow exp(-i(\omega_n+\omega_m)t). \tag{2.13}$$

2.2. Second harmonic generation (SHG)

In second harmonic generation a pump (fundamental) wave of frequency ω after propagation through nonlinear media with nonzero $\chi^{(2)}$ generates a signal at frequency 2ω [51]. By employing Equation (2.12) and performing summation over field frequencies second-harmonic polarization field can be obtained

$$P_i(2\omega) = \varepsilon_0 \sum_{jk} \chi^{(2)}_{ijk}(2\omega,\omega,\omega)E_j(\omega)E_k(\omega). \tag{2.14}$$

Assuming that optical field is polarized along x direction, then Equation (2.14) becomes

$$P_i(2\omega) = \varepsilon_0 \chi^{(2)}_{ixx}(2\omega, \omega, \omega) E_x^2(\omega). \tag{2.15}$$

In the wurtzite crystal structures, when light is polarized along optical axis, due to symmetry $\chi^{(2)}_{ijk}(2\omega, \omega, \omega)$ is reduced to

$$\chi^{(2)} = 2\varepsilon_0 d_{33}. \tag{2.16}$$

Explanation of conditions required for generating second harmonic wave starts from solving the wave propagation equation derived from Maxwell in a weakly nonlinear medium. To simplify wave equation, relation of $\nabla \times (\nabla \times \vec{E}) = \nabla(\nabla \cdot \vec{E}) - \nabla^2 \vec{E}$ can be used. Thus following equation is

$$\nabla^2 \vec{E} - \frac{1}{c^2}\frac{\partial^2 \vec{E}}{\partial t^2} = \frac{1}{\varepsilon_0 c^2}\frac{\partial^2 \vec{P}_{NL}}{\partial t^2}. \tag{2.17}$$

The term appearing on the right-hand side, nonlinear polarization, in Equation (2.17) is responsible for inducing electromagnetic wave with the same frequency ω as the nonlinear polarization wave $\vec{P}(\vec{r}, t)$. Assuming that optical and nonlinear polarization waves are plane waves and propagate along the z-axis then $\vec{E}$ field and $\vec{P}$ are

$$\vec{E}(\vec{r}, t) = Re[\vec{e}A(z,t)exp[i(kz - \omega t)]], \tag{2.18}$$

$$\vec{P}_{NL}(\vec{r}, t) = Re[\vec{e}_p P_{NL}(z,t)exp[i(k_p z - \omega t)]]. \tag{2.19}$$

In Equation (2.18) k and $A(z,t)$ are the wave vector and envelope of the electric field (slowly varying amplitude in time), while in Equation (2.19) k_p and $P_{NL}(z, t)$ are the wave vector and the envelope of the polarization wave, respectively. For slowly varying envelope function, relations of $|\partial^2 A/\partial z^2| \ll |k\partial A/\partial z|$, $|\partial^2 A/\partial t^2| \ll |\omega \partial A/\partial t|$, and $|\partial^2 \vec{P}_{NL}/\partial t^2| \approx -\omega^2 \vec{P}_{NL}$ can be applied to Equation (2.17). Inserting Equation (2.18) and Equation (2.19) into Equation (2.17), the latter can be reduced

$$\frac{\partial A}{\partial z} + \frac{1}{u}\frac{\partial A}{\partial t} = \frac{i\omega^2}{2\varepsilon_0 k c^2} P_{NL} exp(i\Delta k z). \tag{2.20}$$

In Equation (2.20) u denotes for light velocity. If light propagates in nondispersive medium, then u is the light speed in a vacuum. Otherwise, group velocity $u = (\partial k/\partial \omega)^{-1}$ and $\Delta k = k_p - k$ is the wave vector mismatch [52].

For simplicity, let assume that A does not depend on time, then Equation (2.20) can be written as

$$\frac{\partial A}{\partial z} = \frac{i\omega^2}{2\varepsilon_0 k c^2} P_{NL} exp(i\Delta kz), \tag{2.21}$$

also fundamental and second harmonic waves exhibit this form:

$$E_\omega(z,t) = A_\omega(z) exp[i(k_\omega z + \omega t)], \tag{2.22}$$

$$E_{2\omega}(z,t) = A_{2\omega}(z) exp[i(k_{2\omega} z + 2\omega t)]. \tag{2.23}$$

As already was mentioned second-order polarization results from the fundamental optical wave with frequency ω, thus nonlinear polarization is written as

$$\begin{aligned} P_{NL}(z,t) &= \varepsilon_0 \chi^{(2)} (A_\omega exp[i(k_\omega z - \omega t)])^2, \\ &= \varepsilon_0 \chi^{(2)} (A_\omega^2 exp[i(2k_\omega z - 2\omega t)]). \end{aligned} \tag{2.24}$$

Then substituting Equation (2.23) and Equation (2.24) into Equation (2.17) and perform similar reduction presented earlier, the resulting equation for second harmonic wave can be written as

$$\frac{\partial A_{2\omega}}{\partial z} = \frac{i(2\omega)^2 \chi^{(2)}}{2\varepsilon_0 k_{2\omega} c^2} |A_\omega|^2 exp(i\Delta kz), \quad \chi^{(2)} = 2\varepsilon_0 d_{33},$$

$$\frac{\partial A_{2\omega}}{\partial z} = \frac{i(2\omega)^2 d_{33}}{k_{2\omega} c^2} |A_\omega|^2 exp(i\Delta kz). \tag{2.25}$$

In Equation (2.25) $\Delta k = 2k_\omega - k_{2\omega}$ is the wave vector mismatch between fundamental and second harmonic waves and A_ω is the field amplitude of the fundamental wave. Taking into account that $k = n2\pi/\lambda$, thus Δk is

$$\Delta k = 2\frac{2\pi}{\lambda} n_\omega - \frac{2\pi}{\lambda/2} n_{2\omega} \Rightarrow \Delta k = \frac{4\pi}{\lambda}(n_\omega - n_{2\omega}), \tag{2.26}$$

where λ is a fundamental wavelength and n_i, where $i = \omega, 2\omega$ – material refractive index for fundamental and second harmonic wavelengths, respectively. In the undepleted pump approximation ($A_\omega = const$), by integrating Equation (2.25) expression for the generated second harmonic wave $A_{2\omega}(L)$ as a function of propagation length L can be found:

$$A_{2\omega}(L) = \frac{i(2\omega)^2 d_{33}}{k_{2\omega} c^2} |A_\omega|^2 \left(\frac{exp(i\Delta kL) - 1}{i\Delta k} \right). \tag{2.27}$$

Intensities of these optical signals are given as [49]:

$$I_{2\omega} = 2n_{2\omega}\varepsilon_0 c |A_{2\omega}(L)|^2, \quad I_\omega = 2n_\omega \varepsilon_0 c |A_\omega|^2. \tag{2.28}$$

By substituting $A_{2\omega}(L)$ from Equation (2.27) into Equation (2.28) and performing mathematical manipulation, the following equation of the second harmonic intensity as a function of propagation length can be found. Its form is presented down below:

$$I_{2\omega} = \frac{2\omega^2 d_{33}^2}{\varepsilon_0 c^3 n_\omega^2 n_{2\omega}} |I_\omega|^2 L^2 \operatorname{sinc}^2\left(\frac{\Delta k L}{2}\right). \tag{2.29}$$

From Equation (2.29) can be seen that if $\Delta k \neq 0$ second harmonic intensity follows a sinusoidal function over the propagation length L. The phase-matching condition case, $\Delta k = 0$, gives a constant increase in the second harmonic intensity over the L. This means that in order to continuously increase the second harmonic intensity wave vector of the second harmonic wave must be in phase with a polarization wave induced by the fundamental wave with frequency ω. Equation (2.26) gives the most straightforward idea of how the phase-matching condition can be achieved. One more parameter can be derived from Equation (2.29). It is coherence length l_c, which describes a propagation length after which phase-mismatch between fundamental and second harmonic waves reaches π value

$$l_c = \frac{\pi}{\Delta k}. \tag{2.30}$$

2.3. Optical Waveguiding principles

The previous section gives an overall idea of the second harmonic generation. The main conclusion that must be taken out is that fundamental and second harmonic waves must be phase-matched to have continuous coupling between these waves. But this notation describes the effect while electromagnetic waves propagate in a bulk material. However, in MOVPE technology, GaN and AlN layers thickness does not exceed 20 μm for the GaN case. For AlN, thicknesses are even lower. Then optical waveguiding principles come to play and it is necessary to consider the propagation of transverse-magnetic (TM) and transverse-electric (TE) optical modes. As mentioned in Section 1.2, second-order nonlinear susceptibility coefficient $\chi_{33}^{(2)}$, which is along the c-axis, exhibits larger values than $\chi_{31}^{(2)}$, which is in-plane of a waveguide. Thus, TM optical mode could lead to higher second harmonic conversion efficiencies than TE optical modes. Due to this fact, a larger emphasis by other scientists is made on TM mode description in group-III nitrides waveguides.

Let's consider a three-layer planar waveguide, presented in Figure 2.1. The layers are assumed to be infinite in the z and y directions, while the n_2 waveguide core material is finite in x direction with a thickness of D. The model structure presented in Figure 2.1 is infinite in two directions. It cannot be considered a real waveguide from a strict point of view, but this platform creates a base for further analysis of more complex waveguide structures.

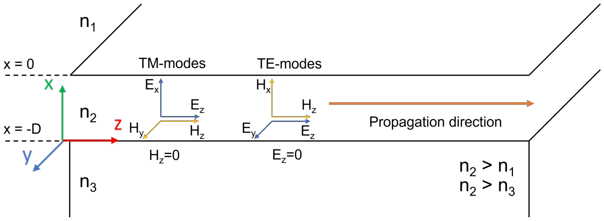

Figure 2.1: Schematic diagram of a three-layer planar waveguide. Waveguide core material (n_2) is optically denser in comparison to the other structure materials (n_3, n_1).

Optical mode is a spatial distribution of optical energy in one or more dimensions [53]. Another more mathematical description of optical modes is orthogonal solutions of Maxwell's wave equation [54] given in Equation (2.31). It is worth noting that light (photons) within the same optical mode is coherent and does not interfere.

$$\nabla^2 \vec{E}(\vec{r},t) - \frac{n^2(\vec{r},t)}{c^2}\frac{\partial^2 \vec{E}(\vec{r},t)}{\partial t^2} = 0, \tag{2.31}$$

where $\vec{E}(\vec{r},t)$ is the electric field vector, $\vec{r}$ – radius vector and $n(\vec{r})$ index of refraction dependent on the radius vector. Remembering that $\vec{E}(\vec{r},t) = \vec{E}(\vec{r})exp(i\omega t)$ and optical mode is propagating along the z direction $\vec{E}(\vec{r}) = \vec{E}(x,y)exp(i\beta z)$, Equation (2.31) can be rewritten as

$$\frac{\partial^2 \vec{E}(x,y)}{\partial x^2} + \frac{\partial^2 \vec{E}(x,y)}{\partial y^2} + [k^2 n^2(\vec{r}) - \beta^2]\vec{E}(x,y) = 0, \tag{2.32}$$

where β is the propagation constant of a particular optical mode. Since the waveguide structure described here is infinite in the y direction, Equation (2.32) can be rewritten for three regions in the x direction as

$$\begin{aligned} n_1 :\quad & \frac{\partial^2 E(x,y)}{\partial x^2} + [k^2 n_1^2 - \beta^2]E(x,y) = 0 \\ n_2 :\quad & \frac{\partial^2 E(x,y)}{\partial x^2} + [k^2 n_2^2 - \beta^2]E(x,y) = 0 \\ n_3 :\quad & \frac{\partial^2 E(x,y)}{\partial x^2} + [k^2 n_3^2 - \beta^2]E(x,y) = 0. \end{aligned} \tag{2.33}$$

$E(x,y)$ is one of the Cartesian $\vec{E}(x,y)$ components. Depending on $k^2 n_i^2 - \beta^2, i = 1,2,3$, whether it is greater or less than 0, solutions of Equation (2.33) can be either sinusoidal or exponential functions of x for every region. Two assumptions must be taken into account that $E(x,y)$ and $\partial E(x,y)/\partial x$ must be continuous between layers (at $x = 0$ and $x = -D$).

To derive TE and TM modes for the waveguide presented in Figure 2.1 one more assumption must be made, i. e. there are no reflections in the x direction, except for reflections occurring at the n_1–n_2 and n_2–n_3 interfaces. For TE mode case traveling along the z direction, E_x, E_z and H_y are zero [53, 55], while H_x and H_z have the form

$$H_x(x,z,t) = -\frac{\beta}{\omega\mu_0} E_y(x,z,t), \tag{2.34}$$

$$H_z(x,z,t) = \frac{i}{\omega\mu_0} \frac{\partial E_y(x,z,t)}{\partial x}. \tag{2.35}$$

Wave equation solutions (Equation (2.31)) for TE optical modes have the form

$$E_y(x,z,t) = \mathcal{E}_y(x) exp[i(\omega t - \beta z)], \tag{2.36}$$

where $\mathcal{E}_y(x)$ is transverse function

$$\mathcal{E}_y(x) = \begin{cases} C exp(-qx), & (0 \leq x \leq \infty); \\ C[\cos(hx) - \frac{q}{h}\sin(hx)], & (-D \leq x \leq 0); \\ C[\cos(hD) + \frac{q}{h}\sin(hD)] exp[p(x+D)], & (-\infty \leq x \leq -D). \end{cases} \tag{2.37}$$

D is the thickness of the given waveguide and C is a normalization constant. The following q, h and p constants are obtained from the substitution of Equation (2.37) into Equation (2.36) and then by solving the Maxwell equation for $E_y(x,z,t)$ and taking into count continuity requirements at the interfaces. These results are

$$\begin{aligned} q &= \sqrt{\beta^2 - n_1^2 k^2}, \\ h &= \sqrt{n_2^2 k^2 - \beta^2}, \\ p &= \sqrt{\beta^2 - n_3^2}, \\ k &= \omega / c. \end{aligned} \tag{2.38}$$

All the constants given in Equation (2.38) are expressed in terms of the unknown propagation constant β, which is the propagation constant along the z direction. β can be derived by taking $\partial E_y / \partial x$ on Equation (2.37) and making it continuous at $x = -D$. Thus after some mathematical operations, the equation for β has the form of

$$\tan(hD) = \frac{p+q}{h(-pq/h^2)}. \tag{2.39}$$

The latter equation is transcendental, in conjunction with Equation (2.38) can be solved graphically by plotting two sides of Equation (2.39) as a function of β and finding the intersection points, or solved numerically. As only the case for total internal reflection is considered, the value of β is limited by the surrounding layer. Thus β value varies between kn_3 and kn_2: $kn_3 < \beta < kn_2$. After solving Equation (2.39) a discrete number of solutions for $\beta_{(m)}, m = 0, 1, 2, ...$ are obtained. An effective refractive index for a particular optical mode can be derived with

$$n_{(m),eff} = \frac{\beta_{(m)}}{k}. \tag{2.40}$$

Normalization constant for TE modes is given as

$$C_{(m)} = 2h_{(m)} \left[\frac{\omega\mu_0}{|\beta_{(m)}|(D + 1/q_{(m)} + 1/p_{(m)})(h_{(m)}^2 + q_{(m)}^2)} \right]^{1/2}, \tag{2.41}$$

where μ_0 is magnetic permeability.

The TM optical modes derivation process is similar to the TE modes case. In the TM modes case, non-zero components of the electromagnetic field are H_y, E_x and E_z, while in the TE case, non-zero components are E_y, H_x and H_z. The resulting field components for the TM case are:

$$H_y(x, z, t) = \mathcal{H}_y(x) exp[i(\omega t - \beta z)], \tag{2.42}$$

$$E_x(x, z, t) = \frac{i}{\omega\varepsilon_0}\frac{\partial H_y}{\partial z} = \frac{\beta}{\omega\varepsilon_0}\mathcal{H}_y(x) exp[i(\omega t - \beta z)], \tag{2.43}$$

$$E_z(x, z, t) = -\frac{i}{\omega\varepsilon_0}\frac{\partial H_y}{\partial x}. \tag{2.44}$$

Then transverse function for the TM modes case $\mathcal{H}_y(x)$ is given by

$$\mathcal{H}_y(x) = \begin{cases} C - \frac{h}{\tilde{q}} exp(-qx), & (0 \leq x \leq \infty); \\ C[-\frac{h}{\tilde{q}}\cos(hx) + \sin(hx)], & (-D \leq x \leq 0); \\ -C[\frac{h}{\tilde{q}}\cos(hD) + \sin(hD)] exp[p(x + D)], & (-\infty \leq x \leq -D). \end{cases} \tag{2.45}$$

where h, q and p are the same constants as in Equation (2.38) with one additional $\tilde{q}$ defined as

$$\tilde{q} = \frac{n_2^2}{n_1^2} q. \tag{2.46}$$

A similar method to the TE case is used to find the $\beta_{(m)}$ propagation constant for particular TM optical modes. The transcendental equation for the TM case is

$$\tan(hD) = \frac{h(\tilde{p}+\tilde{q})}{h^2\tilde{p}\tilde{q}}, \tag{2.47}$$

where $\tilde{p}$ is given by

$$\tilde{p} = \frac{n_2^2}{n_3^2}p. \tag{2.48}$$

The normalization constant for TM modes is given as

$$C_{(m)} = 2\left(\frac{\omega\varepsilon_0}{\beta_{(m)}D_{eff}}\right)^{1/2}, \tag{2.49}$$

where D_{eff} is effective thickness and is given by

$$D_{eff} = \frac{\tilde{q}^2+h^2}{\tilde{q}}\left(\frac{D}{n_2^2} + \frac{q^2+h^2}{\tilde{q}^2+h^2}\frac{1}{n_1^2 q} + \frac{p^2+h^2}{\tilde{p}^2+h^2}\frac{1}{n_3^2 p}\right). \tag{2.50}$$

Boundary conditions assumed in this modeling and transcendental equations (Equation (2.39) and Equation (2.47)) give an overall understanding that $\beta_{(m)}$has only discrete values giving rise to the multiple and discrete TE and TM optical modes. It is worth noting that allowed optical modes are dependent on the waveguide thickness D, refractive index n_i of the three layers and the wavelength λ.

2.4. Modal dispersion phase matching (MDPM) in group-III nitrides

One second harmonic generation method in the waveguides is modal-dispersion-phase-matching (MDPM). Due to large modal dispersion in GaN and AlN waveguides, MDPM cannot be achieved between zero-order modes. Generally, MDPM is achieved between zero-order fundamental wave and higher-order modes of second harmonic wave [14, 56, 57]. The main drawback of the MDPM method in second harmonic generation efficiency is that interaction between fundamental and higher order modes depends on their modal field overlap. As mentioned before, using TM mode SHG efficiency can potentially be higher due to a larger second-order nonlinear coefficient.

Using Equation (2.43) which describes the electric field along the x direction in the waveguides, Equation (2.25) can be transformed into

$$A_{2\omega}^{(s)}(L) = \left(\frac{4\omega n_{2\omega}^2}{\beta_{2\omega}^{(s)}}\right)\left(\frac{\beta_{\omega}^{(m)}}{\omega n_{\omega}^2}\right)^2 \frac{i(2\omega)^2}{\beta_{2\omega}^{(s)}c^2} d_{33}|A_{\omega}^{(m)}|^2 \left(\frac{[exp(i\Delta\beta L)] - 1}{i\Delta\beta}\right)\sqrt{\Gamma_{2\omega,\omega}}, \tag{2.51}$$

where $\Gamma_{2\omega,\omega}$ is already mentioned overlap of the fundamental and second harmonic modes, $\beta_{2\omega}^{(s)}$ and $\beta_{\omega}^{(m)}$ are the waveguide modes for second harmonic and the fundamental waves, respectively. Again, $\Delta\beta$ is the wave vector mismatch between optical modes, which in this case between fundamental and second harmonic waves. The overlap is described by

$$\Gamma_{2\omega,\omega} = C\left(\int_{-\infty}^{+\infty} d_{33}(x)(\mathcal{H}_y^{\omega,(m)}(x))^2 \mathcal{H}_y^{2\omega,(s)}(x)\, dx\right)^2. \tag{2.52}$$

In Equation (2.52), C is a normalization constant referenced to a perfect overlap between fundamental and second harmonic waves. The intensity for the second harmonic wave is related to the propagation distance as

$$I_{2\omega}(L) \sim |I_{\omega}|^2 L^2 \Gamma_{2\omega,\omega} \operatorname{sinc}^2\left(\frac{\Delta\beta L}{2}\right). \tag{2.53}$$

When the phase-matching condition is fulfilled as $\Delta\beta = 2\beta_{\omega}^{(m)} - \beta_{2\omega}^{(s)} = 0$, then Equation (2.53) is only dependent on the intensity of fundamental wave I_0, propagation distance L and overlap between those modes.

MDPM can be reached either in planar or ridge-type waveguides. The first type does not require any sophisticated fabrication steps after the growth process of the GaN or AlN layers. Nevertheless, it is essential to control surface roughness. Every surface imperfection gives rise to propagation losses, as stated Gromovyi *et al.* [14]. According to his work, relatively small surface roughness with RMS = 4.5 nm can be responsible for relatively high losses as 7 dB/cm for TM0 at 633 nm in planar GaN waveguides. While after optimization processes, when surface roughness was reduced to 1 nm, propagation losses in the planar GaN waveguide were reduced to less than 1 dB/cm for TM0 at 633 nm. Alden *et al.* [15] uses Rayleigh criterion expressed as $RMS < \lambda/(8\cos(\theta_m))$ to evaluate when the surface might be considered as smooth. θ_m in this criterion is an angle of incidence for the mth-order optical mode in the guiding layer. According to Alden's work AlN waveguide with 650 nm thickness, 550 nm fundamental wavelength and the highest-order mode maximum allowed surface roughness RMS value must be less than 60 nm.

On the contrary, Chen *et al.* [58] managed to fabricate a ridge waveguide with 2.5 dB/cm propagation loss at 700 nm wavelength despite the surface roughness in his work being 3.5 nm. In another work done by Soltz *et al.* [59], the propagation loss at 1550 nm wavelength in an optimized planar GaN waveguide reached 0.65 dB/cm, while not optimized planar GaN waveguide exhibited 4 dB/cm propagation loss. It must be mentioned that any surface roughness value in the latter work was not presented. Thus, the second quite important parameter for the performance of the waveguide is a crystal structure or threading dislocation density responsible for charge carriers' mobility deterioration. According to Drude, free carrier loss is proportional to N/μ, where N is the carrier density and μ – carrier mobility. Since GaN is intrinsically n-type doped, it possesses a high density of free carriers ($10^{15} \div 10^{17}$ cm^{-3}), which will contribute to free carrier loss. Threading dislocation reduction results in carrier mobility enhancement and, according to cited [58, 59] works, enhances GaN waveguides performance.

There are not many works that actually present second-harmonic generation in GaN or AlN planar/ridge waveguides. The best-known work, which presents SHG in GaN planar waveguide is Gromovyi's group work [14]. Power conversion efficiency in the latter work was 2%, where the wavelength of a fundamental wave was 1260 nm and propagation losses were less than 1 dB/cm at 633 nm. It is worth noting that propagation losses decrease for the same structure for longer wavelengths. AlN waveguides showed quite outstanding conversion efficiencies. Guo *et al.* fabricated polycrystalline AlN waveguides, which were optimized for a fundamental wave of 1550 nm [60]. Latter work does not provide propagation loss value, but due to optimized ridge waveguide for fundamental and second harmonic optical modes and low propagation losses, the power conversion efficiency was 12%. One more parameter, expressed as $P_{SHG}/P^2_{Fundamental}$, is used in order to describe SHG conversion efficiency in the waveguides. P_{SHG} stands for SHG power and $P_{Fundamental}$ – fundamental wave (pump) power. Thus latter parameter in Guo *et al.* work was 2500%/W. SHG conversion efficiency parameter has been improved by Brunch *et al.* recently [61]. Even though power conversion efficiency in Brunch *et al.* work is comparable to Guo *et al.* work, SHG efficiency was improved from 2500%/W to 17000%/W for a fundamental wave of 1556 nm. Latter work presents SHG generation from single-crystalline AlN waveguides fabricated using AlN epitaxial layers grown by MOCVD. Such improvement in SHG generation efficiency was influenced by lower propagation losses and a larger second-order nonlinear coefficient in single-crystalline AlN than in polycrystalline AlN layers.

2.5. Quasi-phase matching (QPM) in group-III nitrides

Another approach to achieving SHG in weak birefringent materials is the quasi-phase-matching (QPM) technique. In this technique. As was mentioned in Section 2.1, second harmonic intensity periodically oscillates when phase matching is not fulfilled. This is a consequence of the continuous phase slip between fundamental and second harmonic waves, which leads to an alternation in the direction of the flow of power. When the latter condition is fulfilled – the second harmonic intensity grows quadratically with the propagation distance. QPM involves repeated inversion of the relative phase between the fundamental and second harmonic waves after an odd number of coherence lengths [62]. The phase is "reset" periodically so that on average the proper relationship is maintained for the growth of the second harmonic. The most popular approach to achieving periodically phase "resets" is by implementing periodical change in the sign of second-order nonlinear coefficient $\chi^{(2)}$ (or d_{33}) after a propagation distance of coherence length. In group-III nitrides, this can be achieved by periodically inverting crystals' polarity.

Thus in this situation, nonlinear susceptibility coefficient is expressed as follows [63]

$$d_{33}^{eff}(z) = \sum_{m} \frac{2d_{33}\sin(\pi m D)}{m\pi} exp[iK_m z], \tag{2.54}$$

where K_m is the mth-order grating wave vector described as $K_m = (2\pi m)/\Lambda$. Λ is a modulation period of the second-order susceptibility coefficient and is expressed as

$$\Lambda = \frac{\lambda_\omega}{2(n(2\omega) - n(\omega))}. \tag{2.55}$$

The modulation period depends only on the wavelength of the fundamental wave and on the difference in refractive indices. The smaller the difference in refractive indices between fundamental and second harmonic waves, the longer the modulation period. Duty cycle D is expressed as $D = l/\Lambda$, where l is the length of the defined positive direction ($+\chi^{(2)}$, or $+d_{33}$) of the crystal. m denotes the order of QPM. The largest QPM nonlinear coefficient is obtained when $m = 1$. By substituting Equation (2.54) into Equation (2.51) and considering that $\Delta\beta$ converts into ΔK, which is described as $\Delta K = 2\beta_\omega^{(m)} - \beta_{2\omega}^{(s)} + K_m$ amplitude of the second harmonic wave in the QPM method can be obtained. In contrast to MDPM, in QPM it is possible to find such optical modes that their overlap integral $\Gamma_{2\omega,\omega}$ can reach unity. Then by fulfilling the phase-matching condition by tweaking modulation period Λ such $\Delta K = 0$, the intensity of the second-order harmonic wave over the traveled distance is related as follows

$$I_{2\omega}(L) \sim \left(\frac{2d_{33}\sin(\pi m D)}{m\pi}\right)^2 |I_\omega|^2 L^2. \tag{2.56}$$

It is clearly seen that the largest conversion efficiency can be achieved for the first order QPM (m =1) and for duty cycle D =0.5. Taking into account the latter points, Equation (2.56) can be reduced to

$$I_{2\omega}(L) \sim \left(\frac{2d_{33}}{\pi}\right)^2 |I_\omega|^2 L^2. \tag{2.57}$$

From Equation (2.57) results that conversion efficiency is equal about to 40% compared to an ideal case.

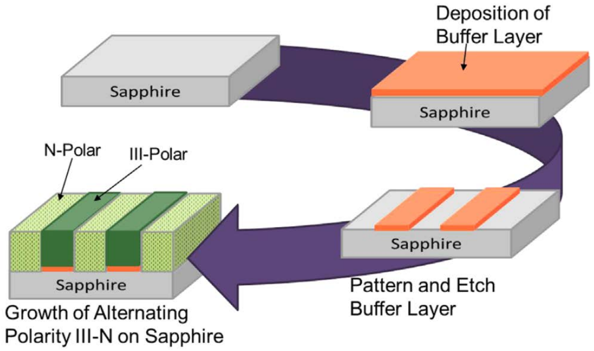

Figure 2.2: Process scheme used to create periodic lateral polarity structures. Adapted from [64].

Several works present second-harmonic generation in GaN and AlN periodic lateral polarity structures. Compared to the MDPM method, samples in the QPM method must be prepared in three steps. These steps are presented in Figure 2.2. The first step starts from the growth of a low-temperature AlN buffer layer which usually exhibits Al-polarity. This first step is done regardless of the GaN or AlN growth. Then, the low-temperature AlN buffer layer is patterned by implementing photolithography and etching techniques. After etching, usually reactive ion etching, process part of the buffer layer is removed and the substrate surface is revealed, where N-polarity GaN or AlN will be grown. The last third step is a simultaneous growth of alternating polarity domains.

The first who presented GaN periodic lateral polarity structure (also known as periodically poled structures) and the second harmonic generation was Chowdhury *et al.* [17]. Latter work GaN lateral polarity structures surface image is presented in Figure 2.3 (a). Moreover, Alden *et al.* was the first who presented a second harmonic generation in AlN lateral polarity structures, which were fabricated in a waveguide form [15, 16]. One of the AlN lateral polarity structure waveguide examples is presented in Figure 2.3 (b). Despite the difference in the growth methods (Chowdhury *et al.* MBE, Alden *et al.* MOCVD), there is one significant similarity between these two samples, i.e., N-polarity GaN or AlN surfaces in these cited works exhibit rough surface morphology. As mentioned before in Section 2.4, it is crucial to control the

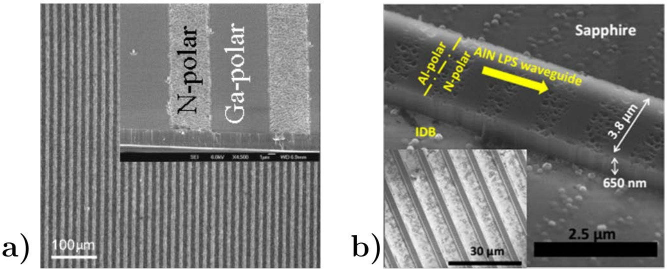

Figure 2.3: (a) GaN QPM structure with periodicity of 17.2 μm, adapted from [17]. (b) AlN QPM waveguide structure with periodicity of 1.2 μm, adapted from [15]. LPS in (b) picture stands for lateral polarity structure, IDB – inversion domain boundary.

surface roughness to avoid optical scattering losses. Alden et al. proved that optical scattering in the N-polarity domains is significantly higher than in the Al-polarity domains due to rough surface morphology. Moreover, the surface uniformity of these structures must be neatly controlled. In other words, there must be the same growth rate for N-polarity and metal-polarity domains. Regardless of scattering losses in Chowdhury *et al.* work they have achieved 0.1% power conversion efficiency at a fundamental wavelength of 1660 nm [17]. Alden *et al.* have exploited third and fifth orders of QPM at fundamental wavelengths of 690 nm and 940 nm, respectively. SHG measurements suggested that power conversion efficiency in the latter work was less than 1% [16].

3. MOVPE TECHNOLOGY (LITERATURE OVERVIEW)

3.1. MOVPE Reactor

MOVPE was a growth method discussed in this thesis for the growth of III-nitrides structures. The equipment used in every growth experiment was Aixtron Ltd. 3x2" (three substrates holding places of 2-inch diameter) Closed-Coupled Showerhead (CCS) MOCVD Reactor, which is presented in Figure 3.1 (left). The main difference between this reactor and conventional ones (vertical or horizontal) is the gas inlet system in a reactor chamber that is placed very close above a susceptor (ranges between $5 \div 25$ mm). The last word of the CCS abbreviation is "showerhead", which describes the whole idea of the gas inlet part shown in Figure 3.1 (right). This is a water-cooled reactor head with two plenums where ones plenums are for III-group precursors and other ones – for V-group precursors. The CCS reactor is based on forming a uniform boundary layer over the substrate and susceptor surfaces [65]. The low distance between the susceptor and showerhead suppresses the risk of the onset of buoyancy within the chamber and ensures a uniform, stable gas flow distribution.

Figure 3.1: Aixtron Ltd. 3x2" CCS reactor and reactor chamber. Left-hand picture adapted from [66].

3.2. MOVPE growth process

The concept of epitaxy originated from observations of mineral paragenesis [67]. Exists a wide variety of mineral paragenesis with definite crystallographic relations between host and guest crystals. Royer [68], who systematically investigated epitaxial relations in mineral crystals, proposed the concept of misfit ratio. Since then, extensive works have been carried out on the mechanism of epitaxial growth. The word "epitaxy" is derived from the ancient Greek words "epi", meaning on and "taxis", meaning arrangement. An epitaxial layer is one that has the same structure as the substrate it is deposited on.

MOVPE is a non-equilibrium growth technique that is based on the vapor transport of the precursors, i. e. for III-V based compounds, group III alkyls – R_3M where R is an organic radical (like CH_3 or C_2H_5) and M is a metal from Group III (like Ga, Al, In or B) and binary hydrogen molecule of group V – EH_3 where E denotes for nonmetal from Group V (like N or As) and their following chemical reactions on a heated substrate resulting in epitaxial growth of a thin film. A general reaction can be written as follows:

$$R_3M_{(g)} + EH_{3(g)} \longrightarrow ME_{(s)} + 3RH_{(g)}. \tag{3.1}$$

The precursors for III-V MOVPE called metalorganics are generally simple alkyl compounds for the group III source and a hydride for the group V source. Group III precursors such as trimethylgallium (TMGa) and trimethylaluminum (TMAl) are liquids and trimethylindium (TMIn) is solid. These compounds are extremely pyrophoric and highly flammable. Group V precursor in the nitride MOVPE technology usually is ammonia (NH_3). Both have the key properties of being volatile in a carrier gas stream and chemically stable at ambient temperature. The metalorganic compounds are usually monomers in the vapor phase except for TMAl, which is dimeric. Metalorganic compounds are stored in containers through which a carrier gas flows. These containers are kept at a specific constant temperature to prevent the possibility of condensation of the chemicals on the walls of the tubing that leads to the reactor chamber and precisely control the vapor pressure of the source material. For example, TMGa has a vapor pressure of 65.4 Torr at 0°C, while triethylgallium (TEGa) has – 4.4 Torr at much higher temperature of 20°C [69]. The carrier gas will saturate with vapor from the metalorganic source and transport it to the heated substrate. The compound molecules will begin to thermally decompose in the MOVPE reactor chamber as they approach the hot susceptor. The temperature at which metalorganic compounds start to decompose is not well defined. This temperature depends on both the surfaces with which a particular compound comes with contact and the gas ambient [70, 71]. The decomposition of metalorganic compounds will also be affected by the residence time near the hot pyrolyzing surface, which depends on a flow rate and reactor geometry. Generally, for most metal alkyls reported decomposition temperatures range between 200°C ÷ 400°C [70–72]. The second purpose of the carrier gas is to carry out the byproducts of the reaction. Typically used carrier gases in MOVPE technology are hydrogen (H_2) and nitrogen (N_2).

Assuming the carrier gas and precursors are ideal gases and are in thermodynamic equilibrium between the condensed source and vapor above it, the molar flow, ν, can be written:

$$\nu = \frac{P_\nu f_\nu}{kT_{std}} \frac{P_{std}}{P_{container}}, \tag{3.2}$$

where ν is the molar flow in mol/min, P_ν is the vapor pressure of the metalorganic compounds at the particular container temperature, f_ν is the volume flow rate of the carrier gas through the container in l/min, k is the gas constant, $T_{std} = 273°C$, $P_{std} = 1$ atm, and $P_{container}$ is the total pressure in the metalorganic container. If $P_{container} < P_\nu$, the content in the container will boil and the molar flow will become unstable. P_ν for TMGa, TMAl and TMIn can be calculated using (3.3), (3.4), (3.5) equations, respectively (P_ν in Torr and T in °K) [69]:

$$TMGa : \log P_\nu = 8.07 - \frac{1703}{T}, \tag{3.3}$$

$$TMAl : \log P_\nu = 8.224 - \frac{2134.83}{T}, \tag{3.4}$$

$$TMIn : \log P_\nu = 10.52 - \frac{3014}{T}. \tag{3.5}$$

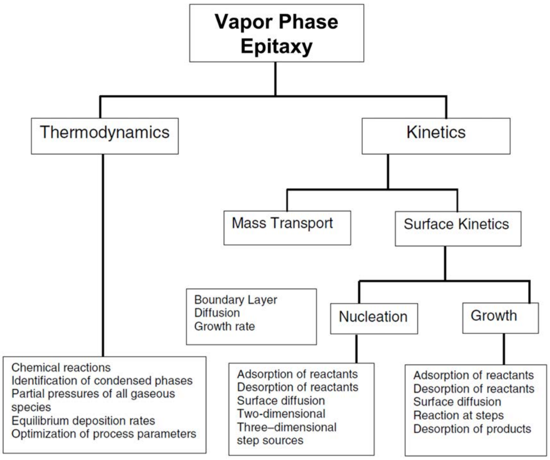

Figure 3.2: Various fundamental driving factors in a MOVPE process. Adapted from [73].

The MOVPE process is very complex and consists of many fundamental factors represented in Figure 3.2,which includes homogeneous and heterogeneous reactions of the group III and group V precursors molecules as well as growth-related surface processes such as adsorption, surface diffusion and desorption. The process is governed by two major mechanisms. The first one is the thermodynamics factor which determines the driving forces of the MOVPE process, giving the direction of chemical change and predicting the equilibrium in the MOVPE system. The second one is kinetics which determines the rate control of homogeneous and heterogeneous chemical reactions. The third one not listed in Figure 3.2 is hydrodynamics, which controls the mass transport of the reactants to the growing solid/vapor interface, velocity profile and total pressure in the reactor. Figure 3.3 schematically represents all the factors mentioned earlier in Figure 3.2 in a very simplified manner and main growth steps. The carrier gas transports the group III and V precursors into the heated reactor zone and gaseous boundary layer, where they undergo gas-phase reactions. Homogeneous gas-phase reactions like pyrolysis and adduct formation occur in a boundary layer. Adduct formation often leads to flaky and/or nonadherent layers. The pyrolysis process partly releases the group III and V atoms (in this case Ga/Al/In and N) [74]. Then atoms and reactants (species) diffuse through a gaseous boundary layer approaching the growing surface. At this moment, heterogeneous reactions begin to play a role. Heterogeneous reactions, which determine growth rate, occur at the vapor/solid phase interface. The best example of a heterogeneous reaction is the adsorption and desorption of the species [74]. Adsorbed species can desorb or migrate along the surface. A heterogeneous pyrolysis reaction can occur for the reactants adsorbed on the growth surface, thus releasing the atoms. Desorbed species from the substrate surface and gaseous byproducts with the help of carrier gas are removed from the boundary layer and exhausted. Adsorbed from the vapor phase and released by heterogeneous pyrolysis reaction atoms diffuse along the surface before the final incorporation reactions into the film occur, thus forming new chemical bonds.

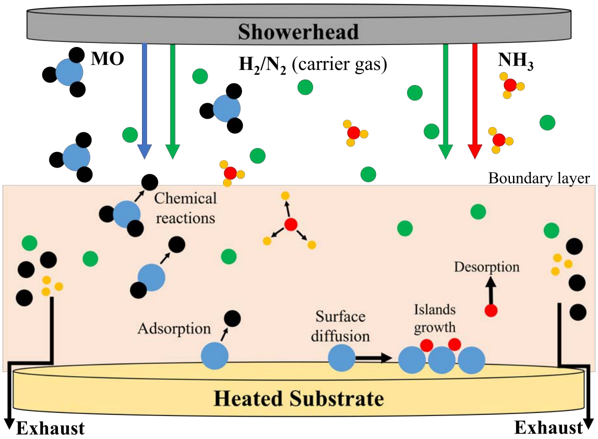

Figure 3.3: Key steps of a MOVPE process. MO denotes for metalorganics.

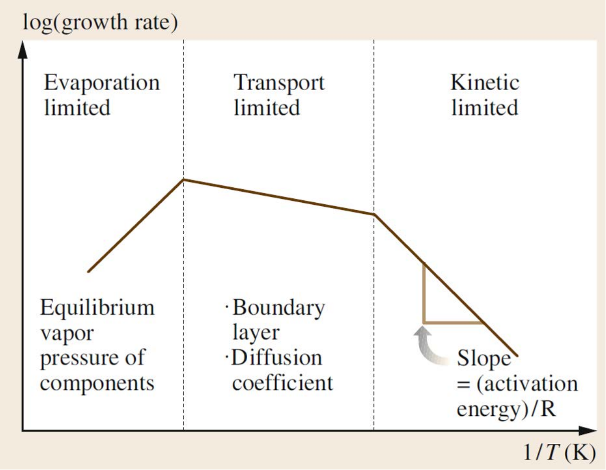

Figure 3.4: Schematics of the three different temperature regimes for epitaxial layer growth in MOVPE technology. Adapted from [75].

One of the most basic growth parameters that are varied in MOVPE is the growth temperature (susceptor's surface temperature). Three regions can be distinguished in Figure 3.4 where growth rate (in log scale) dependence on reciprocal thermodynamic temperature qualitatively is presented. As MOVPE is an exothermic process, the growth rate is controlled by the kinetics of reactions occurring either in the gas phase or on the substrate surface at lower growth temperatures. This region generally is termed a *kinetically limited regime*. According to the Arrhenius equation, the film growth rate in this region can be expected to be a function of the temperature:

$$Growth\ rate \propto \exp(E_A/RT), \tag{3.6}$$

where E_A is the activation energy, R is the gas constant and T is the temperature. At low temperatures, the chemical reaction kinetics is slower than mass transport and will limit the overall growth rate, which will increase exponentially with the temperature.

As the temperature increases, the rate of chemical reactions also increases. The growth rate becomes nearly independent of the temperature. Then, the reactants diffusing (mass transport) to and away from the growth surface through the boundary layer control the growth rate. Since mass transport has weak temperature dependence, the film growth rate is nearly constant. This temperature regime is termed a *mass transport limited regime.*

At high temperatures, the thermodynamics will try to restore the equilibrium through an increased rate of desorption of film precursors or matrix elements from the growth surface. Another equilibrium restoration way is through depletion of reagents on the reactor walls due to parasitic gas-phase side reactions [76]. Gas-phase reactions become more critical with increasing temperature and higher partial pressures of the reactants. The following temperature regime is termed a *thermodynamically limited regime*.

A crucial factor determining the relative importance of each regime is the reactor's pressure [76]. Gas-phase reactions are essential from the atmospheric to the intermediate pressure (10 Torr). A significant role plays kinetics and mass transport in a deposition. As pressure decreases, gas-phase reactions become less critical. At pressures below 1 Torr, layer growth is controlled by surface reactions. By decreasing pressure further ($< 10^{-4}$ Torr)), mass transport is absent and layer growth is influenced by the gas and substrate temperature and by desorption of precursor fragments and grown layer elements from the growth surface [76].

Besides the growth temperature, there are a lot of parameters to consider. In the kinetically limited regime, where the surface plays an important role, surface preparation and orientation must be considered. When the mass transport limits the overall growth rate, parameters such as total flow, which enters the reactor and flow velocity must be considered. These parameters, which influence the overall growth rate, define the optimal parameter window for an efficient growth process.

3.3. Epitaxy of Ga-polarity and N-polarity GaN

For the group III-nitrides growth – in this work, GaN and AlGaN precursors such as TMGa, TMAl and NH_3 were used as sources for Ga, Al and N atoms. In this subsection, the focus will be made mainly on the growth of Ga-polarity and N-polarity GaN kinetics. The following chemical reaction based on the basic formula form (Equation (3.1)) for GaN can be written:

$$(CH_3)_3Ga_{(g)} + NH_{3(g)} \longrightarrow GaN_{(s)} + 3CH_{4(g)}. \tag{3.7}$$

Although the chemical reaction formula (Equation (3.7)) of the GaN growth is straightforward, the growth of the GaN itself is very complicated. The main challenge comes from the lack of lattice-matched growth substrates. Typically, lattice mismatched substrates such as sapphire or silicon carbide (6H-SiC) are employed. Lattice mismatch between GaN basal plane and the sapphire basal plane is about 32%, between GaN and 6H-SiC – -3.5%. (-) sign shows that GaN on 6H-SiC is compressed. Although SiC substrates have a smaller lattice mismatch and are electrically conductive, they are expensive compared to sapphire substrates.

Continuum elasticity theory states that for small lattice misfits ($< 15\%$), epitaxy can occur by the formation of layers that are initially pseudomorphic (strained) [77].While the epilayer thickness increases, its elastic strain increases until it is sufficient to activate misfit dislocation, which occurs when plastic relaxation occurs. For large misfit systems, an elastic theory is no longer valid and is expected to result in a breakdown of epitaxial growth. With a lattice mismatch higher than 15%, polycrystalline growth is observed. This thickness after which plastic relaxation occurs is called as critical thickness and it varies inversely to mismatch value. Nevertheless, the problems related to the lattice-mismatch were first overcome by H. Amano, I. Akasaki and later S. Nakamura. They all managed to grow high quality, single-crystal GaN layer on the sapphire substrates by employing a two-step growth technique. Amano and Akasaki have used a thin low-temperature (LT) AlN layer (900 ÷ 1000°C), which served as a buffer layer for high-quality GaN [78, 79], while Nakamura has used low-temperature (LT) GaN (450 ÷ 600°C) as buffer layer [80].

However, though Amano, Akasaki and Nakamura teams have shown a high degree of mastery over the III-N material system, the growth of high-quality GaN was then far from being well understood. It has been evidenced that the use of a LT buffer layer must be related to a nitridation step of a sapphire substrate before the GaN growth. Later, it was reported that the nitridation process is crucial for growing high-quality III-N compounds on the sapphire substrates, whatever the growth technique [81–86]. The first who attempted to explain the nitridation effect and GaN growth on the sapphire substrates was Grandjean and his team [87]. He studied different GaN layers grown by molecular beam epitaxy (MBE) on the nitrided and non-nitrided sapphire substrates by employing reflection high-energy electron diffraction (RHEED) and high-resolution transmission electron microscopy methods. He has measured in-plane lattice mismatch, which formed during nitridation and growth processes. After 10 minutes of the nitridation process, lattice-mismatch saturated at ~13%, which corresponds to the theoretical mismatch between AlN and sapphire. Such lattice mismatch can only be reached if the AlN lattice with respect to the sapphire substrate unit cell is rotated by 30° in the basal plane.After the nitridation process, GaN growth was followed and lattice-mismatch resulted in about 16%, which is about two times smaller than reported earlier (32%). The growth direction of GaN, which is denoted as *c*-direction (0001), was preserved with nitrided sapphire substrates *c*-direction (0001). These results mean that III-N nitride compounds crystal lattice rotates by 30° with respect to sapphire substrate crystal lattice in the basal plane. The epitaxial relationship between III-N compounds and sapphire is $[11\bar{2}0]_{\text{III-N}} \| [1\bar{1}00]_{\text{sapphire}}$ in the basal plane, and $[0001]_{\text{III-N}} \| [0001]_{\text{sapphire}}$ in the out-of-plane direction. Indeed, this 30° rotation gives a possibility to grow III-N compounds on the sapphire substrates. This epitaxial relationship is presented in Figure 3.5.

The growth of Ga-polarity and N-polarity GaN concerning the growth process itself does not have many differences. A two-step growth technique is employed for both Ga-polarity and N-polarity GaN layers. Although the GaN growth is called a two-step process, the entire process is a sequence of more

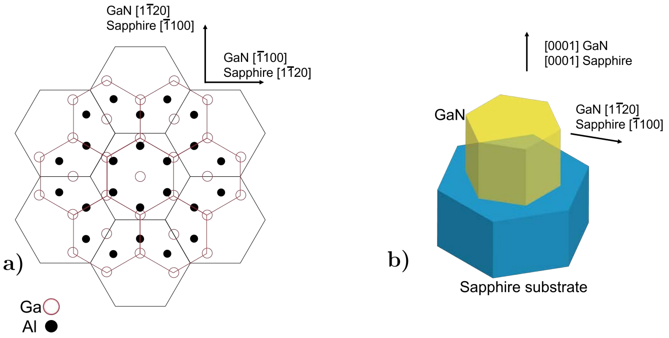

Figure 3.5: (a) Projection of bulk basal-plane sapphire and GaN cation positions for the observed epitaxial relationship. The black circles mark aluminum atom positions and the black lines show the sapphire basal-plane unit cells. The open red circles marks gallium atom positions and the red lines show the GaN basal-plane unit cells. The aluminum atoms on the sapphire plane sit at positions approximately 0.5 Å above and below the plane position. Figure based on [88]. (b) Shows a schematic illustration of the epitaxial relationship between GaN and sapphire (0001) representing the 30° rotation of the GaN basal plane. Figure based on [77].

than the two mentioned steps. The main difference in the growth of two different polarities is growth parameters and starting conditions. Growth diagrams of Ga-polarity and N-polarity GaN are presented in Figure 3.6 with important growth processes.

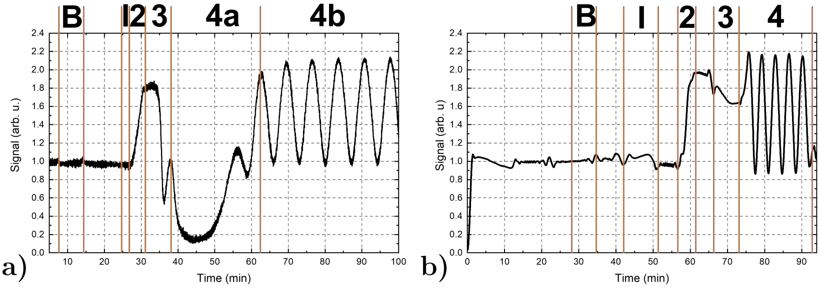

Figure 3.6: (a) Ga-polarity GaN growth diagram. (b) N-polarity GaN in situ growth diagrams.

For Ga-polarity GaN layer growth, sapphire substrates with lower off-cut angle (0.2° ÷ 0.3°) are usually chosen, while for N-polarity GaN – sapphire substrates with higher off-cut angle (2° ÷ 4°) are preferred. The whole growth process starts with high-temperature (HT) heat treatment of the sapphire substrate under H_2 ambient. Usually, temperatures are elevated up to 1130°C (in our reactor) and the treatment lasts for 5 minutes. This heat treatment is denoted as "B" in Figure 3.6. The same high-temperature treatment process is employed for N-polarity GaN also. The Sapphire surface is cleaned out of possible adsorbed organic molecules (contaminants), which will desorb from the surface during this treatment. After the high-temperature treatment process, each growth diagram presented in Figure 3.6 can be divided into four major stages.

- Nitridation stage: In Figure 3.6, it is denoted as "I". It is the most crucial step for determining the polarity of the GaN layer. Although nowadays, every growth process after substrate cleaning starts with the nitridation process, no one fully understands what happens during this initial stage. Several observations will be presented later. In polarity selection, the duration and temperature of the nitridation process play an essential role. For Ga-polarity GaN nitridation process lasts for 2 ÷ 3 minutes at 575°C, while for N-polarity GaN – 7 ÷ 8 minutes at 990°C. There is no difference in Figure 3.6 (a and b) reflectance signal during this process and signal stays at the bare sapphire level.

- LT-GaN buffer growth stage: In Figure 3.6, it is denoted as "2". During this stage GaN nucleation layer is grown. The sapphire is covered with GaN nuclei, randomly distributed on the surface. Those nuclei thickness does not exceed the critical value, after which the layer becomes polycrystalline with a rough surface [79]. Because different initial sapphire substrates are used for different GaN polarities, more densely packed and uniform nuclei are formed on the sapphire substrates with a higher offcut angle. It is crucial for N-polarity GaN's further growth process. In this stage reflectance signal in Figure 3.6 (a and b) rises, showing the formation of the GaN buffer layer. This increase is due to the difference between the refractive index of the sapphire and GaN. Usually, for Ga-polarity GaN layers, buffer growth temperatures are much lower than for N-polarity GaN. Our case is 575°C (Ga-polarity GaN) and 720°C (N-polarity GaN). Due to hindered diffusion for Ga atoms on the N-terminated N-polarity GaN surface compared to the Ga-terminated Ga-polarity GaN surface, higher temperatures are needed [89, 90].

- Buffer annealing stage: In Figure 3.6, it is denoted as "3". In this step, the reactor temperature is ramped and the annealing process starts to present itself as a decrease in reflectance signal in Figure 3.6 (a, b). The Ga-polarity case annealing process ends with a slight increase in the reflectance signal after a sharp decrease. This behavior is attributed to a scattering effect by a newly modified rough surface due to the formation of larger islands by the Ostwald ripening effect [91] (recrystallization) and an overall decrease in the layer thickness resulting from the partial evaporation process. Only a slight signal drop is present for N-polarity GaN during the whole annealing process (see Figure 3.6 (b)). In the latter case, the surface consists of a high density of grains and no recrystallization occurs. It is likely due to the limited Ga atom diffusion mentioned earlier. During this process, there is no any source of Ga apart from evaporated GaN nuclei. Only NH_3 and carrier gas are fed to the reactor chamber.

- HT-GaN growth stage: In Figure 3.6, it is denoted as "4". This stage for Ga-polarity GaN begins by completing the previously started coalescence of the annealed layer. Ga source in this stage is resumed and the GaN layer starts to grow in both directions, i. e., in the lateral and vertical directions. A three-dimensional (3D) growth mode makes GaN islands coalesce into a single-crystal layer. At the end of coalescence step (see Figure 3.6 (a) "4a" and "4b" transition), the growth in the lateral direction is promoted. Thus 3D growth mode switches into two-dimensional (2D) growth mode. The surface at this transition point is already optically smooth and further GaN growth established a smooth surface with well-defined steps on the surface. These growth steps manifest themselves in Figure 3.6 (a) as reflectance signal drop and then full recovery. N-polarity GaN growth, in contrast, proceeds with an instant full amplitude oscillation in reflectance (see Figure 3.6 (b) "4"). During subsequent growth of N-polarity GaN, the selective incorporation of Ga atoms is hindered by the densely packed homogeneous grains and the limited surface diffusion, thus indicating a quasi-2D growth mode [92]. In this situation, coalescence of densely packed homogeneous grains occurs at a much earlier stage than for Ga-polarity GaN.

Sumiya *et al.* have tried schematically to explain the difference between Ga-polarity and N-polarity GaN layers growth [93]. A schematic diagram of the GaN surface structure is presented in Figure 3.7. They have assumed that the GaN layer is grown in a Ga-limited regime and a large amount of nitrogen. It means that growing surfaces are terminated with nitrogen. By considering this fact and employing calculation results from [90] made by Zywietz *et al.*, Ga atom migration length on the N-polarity GaN surface is expected to be longer than on Ga-polarity GaN. It is due to a number of nitrogen dangling bonds on the different polarities GaN surface. Ga-polarity GaN is covered with a nitrogen atom and their three dangling bonds, while N-polarity GaN nitrogen atoms on the surface have only one dangling bond (see Figure 3.7 (a) and (b)). Since the Ga atoms have to break three Ga–N bonds during migration, a shorter migration length is expected on the Ga-polarity GaN surface.

Sumiya *et al.* also considered that Ga atoms have different sites at which they are incorporated into a grown layer [93]. The probability of Ga atoms incorporation into the layer rises at the sites formed by A, B and C dangling

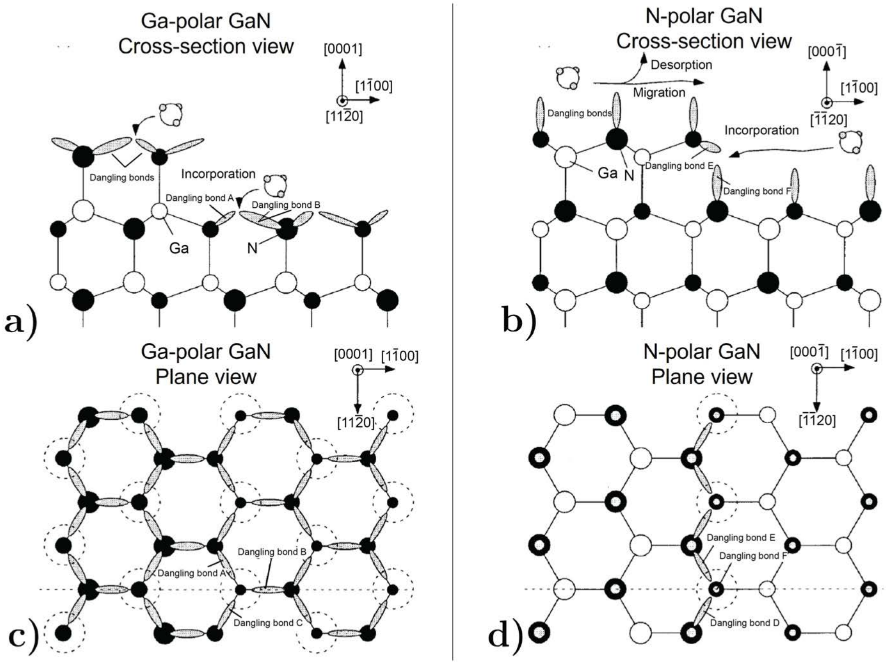

Figure 3.7: Atomic arrangement of Ga-polarity and N-polarity GaN surface. (a) and (b) are cross-sectional views along the [11$\bar{2}$0] direction for Ga-polarity and N-polarity GaN, respectively. (c) and (d) are *c*-plane views for Ga-polarity and N-polarity GaN, respectively. Adapted from [93].

bonds and is presented by the dotted circles in Figure 3.7 (c) in the case for Ga-polarity GaN. Whatever site Ga atoms adsorb, they are likely to be incorporated with less migration due to three dangling nitrogen bonds. It results in more predominant growth along the *c*-axis for Ga-polarity GaN. In contrast, different incorporation sites are formed on the N-polarity GaN surface. In the latter situation, two dangling bonds of nitrogen on the top surface point down along the [10$\bar{1}$0] and [01$\bar{1}$0] directions and one dangling bond of nitrogen in the beneath layer point up (see Figure 3.7 (b) and (d)). Those higher probability incorporation sites are formed by the step edge and denoted as D, E and F dangling bonds and are represented by the dotted circles. Due to such nitrogen dangling bonds configuration, weaker adsorption of Ga atoms on the N-polarity GaN surface is to be expected. It can lead to longer migration lengths for Ga atoms or even desorption and reabsorption of Ga atoms. Therefore, the Ga atoms on the N-polarity GaN surface may be more likely to adhere to the site of the step edge at which lateral growth mode dominates.

As mentioned earlier, what happens during the nitridation process is not yet fully understood. Several works report the formation of AlN and aluminum oxynitride ($\mathrm{Al_xO_zN_z}$) [84–86, 93]. X-ray photoelectron spectroscopy measurements performed by Jablonska *et al.* suggest that a thin AlN layer on the sapphire substrate is formed at the initial nitridation steps. After prolonged nitridation (80 min), AlN and $Al_xO_zN_z$ phases concentration on the surface was nearly equal, while more AlN was detected in the bulk of the sapphire substrate. This observation concludes that AlN and $Al_xO_zN_z$ compounds can control the overall III-N polarity somehow. Sumiya, Mohn, and Stolyarchuk agree that $Al_xO_zN_z$ plays a vital role in selecting the layers' polarity. Mohn explained his findings that the nitridation layer consists of N-polarity AlN followed by $Al_xO_zN_z$ and this heterostructure was enclosed by the LT-GaN buffer layer. The LT-GaN buffer layer was Ga-polarity, while the HT-AlN layer grown on the nitrided sapphire exhibited pure N-polarity. Mohn concluded his work that the role of the LT-buffer GaN layer is to preserve the metal-polarity established by the $Al_xO_zN_z$ layer and protect it against dissolution in high-temperature epitaxial environments [85]. Stolyarchuk *et al.* have found that after excessive sapphire nitridation at high temperatures, sapphire substrate starts to decompose and stable AlN islands, exhibiting metal polarity and the $Al_9O_3N_7$ layer was found to be formed [86].They also concluded that embedding $Al_9O_3N_7$ by the LT-buffer layer, the top-most layer will exhibit metal-polarity, while the decomposition of $Al_9O_3N_7$ at high temperatures leads to N-polarity.

4. CHARACTERIZATION METHODS

4.1. *In-situ* growth rate control by reflectometry

MOVPE reactor chamber without in-situ monitoring is like a "black box", where input parameters such as susceptor temperature, precursors flow rates, reactor pressure, etc., are established and then results are unfolded only after the whole growth process. Molecular beam epitaxy (MBE) utilizes electron-based in-situ monitoring and growth control techniques. Unlike MBE, electron-based techniques can't be utilized in a gas phase environment like MOVPE due to the lower vacuum level because electrons' free mean path is reduced strongly. Optical methods are more suitable in MOVPE technology [94–96]. These methods include spectroscopic ellipsometry (SE), reflectance anisotropy (RAS) and normalized reflectometry (R). These methods can be applied in-situ in both MOVPE and MBE as well as ex-situ in the air. Worth to mention that these optical monitoring methods are not surface-sensitive probes since the penetration depth of visible light is in the micron range. In this work, normalized reflectometry with 650 nm wavelength has been used for *in-situ* monitoring.

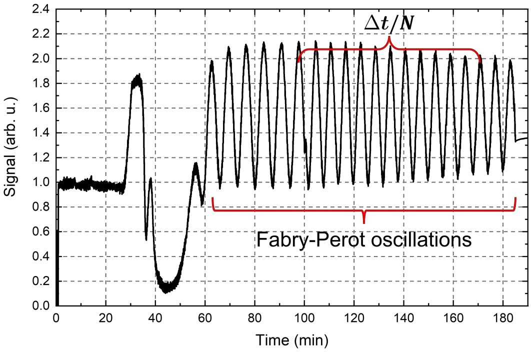

Figure 4.1: Typical Ga-face GaN growth diagram measured at a 650 nm wavelength.

It is worth noting that if the penetration depth of the light is larger than the thickness of the layer, then the optical properties of the substrate will also contribute to the reflected signal. Continuously measuring reflected signal during the growth process typical result presented in Figure 4.1 can be acquired. In the last plot, the reflectivity of the substrate (first 20 minutes) is used as a reference for signal normalization.

Using Figure 4.1 growth rate can be calculated. Suppose the laser light of wavelength λ is used and n is the refractive index of the layer. In that case, the maximum of the Fabry-Perot oscillations due to interference of the reflected light from the thickness d layer surface and substrate surface can be written as:

$$nd = m\frac{\lambda}{2}, \tag{4.1}$$

where m is an integer ($m \geqslant 1$). During the growth process, layer thickness constantly increases and at some point in time, maximum reflection is reached, and the (4.1) condition is fulfilled. Growth rate v can be calculated by using the time interval Δt between N maxima and $m = 1$:

$$v = \frac{N\lambda}{2n\Delta t}. \tag{4.2}$$

Apart from the growth rates, Figure 4.1 can give additional information about the growth process described in Section 3.3.

4.2. *Ex-situ* surface characterization methods

4.2.1. Scanning electron microscopy (SEM)

Scanning electron microscopy (SEM) is one of the analytical techniques capable of producing high-resolution images of a sample surface. The basic principle of this technique consists in scanning a focused electron beam (primary energy typically up to 30 kV, or wavelength about 7 pm) over the surface under study and simultaneously detecting electrons emitted from the surface [97]. A schematic diagram of the SEM setup is presented in Figure 4.2. The electron beam is produced in an electron microscope column. The voltage is applied between a conductive sample holder and a filament (cathode). Typically electrons are emitted from a heated tungsten (W) filament (or field emission cathode) and are focused by an anode aperture into a so-called cross-over point [97].

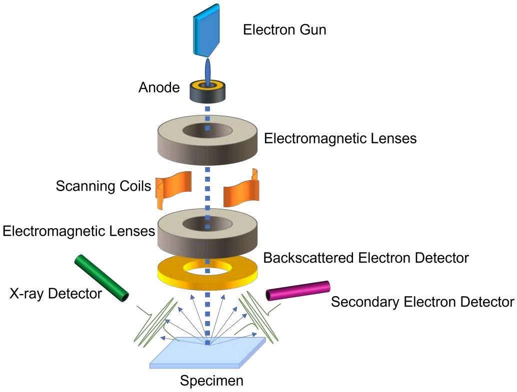

Figure 4.2: Schematic diagram of SEM setup.

Electrons are guided by a series of electromagnetic lenses in the electron column. Electron guiding occurs in a vacuum environment ranging from 10^{-4} to 10^{-10} Torr. Two magnetic coils (scanning coils) which perform a scan in the x-y direction are placed between electromagnetic lenses. The beam current and final spot size on the sample surface determine the resolution and depth of the field of the image. While SEMs cannot provide atomic resolution, typical floor model SEMs can achieve resolutions of the order of 4 to 20 nm.

Specimen surface irradiated by electron beam starts to emit electrons of different origin and X-ray photons. Energy distribution of scattered electrons and schematic model of primary electron beam interaction with a specimen, known as "pear", are presented in Figure 4.3 (a) and Figure 4.3 (b), respectively. These electrons are elastically and inelastically backscattered (BE) (region I and II in Figure 4.3 (a)), Auger electrons and secondary electrons (SE) (region III(inset) and IV in Figure 4.3 (a)). Different origin electrons bring diverse information about the specimen due to the different interaction depths presented in Figure 4.3 (b). BE and X-ray photons originate typically from a zone below the surface and reveal a specimen's compositional difference. SE and Auger electrons carry information from the narrow part of the "pear" near the specimen surface, thus creating a morphological image of the specimen surface.

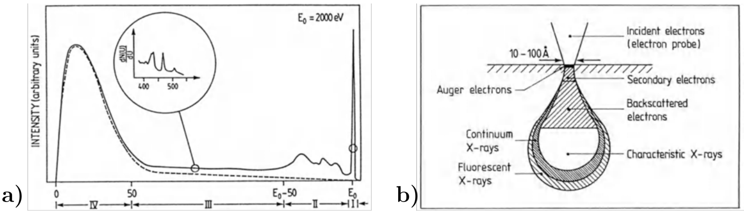

Figure 4.3: (a) Qualitative overview of the energy distribution of electrons emitted from a irradiated surface by an electron beam of energy E_0. (b) Schematically shown primary electron beam interaction with a specimen surface. Adapted from [97].

In this work, surface images of the samples were acquired with Hitachi-SU8230 and CamScan Apollo 300 SEMs using SE detectors.

4.2.2. Atomic force microscopy (AFM)

Atomic force microscopy (AFM) gives a three-dimensional view of the surface morphology. It provides information about the quality of the surface, especially in terms of root-mean-square (RMS) roughness value. The AFM technique was derived from the scanning tunneling microscope (STM) by Binning, Quante and Gerber in 1986 [98].

A schematic view of the AFM microscope is presented in Figure 4.4. Its principle is based on the cantilever/tip assembly that interacts with the sample surface. Cantilever/tip assembly consists of a very sharp tip usually made from either silicon (Si), silicon nitride (Si_3N_4), or diamond.Usually, cantilevers are made from the same material as the tips. It is worth noting that Si_3N_4 is reserved for softer cantilevers with lower spring constants. The typical curvature radius at the end for commercial tips ranges between 5 nm and 10 nm. The following important parameter of the AFM microscope assembly is cantilever stiffness or spring constant. The tip is placed in proximity to the sample's surface so that inter-atomic forces influence the atoms on the tip. This leads to a deflection of the cantilever, which is then measured via a laser beam reflected from the cantilever surface into a four-section photodiode. As the tip scans across the surface, it reproduces the surface topography. Several modes of operation have been developed for the AFM. One is known as contact mode and another – tapping mode [100].

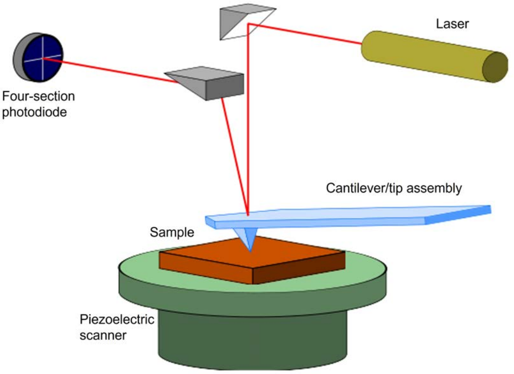

Figure 4.4: Schematic view of AFM microscope. Adapted from [99].

In the contact mode, the cantilever/tip assembly is in continuous contact with the sample surface while the scan process is performed and the change in cantilever deflection is measured. In this configuration, constant force or cantilever deflection is maintained between the sample surface and the cantilever/tip assembly by a feedback loop and adjusting the z position of a scanner. Based on the x, y, and z position of the cantilever/tip assembly, the topography of the sample is computed.

In the tapping mode, the cantilever/tip assembly oscillates near its resonant frequency ($\sim$ 300 kHz), and the tip is made to strike the sample surface on each oscillation [100]. Oscillation amplitude ranges between 20 $\div$ 100 nm. The oscillation amplitude is measured as an RMS value of the deflection detector signal. The feedback system detects the change in the oscillation amplitude caused by tapping the surface and adjusts the z position of the cantilever/tip assembly to maintain the RMS value of the oscillation constant, thus generating a topographic image of the sample surface.

In this work, surface morphology for all samples was analyzed using Bruker Dimension Icon with ScanAsyst AFM in tapping mode. RMS roughness of the surface was acquired using open-source software "Gwydion".

4.3. *Ex-situ* structural characterization methods

4.3.1. X-ray diffraction (XRD)

X-ray diffraction (XRD) is a powerful, non-destructive and widely used tool/method in material sciences for detailed identification of the crystallographic structure. It provides information on structures, phases, preferred crystal orientations (texture), and other structural parameters, such as average grain size, crystallinity, strain, and crystal defects [101].

X-ray diffraction can be explained as the "reflection" of an incident X-ray beam from many parallel atomic planes where the distance between them is d_{hkl}. hkl numbers stands for Miller indices for a particular atomic plane. It can be considered that a small portion of the X-ray beam is reflected at each atomic plane. Those reflected beams produce constructive interference (and a diffracted ray) when conditions satisfy Bragg's law, which can be derived from trigonometric reasoning (see Figure 4.5):

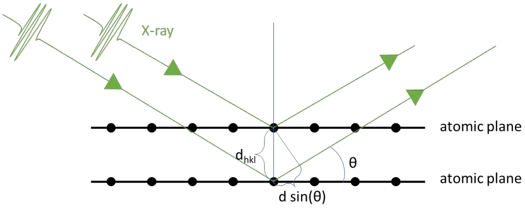

Figure 4.5: Schematic view of X-ray diffraction.

$$n\lambda = 2d_{hkl}\sin(\theta), \tag{4.3}$$

where n is an integer describing the order of reflection, λ – wavelength of the X-rays and θ – Bragg or diffraction angle. Usually, the X-ray source is (and in this work was) a X-ray tube with a copper (Cu) cathode. A monochromator is used to select the Kα characteristic spectra line of Cu (Cu-Kα), which equals to $\lambda = 1.5406$ Å. This wavelength is comparable to the distance between atomic planes in a crystal.

In order to determine GaN crystal quality and lattice parameters, SmartLab Rigaku high-resolution XRD (HRXRD) system in out-of-plane and in-plane configurations in this work was used. Out-of-plane configuration is presented in Figure 4.6 (a). By adjusting incident (IS) and receiving slits (RS), XRD measurement precision can be improved. A symmetrical reflection of

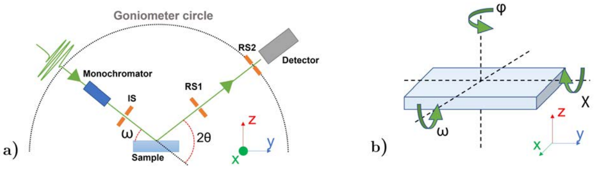

Figure 4.6: (a) Schematic view of out-of-plane configuration. (b) Key angles in XRD measurements.

$2\theta/\omega$ and ω-rocking scans were performed for (0002) GaN planes in the out-of-plane XRD configuration. In the $2\theta/\omega$ scan, detector is rotated two times faster than the sample rotation stage. The key angles of the sample rotation stage are presented in Figure 4.6 (b). By performing the $2\theta/\omega$ scan, lattice parameters and material strain can be evaluated. In ω-rocking scan, or rocking curve scans (XRC) the diffraction angle 2θ is fixed while scanning the incident angle ω. The degree (mosaicity) of preferred orientation can be obtained by the ω-rocking scan [102]. The higher the crystal quality, the lesser mosaicity, thus narrower full width at half maximum (FWHM) of rocking curve profile.

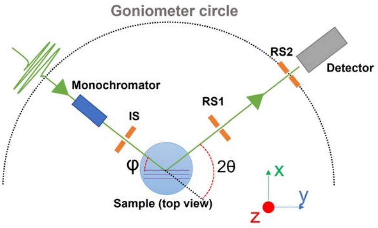

Figure 4.7: Schematic view of in-plane configuration. Lines in the samples represents crystal planes.

In-plane XRD is a configuration used for measuring diffraction intensities from lattice planes normal to the surface of a sample [103]. The latter setup lets to minimize background intensities from the substrate and detect diffraction signals from extremely thin films. In an in-plane XRD configuration, a grazing incident X-ray beam is employed. It lets the beam to travel a long distance inside the thin film. Thus high intensities of diffraction signal from the film can be obtained. Reaching characteristic critical angles for different materials, a total external reflection of the X-ray beam can occur. This angle depends on the wavelength and density of the material.

In in-plane XRD configuration, the sample rotation angle is denoted as φ (see Figure 4.7). The ideas of $2\theta/\varphi$ and φ-rocking scans are the same as in the out-of-plane configuration for $2\theta/\omega$ and ω-rocking scans. The difference is that earlier mentioned parameters can be determined for perpendicular planes to the sample surface. Symmetrical reflection $2\theta/\varphi$ and φ-rocking scans were performed for $(11\bar{2}0)$ GaN planes.

4.3.2. Transmission electron microscopy (TEM)

Transmission electron microscope (TEM) or high-resolution TEM (HRTEM) like SEM also uses electrons as a source for visualization. Conceptually it is very similar to the optical transmission microscope in the arrangement of the specimen, the "light source" and the image plane. Detection is done with the help of a fluorescent screen. As the SEM technique is used to characterize a surface of the sample, TEM is a powerful technique to characterize microstructural features such as atomic configuration and their arrangement in the sample. Typically in TEM, 200 kV voltages for accelerating electrons are applied (SEM up to 30 kV). Such a high voltage electron beam corresponds to de Broglie wavelength of about 2.7 pm and can provide few angstrom resolutions. The TEM resolution can be improved even further and reach a sub-angstrom regime with the developments in aberration correction. [104–106].

The problems in TEM technology are the complex specimen preparation process and its thickness. Permissible specimen thickness for TEM-based observations is limited to a few hundred nm (usually from 50 nm to 100 nm) [107]. In such thin samples, part of information as original structures of dislocations are hardly maintained since most of the material is removed from the bulk. By applying much higher accelerating voltages (up to 1 MV), few µm thickness samples can be scanned in a high spatial resolution. By combining electron energy-loss spectroscopy (EELS) and high accelerating voltages, Sadamatsu *et al.* have managed to acquire high-resolution images for 10 μm thickness p-type silicon (Si) (001) wafers [107].

There are seven main techniques of TEM: conventional imaging (bright-field and dark-field TEM), electron diffraction, convergent-beam electron diffraction (CBED), phase-contrast imaging (HRTEM), Z-contrast imaging, energy-dispersive X-ray spectroscopy (EDS or EDX) and EELS [108]. The diffraction patterns measured by XRD methods are quantitative electron diffraction patterns, but electrons have a significant advantage over X-rays – electrons can be focused easily. By focusing the electron beam, diffraction patterns can be acquired from microscopic regions, and it is often possible to select a single microcrystal for diffraction measurements. A diffraction-contrast method is useful for making images of defects such as dislocations, interfaces and other phase particles or inclusions. Next to diffraction-contrast microscopy, where the intensity of diffracted electron waves is measured, is high-resolution TEM. In the latter method phase of the diffracted electron waves is preserved and interferes constructively or destructively with the phase of the transmitted wave. This method is termed phase-contrast imaging and is used to form images of columns of atoms.

After electron beam interaction with a specimen, electrons lose their initial energy. A method that measures electron energy losses is called electron energy-loss spectroscopy (EELS). Information on local chemistry and structure can be obtained from features in EELS spectra caused by plasmon and core electron excitations [108]. As mentioned in Section 4.2.1, X-ray photons are also emitted after the interaction of high-energy electrons with a sample. X-ray spectrum can be acquired from small regions of the specimen using a focused electron beam. Characteristic X-rays from the chemical elements can be detected and used to map and determine the concentrations of the different elements in the specimen. This method is termed energy-dispersive X-ray spectrometry (EDS or EDX).

As sample preparation for TEM is quite complicated and time-consuming, only a few samples were analyzed using HRTEM and EDX methods. HRTEM images of the samples were acquired using Tecnai G2 F20 X-TWIN TEM.

4.4. Electron-beam induced current (EBIC)

In semiconductors, electron beam interaction with a sample can result in a current generation within that sample, which then can be measured. This process stands for the electron-beam-induced current (EBIC) method. The EBIC can be used to image recombination sites directly; to measure transport properties like minority carrier diffusion length, lifetime, and surface recombination velocity; to determine junction depths and shallow trap energy levels; to image inversion layers in the integrated circuits and to map leakage paths [109].

The energy of the electrons in the beam ranges up to $20 \div 30$ keV (typical SEM accelerating voltages are up to 30 kV). The minimum energy in semiconductors required to create electron-hole pairs is band gap energy. For the GaN case, it is about 3.39 eV. It means that high-energy electrons from the beam incident on the semiconductor can excite electron-hole pairs on the order of 10^3 to 10^4 per incident electron. Electron-hole pairs are generated within the sample in a volume. The important carriers here are the minority carriers [109]. If the diffusion length to the particular junction (e. g. p-n junction, metal-semiconductor (Schottky) junction) is long enough, then minority carriers will possibly diffuse to the junction. Due to the existence of an electric field in the junction region, the minority carriers will be swept by this field, thus generating a current that can be measured. The result is a mapping of the current measured at every scanned point. If a defect is present, the resulting recombination will produce less collected current and a darker image will be generated at the defect sites.

Figure 4.8 (a) represents EBIC schematic setup used in this work. Figure 4.8 (b) is a typical Ga-face GaN EBIC result. The brighter the spot, the larger current was generated. Samples were partly covered by a thin layer of gold (Au), thus forming Schottky contact. InSn paste which was applied on the

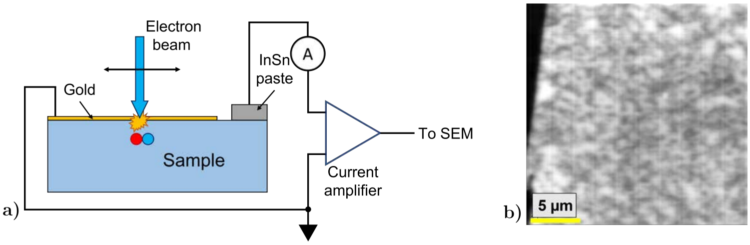

Figure 4.8: (a) Schematic setup for EBIC measurements. (b) Ga-face GaN EBIC measurement example.

sample, formed Ohmic contact. EBIC measurements were performed using SEM Apollo 300 and Gatan G10539 EBIC add-on equipment.

4.5. Polarity determination by KOH etching

There are several methods like CBED, coaxial impact collision ion scattering spectroscopy and piezoelectric force microscopy to determine polarity of GaN films [110–113]. But for the listed methods, either sophisticated equipment or complex analysis is needed. Luckily, more straightforward methods like etching in potassium hydroxide (KOH) solution or observing surface morphology by a conventional optical microscope (OM) are used to determine GaN polarity. Usually, large hillocks are present on the N-polarity GaN surface if the off-cut angle of the sapphire substrate or growth parameters are not optimized. One of the examples is presented in Figure 4.9 (a). However, the N-polarity GaN surface becomes featureless when using sapphire substrates with larger off-cut angles (see Figure 4.9 (b)). Due to its simplicity in determining the GaN polarity etching method is the most attractive among others.

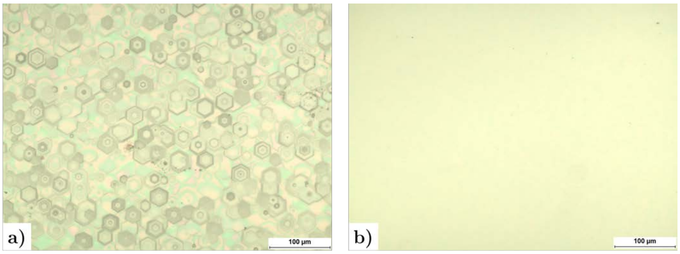

Figure 4.9: (a) N-polarity GaN on the sapphire substrate with 0.3° off-cut angle. (b) N-polarity GaN on the sapphire substrate with 2° off-cut angle.

Ga-polarity GaN surface is found to be chemically stable in KOH solution in comparison with N-polarity GaN surface. Ga-polarity GaN surface can only be affected by the molten KOH at high temperatures (300 ÷ 450°C) or in the NaOH/KOH eutectic [114,115]. Figure 4.10 shows a change in N-polarity GaN

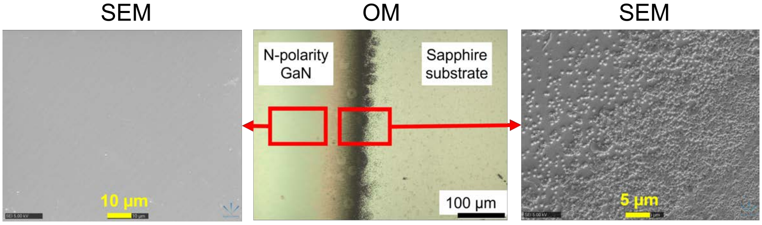

Figure 4.10: N-polarity GaN surface after etching process. Left side of the figure presents the surface image which was not affected by 6M KOH solution. Right side – a result after 6M KOH solution etching.

surface morphology after the KOH etching process. The surface, which was not affected by the KOH solution, stays featureless. In contrast, the surface affected by KOH solution changed the morphology from featureless to densely packed hexagonal-shaped pyramids evidencing the N-polarity. In this work, the samples' polarity was tested using a 6M KOH solution. Every etching experiment was performed at 90°C temperature for 10 minutes.

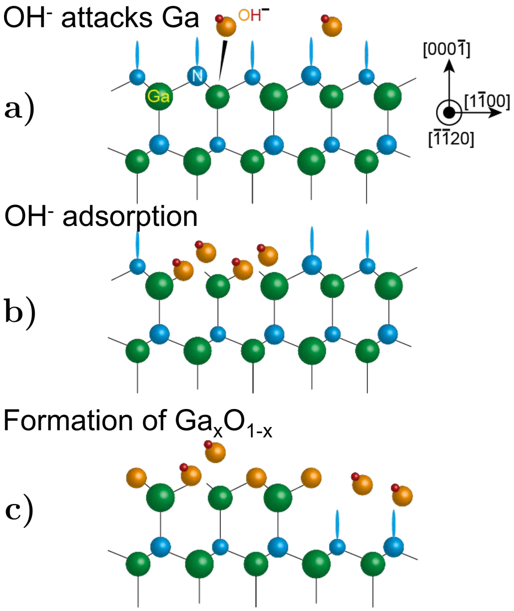

Figure 4.11: Schematic diagrams of the cross sectional GaN film viewed along the $[\overline{11}20]$ direction for $-c$ GaN to explain the mechanism of the selective etching. Adapted from [116].

The process of such polarity selective etching was explained by Li *et al.*. They studied the change of the surface chemistry before and after etching in KOH solutions for Ga- and N-polarity GaN using X-ray photoelectron spectroscopy and found that the different etching processes are due to different bonding configurations in Ga- and N-polarity GaN [116]. Figure 4.11 presents a schematic diagram of the etching mechanism for N-polarity GaN. In Ga-polarity GaN, hydroxide ions (OH^-) cannot attack the N-terminated surface due to large repulsion between OH^- and three occupied dangling nitrogen bonds. It is why the Ga-polarity GaN surface is resistant to the etching in KOH solution. N-polarity GaN exhibit only a single dangling bond of nitrogen atom upward on the surface. This makes the surface less negative to OH^- ions. The ions can attack the back bond of the Ga atoms (see Figure 4.11 (a)) coordinated tetrahedrally and be adsorbed on the surface (see Figure 4.11 (b)). Adsorbed OH^- ions react with GaN forming gallium oxide (Ga_2O_3) and NH_3 (see Figure 4.11 (c)):

$$2GaN + 3H_2O \xrightarrow{KOH} Ga_2O_3 + 2NH_3. \tag{4.4}$$

Here KOH is working as a catalyst. Ga_2O_3 is then dissolved in the KOH solution and the surface oxidation process starts to repeat.

4.6. External quantum efficiency (EQE) measurement

There are two types of quantum efficiencies: external quantum efficiency (EQE) and internal quantum efficiency (IQE). EQE is the ratio of the number of collected charge carriers by the pn junction or solar cell (further device) and the number of incident photons [117]. Therefore, IQE only considers the absorbed photons in the device [117, 118]. EQE measurement lets to observe devices' behavior in specific spectral ranges.

A flowchart of the EQE calculation process is presented in Figure 4.12. The general equation that is used to calculate EQE is formulated as:

$$EQE(\lambda) = \frac{hc}{q\lambda} \cdot SR, \tag{4.5}$$

where h is Planck's constant, c is the speed of light, q is the electronic charge, λ – is the wavelength and SR is the spectral response of the device. Spectral response (SR) is a ratio between the current generated by the cell and the power of monochromatic incident light [117]. The measurement starts from the background signal level measurements. Then the reference device is used in order to measure photocurrent I_{RC} that is used to calculate the incident power of the monochromatic beam.

$$P(\lambda) = \frac{I_{RC}(\lambda)}{R_{RC}(\lambda)}. \tag{4.6}$$

The incident illumination power is determined by dividing the reference de-

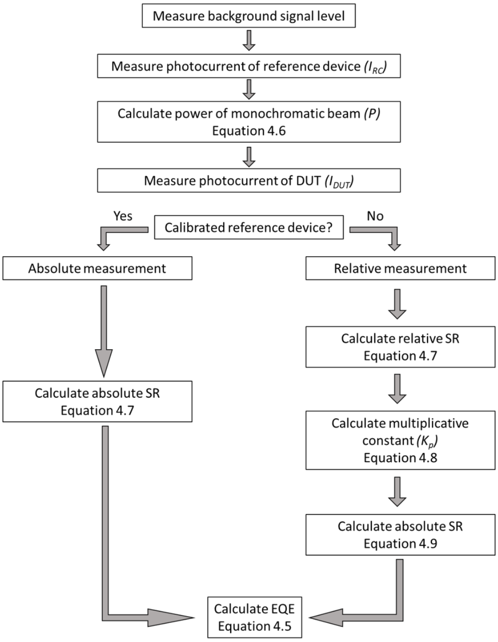

Figure 4.12: A flowchart of the EQE calculation process [117]. DUT stands for "device under test".

vice's photocurrent readings with its wavelength-specific SR calibration data (R_{RC}). After the photocurrent of the reference device measurement, photocurrent (I_{DUT}) measurements of the device under test (DUT) is followed. After the latter measurement and using calculated incident beam power, the SR can be then calculated:

$$SR(\lambda) = \frac{I_{DUT}(\lambda)}{P(\lambda)}. \tag{4.7}$$

If the reference device is not calibrated for the whole spectrum but only for the one wavelength λ_0, then after acquiring the absolute value of the SR for this particular wavelength, an absolute SR values of the DUT for the whole spectrum can be calculated by introducing multiplicative constant (K_p):

$$K_p = \frac{SR_{abs}(\lambda_0)}{SR_{rel}(\lambda)}, \tag{4.8}$$

$$SR_{abs}(\lambda) = K_p \cdot SR_{rel}(\lambda). \tag{4.9}$$

$SR_{rel}(\lambda)$ in Equation (4.8) and Equation (4.9) is expressed as $SR_{rel}(\lambda) = \frac{I_{DUT}(\lambda)}{P(\lambda)}$, while $SR_{abs}(\lambda_0)$ in Equation (4.8) is expressed as $SR_{abs}(\lambda_0) = \frac{I_{DUT}(\lambda_0)}{P(\lambda_0)}$.

5. FABRICATION OF GaN/AlGaN PLANAR WAVEGUIDE

This chapter is based on the research published in the paper [**A1**]. Latter work reports on fabricating a GaN/AlGaN waveguiding structure dedicated to modal phase matching, where the GaN waveguide has planar face inversion. The paper consists of the presentation of Al-polarity AlN as a buffer layer and AlGaN as optical cladding layer growth processes using different growth conditions. Then the growth process of Ga-polarity GaN – Al_2O_3 – N-polarity GaN "active" waveguiding structure (core) is following. Lastly, characterization results of AlGaN, Ga-polarity GaN and N-polarity GaN are presented.

5.1. Modeling Results

Modeling results will be presented first. It will mainly be focused on the different combinations of planar AlGaN/GaN waveguiding structures. It also will contain results of the distribution of the optical modes in those structures respectively and various combinations of second harmonic generation possibilities. This section aims to explain and find AlGaN/GaN structures capable of sustaining optical modes, which enables second harmonic generation by exploiting the modal-phase-matching technique, especially for 1064 nm fundamental and 532 nm second harmonic waves wavelengths.

The main platform used during this PhD project was AlGaN/GaN structure. The structure consists of optical cladding and waveguiding layers. It also provides a relatively high refractive index contrast (for GaN 2.3330 [10] and AlN 2.1297 [11] at 1064 nm for ordinary refractive index). Moreover, AlGaN optical cladding layer helps isolate the guided modes from the substrate and initial imperfections in the low-quality epitaxial layers, such as the low-temperature Ga-polarity GaN buffer layer with a high density of threading dislocations. Everything mentioned before helps reduce the propagation losses and improve the SHG efficiency. Another advantage of the structure is that the high refractive index contrast between AlGaN and GaN layers creates a possibility to use the interaction between different order modes in multi-mode waveguides and satisfy phase-matching conditions by implementing the modal phase-matching technique.

The structure consisting of a 1.2 μm Ga-polarity GaN layer which is grown on the 1.25 μm Al-polarity AlGaN based on the sapphire substrate is presented in Figure 5.1. Al concentration in the AlGaN layers is 65%. An explanation of why the Al concentration was chosen to be 65%, in this case, will be given later. $Al_{0.65}Ga_{0.35}N$ ordinary (n_o) and extraordinary (n_e) refractive indices were calculated by using linear approximation of $n_{o,e}[Al_xGa_{1-x}N] = xn_{o,e}[AlN] + (1-x)n_{o,e}[GaN]$. Latter approximation was made due to a lack

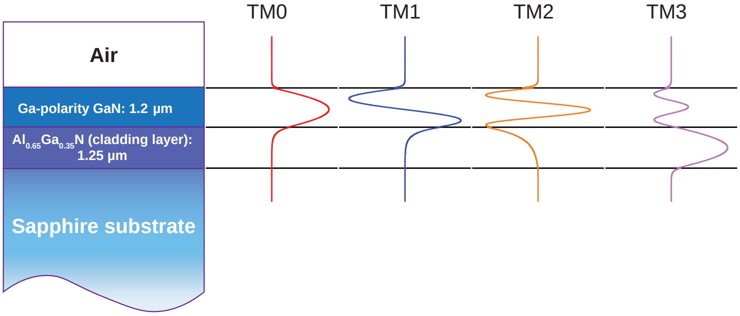

Figure 5.1: A scheme of AlGaN/GaN based waveguide with a TM-modes profiles at 633 nm wavelength.

of information on the refractive index dependence on Al concentration in the AlGaN layer. For the optical modes visualization in the given structure, 633 nm wavelength was used. Four transverse magnetic (TM) optical modes are presented in Figure 5.1. Optical mode profiles for the transverse electric (TE) case look similar. One of the advantages of this structure is based on the nonlinear interaction between fundamental and higher optical modes. TM0, TM1 and TM2 optical mode power is highly confined in the GaN layer, but a significant part of the optical power of TM3 mode is mostly confined in the AlGaN layer (see Figure 5.1). For the latter, there won't be any interaction with the first harmonic fundamental mode, which is confined in the GaN layer.

The evolution of the effective refractive index and optical mode power confinement coefficient for TM and TE cases for 633 nm wavelength are given in Figure 5.2 (a, b) and Figure 5.3 (a, b). Numbers placed above Figure 5.2 (b) and Figure 5.3 (b) represent particular mode cut-off thicknesses. The horizontal axis of these all plots represents GaN waveguide thickness. A vertical scale of Figure 5.2 (a) and Figure 5.3 (a) are set so that the lowest value of the vertical axis shows bulk AlGaN refractive index, while the highest value – bulk GaN refractive index. As GaN thickness decreases, an effective refractive index of optical modes approaches AlGaN refractive index and at the cut-off GaN thicknesses, optical modes exhibit a pure AlGaN refractive index. This behavior is since more optical power of a particular mode is confined in the AlGaN cladding layer. It is worth noting that the behavior of TM and TE modes is almost identical. From Figure Figure 5.2 (b) and Figure 5.3 (b), at each successive optical mode cut-off thickness, more than 90% of the optical power of the previous optical mode is already confined in the GaN waveguide. By using TM2 mode for SHG, it would be wise to have GaN thickness that will be equal to a cut-off thickness of TM3 mode. Changing GaN waveguide thickness (or overall waveguide parameters) makes it possible to filter unwanted higher optical modes that do not take part in any generation process but preserve the lower ones, thus optimizing the waveguide structure for SHG.

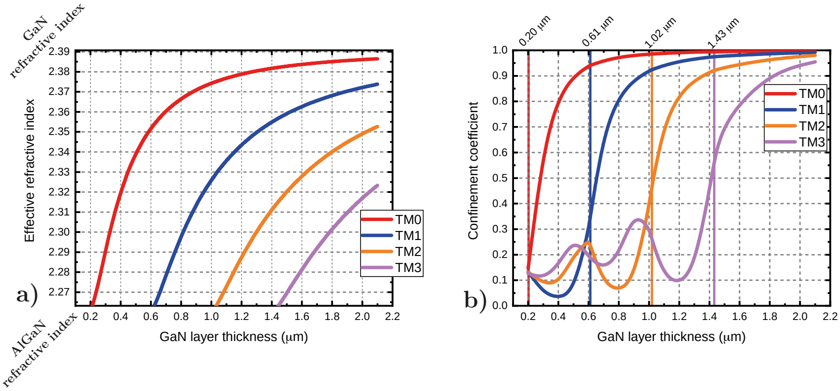

Figure 5.2: Effective refractive index (a) and optical power confinement coefficient (b) for the TM optical modes as a function of the GaN layer thickness for the 633 nm wavelength. GaN and AlGaN have extraordinary, $n(e)$ refractive index for the TM mode case.

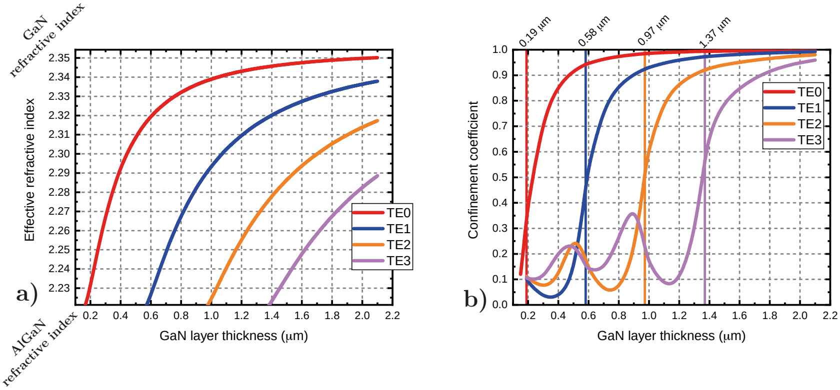

Figure 5.3: Effective refractive index (a) and optical power confinement coefficient (b) for the TE optical modes as a function of the GaN layer thickness for the 633 nm wavelength. GaN and AlGaN have ordinary, $n(o)$ refractive index for the TE mode case.

Calculated dispersion curves of the structure in Figure 5.1 for TM0 fundamental and TM1, TM2 second-harmonic waves are presented in Figure 5.4, where $\lambda/2$ means wavelength of the second harmonic wave. The horizontal axis in the plot represents the wavelengths of the fundamental wave. For TM0 $n_{\mathrm{TM0}}(\lambda)<n_{\mathrm{TM0}}(\lambda/2)$, there is no possibility to achieve SHG between the same order optical modes due to dispersion. Intersection points in the plot present conditions satisfying phase matching, thus enabling SHG. One case is between TM0 at 2100 nm fundamental and TM1 at 1050 nm second-harmonic waves,

the second one – between TM0 at 1280 nm fundamental and TM2 at 640 nm second-harmonic waves. These modes calculated intensity profiles after 4 mm propagation distance are given in Figure 5.5 (a, b). It is worth noting that the

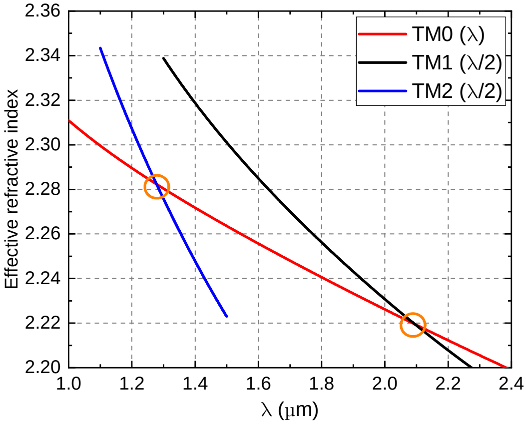

Figure 5.4: Dispersion curve for the effective refractive indices of three guided mode for the waveguide in Figure 5.1. A modal phase matching (shown by circles) is reached between TM0 (2100 nm, IH) and TM1 (1050 nm, IIH), or TM0 ((1280 nm, IH)) and TM2 (640 nm, IIH) [**A1**].

power confinement factor depends not only on the waveguide thickness but also on the wavelength. It can be seen clearly in Figure 5.5 (a) that a much longer intensity tail is penetrating the AlGaN cladding layer than Figure 5.5 (b). Thus the shorter wavelength for a particular GaN thickness, the more optical mode power is confined in that layer. Gromovyi *et al.* have evaluated that phase matching wavelengths strongly depend on the thickness of the GaN waveguiding layer and less on Al content in the AlGaN cladding layer [14]. Al content determines the index contrast, while GaN thickness – waveguide functionality as multi-mode or single-mode waveguide for the fundamental wave. By controlling these two factors, the given material configuration allows to cover a broad spectral range from UV to mid-infrared due to the large transparency window.

As a rule, a drawback of MPM is the interaction between a fundamental mode and oscillating higher-order modes, leading to poor overlap of fields and low second harmonic conversion efficiencies [119]. Figure 5.6 (a) and Figure 5.6 (b) present power conversion efficiencies dependency over propagation distance for the cases presented in Figure 5.5 (a) and Figure 5.5 (b), respectively. In a model described in Section 2.4, power conversion efficiency over distance in the nondepleted pumping regime rises quadratically when the phase-matching condition is fulfilled. Nevertheless, a difference can be spotted in conversion efficiency values. This difference in conversion efficiency values comes from the different overlap between TM0 – TM1 and TM0 – TM2. A larger overlap

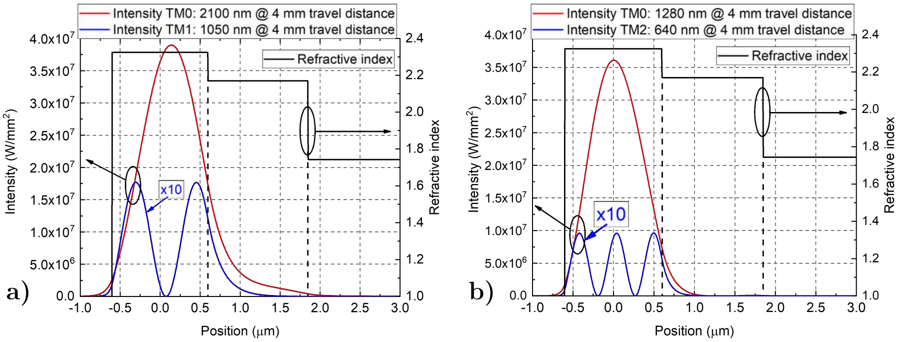

Figure 5.5: TM optical modes intensity profiles in the waveguide presented in Figure 5.1 after 4mm travel distance and for the modal phase matching case between TM0 (2100 nm) – TM1 (1050 nm) (a), and TM0 (1280 nm) – TM2 (640 nm) (b).

between optical modes is in TM0 – TM2 case, thus giving larger conversion efficiencies values over propagation distance.

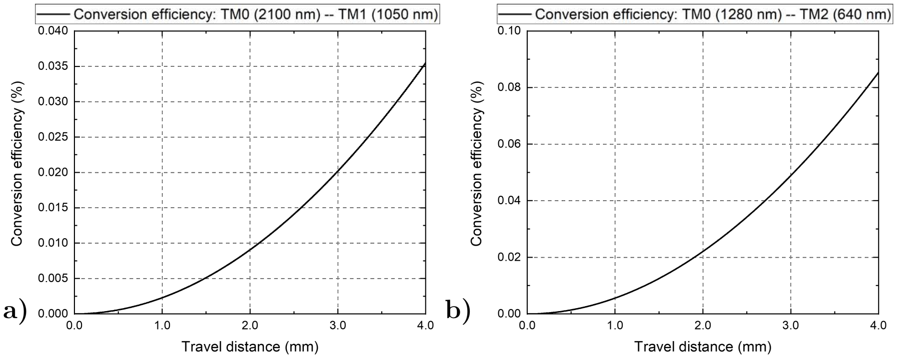

Figure 5.6: Second harmonic generation conversion efficiencies for both TM modes cases: TM0 (2100 nm) – TM1 (1050 nm) (a) and TM0 (1280 nm) – TM2 (640 nm) (b).

The overlap depends not only on modal field profiles but also on the distribution of second-order nonlinear coefficient d_{33} along the growth direction (Section 2.4, Equation (2.52)). Thankfully, an elegant solution exists that allows to improve of modal field overlap by implementing a planar polarity inversion. Figure 5.7 (a) and Figure 5.7 (b) present the structures with inverted polarity layers. Inversion layers thickness is based on the modal field profiles where higher-order mode modal field goes into negative values range. Since the d_{33} parameter is determined by GaN polarity, sign inversion of the d_{33} parameter compensates negative values in the modal field of higher-order modes, thus increasing the overlap integral between the fundamental wave and higher-order mode of a second harmonic wave. It automatically results in higher conversion

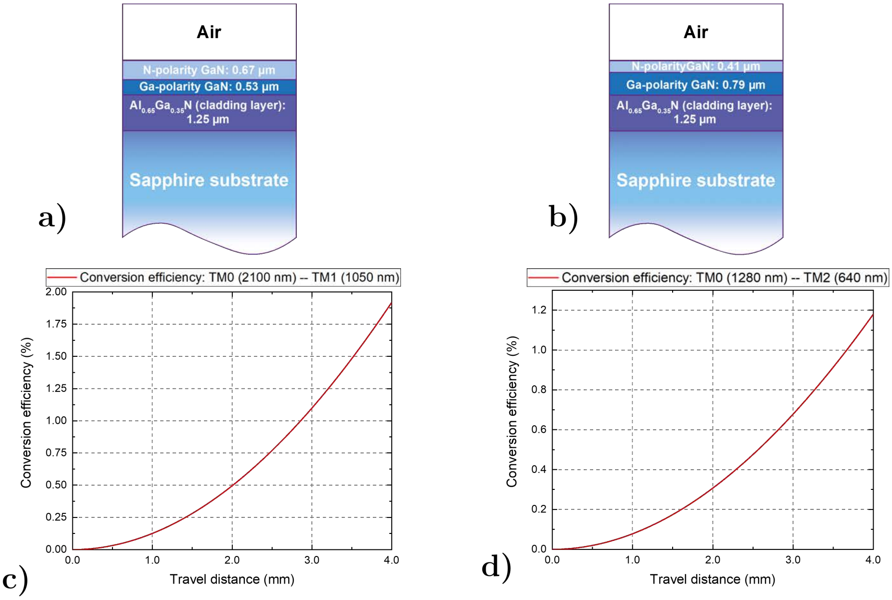

Figure 5.7: Second harmonic generation conversion efficiencies for the structures with inverted GaN face for TM0 (2100 nm) – TM1 (1050 nm) (a, c) and TM0 (1280 nm) – TM2 (640 nm) (b, d).

efficiencies presented in Figure 5.7 (c) and Figure 5.7 (d). After 4 mm propagation conversion efficiency in the GaN waveguide with inverted polarity layers for TM0 – TM1 case exceeds over 1.75%, while for TM0 – TM2 case exceeds over 1.1%.

This work was mainly focused on the growth of planar inversion GaN waveguides. MOVPE growth results and approach to the final structure will be presented later. Extensive experiments by growth parameter optimization were done on achieving GaN inversion polarity layers. A structure presented in the next paragraph was evaluated only for comparison purposes.

Figure 5.8 (a) presents a more sophisticated GaN waveguide where a periodic lateral polarity type structure is implemented. In this case, second-order nonlinear coefficient d_{33} changes its sign in the propagation direction periodically. This structure enables interaction between the same optical modes order of fundamental and second harmonic waves. An intensity distribution of TM0 fundamental wave at 1260 nm and TM0 second harmonic wave at 630 nm is presented in Figure 5.8 (b). Because the interaction of fundamental and second harmonic waves are between the same optical modes order (TM0 – TM0) overlap integral becomes unity. It translates into relatively higher conversion efficiency presented in Figure 5.8 (c), where after 4 mm propagation distance, conversion efficiency rises above 3%.

Lastly, Figure 5.9 (a) presents a GaN waveguide structure suitable for the

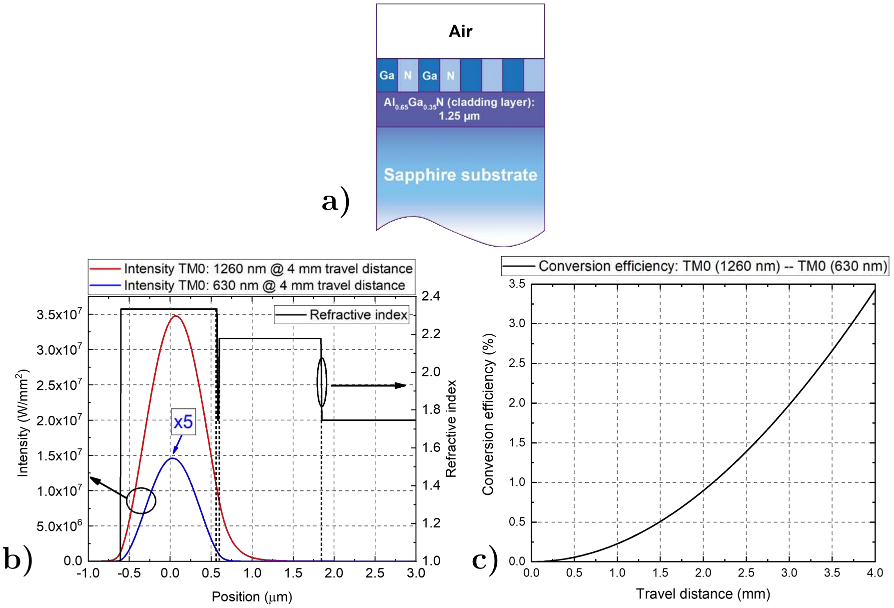

Figure 5.8: Periodically-poled-GaN (PPO-GaN) structure (a). TM optical modes intensity profiles in the PPO-GaN waveguide (b) and its second harmonic generation conversion efficiency chart (c).

generation of a “classical" second harmonic wavelength, which is equal to 532 nm. A small difference can be spotted between the previously presented and the latter structures. This structure is a "spoiler" of the GaN polarity inversion method used in this work. An explanation of using aluminum oxide (Al_2O_3) deposited by atomic layer deposition as a polarity inversion layer will be given later. Calculated dispersion curves of the structure presented in Figure 5.9 (b) prove that MDPM is achieved between 1064 nm TM0 fundamental and 532 nm TM2 second-harmonic waves. Conversion efficiency over propagation distance is presented in Figure 5.9 (c). More than 1.4% second harmonic conversion efficiency can be achieved after a 4 mm propagation distance.

In summary, due to the low birefringent effect in GaN mentioned in Chapter 1, birefringent phase-matching can’t be achieved. MDPM is a promising method in GaN technology to generate second harmonic, but conversion efficiencies are quite low due to low modal field overlap between fundamental and second harmonic waves. In order to enhance the conversion efficiency of second harmonic generation, inversion of GaN polarity in the waveguide structures is inevitable.

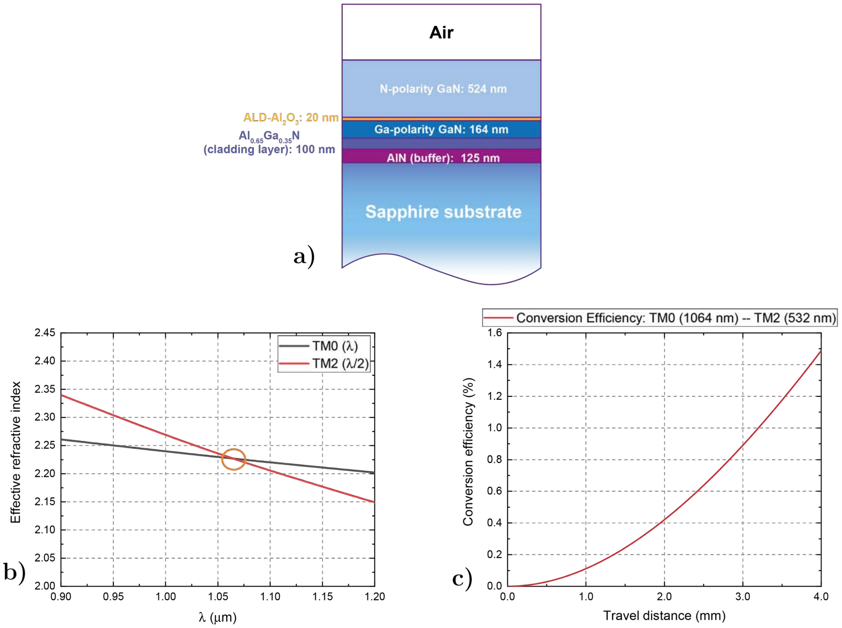

Figure 5.9: (a) AlGaN/GaN waveguide design capable for generation of 532 nm IIH wavelength. (b) Dispersion curves of the given structure for the effective refractive indices of two guided modes (b) and (c) second harmonic generation conversion efficiency dependency on travel distance in the waveguide.

5.2. Growth of GaN/AlGaN structure

Epitaxy is the main activity of a lab where I was working during my PhD project. The main materials which are grown in this lab are III-group nitride (III-N) semiconductors (GaN, InN, AlN and BN) and their alloys for the light-emitting-diodes (LED) and high-electron-mobility-transistors (HEMT) applications. The lab had never worked with III-N waveguide structures and it was a novelty for the lab. Moreover, the growth of the N-polarity GaN and its application in the waveguinding structures in the lab was like an undiscovered and challenging road. From the growth of singular N-polarity GaN and AlGaN layers on the sapphire substrates separately to understand how the growth parameters affect these layers' structural parameters to the growth of the whole AlGaN/GaN waveguiding structure. Despite the efforts, time and work done during this PhD project, there left plenty of room for continuing to research this field further. All growth experiments were performed in a close-coupled-showerhead (CCS) 3x2" MOCVD reactor (Aixtron Ltd., UK).

The structure that was grown and will be presented in these following subsections is very similar to the one used in Section 5.1, Figure 5.7 (a) to calculate SHG conversion efficiency while having one part of the GaN waveguide with the inverted polarity. A slight difference is in the structure. The resulting structure of this is presented in Figure 5.10. The structure was grown on the 2-inch,

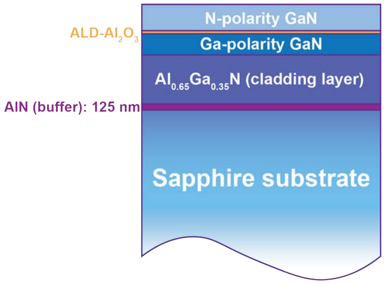

Figure 5.10: The geometry of the GaN/AlGaN waveguiding structure for modal phase matching.

c-oriented (0001) sapphire substrates with 0.3° off-cut angle toward *m*-plane. Trimethylaluminum (TMAl), trimethylgallium (TMGa) and ammonia (NH_3) were used as a source of aluminum (Al), gallium (Ga) and nitrogen (N) atoms, respectively. Hydrogen (H_2) or nitrogen (N_2) were used as carrier gases.

5.2.1. Growth of the Al-polarity AlGaN as optical cladding layer

The starting point in the AlGaN/GaN waveguiding structure is the AlN buffer and AlGaN cladding layer. Section 5.1 already explained why using the AlGaN cladding layer is better than using the low-temperature Ga-polarity GaN layer from the structural perspective. Figure 5.11 shows typical traces of

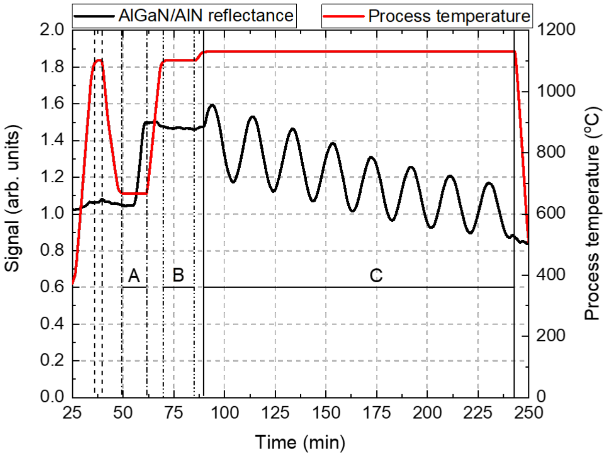

Figure 5.11: In situ optical reflectance and reactor temperature chart of a typical AlGaN/AlN growth [**A1**].

both the reactor temperature and the optical reflectance of the AlN layer, then the AlGaN (Al = 65%) layer, during a MOCVD growth of the AlGaN/AlN part of the structure in Figure 5.10. In the temperature trace, a narrow interval distinguished with a dashed line without any notation (on the time scale (Time) is about at 37 minutes) corresponds to the cleaning process of the sapphire substrate. After cleaning, the reactor temperature was set down to 645°C. The sharply increasing reflectance in the range "A" corresponds to the sapphire nitridation and deposition of the 100 nm low-temperature AlN (LT-AlN) layer. Then, the reactor temperature was ramped up to 1100°C for annealing the LT-AlN (range "B"). For the most time-consuming AlGaN layer growth process, this last part was performed at a slightly increased reactor temperature of 1130°C (range "C"). An oscillating optical reflectance pattern started to emerge due to the Fabry-Perot thin-film interference [120]. The constant difference between reflectance minimum and maximum indicates a quasi-2D growth process, though the decrease in reflectance means surface roughening. A typical growth rate for the AlGaN layers was 0.44 μm/h resulting in a thickness of 1.2 μm layer thickness. But to achieve this specific growth result, a long road of trials and errors has been overcome.

The optimization of the AlGaN epilayers was divided into two parts. First, the optimization of growth conditions for AlN, second – for AlGaN. These two experiments enhanced the crystalline quality and surface smoothness of the AlGaN epilayer. The experiments started with the AlN nitridation process. As mentioned in Chapter 3, Section 3.3, nitridation is the most crucial process step in face controlling of group III-nitrides semiconductors. In order to obtain the Al-polarity AlN layer nitridation process was conducted under the low-temperature range 600°C ÷ 660°C and for a short time (200 s).

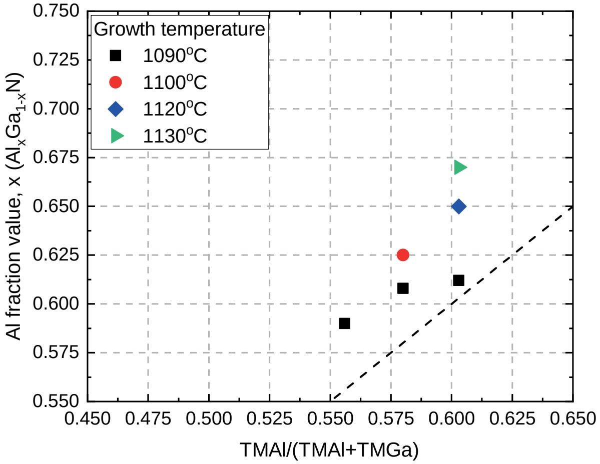

Figure 5.12: Al fraction dependency on the IIIrd group precursor ratio and AlGaN growth temperature. The dashed black line is for eye guiding [**A1**].

Next, an estimation of the Al fraction in the AlGaN layers was conducted, neglecting their crystalline quality and surface roughness. Al fraction was estimated using XRD $2\theta/\omega$ scan of (0002) crystallographic planes. The results are presented in Figure 5.12. The black dashed lines in Figure 5.12 represent the case when the Al fraction in the AlGaN layers would depend on a III$^{\text{rd}}$ group precursor ratio as a function of $f(x) = x$. Increased precursor ratio (increasing TMAl flow) results in a higher Al fraction. This result was expected from a logical point of view. Another major factor that changes the Al fraction in the AlGaN layer is temperature. The higher the growth temperature, the higher the Al fraction can be obtained at the same TMAl and TMGa flow ratio. It mainly occurs due to Ga atom desorption during the growth at higher temperatures because Ga-N (2.2 eV) bond energy is smaller than Al-N (2.88 eV) [121]. The optimal growth temperature for high crystallinity GaN epilayer is about 1060°C ÷ 1080°C [122], while instead, for the AlN epilayer, it must be much higher, i.e., 1200°C and higher [123–125]. As the Al-N bond is stronger than the Ga-N, higher temperatures are needed to increase Al atoms' mobility on the growth surface, thus allowing a 2D growth regime. To grow a high crystalline quality AlGaN epilayer, a mid-point between high and low temperatures must be considered. The AlN growth conditions don't impact the Al fraction in the AlGaN layers.

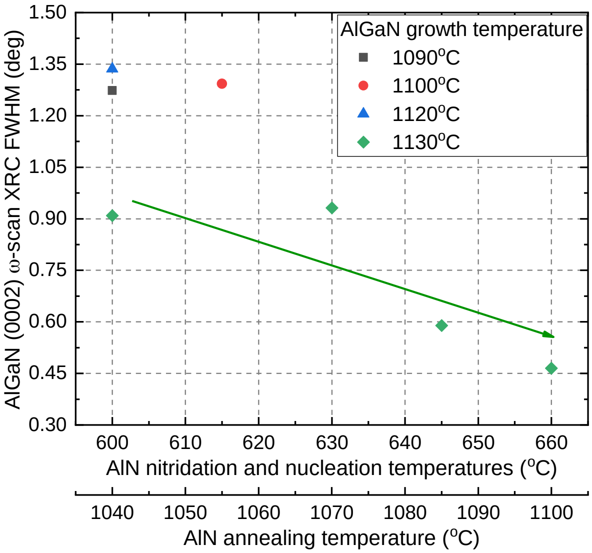

Figure 5.13: X-ray rocking curve (XRC) FWHM of AlGaN layers dependency on AlN growth conditions and AlGaN growth temperature. The solid green line is for eye guiding [**A1**].

As the AlN growth conditions don't impact Al fraction in the AlGaN layers, subsequent AlN growth process optimization was conducted by constantly checking the AlGaN layers' crystal quality, growth kinetics and surface rough-

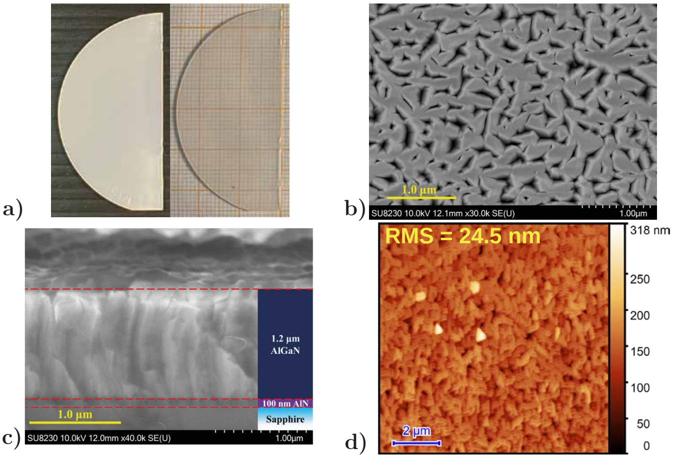

Figure 5.14: (a) The photo of the same AlGaN sample on the dark background and millimeter paper. (b) SEM images of the surface and (c) cross-section of this sample. (d) 10×10 μm AFM image of AlGaN surface.

ness. As presented in Figure 5.13, the growth parameters optimization for AlN resulted in the possibility of reaching a good crystalline quality for AlGaN layers. It is seen that the higher growth temperature the better crystallinity can be obtained, but only for temperatures higher than 1120°C, as indicated by a gradual decrease in the XRC full width at half maximum (FWHM). Also, it means smaller orientation fluctuation in the (0002) plane [126]. The first growth result of the AlGaN layers on the AlN is presented in Figure 5.14. The AlGaN layer shown in Figure 5.14 was grown on the AlN layer with nitridation and deposition temperatures of 600°C, and 1040°C annealing temperature, while the growth temperature of AlGaN was 1090°C. The first inspection was made by eye and the optical images represent how the sample looks under the room illumination. The AlGaN layer seemed to be transparent and had a mirrorlike surface, but when it was taken on a dark background, the sample turned out to be "white". It means that the light was scattered by imperfections on the surface of the layer. SEM and AFM images were taken to evaluate the quality and smoothness of the surface. To ensure that only the surface is responsible for the light scattering SEM image of the AlGaN/AlN cross-section was taken (see Figure 5.14 (c)). This measurement confirmed that the bulk of AlGaN is fully coalesced and only the sample's surface has not coalesced. The AFM image presents the same results as the SEM surface image and allows the evaluation of AlGaN surface smoothness (RMS = 24.5 nm).

AlGaN crystal quality and surface smoothness were noticeably improved by raising the processes temperatures for AlN and AlGaN. The evolution of the AlGaN surface by changing the growth conditions is presented in Figure 5.15. The threshold temperature of 1130°C for AlGaN layer growth means that Al

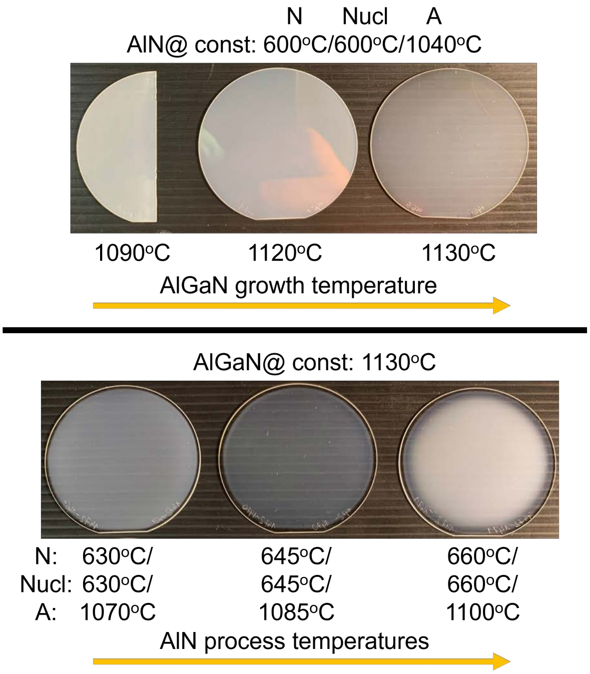

Figure 5.15: Evolution of AlGaN surface under different growth parameters for AlGaN and AlN. N; Nucl; A denotes for N – nitridation, Nucl – nucleation, A – annealing processes.

atoms have sufficient surface mobility, allowing them to find the most suitable energetically site on the surface and form uniformly oriented crystallites. With the growth temperature and higher Al fraction in the AlGaN layer, the lattice mismatch between AlN and AlGaN layers decreases [126]. The crystalline quality of the AlGaN layers was improved significantly when the LT-AlN layer was nitrided, nucleated, and annealed at a higher temperature. It means that the optimal nitridation condition can effectively relieve the lattice mismatch between LT-AlN and sapphire so that a majority of LT-AlN layer grains have uniform [0001] orientation parallel to sapphire [0001] [123]. There was no substantial crystal quality change for the temperature range from 1090°C to 1120°C.

Figure 5.16 presents AlGaN layer RMS dependency on AlN layer growth conditions. A decrease was observed in RMS values reaching their minimum value of 3.5 nm with the AlN layer nitridation and nucleation temperatures. Moreover, there are some threshold temperatures where a steep jump toward high RMS values can be observed. Surface morphology also changes from wrinkled to the columnar pattern. Most probable is that the change originates from the underneath grown AlN layer [125]. At the optimal AlN nitridation and nucleation temperatures of 645°C, the AlGaN layer in the initial growth

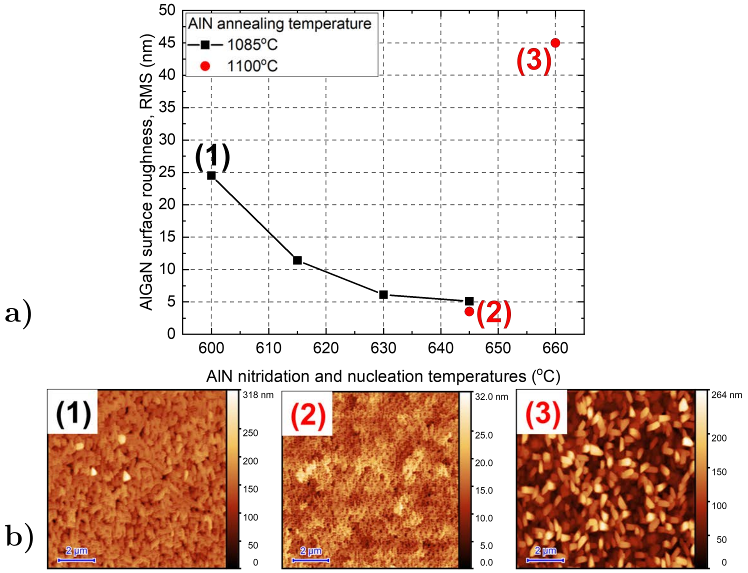

Figure 5.16: (a) AlGaN surface roughness (RMS) dependency on AlN nitridation, nucleation, and annealing temperatures. (b) 10×10 μm AFM surface images of AlGaN layers grown on the differently prepared AlN layers [**A1**]. The curve is only for eye-guiding purposes.

stage forms large hillocks, which coalesce, creating loops of dislocations but not propagating to the surface. Wrinkled AlGaN surface, however, results from not fully coalesced large hillocks. After increasing the AlN nitridation and nucleation temperature to 660°C, AlGaN crystalline quality improves further (see Figure 5.13), but the surface drastically deteriorates (see Figure 5.16 point (3)). In this case, the initial growth of the AlGaN layer may occur layer-by-layer on better quality AlN surface formed either due to better Al atom mobility or layer restructuration. It implies larger strain energy for a thicker layer, which can be lowered by the islands formation [125].

5.2.2. Growth of the Ga-polarity GaN layer on the AlGaN

Extensive work was also conducted by optimizing the Ga-polarity GaN growth parameters on the AlGaN layers. Ga-polarity GaN growth results under different growth conditions are summarized in Table 5.1. The presented table summarizes the surface morphology change of Ga-polarity GaN layers using different V/III ratios and growth temperatures. The surface roughness RMS value of Ga-polarity GaN layers was a parameter of interest. It was imperative to keep the Ga-polarity GaN layers surface as smooth as possible to achieve abrupt surface between N-polarity and Ga-polarity GaN layers to keep optical losses in the form of scattering as low as possible.

Table 5.1: 10×10 μm AFM images of Ga-polarity GaN surface morphologies under the different growth temperatures and V/III ratios.

Temperature V/III ratio	1065°C	1075°C
409		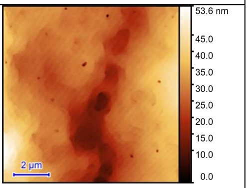
546		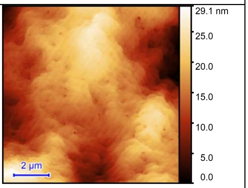
682	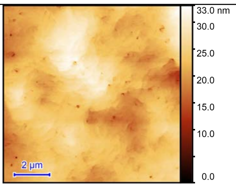	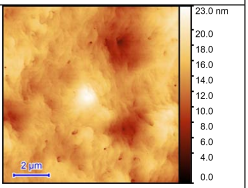
955	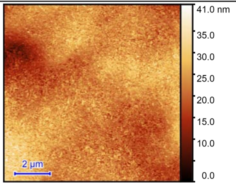	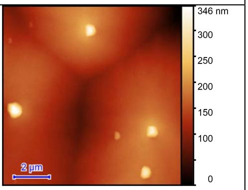

Figure 5.17 presents in situ optical reflectance of two growth processes. After the AlGaN growth process, the temperature was reduced to GaN growth temperatures and TMGa source and NH_3 source flow rates were set accordingly to V/III ratios presented in Table 5.1. It is why there is no oscillation between AlGaN and GaN reflectance oscillations. It also indicates no surface deterioration during temperature and flow rates change because the reflectance signal keeps its level at the end of AlGaN growth. Different V/III ratios were controlled by varying the NH_3 source flow rate and keeping the TMGa source at a constant flow rate. Even though the GaN layer exhibits Ga-polarity, which was determined by the AlGaN layer beneath, in situ optical reflectance compared to Figure 3.6 (a) from Chapter 3 presents quite a significant difference. Mentioned difference between these reflectance signals comes from different growth regimes. As mentioned in Chapter 3 GaN on the sapphire substrates at the beginning exhibit 3D growth regime due to a large lattice mismatch with a sapphire substrate. In this situation, Ga-polarity GaN starts to grow on the

AlGaN layer, where lattice mismatch is drastically reduced. The first oscillation in Figure 5.17 has a lower reflectance signal than subsequent oscillations. This latter fact indicates that GaN starts to grow in a quasi-2D regime. But after the first period, GaN changes its growth regime from quasi-2D to 2D.

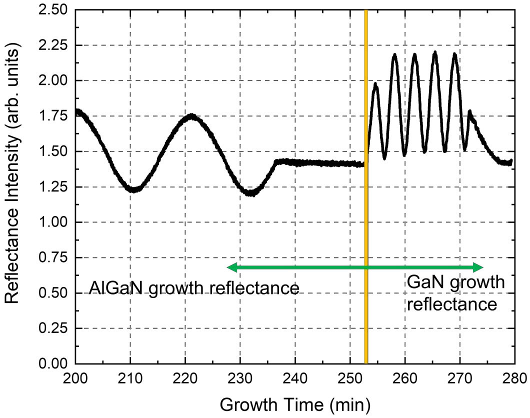

Figure 5.17: In situ optical reflectance of Ga-polarity GaN layer with 682 V/III ratio at 1075°C temperature.

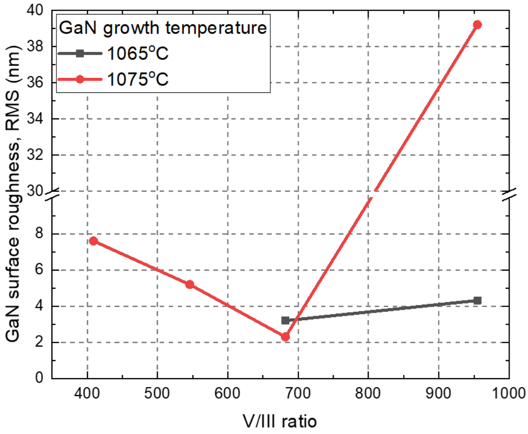

Figure 5.18: GaN surface roughness (RMS) dependency on the V/III ratio at different growth temperatures. Graph summarizes the table Table 5.1. Red and black lines are only for eye-guiding purposes.

Measured surface roughness values of Ga-polarity GaN layers grown on the AlGaN are presented in Figure 5.18. The latter figure is based on Table 5.1. Optimized parameters for Ga-polarity growth, in this case, are found to be at 1065 ÷ 1075°C temperatures for a V/III ratio of 682. By increasing the V/III ratio, the surface of GaN layers deteriorates much more than using lower V/III ratios. It is evidenced by much more increased RMS values for a higher V/III ratio in comparison to a lower V/III ratio. From Figure 5.18 and Table 5.1 can be seen that a significant difference occurs in GaN layers' surface roughness values and morphology for 955 V/III ratio and different growth temperatures. These two cases are absent of any terraces on the GaN surface. Such morphology can be attributed to two factors. Firstly, a change in growth temperature by 10°C enhances GaN evaporation. Secondly, due to higher V/III ratios, a saturation of NH_3 occurs. It causes a decrease in the Ga diffusion length on the layer surface, suppressing lateral growth, forming nuclei on the terraces and resulting in uncoalesced islands [90, 127]. While at lower V/III ratios, lateral growth is enhanced thanks to increased Ga diffusion length. Hence, the surface starts to exhibit terraces resulting in step flow. At lower V/III ratios (<682), due to excess of Ga and high nitrogen desorption rate, Ga may accumulate on the surface [127]. It can lead to increased surface roughness values.

5.2.3. ALD-Al_2O_3 as polarity inversion layer

To this date, few polarity inversion methods have been demonstrated. The first method is by introducing a highly magnesium (Mg) doped GaN interlayer [128]. The latter approach is unsuitable for optical purposes due to surface deterioration after such layer introduction and the formation of a highly defective region [129] (inversion direction from Ga to N) where optical scattering could be increased, thus resulting in propagation losses. On the contrary, Wong *et al.* [130] stated that the magnesium nitride (Mg_xN_y) layer didn't generate defects, but it must be noted that in Wong's case inversion direction was different (from N to Ga). This method lets inverse polarities from Ga to N and vice-versa. The second one – by introducing a thin AlN interlayer [131]. But this work is quite unique. Latter work presents GaN polarity inversion through AlN thin interlayer from N- to Ga-polarity GaN. The third one, presented recently, is by introducing oxidized AlN layer or aluminum oxide (Al_yO_x) interlayers [130, 132]. The third method is as follows, AlN is grown on the N-polarity GaN layers and then oxidized. By introducing oxygen (O) into AlN, a formation of $Al_xO_zN_z$ or Al_yO_x is to be believed. Stolyarchuk *et al.* [132] demonstrated this inversion method with AlN layers. Firstly, AlN layers were grown on a sapphire substrate and exhibited Al-polarity. Then these layers were oxidized and after the oxidation process, growth of AlN was resumed, which resulted in N-polarity AlN layers. It is worth noting that the word "thin" is not well defined, but the inversion boundary layer itself does not exceed 20 nm.

The abrupt interface between two polarities GaN layers was demonstrated by Hite *et al.* [21]. Latter work shows that inversion of GaN polarity happens after introducing 15 nm of Al_2O_3 deposited by atomic layer deposition (ALD) technique. It was demonstrated in a periodically poled GaN structure. By annealing ALD-Al_2O_3 at high temperature in the presence of NH_3, it is believed that ALD-Al_2O_3 transitions into a sapphire-like structure with a thin AlN layer which determines GaN polarity, wherein this case must be N-polarity. Thus, in my PhD work, the latter method was implemented to inverse GaN polarity from Ga to N.

Before growing the N-polarity GaN, ALD of Al_2O_3 on the Ga-polarity GaN was performed. The process was held at 200°C temperature under reduced pressure (N_2 atmosphere) of 3 mBar in a Picosun R-200 (Picosun Oy, Finland) deposition tool equipped with a Hine-loader. The TMAl precursor was vaporized from PicoSolution (Picosun Oy, Finland) source containers at room temperature (RT). Thermal ALD processes with a layer-by-layer deposition method were used to build up the layer, where N_2-purge separated the two different precursor materials. The oxidizing agent was water. III-polarity GaN/AlGaN structures were placed on a silicon wafer holder and loaded into the ALD reactor for the oxide layer deposition.

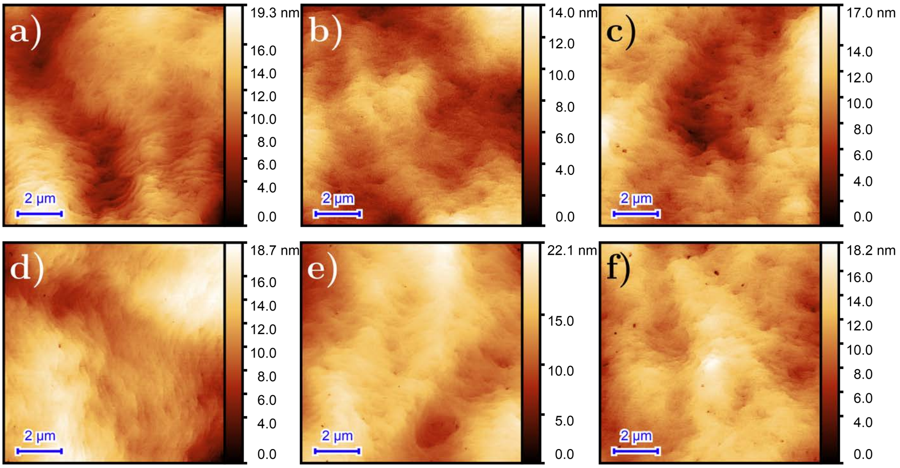

Figure 5.19: 10×10 μm AFM images of: (a) Ga-polarity GaN surface on the AlGaN layer and the surfaces of the different thickness ALD-Al_2O_3 layers on the III-polarity GaN/AGaN structure (b) 10 nm; (c) 15 nm; (d) 20 nm; (e) 30nm; (f) 40nm.

Figure 5.19 presents AFM surface images of different thickness ALD-Al_2O_3 layers deposited on Ga-polarity GaN/AlGaN structure. Figure 5.19 (a) shows a Ga-polarity GaN surface without a Al_2O_3 layer and was used as a reference image. No significant change in surface morphology can be observed from the latter figure. Analyzed RMS surface roughness dependency on ALD-Al_2O_3 thickness is presented in Figure 5.20. RMS values deviate from the reference value ±0.5 nm, which is the RMS surface roughness of Ga-polarity GaN. These two figures conclude that no surface deterioration is observed after the Al_2O_3 deposition process.

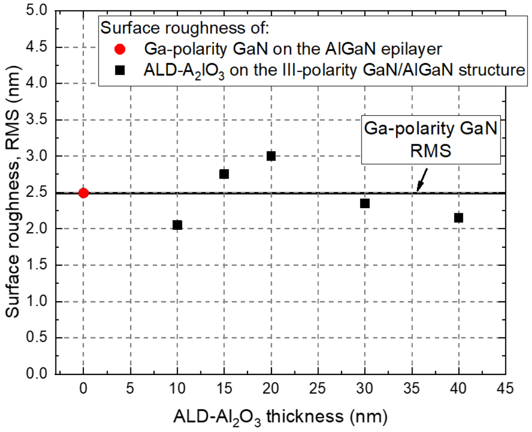

Figure 5.20: Surface roughness RMS values of Figure 5.19 AFM measurements of the Ga-polarity GaN on the AlGaN layers and of ALD-Al_2O_3 layers of different thicknesses on the III-polarity GaN/AlGaN structure.

5.2.4. Growth of the N-polarity GaN layer on the ALD-Al_2O_3

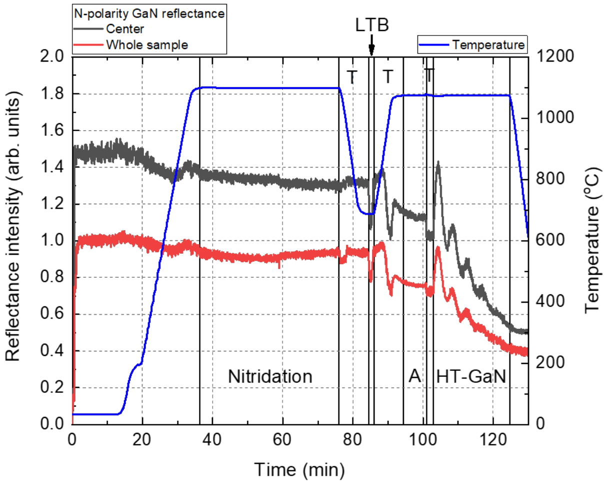

Figure 5.21: Growth diagram of N-polarity GaN layer. Letters denote for: T – temperature stabilization; A – annealing, LTB, and HT-GaN low and high temperature GaN growth, respectively [**A1**].

Before the growth of the N-polarity GaN, annealing and nitridation processes were conducted on the samples simultaneously at high temperature (segment Nitridation). One of the first experimental growth kinetics of the N-polarity GaN on the ALD-Al_2O_3 layer is shown in Figure 5.21.Latter shows a typical growth process that was used in most experiment cases during the PhD project. During annealing and nitridation processes (in Figure 5.21 denoted as "Nitridation"), the reflection signal which comes from the surface does not change nor rise, but more importantly, does not drop. It indicates that the sample surface is not evaporating nor roughening. Nitridation and annealing were performed for the different duration (5, 40 and 60 minutes) in H_2 or N_2 ambient at $1100°C \div 1130°C$ temperatures. The conditions for nitridation and annealing processes were similar to those for normal nitridation of sapphire substrates before the N-polarity GaN growth but of longer duration and higher temperatures [21]. After a prolonged nitridation process of ALD-Al_2O_3 temperature was reduced, the reactor was prepared for low-temperature buffer (LTB) layer growth. The latter process can be seen in Figure 5.21 as a sharp oscillation after the temperature stabilization step (segment LTB). After LTB growth annealing process of the buffer layer was followed. Although TMGa source was off during temperature stabilization steps, a change in reflectance signal can be observed during the temperature rise step in Figure 5.21. It likely comes from the interference of reflected rays from different layers, each of them with a different refraction index and different refraction index temperature dependency. When the temperature is stabilized, the reflection signal also gets stabilized. After the LTB layer annealing process reactor has been prepared for high-temperature GaN (HT-GaN) growth in H_2 ambient. The work was mainly concentrated on the N-face GaN growth, and many growth parameters were tested. More detailed growth parameters and characterization results will be presented in the next Chapter 6.

6. CHARACTERIZATION OF N-POLARITY GaN

A lot of effort was given to find the growth parameters for N-face GaN layers on the ALD-Al_2O_3. Moreover, there is no easy way to grow N-face GaN on the substrates (i.e., sapphire) using lower off-cut angles ($0.1° \div 1°$) because N-face GaN layers prefer to form hexagonal hillocks at the surface. To have a good crystalline quality and smooth surface N-face GaN layers the growth must be performed on the substrates with higher off-cut angles ($1° \div 2°$ and larger). But the difficulty comes from the structure design grown on the lower off-cut (0.3°) sapphire substrate. The structure presented in this work (Chapter 5, Section 5.2) exhibits Al-polarity AlN and AlGaN buffer and cladding layers, respectively. Starting the structure from the N-polarity AlN and AlGaN layers is possible, but not in this case, as the limitations come from the MOCVD reactor build. To grow a good crystalline quality and smooth surface N-face Al-based layers, quite elevated (up to $1150°C \div 1300°C$ for N-polarity AlN) growth temperatures are needed [133–135]. The higher the growth temperature, the higher AlN crystalline quality can be obtained. Such high temperatures are necessary for Al adatoms to freely migrate on the substrate surface, as the Al adatom mobility compared to Ga and In is the lowest. Such model reactor in the lab cannot withstand such elevated temperatures.

This chapter will be focused mainly on the N-face GaN characterization results. It will present the first growth results on the ALD-Al_2O_3 layers. The whole approach process from the N-face GaN on the sapphire substrates to the N-face GaN on the metal-polarity waveguiding structure using ALD-Al_2O_3 layers as a polarity inversion layer. The key parameter here was the surface roughness of the N-face GaN layer. The lower the surface roughness, the more effective mode coupling into the waveguide and the less scattering of light will occur.

This chapter is based on the research published in papers [**A1**] and [**A2**].

6.1. N-polarity GaN growth experiments – finding core growth process

Before performing N-polarity GaN growth experiments on the waveguiding structure, core recipe steps were found from the N-polarity GaN growth experiments on the 2° off-cut angle sapphire substrates. The recipe's core, as already was mentioned before, consisted of four steps, i. e. nitridation, growth of low-temperature buffer layer, low-temperature buffer layer annealing and growth of high-temperature layer. Every growth experiment started with the cleaning process in order to remove any contaminants from the sapphire substrates. During the latter process temperature in the reactor was elevated to 1100° for 5 minutes. The cleaning process was held in an H_2 atmosphere.

After the cleaning process, the N-polarity GaN layer growth process was followed. Luckily, growth parameters optimization of N-polarity GaN layers grown on the 2° off-cut angle sapphire substrates was not so complicated. The recipe's core parameters are listed in Table 6.1. As mentioned before, to achieve N-polarity GaN layers, a prolonged nitridation process at a high temperature was held. In this case, the nitridation duration was 432 s (7.2 min). It is about 3 times longer than our standard Ga-polarity GaN nitridation process.

Table 6.1: Growth parameters of N-polarity GaN layer grown on the 2° sapphire substrates core recipe.

Process	Temperature (°C)	Time (s)	Pressure (mBar)	Ambient	V/III ratio
Nitridation	970	432	100	H_2+NH_3	–
LTB-GaN	700	90	100	H_2+NH_3	1091
Annealing	1075	400	150	H_2+NH_3	–
HT-GaN	1075	1044	150	H_2+NH_3	546

Optimized N-polarity GaN layer XRD results are presented in Figure 6.1. In order to inspect N-polarity GaN layers' crystal configuration, out-off-plane $2\theta/\omega$ of (0002) and in-plane $2\theta/\varphi$ of (11$\bar{2}$0) planes scans were performed. From Figure 6.1 (a) one can be seen that N-polarity GaN in the [0002] direction is almost fully relaxed. This conclusion was made according to the (0002) XRD peak position for GaN. When GaN is fully relaxed in the [0002] direction (0002) XRD peak position is at 34.57°. From the $2\theta/\omega$ measurement of (0002) peak position was found to be at 34.55°. While N-polarity GaN in the [0002] direction was almost fully relaxed, in the [11$\bar{2}$0] direction exhibited in-plane tensile strain. A latter conclusion was made from Figure 6.1 (a) $2\theta/\varphi$ scan. Red curve is shifted toward smaller 2θ angles from the nominal value of fully

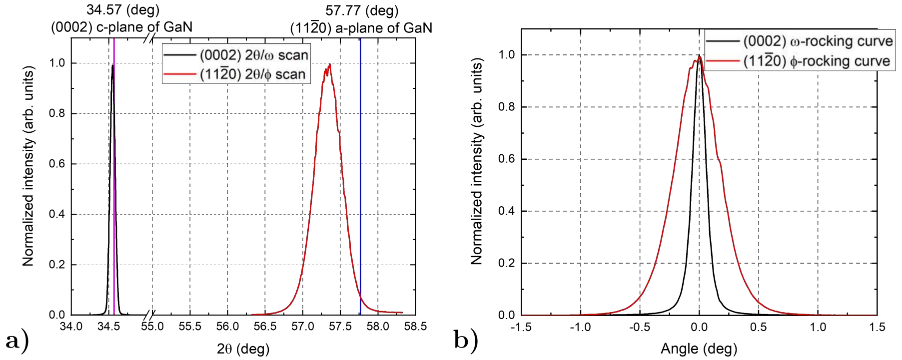

Figure 6.1: XRD scans of optimized N-polarity GaN : (a) 2θ scan of (0002) and (11$\bar{2}$0) planes; (b) rocking curves of (0002) and (11$\bar{2}$0) planes. Magenta and blue colored vertical lines indicates the values of angle for a relaxed layer.

relaxed $(11\bar{2}0)$ GaN planes. 2θ angle value for fully relaxed $(11\bar{2}0)$ GaN planes is 57.77°. The peak position of the curve resulted at 57.338°. In order to be sure that this strain does not come from the bowing of sapphire substrate due to different thermal expansion coefficients between sapphire and GaN radius of the 2-inch sample, curvature was evaluated. The measured curvature radius was about 416 m, resulting in the sample being flat. Thus latter strain comes only from lattice parameters mismatch between sapphire and GaN.

XRD ω rocking curve (XRC) scan of (0002) plane was performed in order to evaluate crystalline quality along [0002] direction (see Figure 6.1(b) black curve). From fitting results, the full-width-half-maximum (FWHM) of the (0002) XRC peak was found to be 487 arcsec, which is comparable to the ones presented in the literature [136, 137]. XRC φ scan of $(11\bar{2}0)$ planes (see Figure 6.1(b) red curve) crystalline quality in comparison to (0002) planes is deteriorated. The red curve is broader than the black curve presented in Figure 6.1(b), resulting in FWHM of 1609 arcsec. Due to lattice mismatch between GaN and sapphire, generation of threading dislocation is enhanced, thus deteriorating crystalline structure in $[11\bar{2}0]$ direction. There is also speculation that geometrical partial misfit dislocations, which are generated at the step edges in order to correct for the mismatched stacking sequences can also have an impact on the deterioration of crystalline structure [136]. The off-cut angle of sapphire substrate predetermines latter dislocation density. A larger off-cut angle can lead to higher geometrical partial misfit dislocation density [138].

Surface 10x10 μm AFM and OM images of optimized N-polarity GaN on the 2° off-cut sapphire substrates are presented in Figure 6.2. GaN exhibits prominent surface steps and no hexagonal hillocks can be observed on the surface. Annealed LTB layer of N-polarity GaN exhibit densely packed islands. It is evidence that N-polarity GaN starts to grow from densely packed islands and during the HT-GaN growth step, islands coalesce relatively fast and switch to a 2D growth regime giving smooth surface morphology. To compare the surface morphology of N-polarity GaN, a couple of experiments were performed on LTB layers by changing their growth parameters. One experiment was done by increasing LTB growth time from 90 s to 135 s. The second one – LTB with

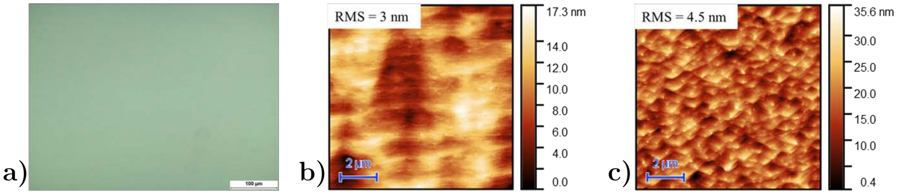

Figure 6.2: OM surface image (a) and 10×10 μm surface AFM images and surface roughness values of optimized N-polarity GaN layer (b) and its LTB layer after annealing process (c).

prolonged growth time was grown in N_2+NH_3 ambient. 10x10 μm AFM surface images of different LTB layers are presented in Figure 6.3. The prolonged LTB GaN growth layer resulted in bigger islands in comparison to the optimized N-polarity GaN growth parameters case (see Figure 6.3 (a) and Figure 6.2 (c)). Due to bigger islands, fluctuations in height were increased, resulting in the surface roughness increase. LTB surface roughness increase also was reflected in the HT-GaN surface roughness increase (see Figure 6.3 (c) and Figure 6.2 (b)). Quite a significant surface roughness increase was observed when the LTB GaN layer was grown under N_2+NH_3 ambient. The latter case resulted in even more increased islands (see Figure 6.3 (b)) and height fluctuation. It is evidence that H_2 helps to smooth the LTB GaN layer by enhancing its evaporation, thus reducing the size of the islands. This concludes that the smoother surface of LTB GaN is achieved, the smoother resulting surface of the HT N-polarity GaN would be achieved. It is worth noting that every sample exhibited an optically smooth surface and no hexagonal hillocks were observed.

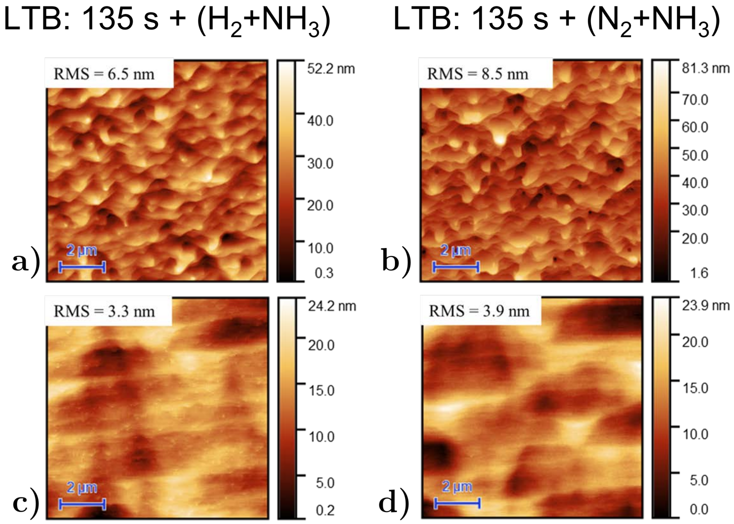

Figure 6.3: 10×10 μm AFM surface images of (a), (b) annealed LTB GaN layer grown under different ambient and (c), (d) resulting HT-GaN layer.

All samples grown on the 2° off-cut sapphire substrates exhibited N-polarity. This was proven by KOH etching method presented in Section 4.5.

6.2. N-polarity GaN on the different thickness ALD-Al_2O_3 layers

The core recipe for N-polarity GaN growth on the different thickness ALD-Al_2O_3 layers is presented in Table 6.2. Compared to Table 6.1 temperature of the nitridation process was elevated and the process time was extended. It

Table 6.2: Growth parameters of N-polarity GaN layer grown on the different ALD-Al_2O_3 thicknesses core recipe.

Process	Temperature (°C)	Time (s)	Pressure (mBar)	Ambient	V/III ratio
Nitridation	1100	2400	100	H_2+NH_3	–
LTB-GaN	670	90	100	N_2+NH_3	1091
Annealing	1075	400	150	N_2+NH_3	–
HT-GaN	1075	1311	150	H_2+NH_3	955

was done in order to impart crystallinity of the amorphous ALD-Al_2O_3 areas. Secondly, the growth of LTB GaN and its annealing process was conducted under N_2+NH_3. The latter change was made to ensure that GaN will grow on the annealed ALD-Al_2O_3 and won't be etched by H_2.

Figure 6.4 represents the OM and SEM images of the GaN epilayer grown on different thickness ALD-Al_2O_3 layers. The latter image presents three different of ALD-Al_2O_3 were deposited on the III-polarity GaN/AlGaN structure. The thicknesses of ALD-Al_2O_3 were 10nm, 15 nm and 20 nm. Samples that were indicated by an inset with a blue box ("Etching") featured an ability to be etched in the KOH solution; therefore, the inset with a red box ("No Etching") means that these samples cannot be etched and probably exhibiting Ga-polarity. From Figure 6.4, two different surface morphologies can be distinguished. GaN grown on the 10 nm ALD-Al_2O_3 layer in both OM and SEM images formed large rounded hillocks with a flat surface on the top (see Figure 6.4 OM:I and SEM:I). An interesting fact was observed for the GaN layer grown on 15 nm ALD-Al_2O_3. Different surface morphologies were achieved depending on the 15 nm ALD-Al_2O_3 nitridation duration. For a shorter nitridation time (5 min), hexagonal hillocks on the GaN layer surface can be

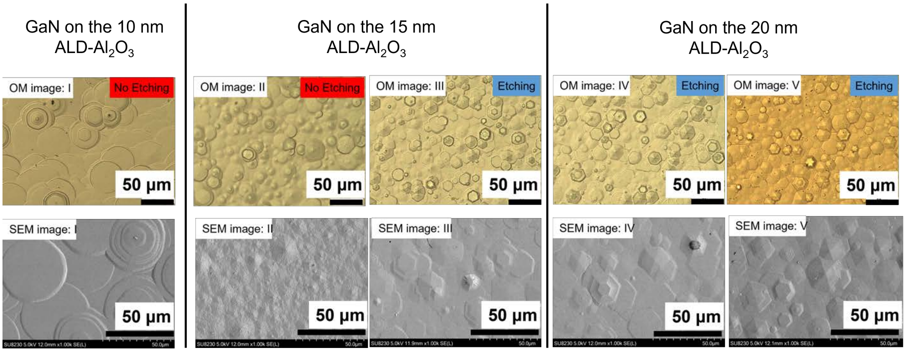

Figure 6.4: OM (above) and SEM (below) surface images of GaN epilayer grown on the ALD-Al_2O_3 of different thickness (10, 15, 20 nm). "No Etching", "Etching" indicate ability to be etched in the KOH solution. Nitridation time for III – 5 min., for I, II, IV, V – 40 min. Based on [**A1**].

observed (see Figure 6.4 OM: III and SEM: III). While after a longer nitridation time (40 min (2400 s)) GaN layer on the 15 nm ALD-Al_2O_3 exhibited a smoother surface with rounded hillocks (see Figure 6.4 OM: II and SEM: II). Thus, for the 15 nm ALD-Al_2O_3 layer, the longer the nitridation duration, the fewer hexagonal hillocks can be observed. Every GaN layer grown on a 20 mn ALD-Al_2O_3 exhibited hexagonal shape hillocks on their surface (see Figure 6.4 OM: IV,V and SEM: IV,V). As mentioned before, hexagonal hillocks may indicate that the GaN layer could exhibit N-polarity [139–141]. These experiments showed that consistent surface morphology results were acquired on the 20 nm ALD-Al_2O_3. Thus further experiments were performed on the latter ALD-Al_2O_3 layer thickness.

Nitridation:	**H_2+NH_3**		**N_2+NH_3**
Temperature **V/III ratio**	**1075°C**	**1100°C**	**1100°C**
600		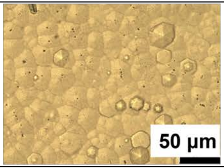	
682	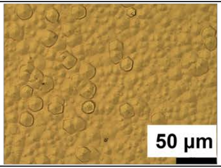		
955	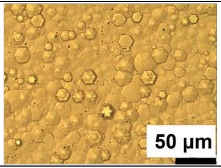	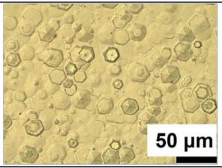	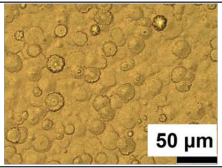

Figure 6.5: OM surface images of GaN layer grown on ALD-Al_2O_3 layer of 20 nm thickness under different V/III ratio and growth temperature (HT-GaN process) preceded by nitridation in H_2+NH_3 or N_2+NH_3 ambient. Based on [**A1**].

Figure 6.5 presents surface morphology for the N-polarity GaN layer grown on the 20 nm ALD-Al_2O_3 under different growth parameters and nitridation ambient. There was any significant difference in surface morphology by changing the nitridation environment. Hexagon-shaped hillocks can be seen either on the surfaces where samples were nitrided under H_2+NH_3 or N_2+NH_3 ambient (see Figure 6.5 third row). Growing HT-GaN under higher V/III ratio hexagon-shaped hillocks also can be observed on the surface. For reduced V/III ratios, the surface becomes smoother (see Figure 6.5 first and second rows). Such surface morphology change on the V/III ratio was also observed by Hite *et al.*

and Deng *et al.* [21, 142]. Reduction of the V/III ratio increases Ga flux at the sample surface while reducing N atom concentration. The latter fact, as mentioned in Section 3.3 according to Zywietz *et al.* [90] calculation, reduces the migration barrier and increases the mobility of Ga at the N-polarity surface. These factors enabled to obtain more coalesced and uniform N-polarity GaN surface.

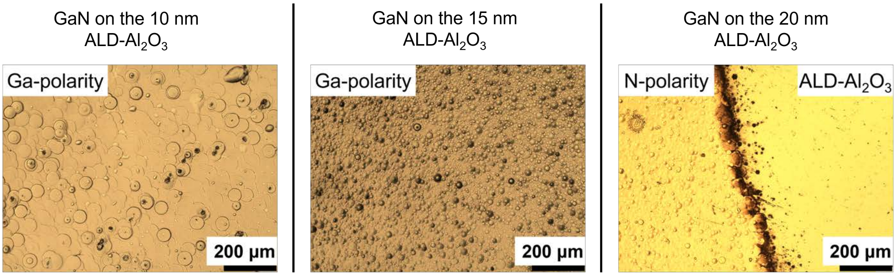

Figure 6.6: OM surface images of GaN layers grown on 10 nm, 15 nm and 20 nm ALD-Al_2O_3 after KOH etching experiments.

For N-polarity GaN testing, all grown samples on either 10, 15 and 20 nm ALD-Al_2O_3 layer were etched in KOH solution by employing earlier mentioned (Section 4.5) process. The result revealed a minimum thickness for the ALD-$Al_2O_3$when N-polarity GaN layers could be achieved. Etching in KOH solution results is presented in Figure 6.6. For 10 nm ALD-Al_2O_3 layers, the GaN layer remained unetched indicating the Ga-polarity GaN growth. GaN layers grown on 15 nm ALD-Al_2O_3 layers also remained unetched, thus also indicating Ga-polarity growth. It is worth noting (not shown here), that one GaN sample with a shorter nitridation time (5 min) grown on the 15 nm ALD-Al_2O_3 layer has been etched in KOH solution indicating N-polarity GaN layer. Therefore all grown GaN samples on the 20 nm ALD-Al_2O_3 layer were easily etched in KOH solution, thus exhibited N-polarity GaN layers.

Moreover, determination of GaN polarity grown under different growth parameters on 20 nm ALD-Al_2O_3 layers was conducted. The etching results of a latter experiment are presented in Figure 6.7. All samples exhibited an N-polarity GaN layer. On the left side of the OM images, the unetched N-polarity GaN surface can be seen, while on the right – the surface of the ALD-Al_2O_3 layer. Differences in etching results can be seen in N-polarity GaN samples where nitridation ambient of 20 nm ALD-Al_2O_3 differed. Residues in the form of dark hexagonal-shaped hillocks remained on the 20 nm ALD-Al_2O_3 surface, where nitridation was held under N_2+NH_3 environment. This fact can indicate that nitridation under N_2+NH_3 environment of 20 nm ALD-Al_2O_3 was insufficient and led to Ga-polarity GaN inclusions which remained on the surface of 20 nm ALD-Al_2O_3 after the etching.

Structural investigation of N-polarity GaN layers grown on 20 nm ALD-

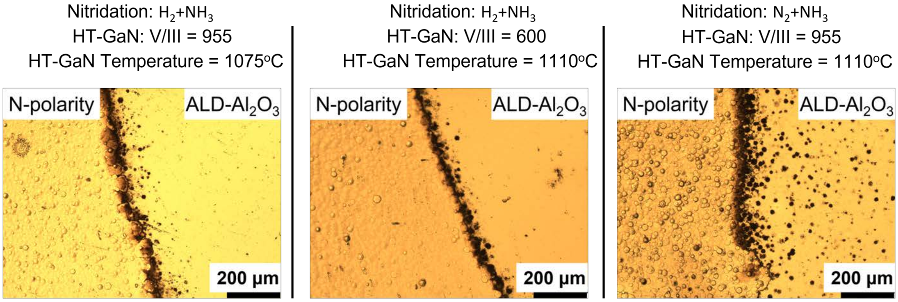

Figure 6.7: OM surface images of etching contrast of N-polarity GaN layers grown under different growth parameters on 20 nm ALD-Al_2O_3 after KOH etching experiments. Left-hand side – unetched GaN layer, on right-hand side – etched away, indicating the presence of N-polarity.

Al_2O_3 layers was performed by measuring a $2\theta/\omega$ scan for the entire GaN waveguide structure. The (0002) diffraction patterns of GaN layers grown under different conditions are presented in Figure 6.8.Two typical peaks representing GaN and AlGaN, where Al concentration is approximately 65% (see Section 5.2.1), can be observed. Due to Al concentration fluctuation, AlGaN $2\theta/\omega$ peaks are slightly shifted between themselves. Although different growth conditions of N-polarity GaN were employed, no significant change in GaN $2\theta/\omega$ peaks can be observed. It is worth noting that all GaN layers presented in Figure 6.8 along [0002] direction (growth direction) are almost relaxed. This fact is confirmed by a magenta line representing fully relaxed GaN along [0002] direction.

To provide more evidence about the N-polarity GaN growth, a ω XRC scan for 15 nm and 20 nm ALD-Al_2O_3 layer samples was performed. These results are presented in Figure 6.9. Figure 6.10 provides a clearer illustration of the legend explanation given in Figure 6.9. Comparing black and green curves in Figure 6.9 (a) GaN layer, which was grown on the 15 nm ALD-Al_2O_3, exhibited similar crystal quality to Ga-polarity GaN beneath the ALD-Al_2O_3 layer. It must be noted that GaN layers grown on 15 nm ALD-Al_2O_3 using growth parameters presented in Table 6.2 didn't exhibit N-polarity. FWHM of (0002) XRC scan for both curves is close to 1188 arcsec. In contrast, the GaN layer grown on the 20 nm ALD-Al_2O_3 layer exhibited a broader FWHM value of 1645 arcsec than the one beneath the layer (see blue and magenta curves in Figure 6.9 (b)). Deteriorated crystal quality may be an indication of N-polarity GaN formation. N-polarity GaN layers FWHM values of XRC (0002) in this work are by far larger than N-polarity GaN given in the literature ($367 \div 615$ arcsec) [140, 141, 143]. However, the complex nature of structure in this work consisting of ALD-Al_2O_3/GaN/AGaN beneath grown N-polarity GaN could explain such crystal quality deterioration.

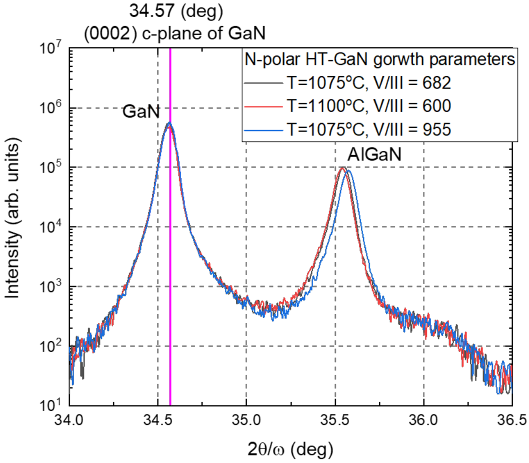

Figure 6.8: $2\theta/\omega$ scan (0002) of GaN waveguiding structure with N-polarity GaN layer grown under different conditions. Magenta line defines fully relaxed GaN $2\theta/\omega$ angle value. Based on [**A1**].

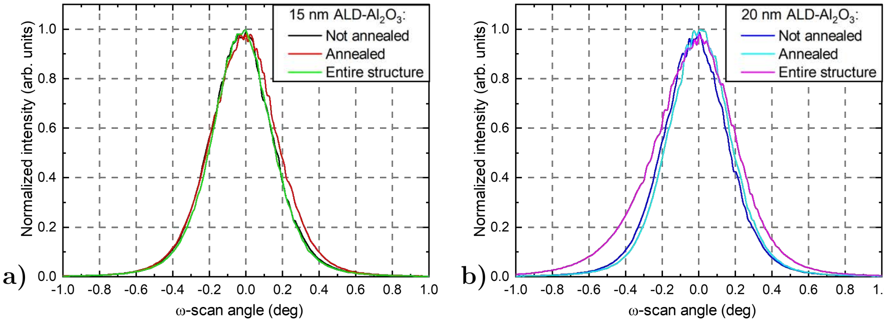

Figure 6.9: XRC of (0002) ω scan of samples grown on (a) 15 nm ALD-Al_2O_3 and (b) 20 nm ALD-Al_2O_3. "Not annealed" – the sample structure up to the ALD-Al_2O_3 layer included, "Annealed" – the same structure annealed under the "Nitridation" in the growth diagram (see Figure 5.21). Based on [**A1**].

Further investigation of the crystal quality was performed among the structures, which exhibited N-polarity GaN on the 20 nm ALD-Al_2O_3 layers. Two ω scans of N-polarity GaN layers grown at different temperatures but using the same V/III ratio XRC results are presented in Figure 6.11. Any substantial difference can be observed in the (0002) XRC scan, but a slightly smaller FWHM value was obtained for the N-polarity GaN layer, which was grown at a lower temperature (see Figure 6.11 (a)). The negligible difference in FWHM values of (0002) XRC scans is quite understandable as the below Ga-polarity GaN from sample to sample was grown under the same growth conditions and has a significant impact on (0002) XRD scans. It is impossible to avoid its influence on the overall signal in this measurement configuration. Therefore, an additional

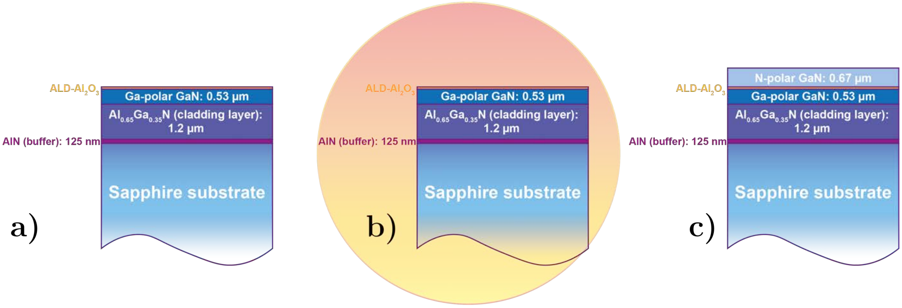

Figure 6.10: Legend explanation of Figure 6.9. (a) "Not annealed", (b) "Annealed" – nitridation/annealing process (red-yellow circle), (c) "Entire structure".

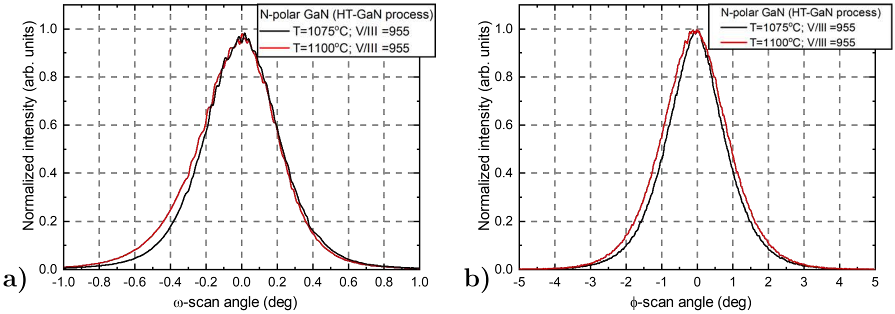

Figure 6.11: (a) (0002) ω and (b) $(11\bar{2}0)$ φ XRC scans of N-polarity GaN layers grown at different temperatures (HT-GaN process). Based on [**A1**].

in-plane XRC scan measurement was performed for the $(11\bar{2}0)$ plane. Results of the latter XRC scans are presented in Figure 6.11 (b). Directing X-ray beam by very small incident angle (i. e. 0.8°) to the surface, penetration depth in GaN crystals equals about 400 nm [144]. It means that X-rays test the upper part of the waveguide structure only and don't exceed the Ga-polarity GaN layer below the ALD-Al$_2$O$_3$. In-plane XRC scan showed a noticeable smaller FWHM value for N-polarity GaN grown at lower temperatures (1.88° vs. 2.13°, where 1°=3600 arcsec).

In order to analyze the morphology of the ALD-Al$_2$O$_3$ layers, as a crucial factor for the GaN layer polarity inversion, TEM and HRTEM analysis for the 10 nm and 20 nm ALD-Al$_2$O$_3$ layers was performed. For the record, GaN layers on the 10 nm ALD-Al$_2$O$_3$ exhibited Ga-polarity, while N-polarity GaN layers were on the 20 nm ALD-Al$_2$O$_3$ layers. The main region of interest was the interface of the GaN layer of both polarities with the ALD-Al$_2$O$_3$ layer. Larger scale TEM images with elemental EDX analysis of the GaN/20 nm ALD-Al$_2$O$_3$/GaN area are presented in Figure 6.12. It was found that a homogeneous 20 nm ALD-Al$_2$O$_3$ layer forms abrupt interfaces with GaN layers which are

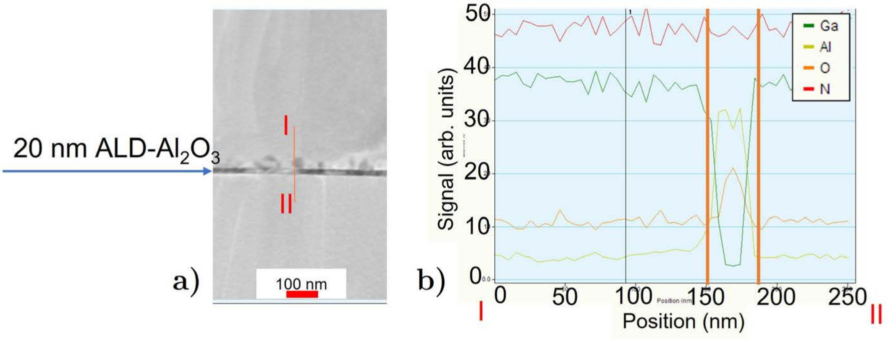

Figure 6.12: (a) TEM micrograph of the GaN/20 nm ALD-Al_2O_3/GaN interface area cross-section. (b) TEM EDX of the GaN/20 nm ALD-Al_2O_3/GaN interface area. The x-axis corresponds to the length of the vertical red color segment in (a). EDX data was acquired along the vertical red segment. (a) and (b) figures based on [**A1**]. Orange vertical lines in EDX spectra shows approximately ALD-Al_2O_3 area.

below and above the latter layer (see Figure 6.12 (a)). Material mapping data in cross-section was acquired from the TEM images presented in Figure 6.12 (a). Unfortunately, such TEM images and EDX analysis weren't done for the GaN/10 nm ALD-Al_2O_3/GaN interface. It can be seen that a persistent signal of nitrogen concentration was acquired along the scanning line, also in the area of 20 nm ALD-Al_2O_3. Oxygen and aluminum signals were acquired in the ALD-Al_2O_3 scanning area indicating of nitrogen-containing $Al_xO_zN_z$ compound which is forming during the early stages of the nitridation process with the simultaneous crystallization of the ALD-Al_2O_3 layer and helps to invert the polarity of the GaN layer [84–86].

HRTEM results are presented in Figure 6.13. To better understand defined planes in Figure 6.13, Miller indices for GaN crystal are given in Figure 6.14. It must be noted that the horizontal direction in Figure 6.13 (a) and Figure 6.13 (e) in one case is $[11\bar{2}0]$, in another – $[10\bar{1}0]$. This was done unintentionally due to mistakenly cutting and preparing the samples for HRTEM measurements. Fast Fourier transformation (FFT) analysis was performed on each segment presented in Figure 6.13 (a) and Figure 6.13 (e). The latter study provides information about each layer's crystallographic phase and lattice orientation (GaN I, ALD-Al_2O_3 and GaN II). FFT analysis of GaN I, ALD-Al_2O_3 and GaN II segments in the sample with the 10 nm ALD-Al_2O_3 layer (see Figure 6.13 (a), (b), (c), (d)) showed that all layers are homogeneous and (0002) planes are strictly oriented parallel to the sample surface. Moreover, FFT results (see Figure 6.13 (b), (c), (d)) show that the 10 nm ALD-Al_2O_3 layer "mimics" and transforms the hexagonal phase of the Ga-polarity GaN layer beneath the ALD-Al_2O_3 layer (GaN I) to the Ga-polarity GaN on top of the ALD-

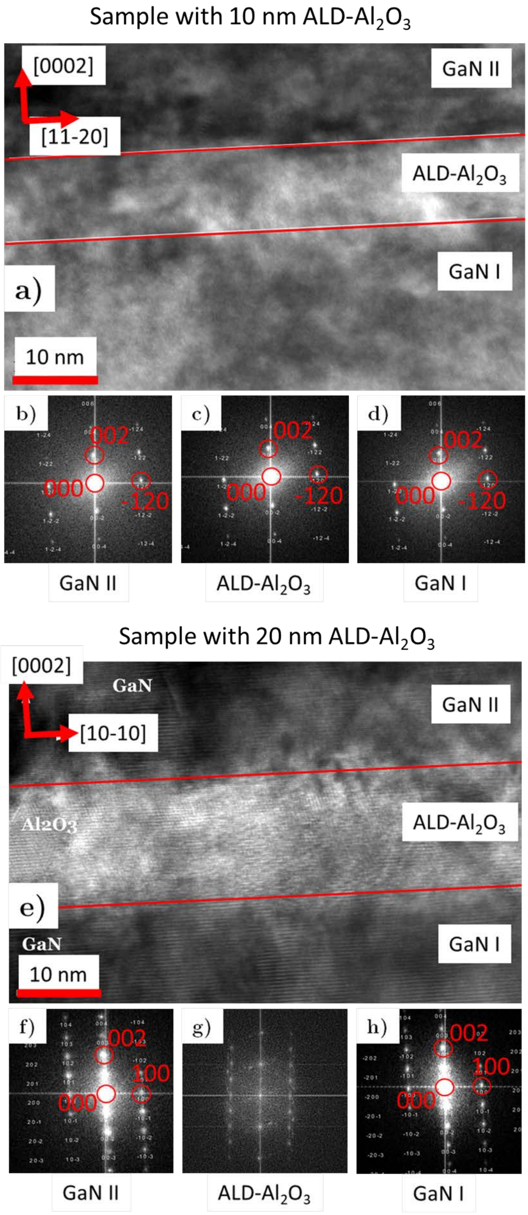

Figure 6.13: HRTEM micrographs of GaN/ALD-Al_2O_3/GaN interface area of sample (a) with 10 nm thickness ALD-Al_2O_3 and (e) with 20 nm thickness ALD-Al_2O_3. GaN I and GaN II label the GaN layers beneath and above the ALD-Al_2O_3 layer, respectively. Fast Fourier transformations (FFT) with assigned diffraction peaks from typical crystal lattice planes (b), (c), (d) for sample with 10 nm thickness ALD-Al_2O_3 layer and (f), (g), (h) for sample with 20 nm thickness ALD-Al_2O_3 layer. Based on [**A1**].

Al_2O_3 layer (GaN II). Worth to notice that the lattice orientation $(\bar{1}2\bar{1}0)$, or equivalent $(11\bar{2}0)$, remains in-plane of the TEM sample for all three segments in Figure 6.13 (a), indicating no (0002) rotation (see Figure 6.14).

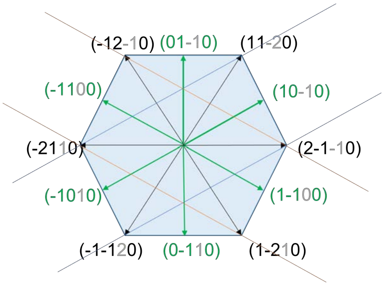

Figure 6.14: Typical crystal lattice planes with corresponding diffraction peak directions used to determine crystallography phase and lattice parameters from FFT of HRTEM images in Figure 6.13.

For the 20 nm ALD-Al_2O_3 sample, some particular differences can be observed for the ALD-Al_2O_3 layer itself (see Figure 6.13 (e), (f), (g), (h)). FFT analysis of the latter ALD-Al_2O_3 layer showed that crystallographic orientation is difficult to determine and attribute to some of the Al_2O_3 crystallographic orientations. Still, the GaN layer, which was grown on top of this ALD-Al_2O_3 layer exhibited N-polarity and [0002] orientation is oriented perpendicular to the sample surface and is parallel to the [0002] Ga-polarity GaN orientation, which is beneath the ALD-Al_2O_3 layer. One expectation from FFT analysis in Figure 6.13 (g) is that part of the ALD-Al_2O_3 layer after nitridation/annealing could exhibit a typical trigonal phase, the same phase as the sapphire substrate and having in-plane $[11\bar{2}0]_{\mathrm{GaN}}||[1\bar{1}00]_{\mathrm{sapphire}}$ epitaxial relation.

From this part of the work, threshold thickness for the ALD-Al_2O_3 layer was found and boarders well with the ones reported by Hite *et al.* [21]. Hite's work showed that the first 10 nm of the ALD-Al_2O_3 layer is damaged due to the nitridation/annealing process. The damage is probably done due to the diffusion of gallium and nitrogen atoms into ALD-Al_2O_3. In the scope of this work 10 nm ALD-Al_2O_3 layer also can be related to its ability to withstand the high nitridation temperature and to achieve a crystalline phase. To summarize, polarity inversion of GaN layers with 20 nm thick ALD-Al_2O_3 layers was achieved successfully. Contrary to Hite *et al.* [21] work, any rotation of the nitrided ALD-Al_2O_3 layer, i.e. $[11\bar{2}0]$ axis perpendicular to the sample surface, was not observed.

6.3. Smoothing the surface of N-polarity GaN

The previous section presented that 20 nm thick ALD-Al_2O_3 is able to invert GaN polarity from Ga- to N-, but the N-polarity GaN surface exhibited rough surface morphology with a high density of hexagon shape hillocks on it. This fact is not plausible for the performance of the waveguide because the rougher the surface of the waveguide, the higher the optical losses due to optical scattering. Thus, several growth parameters were changed from the "primal" growth recipe presented in the previous section to acquire as smooth surface as possible for the GaN layers. All growth experiments were performed on the 20 nm thick ALD-Al_2O_3/Ga-polarity GaN/Al-polarity AlGaN structure.

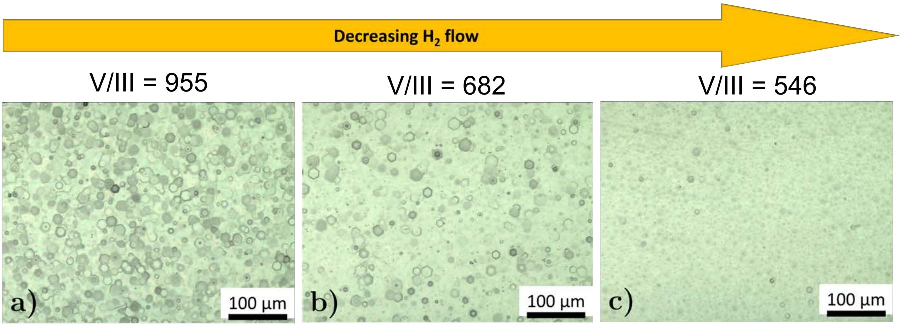

Figure 6.15: OM images of the N-polarity GaN sample surfaces grown in gradually decreased H_2 flow under different V/III ratios: (a) 955, (b) 682, (c) 545.

The first step was to try removing hexagonal shape hillocks from the sample surface. This step was reached by decreasing the overall H_2 presence in the reactor chamber by decreasing H_2 flow during HT-GaN growth. After dissociation of NH_3, it releases H atoms, which form H_2 molecules. Thus, NH_3 flow was also reduced during the HT-GaN growth step. By decreasing NH_3 flow, the V/III ratio decreases as well. TMGa flow was not changed during these experiments. Results of the growth experiments are presented in Figure 6.15. Significant surface morphology change can be seen between Figure 6.15 (a) with a higher V/III ratio and increased H_2 flow and Figure 6.15 (c) with the lowest ones. Due to decreased H_2 flow growth rate of N-polarity GaN was increased. At high GaN growth temperatures in the presence only of H_2 flow, GaN can be etched effectively [145–147]. Reaching a particular NH_3 flow threshold, it suppresses the thermal etching process drastically. Below the latter threshold, thermal decomposition of GaN occurs. While above the threshold, Ga diffusion length decreases [90], resulting in more columnar growth. So the point of this first step was to reduce the GaN etching process in H_2 and increase Ga diffusion lengths.

The second step evaluated the nitridation duration time effect on the N-polarity GaN surface morphology. These results are presented in Figure 6.16. Surprisingly, the most effective change was observed by changing nitridation time from 2400 s (40 min) to 3600 s (60 min) while maintaining all growth parameters at constant values. Quite a significant leap in RMS surface roughness

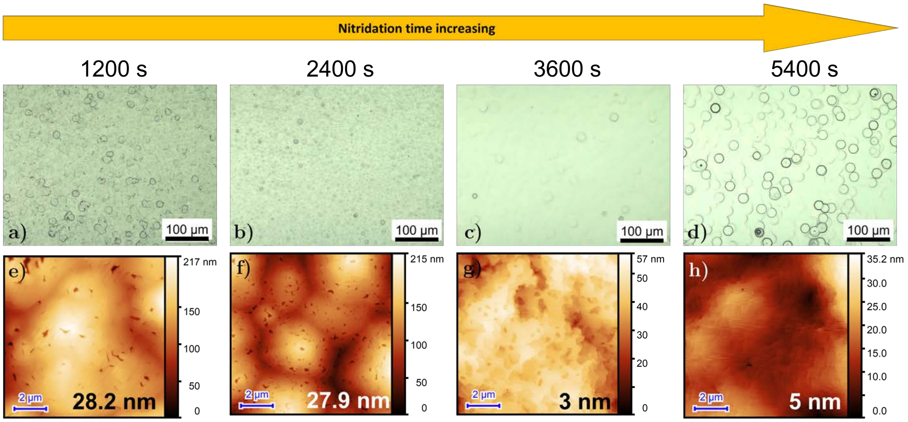

Figure 6.16: (a – d) OM images and (e – f) AFM images (10×10 μm) of the GaN sample surfaces grown after gradually increased nitridation time: (a, e) 1200 s; (d, f) 2400 s; (c, g) 3600 s; (d, h) 5400 s. The numbers given in nanometers are the RMS surface roughness values.

values was observed. From 28 nm for 1200 s nitridation time sample to 5.2 nm for 5400 s nitridation time sample. The similarity of surface morphologies can be observed in the samples grown on the 10 nm and 20 nm thick ALD-Al_2O_3 layers, but prolonged nitridation (5400 s) was used in the latter sample. The surfaces of these samples are presented in Figure 6.17. They both exhibited rounded and flat-surface hillocks on the surface. 10x10 μm AFM images show prominent terraces on both GaN samples' surfaces, where surface roughness RMS value vary between 2 nm to 5 nm. Worth noting that KOH etching results showed that the surface of the GaN sample presented in Figure 6.17 (b) was not affected by the KOH solution, thus indicating of Ga-polarity GaN layer on the 20 nm thick ALD-Al_2O_3 layer after the 5400 s nitridation process. GaN layers where nitridation process time was 1200 s, 2400 s and 3600 s were affected after KOH etching experiments. Some residues were left on the 20 nm thick ALD-Al_2O_3 with 3600 s nitridation process time. An explanation will be presented in the next section.

To conclude, the overall decrease in H_2 in the reactor chamber resulted in less hexagonal shape hillocks on the surface of GaN layers grown on the 20 nm thick ALD-Al_2O_3. Duration of nitridation process changes surface morphology of the GaN layers. With the prolonged nitridation time the GaN surface becomes smoother. The similarity was found between the GaN layers grown on the different ALD-Al_2O_3 layer thicknesses and with different nitridation times. As ALD-Al_2O_3 layer thickness was increased from the 10 nm to 20 nm, increased nitridation process time from 2400 s to 5400 s also resulted in the Ga-polarity GaN layer. It can indicate that the 20 nm thick ALD-Al_2O_3 layer after a prolonged (5400 s) nitridation process, recrystallized into a similar

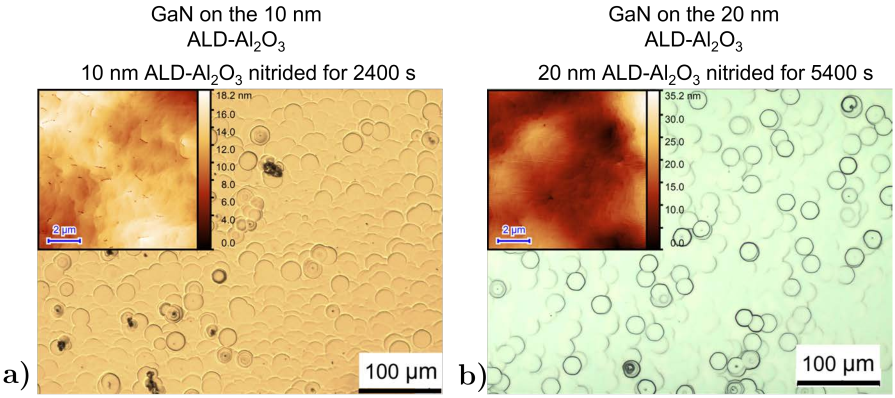

Figure 6.17: OM and AFM (10×10 μm) (insets) images of surface morphologies of GaN layers grown on the (a) 10 nm ALD-Al$_2$O$_3$ nitrided for 2400 s (40 min); (b) 20 nm ALD-Al$_2$O$_3$ nitrided for 5400 s (90 min). Surface roughness values for (a) is 2 nm and (b) 5 nm.

structure as the 10 nm thick ALD-Al$_2$O$_3$ layer after 2400 s nitridation time (see Section 6.2, Figure 6.13 (a, c)).

6.4. Nucleation layer influence on the N-polarity GaN

The most notable benefit of inserting the ALD-Al$_2$O$_3$ interlayer between two polarities GaN faces is that it creates a sharp interface between them. The latter statement was proved in Section 6.2. The layer's surface morphology, roughness and quality are the second critical factor for the waveguides simultaneously preserving the N-polarity GaN on the ALD-Al$_2$O$_3$ layer.

This section will present the influence of the LT-GaN layer growth time on the resulting HT-GaN layer surface morphology and its crystalline quality. It will give complex research on the crystal quality and surface morphology of N-polarity GaN layers on the 20 nm thick ALD-Al$_2$O$_3$.

Due to the reactor maintenance performed during this work, the processes temperatures of the N-polarity GaN layer had to be elevated in order to match the growth rates before the maintenance. Growth parameters of the N-polarity GaN layers on the 20 nm thick ALD-Al$_2$O$_3$ are given in Table 6.3. The samples with different LTB-GaN (nucleation layer) growth times will be denoted as the 60s, 90s, 135s and 195s. The growth rate of the LTB-GaN layers under conditions given in Table 6.3 was 2.23 μm/h. The reference sample to these mentioned samples in this section was the N-polarity GaN layer grown on the 2° off-cut sapphire substrates under the growth parameters presented in Table 6.1. The reference sample will be denoted as "REF". Growth parameters were tweaked according to the results presented in Section 6.3. N-polarity

Table 6.3: Growth parameters of N-polarity GaN layer on the 20 nm thick ALD-Al_2O_3 layers.

Process	Temperature (°C)	Time (s)	Pressure (mBar)	Ambient	V/III ratio
Nitridation	1120	3600	100	H_2+NH_3	–
LTB-GaN	700	60, 90, 135, 195	100	H_2+NH_3	1091
Annealing	1095	400	150	N_2+NH_3	–
HT-GaN	1095	911	150	H_2+NH_3	546

GaN growth kinetics, employing growth parameters shown in Table 6.3, are presented in Figure 6.18. As the LBT-GaN layers' thickness increases, the reflectance signal during this process also increases. The growth kinetics of the LTB-GaN layers does not exhibit any difference between samples. The main difference can be observed during the HT-GaN growth. From Figure 6.18 can be seen that the thicker the LTB-GaN layer, the more surface roughening of the HT-GaN layers is prominent. Decreasing reflectance signal and its oscillations are evidenced as enhanced surface roughening of the HT-GaN layers. The Resulting OM images of the surfaces of the N-polarity GaN layers are presented

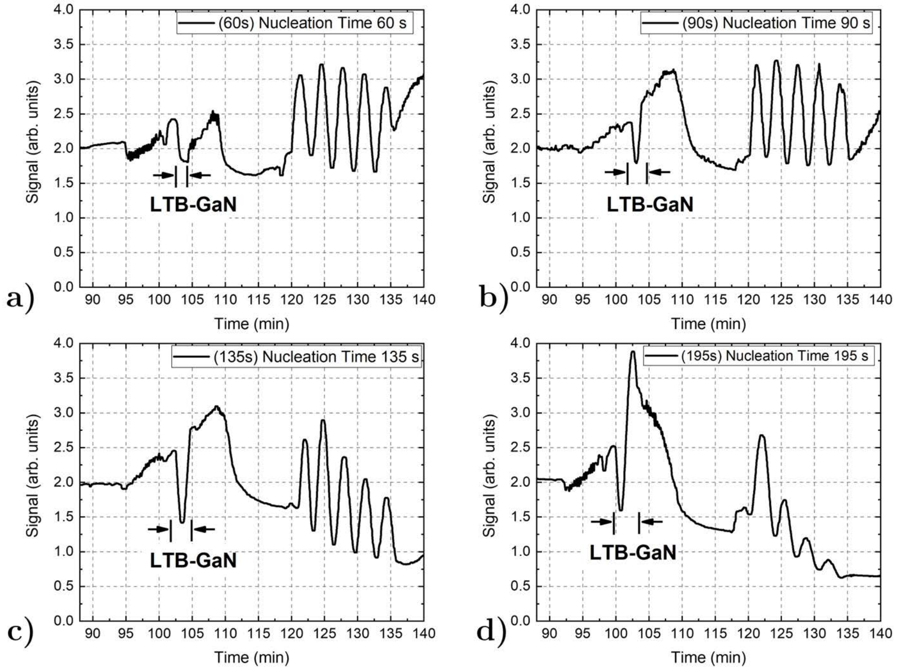

Figure 6.18: Plots of N-polarity GaN growth reflectivities using different nucleation times (LTB-GaN): 60 s (a), 90 s (b), 135 s (c), 195 s (d). Based on [**A2**]

in Figure 6.19. OM surface images confirm growth kinetics results. N-polarity

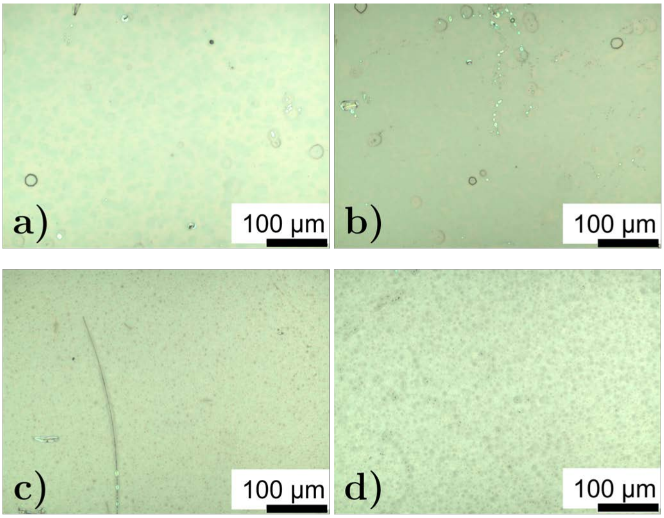

Figure 6.19: OM surface images of the resulting N-polarity GaN samples with LTB-GaN nucleation times: 60 s (a), 90 s (b), 135 s (c), 195 s (d).

GaN sample with a thinner LTB-GaN layer exhibits an optically smoother surface (see Figure 6.19 (a, b)) compared to the N-polarity GaN samples with the thicker LTB-GaN layers (see Figure 6.19 (c, d)).

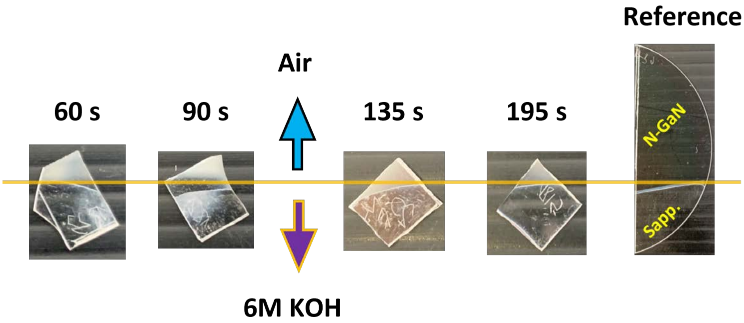

Figure 6.20: The front view of the N-polarity GaN samples. Time above the images represents the LTB-GaN layers' growth duration. Based on [**A2**]

To confirm the existence of the N-polarity GaN layers grown on the 20 nm ALD-Al_2O_3, KOH etching experiments using these samples were performed. Figure 6.20 represents the front view of the etched samples, where the yellow line marks the level of immersion into the KOH solution for the etching. For the samples 135s and 195s, scratched numbers from the sapphire substrate side can be seen, while some residues as a frosted surface on the etched part of the samples 60s and 90s can be observed. These results suggest that the samples 135s and 195s more likely exhibit the N-polarity GaN layers. In comparison, the samples 60s and 90s consisted of mixed Ga-polarity and N-polarity GaN in the layer. A reference etching experiment of a typical N-polarity GaN layer grown on the 2° off-cut angle sapphire substrates at the same etching conditions was performed to test the etching process correctness.

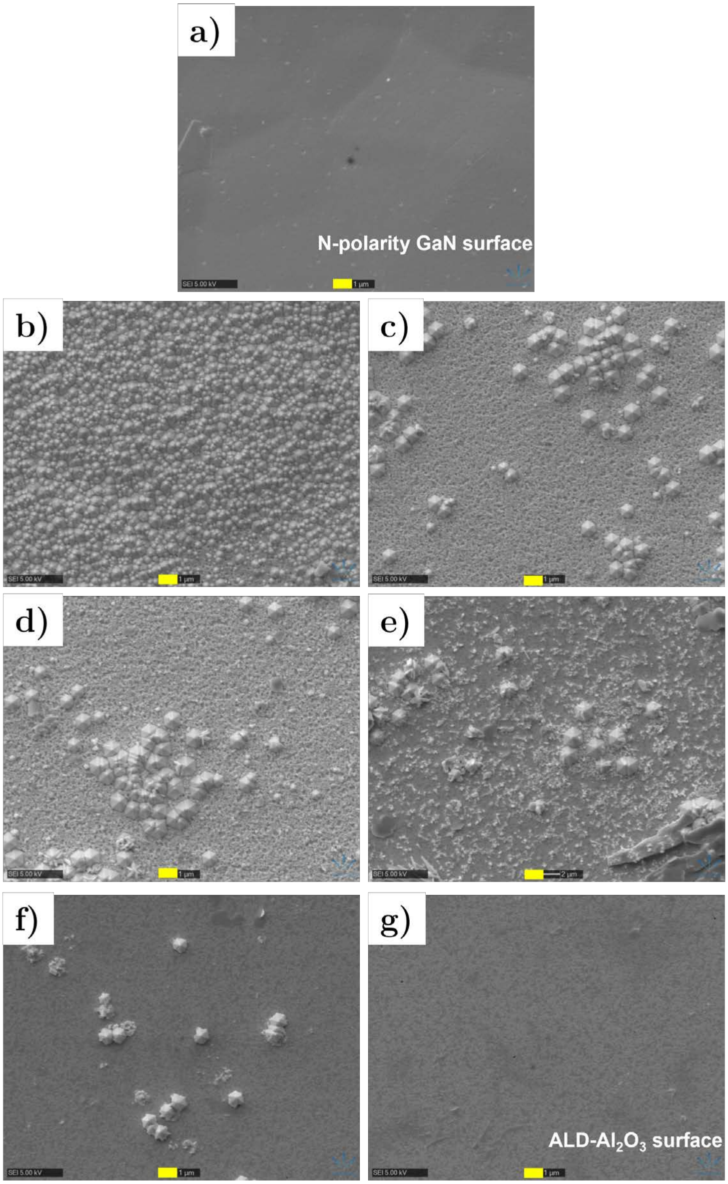

Figure 6.21: SEM images of the sample 195s surface after different etching duration: (a) 0 min, (b) 1 min, (c) 2 min, (d) 3 min, (e) 5 min, (f) 10 min, (g) 60 min. The yellow scale bar represents 1 μm. Based on [**A2**]

To ensure that the 20 nm ALD-Al_2O_3 layer will quench the etching process time-dependent etching experiment on sample 195s was performed. The experiment also gave an understanding of the etching dynamics of the N-polarity GaN layers. These results are presented in SEM images in Figure 6.21. Etching efficiency depends on the number of dangling bonds on the N atom and the atom planar density [148]. The more dangling bonds on each N atom, the stronger the surface energy. In other words, the facet will get more chemically stable and harder to be etched. An etching barrier index (EBI) can be obtained by multiplying these two quantities. The EBI for N-polarity and Ga-polarity GaN are 0.1138 and 0.3414, respectively. The lower the EBI, the more effectively etching process occurs. According to Lai *et al.*, if the $(000\bar{1})$ plane (N-polarity GaN) was etched, then the etching process would have occurred in the layer by layer manner [148]. But neither in this work nor in the literature the N-polarity GaN was not etched in this expected way [19, 149–152]. Instead, hexagonal-shaped pyramids in N-polarity GaN and holes (V-pits) in Ga-polarity GaN after the etching process in KOH solution are observed. After submerging into the KOH solution, the $(000\bar{1})$ plane transforms fast into hexagonal shape pyramids with the $\{10\bar{1}\bar{1}\}$ planes and then is followed by the "shrinkage" of the pyramids [148]. As time passes, those pyramids dissolve in the KOH solution. Tautz *et al.* explain etching stability by the NH_2 group protrusion (see Figure 6.22). After immersion of Ga-polarity GaN, the first layer of Ga atoms is easily accessible to hydroxide ions and this layer is easily

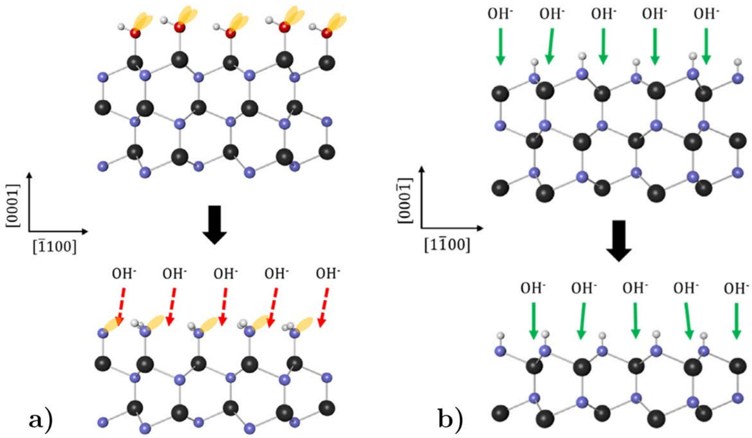

Figure 6.22: (a) Removal of a single Ga atom layer from the Ga-polarity GaN surface. Approaching negatively charged hydroxide ions are blocked by steric and electronic repulsion from negatively polarized NH_2 groups. (b) Removal of a single GaN atom layer from the N-polarity GaN surface results in the termination of the remaining surface with NH groups protruding at a 19° angle angle relative to the lateral N-polarity surface. Black, blue, red, and white spheres represent Ga, N, O, and H, respectively. Adapted from [152].

removed. The surface is then terminated with NH_2 group compounds. As NH_2 groups protrude at 90° angle from the Ga-polarity GaN surface resulting in hydroxide ions blockage. The blockage is thanks to two H atoms presented on every N atom, which provides steric blocking and the free electron pair on each N, which provides electronic blocking. On the contrary, the initial N-polarity surface is terminated with NH groups. The N atoms on the surface bond only one H atom and don't have a free electron pair. The latter factor decreases the blocking effect for hydroxide ions. The angle compared between Ga–N bond and the lateral N-polarity surface is 19° (see Figure 6.22 (b)) compared to 90° in Ga-polarity GaN (see Figure 6.22 (a)). In consequence, hydroxide ions can attack Ga atoms [152].

In this work case, after 1 minute of etching, the N-polarity GaN surface changes from a smooth to the fully covered by hexagonal-shaped pyramids (see Figure 6.21 (a, b)). After 2 and 3 minutes of etching, clusters of the pyramids start to be revealed (see Figure 6.21 (c, d)). The pyramid clusters gradually dissolve for longer etching times, revealing the bottom surface (see Figure 6.21 (e, f)). A longer etching time is needed to etch the pyramid clusters. This latter fact is probably due to the prolonged time required for revealing the $\{10\overline{1}\overline{1}\}$ planes in the cluster's center. After 60 minutes of etching ALD-Al_2O_3 layer is reached (see Figure 6.21 (g)).

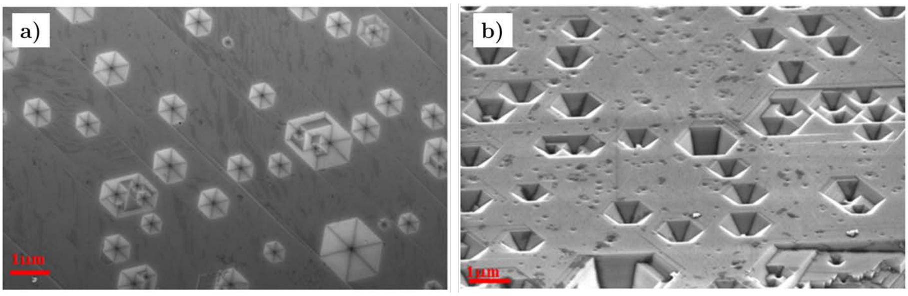

Figure 6.23: SEM images of Ga-polarity GaN sample etched in molten KOH at 350°C for 5 min (a) plane and (b) tilted view, respectively. Adapted from [114].

An interesting observation was made when the etching time varied between 3 and 10 minutes. The etching process forms a porous surface around the pyramid clusters, which dissolve after more than 5 minutes of etching. According to one hypothesis, a porous surface could imply an etched N-polarity AlN. During the prolonged nitridation/annealing process, some of the top-most ALD-Al_2O_3 layers may have changed into the N-polarity AlN layer. Such surface pattern after etching has also been seen in the literature by Bickermann *et al.* [153]. Whilst the latter layer could be relatively thin, 6M aqueous KOH solution dissolved it only after 5 minutes of etching. No V-pits were observed on the surface after the etching process like in the Ga-polarity GaN case presented in the literature (see Figure 6.23) [114]. Thus the ALD-Al_2O_3 layer acts as an auto-stop that suppresses further etching and protects the surface of the Ga-polarity GaN layer beneath the ALD-Al_2O_3.

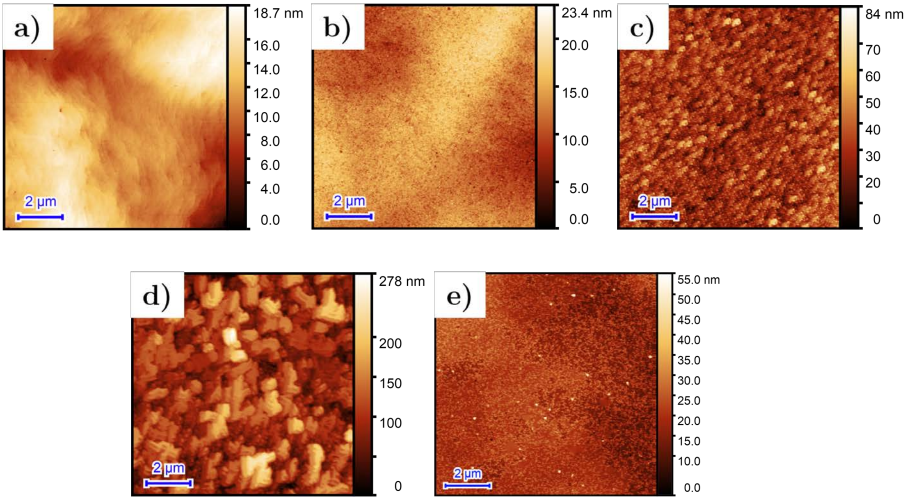

Figure 6.24: AFM (10×10 μm) images of the deposited ALD-Al_2O_3 (a), nitrided/annealed (b), deposited LTB-GaN (c), annealed LTB-GaN (d) and overgrown N-polarity GaN after fully etched till ALD-Al_2O_3 (e). Based on [**A2**]

Another hypothesis could be that this porous surface could be linked to the annealed nucleation layer. Similar phenomena were observed in the literature [151]. According to Tautz *et al.*, the etching rate of the 3D GaN slows down when the KOH solution reaches an interface between the 3D and 2D GaN growth regimes. In the scope of this work, when the etching reaches the annealed LTB-GaN layer, the whole etching process slows down. The latter interpretation is based on the results of the surface morphology change. AFM images of the surface after each process step throughout the formation of the N-polarity GaN samples are shown in Figure 6.24. Each of the HT-GaN grown samples' surfaces will be presented later. It is seen that both SEM (see Figure 6.21 (g)) and AFM (see Figure 6.24 (e)) reveal the same surface morphology after the KOH etching down to the ALD-Al_2O_3 layer until the auto-stop happens. The LTB-GaN starts to grow in the 2D regime. After the annealing process, some part of the LTB-GaN transforms into larger islands that coalesce (see Figure 6.24 (c, d)), and then HT-GaN growth proceeds in a quasi-2D regime. Thus, according to that logic, the HT N-polarity GaN is etched faster than the annealed LTB-GaN layer.

One N-polarity GaN sample was grown on the whole 2" sapphire substrate with the same structure covered by a 20 nm ALD-Al_2O_3 layer. It will be denoted as "90(II)s". Growth parameters used in the latter sample were similar to those in the 90s sample. Only processes temperatures were adjusted to match

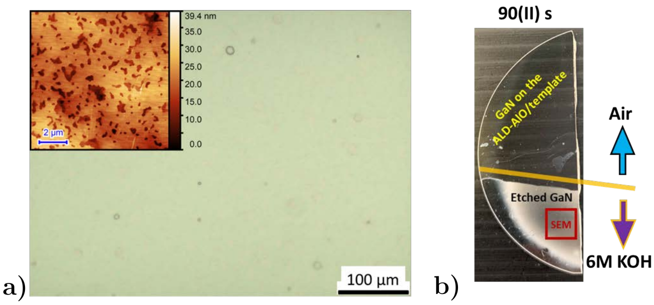

Figure 6.25: (a) OM and AFM (10×10 μm) (inset) images of the 90(II)s sample's surface before the etching experiment. Surface roughness RMS value in the 90(II)s sample was 5 nm. (b) The front view of the 90(II)s sample (based on the 90s growth parameters) after the etching process. Dark-red square represents a place where SEM images were taken. Based on [**A2**]

the growth rate and surface morphology (RMS values) of the sample 90s. This sample was grown as a result of optimized growth parameters on the samples, which sizes were 10x10 mm. OM and AFM images of the surface of 90(II)s sample before the KOH etching experiment are presented in Figure 6.25 (a). After the growth process, the KOH etching experiment was performed and its result is shown in Figure 6.25 (b).

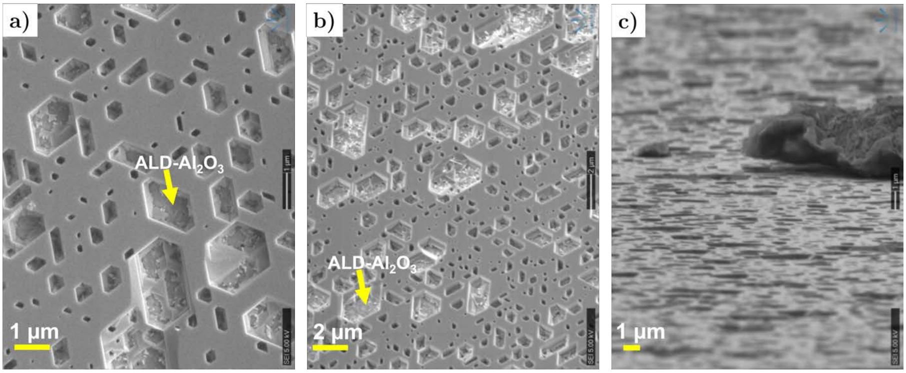

Figure 6.26: SEM images of the surface of sample 90(II)s tilted by 0 (a), 30 (b) and 85 (c) degrees. Images are taken in the etched areas. Based on [**A2**]

One similarity can be observed between the 60s, 90s and 90(II)s samples (see Figure 6.20 and Figure 6.25 (b)). After the etching experiment, they all exhibited frosted surface areas on the surface. To inspect these areas closer and to better understand the surface morphology, SEM images of the samples tilted at different angles were made. 90(II)s sample's SEM images after the etching are presented in Figure 6.26. The sample's surface is covered with two types of hexagonal-shaped holes. Larger ones are about 1 μm in size and the others are smaller than 1 μm in size. As previously stated, Ga-polarity GaN is more chemically stable compared to the N-polarity GaN layers (see Figure 6.23), and only V-pits form at dislocation sites during KOH etching. The rest of the surface remains intact and smooth. Here sample exhibits a smooth surface, implying Ga-polarity GaN existence, while the hexagonal-shaped holes (not V-pits) result from N-polarity GaN etching. The sidewalls of the hexagonal-shaped holes have about 120° angles, which indicates that more resistive to the KOH etching m-planes $\{1\bar{1}00\}$ (EBI of m-plane is 0.1211 or 02422 [148]) are revealed (see Figure 6.26 (a)). Furthermore, the bottoms of these hexagonal-shaped holes resemble the case of sample 195s after 10 minutes of etching (see Figure 6.21 (f)). It shows that the N-polarity GaN layer was present in these specific regions and has been etched down to the ALD-Al_2O_3 layer. SEM images the frosted surface areas of the 60s and 90s samples are presented in Figure 6.27. Based on the previous results and reasoning, residues that are left after the etching process could be Ga-polarity GaN complexes that were embedded in the N-polarity GaN layers. It can be seen that those specific areas exhibit smooth surfaces on the top of Ga-polarity GaN complexes (see Figure 6.27 (a, b)) and holes where N-polarity GaN was etched. To sum it up, samples with relatively short LTB-GaN growth time (samples 60s, 90s and 90(II)s) N-polarity GaN layers exhibit local Ga-polarity GaN inclusions. This fact could imply the over-nitrided ALD-Al_2O_3 areas.

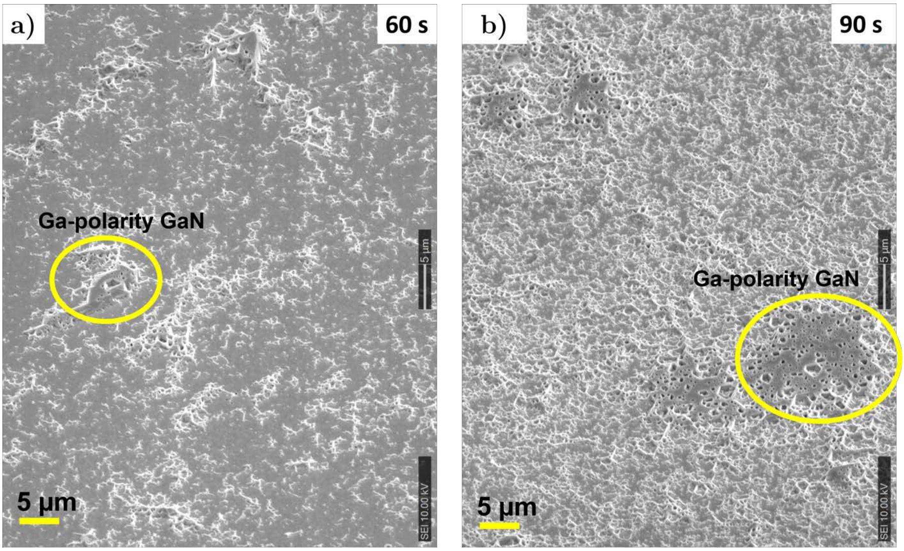

Figure 6.27: SEM images of the surface of sample 60s (a) and 90s (b) tilted by 45 degrees. Images are taken in the etched areas. Based on [**A2**]

Some delaminated areas on the surface of the samples were found. Tilted SEM images of the delaminated regions are presented in Figure 6.28. SEM

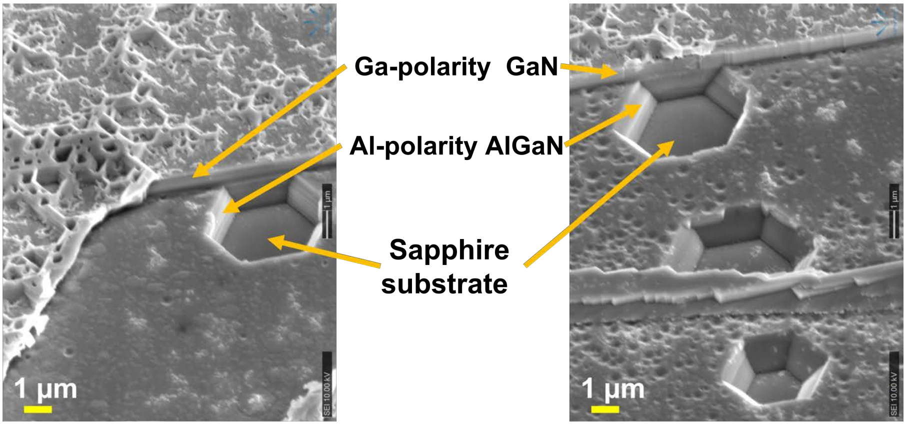

Figure 6.28: Delaminated area on the samples surface presenting consecutive layers of the structure.

images were taken in the etched areas. Abrupt interfaces between consecutive layers can be seen. This finding proves that 20 nm ALD-Al_2O_3 suppresses the etching process and does not deteriorate the Ga-polarity GaN surface. Characteristic V-pits can be observed on the Al-polarity AlGaN layer's surface, indicating that it had contact with the KOH solution. This finding also indicates that the whole structure withstands the processes held during the N-polarity GaN growth.

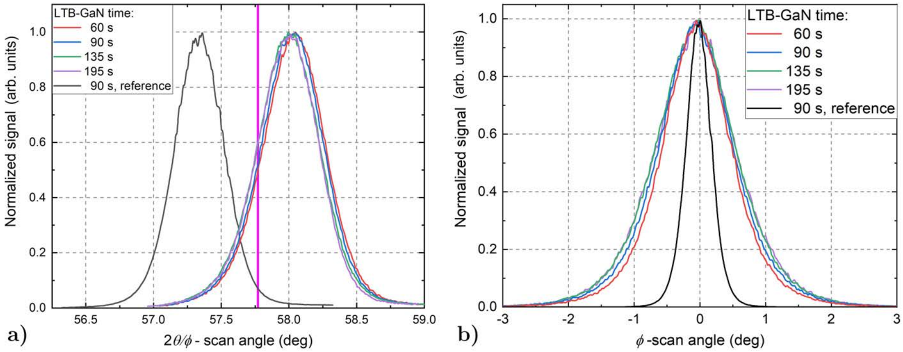

Figure 6.29: (a) $2\theta/\varphi$ scan of the $(11\bar{2}0)$ plane of the GaN layer grown on the 20 nm ALD-Al_2O_3 depending on the LTB-GaN time (60, 90, 135, 195 s), and of the GaN layer grown on 2° off-cut angle sapphire substrate with 90 s LTB-GaN growth time (black curve), and (b) their $(11\bar{2}0)$ plane XRC scans. The vertical magenta line indicates the value of angle for relaxed layer (57.77°). Based on **[A2]**

By measuring X-ray diffraction from the $(11\bar{2}0)$ plane (a-plane), the crystal structure of the top-most N-polarity GaN layer on the 20 nm ALD-Al_2O_3

was examined. The same in-plane XRD configuration measurement was used as in the case mentioned in Section 6.2. The X-rays do not penetrate the Ga-polarity GaN layer beneath the ALD-Al_2O_3 layer, which could affect the outcome. The in-plane $2\theta/\varphi$ scan is presented in Figure 6.29 (a), the XRC curves – in Figure 6.29 (b). The vertical magenta line in Figure 6.29 (a) points out the $2\theta/\varphi$ angle of a relaxed GaN layer. The shift from this particular angle dependence on the LTB-GaN growth time is presented in Figure 6.30 (a), which demonstrates the deviation of the evaluated a lattice parameter from the theoretical value ($\Delta 2\theta/\varphi = 2\theta/\varphi - 57.77°$). Using the results from Figure 6.29 (a), the lattice parameter a for different samples was calculated. The values varied from 3.176 Å(sample 60s) to 3.178 Å(sample 195s). The lattice parameter a for a relaxed GaN layer is 3.189 Å [37,154]. These results suggest that the top-most layer is compressed in the a-direction. It's worth noting that the Ga-polarity GaN layer grown on the sapphire substrate with low off-cut angles shows the compressive in-plain strain as well [154]. An opposite effect was observed for N-polarity GaN layers grown on the 2° sapphire substrates in this work (see the black curve in Figure 6.29 (a)), as well in the literature [136]. The complicated structure beneath causes the strain change. Since the underneath AlGaN layer is relaxed, the N-polarity GaN layer could be expected to be in-plane compressed, as the AlN a lattice parameter is smaller compared to the GaN.

Analysis showed that the thinner the nucleation layer, the more strained is the N-polarity GaN layer and the better its crystallinity, indicated by the decrease of the FWHM (see Figure 6.30 (a)). The interpretation of these results can originate from the N-polarity GaN growth dynamics. N-polarity GaN starts with a 2D growth as expressed by the typical reflectance kinetics. During the annealing of the LTB-GaN layer, a high density of islands is formed. The lack of ripening recrystallization during LTB-GaN annealing is most likely due to limited surface diffusion on the N-polarity GaN surface and low surface energy of the $(000\bar{1})$ plane [90]. Lastly, N-polarity GaN starts to grow in a quasi-2D mode. The thicker the LTB-GaN layer, the larger annealed islands are formed. It results in the mosaicity spread that translates into the FWHM of XRC curves increase. The Ga-polarity GaN growth follows the well-known 3D-to-2D transition. Samples (the 60s and 90s) that exhibited better crystalline quality and smaller surface roughness values had Ga-polarity GaN inclusions in the N-polarity GaN layer matrix. The improvement in the crystallinity of the latter samples can originate from these higher crystalline quality Ga-polarity GaN inclusions.

The surface morphology of the N-polarity GaN layers on the 20 nm ALD-Al_2O_3 was investigated by AFM and SEM measurements. These results are presented in Figure 6.31. The samples with thicker LTB-GaN layers (the 135s and 195s) exhibited the hexagonal-shaped pyramids/hillocks. It is an indication

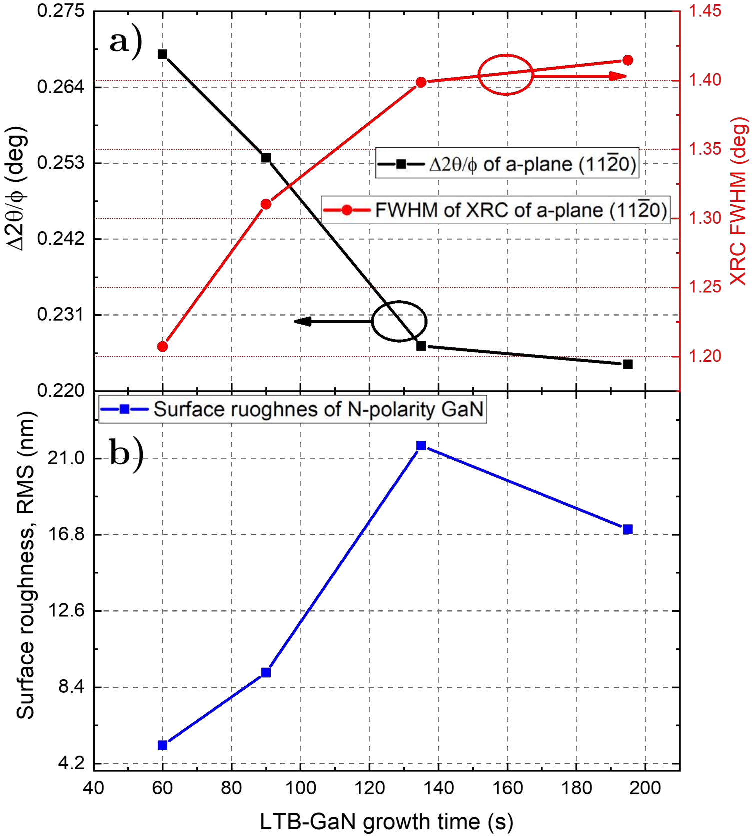

Figure 6.30: Structure and surface morphology characteristics dependence on the LTB-GaN growth time grown on the 20 nm ALD-Al_2O_3: (a) difference between the measured and the theoretical value of the $2\theta/\varphi$ scan angle of the (11$\bar{2}$0) plane (black squares) and the FWHM of the (11$\bar{2}$0) plane XRC (red circles); (b) surface roughness (RMS). The $2\theta/\varphi$ and FWHM data points are taken from the curves in Figure 6.29 (a), (b), respectively. RMS data – from AFM images presented in Figure 6.31. The curves are a guide for the eyes. Based on [**A2**]

of typical N-polarity GaN layers surface. A significant change in the surface morphology was observed for the samples with thinner LTB-GaN layers (the 60s and 90s). The surface roughness (RMS) obtained from the AFM images (from Figure 6.31) showed a decrease in RMS values from 22 nm to 5 nm. The formation of smaller and more uniform grains of the LTB-GaN layers during the annealing process could explain the decrease in surface roughness and change in surface shape. Moreover, Ga-polarity GaN layers exhibit very smooth surface morphology. Thus, the Ga-polarity GaN inclusions in the N-polarity GaN for the 60s and 90s samples helped to smoothen the resulting surface morphology.

EBIC measurements were performed to find the changes in the N-polarity

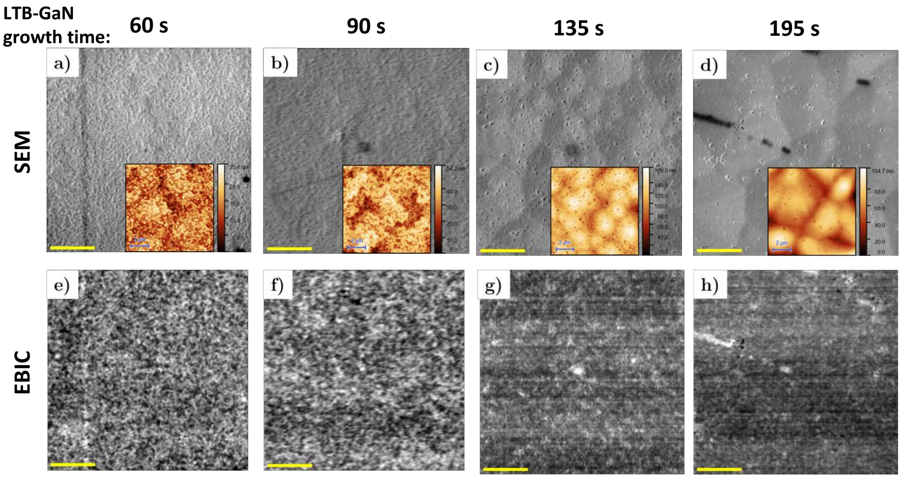

Figure 6.31: SEM and EBIC images of the samples in dependence on the LTB-GaN growth time before etching. Insets show AFM images (10×10 μm) in a corresponding scale. The yellow scale bar equals to 5 μm. Based on [**A2**]

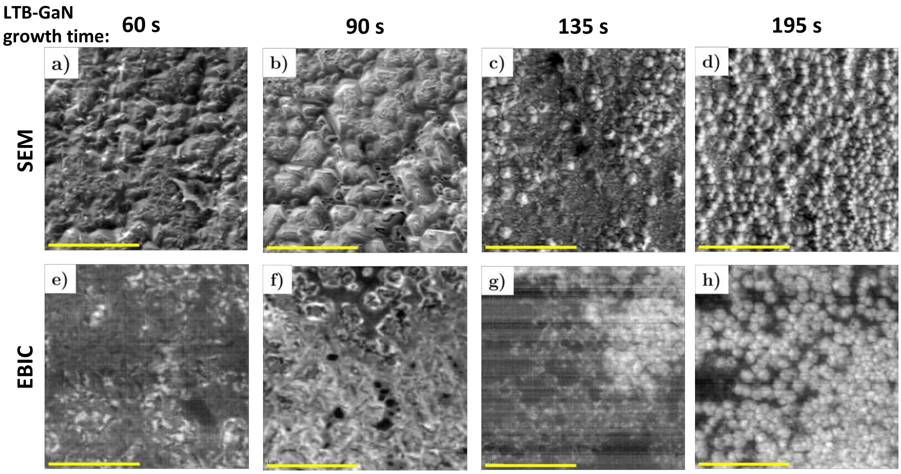

Figure 6.32: SEM and EBIC images of the samples in dependence on the LTB-GaN growth time after 10 min etching time Images were made at the borderline presented be the yellow line in Figure 6.20. The yellow scale bar equals to 5 μm. Based on [**A2**]

GaN samples when different LTB-GaN thicknesses were used. EBIC measurement technique and method were described in Section 4.4. A better charge-carrier separation in Au-GaN Schottky contact was observed for the sample with the shorter growth times of the LTB-GaN layers. It resulted in the less noisy EBIC images (less horizontal lines). It could indicate Ga-polarity GaN predomination in the mixed N- and Ga-polarity GaN layers (see Figure 6.31

and Figure 6.32). A Schottky contact with a higher barrier could originate from the lower donor concentration in the GaN layers [155] grown on the thinner LTB-GaN layers. The incorporation of oxygen (O) atoms into N-polarity GaN layers is enhanced [156, 157]. When O substitutes nitrogen sites (O_N) in the GaN, then it acts as shallow donors that generate more electrons in the layer [158,159] and deteriorates a Schottky contact. Moreover, as the GaN layer exhibits a mix of two polarities (Ga- and N-), then inversion domain boundaries (IDB) between Ga- and N-polarities GaN can be formed. Several works present that microphotoluminescence (μ-PL) and cathodoluminescence (CL) intensity drastically increases at the IDB [160, 161]. This phenomenon was explained by a very high potential difference centered in the IDB core, accompanied by two local minima on each of its sides for the electrons. The holes in the vicinity of the IDB are trapped in a local maximum. The explaining model is presented in Figure 6.33. Such configuration is anticipated to result in significant overlap

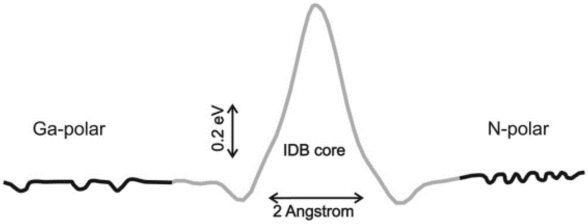

Figure 6.33: Model for the local potential. The potential maximum is accompanied by two local minima in each polar area leading to strong excitonic emission. Additionally, local minima at both sides of the IDB due to defect states are suggested (black). Adapted from [160].

of the electron and hole wave functions, resulting in increased μ-PL and CL. Thus, the potential difference at IDB introduces a built-in electric field that effectively can separate electron-hole pairs generated by the electron beam in EBIC measurement. The bright spots in Figure 6.31 (e) and Figure 6.31 (f) could originate from the built-in electric field that was created due to IDBs.

The latter observations correspond well with the XRD results. Both methods present a smoother GaN layer for the shorter LTB-GaN growth times compared to a domain-like layer for the longer LTB-GaN growth time. SEM and EBIC measurements were performed for the sample after the 10 min etching in KOH solution. The region of interest in these measurements was the borderline between KOH solution and air, which is represented in Figure 6.20. The bright spots representing the pyramids contrast well with the dark background in the EBIC images (see Figure 6.32 (g, h)). The crystallinity and the defect-free structure of the pyramids ensure the long lifetime of the electron beam-generated electron-hole pairs. Hence, a good EBIC signal is acquired. It is worth noting that not all pyramids visible in the SEM image can be seen in the EBIC image (see Figure 6.32). This observation can be related to the layer underneath the pyramids mentioned before. As the layer is partially dissolved, separated or clusters of the pyramids have no good electrical contact with the external circuit. For the shorter LTB-GaN growth time samples, the bright-to-dark contrast is washed out in the EBIC images (see Figure 6.32 (e, f)). Even so, some contrast structures can be seen in these images that can be correlated with the SEM images, thus providing interesting information about the electrical selectivity of particular surface morphological features. In the upper part of Figure 6.32 (f), an almost homogeneous cluster-like morphology is strongly selected electrically with well-defined dark and bright spots and contours. Furthermore, the bright forms could indicate a strong built-in electric field at the cluster's edge.

To sum it up, the investigation revealed the importance of the LTB-GaN layer characteristics on the polarity inversion of the Ga-polarity GaN grown on the 20 nm ALD-Al_2O_3 layers that are the part of the waveguiding structure. Probably due to partially over-nitrided ALD-Al_2O_3 layers, the N-polarity GaN layer exhibited Ga-polarity GaN inclusions in it. Variation of the LTB-GaN growth time revealed that for partially over-nitrided ALD-Al_2O_3, longer LTB-GaN growth times (135 s and 195 s) are needed to obtain pure N-polarity GaN layers. Shortening of the latter layers' growth time resulted in the appearance of Ga-polarity GaN inclusions in the N-polarity GaN layer. However, the last observation smoothened the surface of the entire layer and improved the crystal quality.

6.5. Smoothing N-polarity GaN surface on the 0.3° sapphire substrates

Due to the difficulties caused by the COVID-19 pandemic, the template preparation that looks like in Figure 6.10 (a) was hindered. Thus experiments were continued on the 0.3° off-cut sapphire substrates. The latter sapphire substrates were used because the entire waveguiding structure is also grown on these substrates. This section will present the influence of the TMGa flow rate on the N-polarity GaN surface morphology.

It must be noted that KOH etching experiments revealed the existence of pure N-polarity GaN layers in all samples presented in this section. A slight surface morphology improvement was observed under a more decreased V/III ratio. Still, outstanding surface morphology improvement was observed under the lower TMGa flow rates while keeping the same V/III ratio. Results of the improved surfaces morphologies are presented in Figure 6.34. As it can be thought, a decrease in TMGa flow rate resulted in a decreased GaN growth rate. Compared to the case when only NH_3 flow is reduced, the decrease in the growth rate is not so prominent, meaning that TMGa flow is more critical in controlling layers' growth rate.

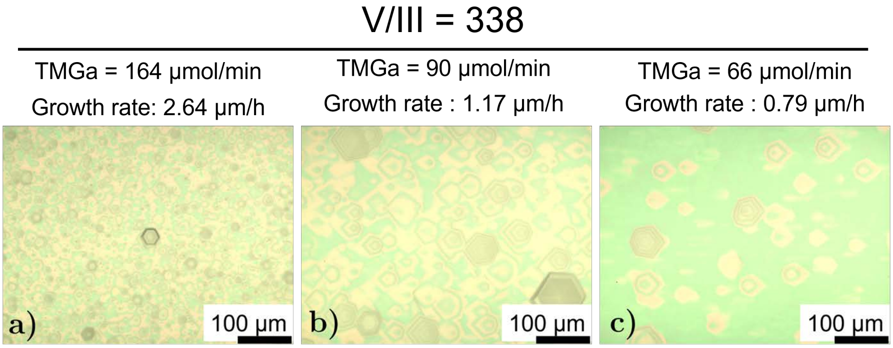

Figure 6.34: OM images of the N-polarity GaN samples grown on the 0.3° sapphire substrates for different TMGa flow rates: 164 μmol/min (a), 90 μmol/min (b), 66 μmol/min (c).

By decreasing the V/III ratio, the growth conditions gradually change from the N-rich to partially Ga-rich conditions. It is known that independent of the chemical growth environment (Ga- or N-rich), polar GaN surfaces turn out to be cation (Ga) stabilized with no N atoms in or on top of the surface layer [90,162,163]. In the high TMGa flows case, excess of Ga atoms can accumulate on the grown surface [164]. As Ga migration on the surface is reduced in the N-polarity GaN case compared to Ga-polarity GaN layers, N atoms create bonds with these Ga excess adatoms on the surface, thus incorporating them into the N-polarity GaN layer. This latter process is repeated in the time leading to hexagonal-shaped hillocks formation. In the lower TMGa flow and in the reduced NH_3 flow, less Ga excess adatoms can accumulate. Ga adatoms also have more time and space for migration on the surface. Reduced NH_3 flow results in a reduced N atom quantity that can create a bond and incorporate Ga adatoms into the layer, resulting in smoother surface morphology with fewer hexagonal hillocks.

Next, N-polarity GaN layers were grown using different LTB-GaN growth times. Results are presented in Figure 6.35. All the samples exhibited N-polarity GaN layers. The same surface morphology pattern as in Section 6.4 was observed. The growth rate of the LTB-GaN layer in these experiments was 2.18 μm/h. The thinner LTB-GaN was used, the smoother the surface morphology of the HT-GaN was acquired. The sample grown with 94 s LTB-GaN layer exhibited hexagonal-shaped hillocks on the surface, a typical feature for the N-polarity GaN layers grown on the 0.3° sapphire substrates. The density of these hexagonal-shaped hillocks also decreased with the use of thinner LTB-GaN layers, meaning that thinner and smaller GaN islands are required in the first growth steps in order to achieve a smooth, almost hexagon-hillocks-free surface. Moreover, KOH etching experiments showed that the purity of

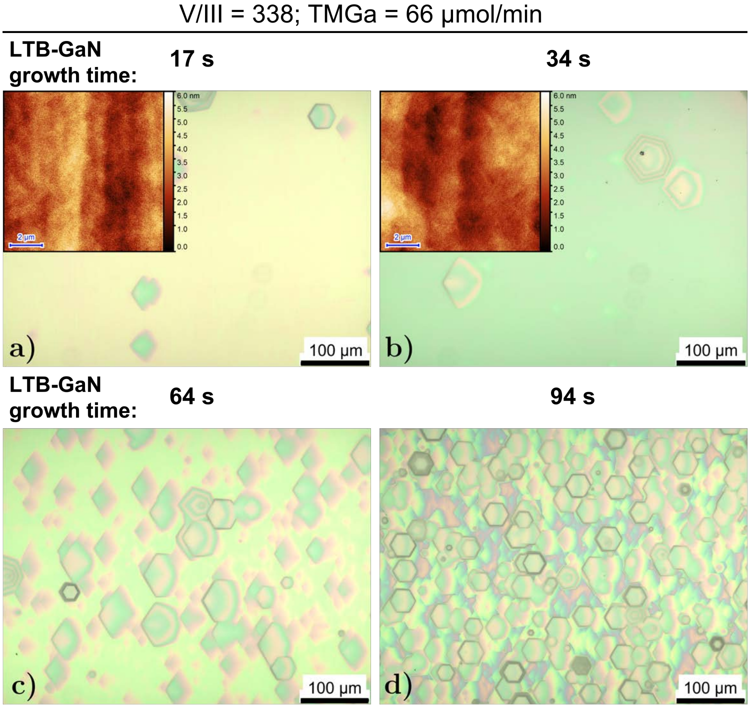

Figure 6.35: OM and AFM (10×10 μm) (insets) images of the N-polarity GaN samples grown under V/III ratio of 338 and TMGa flow 66 μmol/min on the 0.3° sapphire substrates using different LTB-GaN growth times: 17 s (a), 34 s (b), 64 s (c) and 94 s (d).

the N-polarity GaN layers does not depend on the LTB-GaN layers' thickness. Nitridation conditions in these experiments were the same as presented in Section 6.1. These facts confirm that properly nitrided sapphire substrate or ALD-Al_2O_3 results in pure N-polarity GaN layers without Ga-polarity GaN inclusions, independent of LTB-GaN layers' thickness. This fact proves that some areas of 20 nm ALD-Al_2O_3 layers presented in the previous section were over-nitrided. AFM images showed that surface roughness values in the areas free of the hexagonal hillocks for the samples with the 17 s and 34 s LTB-GaN growth times were 0.8 nm and 0.81 nm, respectively.

XRD measurement was performed for the sample with the 34 s LTB-GaN growth time to evaluate the crystalline quality of the N-polarity GaN layers grown on the 0.3° sapphire substrate. XRC of the $(11\bar{2}0)$ plane was measured and compared to the N-polarity GaN grown on the 2° sapphire substrates from Section 6.1. The FWHM of the XRC curve of the GaN layer grown on the 0.3° was 2124 arcsec vs. 1609 arcsec for GaN grown on the 2° sapphire substrates.

To sum it up, the lower the TMGa flow, the smoother the resulting surface of the grown GaN layer. Due to excess of Ga adatoms on the N-polarity GaN

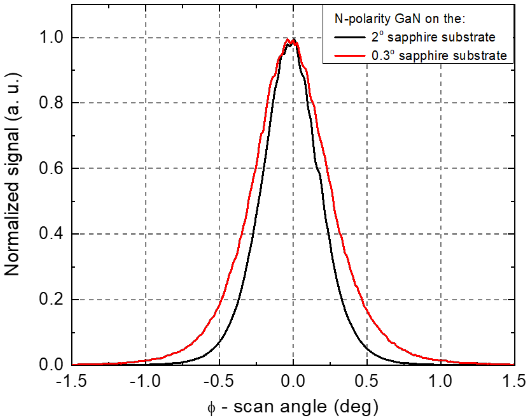

Figure 6.36: XRC φ-scan of the $(11\bar{2}0)$ plane for N-polarity GaN layers grown on the 2° and 0.3° sapphire substrates.

on the surface and higher NH_3 flow formation of the hexagonal-shaped hillocks is enhanced. Reduction in these two quantities enhanced Ga adatom mobility and reduced N atom concentration so that smoother surface is acquired, and the formation of hexagonal-shaped hillocks is suppressed. On the properly nitrided sapphire surface, N-polarity GaN purity does not depend on the thickness of the LTB-GaN layers.

7. A NOVEL PULSED MOVPE GROWTH METHOD FOR THE InN LAYERS

This chapter is based on the research published in paper [**A3**]. The study presents InN and p-type GaN (p-GaN) p-n junction growth results and functionality. The chapter will give an overview of InN MOVPE growth. Then the growth process of InN on the undoped GaN layers. After the growth mechanism was understood, the InN/p-GaN junction was grown using optimized InN growth parameters. Lastly, the junction was characterized.

7.1. InN band gap mystery

InN is one of the most mysterious group-III nitrides semiconductors family member. Firstly, due to its the band gap value. For now InN band gap energy was found to be 0.64 eV – 0.7 eV [12, 13, 165]. But from the historical point of view, InN band gap energy fluctuated from 0.9 eV to 2 eV. Until 2001 InN band gap was believed to be 1.5 eV. After Davydov and Matsuoka groups' calculations InN band gap value reduced from 1.5 eV to 0.7 eV [166, 167]. Davydov tried to grow the InN layer by using the MBE growth technique, but the MBE-InN layer after the measurements resulted in a 0.9 eV band gap. By using MOVPE growth techniques Matsuoka and his group managed to grow InN layers on the GaN/sapphire templates, which exhibited 0.76 eV band gap energy. Later, Briot and his group published results that showed that the InN band gap energy is 1.25 eV [168]. They employed the MOVPE growth technique. Thus deeper investigations have started.

One of the first investigation target was O concentration influence. For the O concentration of 16%, the measured band gap energy for InN was 1.15 eV [169]. The discrepancy in the O concentration values appeared because two independent groups found different oxygen concentration influence on the InN band gap energy. Another group for the 1.5 eV InN band gap recorded only 3% of oxygen in the layer [170]. As proposed by Alexandrov *et al.*, segregated oxygen species could substitute N sites and form a ternary semiconductor of $\mathrm{InO_yN_{1\text{-}y}}$ with y about 0.1 [171]. According to calculations, the higher the compositional ratio of InN to $\mathrm{InO_yN_{1\text{-}y}}$ the higher the band gap energy. But any group has observed this compound in the InN layer from the XRD measurements. Secondly, to reach higher InN to $\mathrm{InO_yN_{1\text{-}y}}$ compositional ratios, the O solubility in the InN must be high. However, it was shown that effective O solubility in the InN layers is very low [172]. From the crystallography point of view, such a pseudo-binary alloy cannot be formed. The group-III metal oxides most readily crystallize in the corundum structure. Group-III nitrides commonly form a wurtzite hexagonal structure. This results in no continuous geometric transformation between the two structures, and no such pseudo-binary compound can be formed [173]. The band gap in the InN layers prepared by various growth methods appears to be independent of oxygen concentration.

Stampfl *et al.* calculated defect formation energies in the InN layers [174]. He found that O atoms occupy a nitrogen site forming an O_N defect. Incorporated O atoms in that way act as donors, thus giving rise into charge carrier concentration. The second factor influencing charge carrier concentration is nitrogen vacancy (V_N). The latter also acts as a donor in the crystal. Stampfl *et al.* stated that due to these facts, InN is a very strong n-type semiconductor, and it is almost impossible to compensate or change its conductivity type. Only recently, a few works showed the p-type conductivity in the InN layers. Those InN layers/microstructures were grown by the MBE technique [175,176]. The InN layers exhibited residual electron densities from 10^{13} to 10^{15} cm^{-3}.

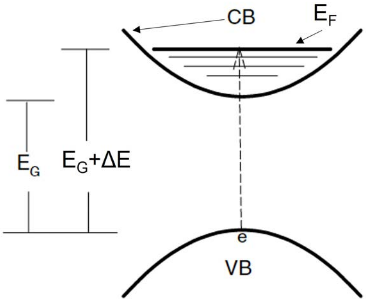

Figure 7.1: Schematically presented the Moss – Burstein effect, where E_G is a band gap energy and E_F denotes for the Fermi energy. ΔE is the energy difference between CB bottom and E_F level due to the Moss – Burstein effect. Adapted from [177]

Several papers have assumed that for InN, all the variation in the measured band gap values can be attributed to the Moss–Burstein effect. Walukiewicz *et al.* attributed an increase in the absorption edge energy from 0.7 eV to 2.3 eV at a carrier concentration of 10^{21} cm^{-3} [178]. Moss–Burstein effect occurs in materials with high carrier concentration: for the effect to operate, the carrier concentration must be above the conduction band density of states, i.e., the Fermi level must be in the conduction band [177]. Schematically this effect is presented in Figure 7.1. When the latter effect occurs, the valence band to conduction band transition energy of electrons increases since the Pauli exclusion principle requires that electrons must transit to unfilled states above or near the Fermi level. Butcher *et al.* reviewed InN band gap values and their dependency on the carrier concentration in the layer. These results are presented in Figure 7.2. It is worth noting that all the InN samples were grown by the MBE technique.

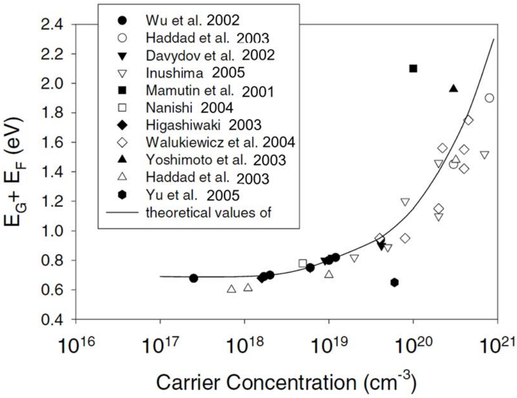

Figure 7.2: Measured band gap versus carrier concentration for the MBE InN layers. Adapted from [177]

Stochiometry is another factor that could influence band gap energy in the InN layers. It had been assumed that InN could not be grown under nitrogen-rich conditions until it appeared that excess nitrogen can be present in quite large concentrations. N:In ratios as large as 4:3 have been observed for sputtered InN [173],while for the MBE growth method [181], InN was observed to be nitrogen-rich, but in lesser extents. XRD was used to observe the excess of nitrogen. For the nitrogen-rich InN layer, lattice constants *a* and *c* were observed to expand with increased amounts of nitrogen. An increase in the lattice constants along the hydrostatic stress line, which was calculated by Specht *et al.* [182], is an excellent indicator for nitrogen-rich InN. The plot and line are presented in Figure 7.3. The majority of epitaxial samples examined by Specht [182] and Cimalla [179] do not align along the biaxial strain line. They also are not aligned along the hydrostatic stress line. Thus indicating that both forms of stress occur simultaneously. Biaxial stress usually is associated with a lattice mismatch and hydrostatic strain – with homogeneous incorporation of point defects. Two samples, S1 and S2, grown on the glass substrate mostly exhibited hydrostatic strain, which is associated with the incorporation of excess nitrogen. The hydrostatic strain related with the incorporation of excess nitrogen has the opposite sign to the case of the hydrostatic stress related to the incorporation point defects. Due to this fact S1 and S2 samples are in opposite site compared with the rest InN samples. To sum it up, these point defects are possibly native defects due to which film stochiometry can be manipulated [173].

Despite the research effort, InN still remains quite mysterious material in the group-III nitrides semiconductor family. The most prominent factors responsible for band gap energy values are the Moss–Burstein effect and InN

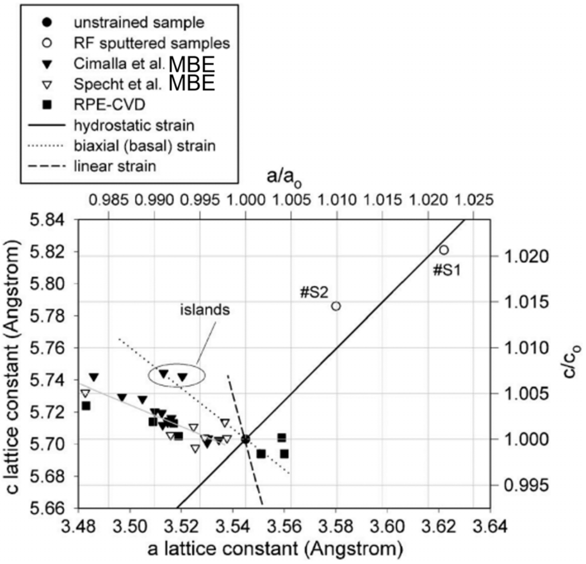

Figure 7.3: Theoretical strain cases for the three different types of stress (hydrostatic, biaxial and uniaxial). S1 and S2 – sputtered nitrogen-rich InN. InN islands reported by Cimalla *et al.* [179]. Adapted from [180]

stochiometry. High carrier concentration values ($>10^{21}$ cm^{-3}) correspond to an impurity level of at least 3% in the InN layers. Due to that band gap change can be expected from alloying effects and lattice changes that result from the inclusion of impurities. This factor would be carrier concentration dependent, but independent of a Moss–Burstein effect. Nevertheless, these two effects have not been well separated [173].

7.2. Overview on the InN MOVPE growth

The growth of InN is the most challenging among the group-III nitrides due to the equilibrium vapor pressure of nitrogen over the InN layers compared to AlN and GaN, as shown in Figure 7.4 [23,183]. Secondly, due to low InN dissociation temperature, the growth of InN layers requires a low growth temperature (500°C ÷ 600°C). The precursors for the InN layers in the MOVPE growth technology usually are NH_3 and TMIn as sources of nitrogen and indium (In), respectively. Such low growth temperatures result in a low NH_3 decomposition rate. Although higher growth temperatures automatically increase the NH_3 decomposition rate, they can also increase thermal decomposition or thermal etching of the grown InN. Growth at lower temperatures <400°C is dominated by the metallic In droplets formation due to the shortage of reactive nitrogen, which comes from the NH_3 dissociation. It must be noted that the carrier gas used in the InN growth process is only nitrogen. Epitaxial growth at lower

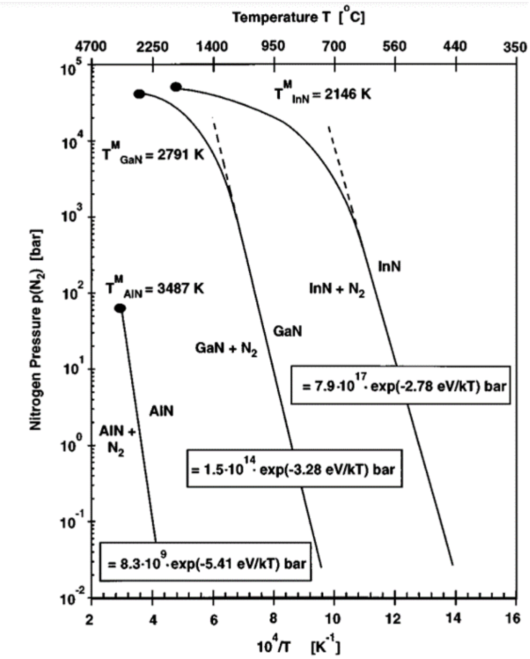

Figure 7.4: Melting temperatures of group-III nitrides and equilibrium nitrogen pressures. Adapted from [183]

temperatures becomes quite challenging due to reduced migration of the deposited adatoms. Koukitu *et al.* performed theoretical growth modeling of the InN layers by the MOVPE method. They concluded that a high V/III ratio, the use of inert carrier gas and a low mole fraction of the decomposed NH_3 are required [184, 185]. Experimental results showed that enhanced NH3 dissociation by increasing growth temperature, V/III ratio favors the MOVPE growth of the InN layers. Matsuoka *et al.* [23] showed that at a V/III ratio lower than $1.6{\cdot}10^4$, metallic InN droplets were found to be on the surface. When this ratio was larger than $8{\cdot}10^4$, the InN samples exhibited a mirror-like surface. These results are presented in Figure 7.5. The amount of In droplets decreases with increasing the V/III ratio. The main object of a high V/III ratio is to bring a sufficient amount of reactive nitrogen since dissociation of NH_3 at lower temperatures is not effective. The latter case is suitable for growth temperatures lower than 600°C. In the case of higher temperatures, the growth mechanism slightly changes. A high V/III ratio restrains the growth and a low V/III ratio is required. Above 600°C, NH_3 decomposition becomes more effective and it results in the increase of hydrogen partial pressure. This fact prevents the growth of InN and results in the InN layers' thermal etching/decomposition. It can be concluded that the temperature interval for the conventional MOVPE process is 400°C ÷ 650°C. A high V/III ratio is preferable for the growth at

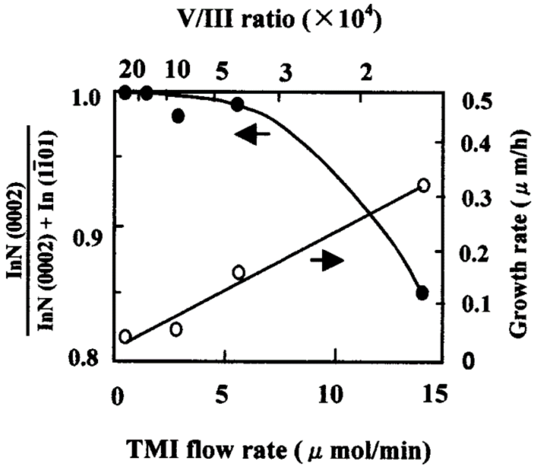

Figure 7.5: X-ray peak intensity ratio of InN (0002) to the sum of InN (0002) and metal-In ($1\bar{1}01$) versus TMIn flow rate and V/III ratio. Adapted from [23]

lower temperatures, while the latter factor must be reduced with the increased growth temperatures. An inert reactor ambient must be ensured during the InN growth process.

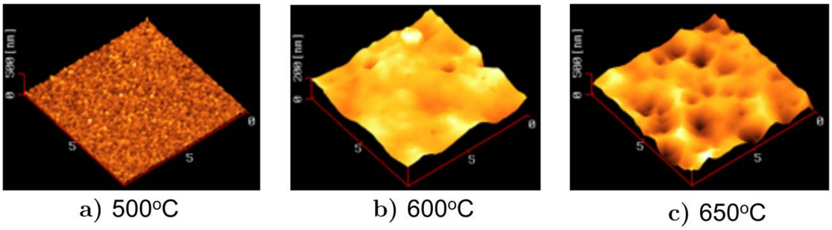

Figure 7.6: InN surface morphology on the sapphire substrates at a different growth temperature. Adapted from [24]

The growth temperature has a strong influence on the InN surface morphology. At the lower growth temperatures, the growth process of the InN layer was found to be columnar due to insufficient migration. With increasing the growth temperature, the 2D growth regime is enhanced. Yamamoto *et al.* [24] have conducted InN MOVPE growth experiments at different growth temperatures on the sapphire substrates. AFM results of the InN layers' surface morphology are presented in Figure 7.6. At 550°C, MOVPE growth of InN was found to be columnar. The continuous film was observed at the growth temperatures higher than 600°C. Latter observation proved that the 2D growth regime was enhanced. For the InN layers grown at 650°C, pits were observed to be formed on the surface. It was likely due to enhanced InN decomposition or thermal etching at the higher growth temperatures.

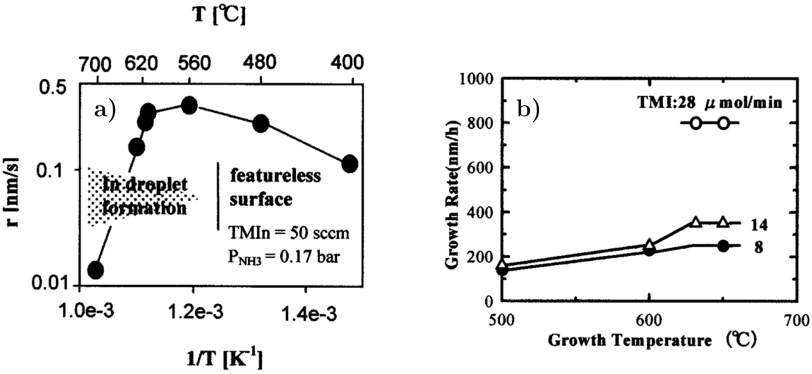

Figure 7.7: (a) Dependence of the growth rate on the InN layers growth temperatures [186]. (b) The growth rate of the InN layers for a different TMIn flow rates at the different growth temperatures [24].

As can be expected, the growth rate of the InN layers is dependent on the growth temperatures. The results are presented in Figure 7.7.With the increased TMIn flow rates, the growth rate of the InN layers also increases. Adachi *et al.* [187] proved that the limiting factor at the growth temperatures suitable for InN is NH_3 decomposition. They showed that the growth rate increases with increasing the temperature at 400°C ÷ 630°C at a constant TMIn flow rate. Secondly, they showed a growth rate saturation with a rise in TMIn flow rate, which indicates that the growth rate is limited by NH_3 decomposition. Keller *et al.* [186] observed similar results. InN growth rate at 630°C ÷ 650°C increases with increasing TMIn flow rate as NH_3 decomposition rate is enhanced. Above 650°C, the growth rate decreased and In droplets formation was observed. The latter observation resulted from enhanced InN decomposition due to the increased hydrogen amount from the enhanced NH_3 decomposition.

The growth temperature also influences the electrical properties of the InN layers. Yamamoto reported that the carrier concentration reduces and Hall mobility increases with the growth temperature increase [24]. It was also found that higher V/III ratios reduce the background carrier concentration at 500°C ÷ 600°C growth temperatures. These results are presented in Figure 7.8. The latter results suggest that the increase in temperature and V/III ratio favors a reduction of defects in the InN layers (probably nitrogen vacancies reduction). An interesting observation was made for the InN layers grown at 650°C under different V/III ratios. It was found that carrier concentration at this growth temperature does not depend on the V/III ratio. The latter result suggests that another mechanism governs the electrical properties of the InN layers, most likely thermal decomposition [23].

Lastly, one of the easily tweaked growth parameters is growth pressure.

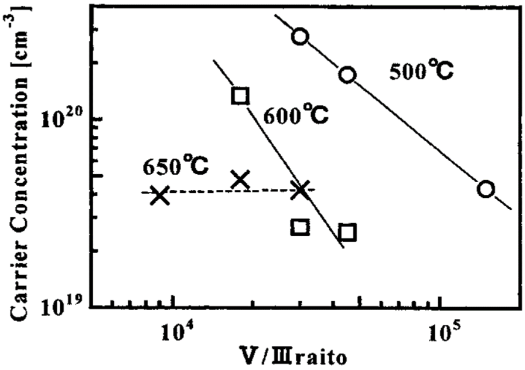

Figure 7.8: Carrier concentration of the InN layers dependence on the different V/III ratios at different growth temperatures. Adapted from [24].

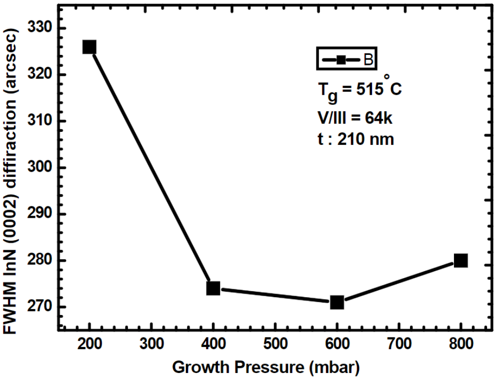

Figure 7.9: Influence of the growth pressure on the InN crystal quality. Adapted from [188].

It influences either crystalline quality and electrical properties of InN layers. Tuna *et al.* [188] demonstrated how the growth pressure affects InN crystal quality. Results are presented in Figure 7.9. Kadir *et al.* [189] also acquired very similar results as Tuna *et al.*. An increase in the growth pressure results in a better InN crystalline quality. It can be seen that quite a sharp decrease in FWHM of the InN XRC (0002) curve when the growth pressure was raised to 400 mBar. It was speculated that such improvement in the InN layers quality could result from the reduced decomposition of the InN layer due to reduced nitrogen evaporation from the surface and suppressed In segregation at the higher growth pressures. Moreover, at higher growth pressures, InN layers exhibit better electrical properties. The results are given in Figure 7.10. Higher InN growth pressures result in lower carrier concentration levels and enhanced Hall mobility. It can be due to enhanced NH_3 decomposition. At the higher growth pressures flow velocity of the reactants gases is reduced and

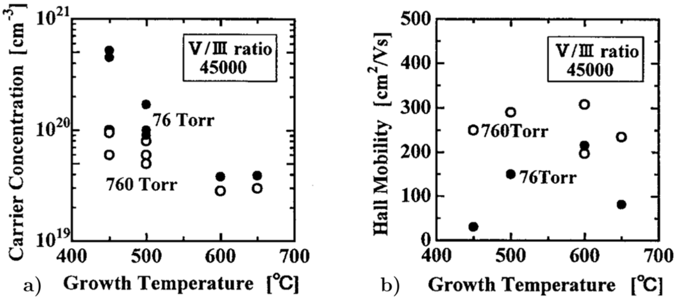

Figure 7.10: (a) Carrier concentration and (b) Hall mobility comparison between InN layers grown at 76 and 760 Torr. Adapted from [24].

more reactive nitrogen can be provided onto the growth surface as well as suppress the nitrogen evaporation from the grown InN layers. These factors reduce defects formation in the InN layers and give better electrical properties.

7.3. Pulsed MOVPE growth of the InN and InN/p-GaN junction

Flow modulation MOVPE growth method, shorter – pulsed MOVPE, attracted interest and has been investigated to obtain high-quality group-III nitride grown layers [12, 23]. The metalorganic precursor in pulsed MOVPE is usually supplied in pulses, while the NH_3 flow is constant [23, 190, 191]. It was found that the growth of InN layers can be executed at higher temperatures and effectively suppresses grain growth, also In droplets formation. The general idea of the pulsed MOVPE is the increased mobility of the adsorbed species on the surface and the consumption of the In droplets during the pause in the In precursor supply [192, 193]. In this work, different thicknesses of InN layers on the GaN/sapphire templates (further templates) were grown by employing the pulsed MOVPE method.

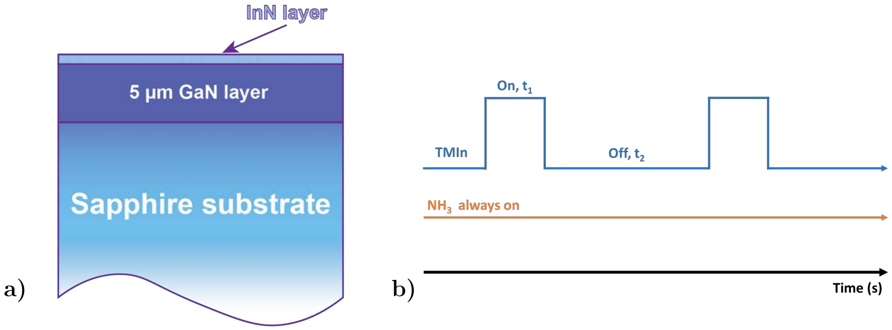

Figure 7.11: Schematically presented (a) InN on the GaN templates structure and (b) pulsed MOVPE growth process for the InN layers.

The structure grown in this experiment is presented in Figure 7.11 (a). Firstly, standard 5 μm GaN was grown on the sapphire substrates with a 0.3° off-cut angle. Then InN growth was followed. TMIn in this growth method was supplied by a pulsed manner into the reactor chamber. t_1 denotes as TMIn supply duration, t_2 – TMIn pause duration. One growth cycle consists of t_1 and t_2 times. Carrier gas flow, which in this case was nitrogen, and NH_3 flow were at constant rate. TMIn pulse duration was t_1=7 s, while the pause was t_2=20 s. One growth cycle equals 27 s. Figure 7.11 (b) schematically presents the growth process for InN layers. The TMIn pulse length controls the thickness of the deposited ultrathin InN layer. In contrast, the pause length controls the time allowed for surface migration of In adatoms on the surface and the amount of additional reactive nitrogen. The growth parameters of the InN layers are presented in Table 7.1. InN layers' thickness was changed by varying the pulse/pause cycle number. Using the same growth parameters but conventional MOVPE growth method, the reference InN layer was grown. The reference sample thickness was 326 nm. The temperature gradient means that the InN growth process was divided into two-step growth processes. It started at the lower 570°C temperature and during the first 100 cycles, the growth temperature ramped to 610°C. Thus, the first 100 cycles of growth were performed under the rising temperature. The mentioned reference sample was grown at 610°C.

Table 7.1: Growth parameters for the InN layers.

Thickness (nm)	Cycle number	Temperature gradient (°C)	V/III ratio	Pressure (mBar)
26	50	570 ÷ 610	9968	400
79	150			
158	300			
236	450			
315	600			
394	750			

AFM surface images of the InN layers after the consecutive cycle numbers are presented in Figure 7.12. It was found that InN layers start to grow from the densely packed islands. Instead of forming a smooth 2D layer, these islands increase in size. This also is evidenced in the surface roughness values. Increasing the thickness of InN layers, surface roughness also increases. The latter result is presented in Figure 7.13. The reference sample exhibits the same surface morphology as the InN layers grown by pulse MOVPE after 600 growth cycles. Due to the 11% lattice mismatch between GaN and InN, the growth itself takes place in Stranski – Krastanov regime [27, 194]. Stranski – Krastanov growth regime promotes 3D-islanding. A high V/III ratio and even higher effective V/III_{eff} ratio [**A3**], which can be calculated as

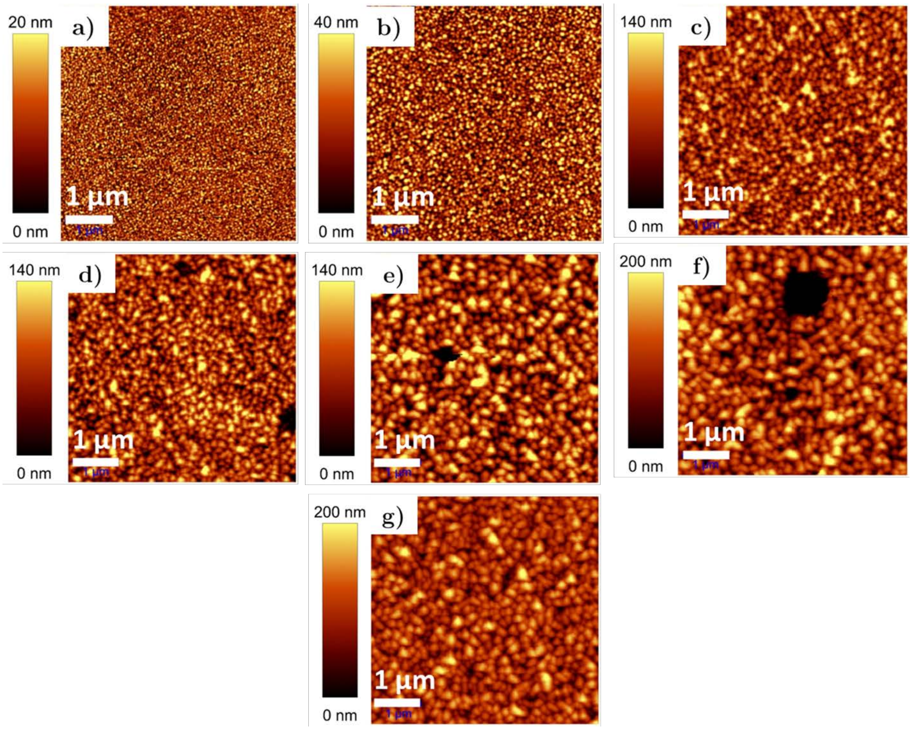

Figure 7.12: 5×5 μm AFM surface images of the InN layers grown on the 5 μm GaN layers after (a) 50, (b) 150, (c) 300, (d) 450, (e) 600, (f) 750 growth cycles and (g) reference sample.

$\left(\frac{V}{III}\right)_{eff} = \left(\frac{V}{III}\right)\left(1 + \frac{t_2}{t_1}\right)$, provides a sufficient amount of reactive nitrogen into the InN surface, thus not letting In adatoms desorb and form metallic In droplets. The effective V/III ratio value reaches about 38000. The TMIn pulse duration and TMIn flow rate combination were selected to deposit 1.5 – 2 monolayers of InN during the TMIn pulse. The thickness of the InN layer deposited during the pulse time can be slightly decreased during the TMIn pause time due to etching by the hydrogen generated after thermal dissociation of NH_3, but not entirely etched/decomposed away [195]. Though the InN decomposition is suppressed, such a high V/III ratio (and V/III effective ratio) reduces the In adatoms migration on the surface and it is not sufficient to form a smooth, step-flow surface. Thus the surface of the resulting InN layers exhibits islandic morphology. But these islands must be less defective and should demonstrate high crystalline quality.

XRD results of the InN layers are presented in Figure 7.14. From Figure 7.14 (a) (black curve) can be seen that with the increase of the InN layer thickness, InN, after 50 growth cycles, is partially relaxed. $2\theta/\omega$ angle value for the relaxed InN layers (0002) plane is 31.38°. When the thickness increases, strain

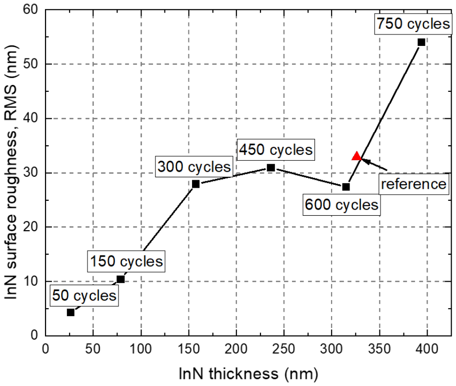

Figure 7.13: Surface roughness value dependence on the InN layers thickness grown by pulsed and conventional MOVPE. Values were acquired from Figure 7.12. The curve in the plot is only for eye-guiding purposes.

forces also rise and InN gets more strained. It can be seen from Figure 7.14 (a) (red curve) as the curve maximum shifts toward the higher angle values. After 100 growth cycles and further, InN gets only relaxed. At a growth cycle value of 600, which corresponds to 315 nm InN layer thickness, InN is fully relaxed. A very similar observation also was made by Yamaguchi *et al.* [196]: InN residual strain rises until when the InN layer reaches 120 nm and after this thickness, InN starts to release the residual strain.

The same results, as in the $2\theta/\omega$ XRD scans, were made in the InN layers mosaicity presented in Figure 7.14 (b). After 50 growth cycles (26 nm) InN layer FWHM of the XRC curve is very narrow and broadens until 300 growth cycles (158 nm). After the latter value, the FWHM of InN XRC curves gets slightly narrower and saturates at about 0.8°. This FWHM evolution is presented in Figure 7.15. According to Yamaguchi *et al.* reduction in the mosaicity (decreased FWHM values of XRC curves) indicates coalescence [196]. It means that in this case, InN layers start to grow as separate, high crystalline quality islands on the GaN surface. Then reaching 80 nm InN thickness, the InN layer exhibits the highest residual strain (according to $2\theta/\omega$ scans, see Figure 7.14(a)). The crystalline quality of the InN layers gets deteriorated. After reaching 158 nm InN thickness, the relaxation process occurs as the peak of the $2\theta/\omega$ XRD scan (see Figure 7.14(a)) starts to move toward the relaxed InN angle value. At this thickness value, the FWHM of the XRC curves reaches a maximum value. At this point, the InN layer, consisting of separate islands, starts to coalesce. As the coalescence occurs, the FWH values of XRC curves decrease, thus indicating a reduction in the mosaicity.

According to AFM and XRD results, the InN layer with 600 growth cycles was chosen as the optimized layer. Lastly, a photoluminescence (PL) experiment at room temperature was performed for the latter and reference sample.

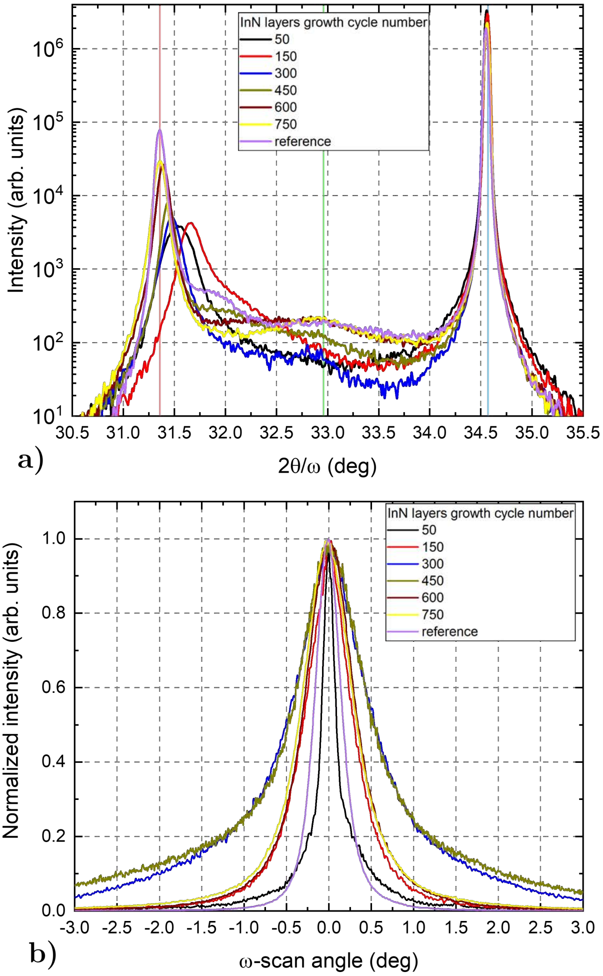

Figure 7.14: XRD results of the InN layers of (a) $2\theta/\omega$ scan of the (0002) plane and (b) XRC of the (0002) plane. Light red, light green and light blue vertical lines presents the relaxed $2\theta/\omega$ angle values for InN (31.38°), metallic In droplets (32.96°) and GaN (34.57°), respectively.

The excitation source in the experiment was a continuous wave He-Ne laser (633 nm). The PL spectrum was collected with an Andor, Shamrock 303 spectrometer (Oxford Instruments, Abingdon, UK) with an InGaAs detector array. The results of the PL measurement are presented in Figure 7.16(a) and summarized in Table 7.2. The InN layer, which was grown by pulsed MOVPE technique, exhibited PL peak position at 1600 nm wavelength, which corresponds to 0.78 eV photon energy. This value can be attributed to the InN band gap transition energy though it exhibits a larger value than mentioned earlier in Section 7.1, most probably due to Moss – Burstein effect. It can be noted that the reference sample exhibit lower integrated intensity (15%)

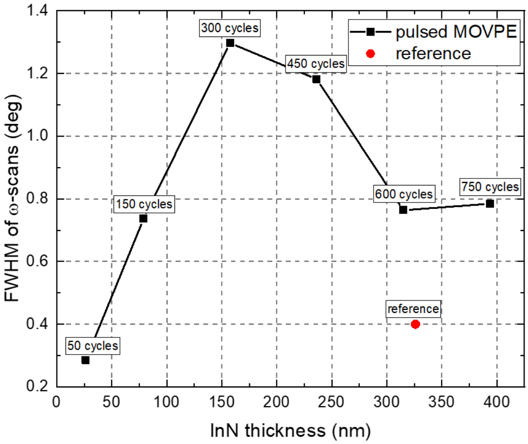

Figure 7.15: FWHM of the XRC scans presented in Figure 7.14 dependence on the thickness of the InN layers. The curve in the plot is only for eye-guiding purposes.

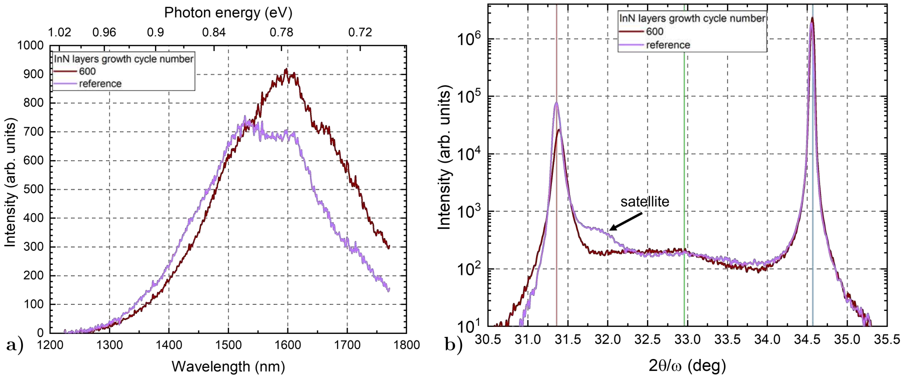

Figure 7.16: (a) Room-temperature PL spectra of InN layers grown on the GaN templates. (b) XRD of $2\theta/\omega$ scan of the (0002) plane for the samples.

compared to the sample grown by pulsed MOVPE. The latter finding can be attributed to the enhanced In adatom migration and more effective nitridation of the sample grown by pulsed MOVPE that exhibits less defects that are responsible for the non-radiative recombination channels [197].

Although the XRC scan (see Figure 7.14 (b) and Figure 7.15) showed that the InN layer grown by the conventional MOVPE method exhibited better crystalline quality than the same thickness InN sample grown by pulsed MOVPE, the PL experiment showed that the FWHM of the spectrum is narrower for the InN layer grown by the pulsed MOVPE method. Moreover, the InN sample grown by the conventional MOVPE exhibited a spectrum where two peak maximums can be distinguished (see Figure 7.16 (a)). It could indicate another phase material existence in the InN matrix. From the XRD $2\theta/\omega$ scans (see

Table 7.2: InN PL experiment results

MOVPE method	Peak position (eV)	Integrated intensity	FWHM (eV)
Pulsed (600)	0.78	227637	0.112
Conventional (reference)	0.8	192636	0.122

Figure 7.16 (b)) can be seen that the InN sample grown by the conventional MOVPE (reference) exhibits a satellite peak near the InN peak. This satellite peak can be attributed to the In-rich InGaN layer, which results from the In atoms diffusion into the GaN layer, or attributed to polycrystalline InN [23]. The InN sample grown by the pulsed MOVPE method didn't have such a satellite peak positioned near the InN peak. Thus a lower photon energy peak comes from the InN layer, while a higher photon energy peak comes from the In-rich InGaN or polycrystalline InN.

InN layer crystalline quality was drastically enhanced after the insertion of 600 nm p-GaN layer between 5 μm GaN template and 300 nm InN layer. The InN sample was grown by the pulsed MOVPE method using the same growth parameters presented in Table 7.1. The InN layer with 600 growth cycles was chosen as the optimized layer. p-GaN growth parameters are shown in Table 7.3. In order to acquire p-type doping, Bis(cyclopentadienyl) magnesium (Cp$_2$Mg) was used as a Mg precursor for the GaN layer. The flow rate of the Cp$_2$Mg in this growth experiment was $7.72 \cdot 10^{-7}$ mol/min. One more process was required for the p-type GaN layers, i.e., annealing under nitrogen and NH$_3$ ambient ambient at 850°C for 20 minutes to activate Mg acceptor states in the p-GaN layers. The annealing process dissociates Mg-related complexes (Mg-H, or interstitial Mg), which are electrically neutral before the annealing process [198–200].

Table 7.3: p-GaN growth parameters

MOVPE method	Temperature (°)	V/III ratio	Pressure (mBar)
Conventional	1030	6296	150

XRC scans of the InN samples grown directly on the 5 μm GaN template and 5 μm GaN plus 600 nm p-GaN are presented in Figure 7.17. The FWHM of the XRC curve for the InN layer grown on the 5 μm GaN plus 600 nm p-GaN decreased from 0.764° to 0.284° value. This value is by far better than those reported in the literature for the MOVPE growth: 0.5° [188], 0.36° [201], 0.27° for the *c*-oriented prismatic InN nanowalls grown on the GaN/sapphire templates [202] and 0.7° on the InAlN layer [203]. Such an improvement probably came from the better adhesion of the InN to the p-GaN grown layer. It was found by the Higashiwaki *et. al* that low temperature GaN greatly improved

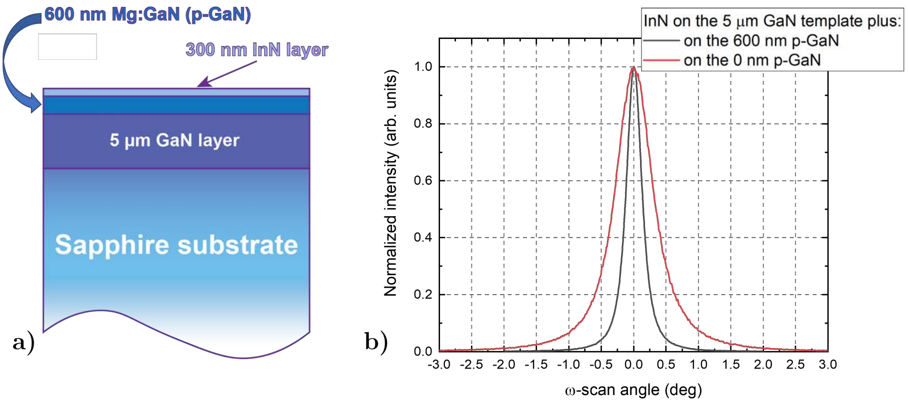

Figure 7.17: (a) Structure consisting of 300 nm InN on the 600 nm p-GaN layer grown on the 5 μm GaN/sapphire template. (b) XRC scans of the InN samples grown on the 5 μm GaN template and 5 μm GaN plus 600 nm p-GaN layers. Based on [**A3**].

the adherence of the InN layer [204]. Low temperature GaN exhibit rougher surface morphology compared to high temperature GaN. In this case p-GaN was grown at the lower temperature (1030°) compared to standard GaN growth (1080°). Moreover, due to the lower growth temperature and Mg doping the surface of the p-GaN layer is slightly deteriorated. The InN growth starts at lower temperatures too (see Table 7.1). It is probably that InN can form uniform grains with a good adherence on the p-type GaN layer, which may help relax the lattice mismatch between GaN and InN that facilitates the high crystalline quality InN growth.

7.4. Characterization of the InN/p-GaN junction

In this last section electrical characterization of the p-GaN/InN junction will be presented. The section will also give modeling results using Nextnano3 software and discuss results acquired from the different electrical measurements. The section is mainly based on [**A3**].

Figure 7.18 shows the SEM and EBIC images of the junction. An EBIC image shows the electrically active areas of the junction, which is the depletion region with a built-in electric field. The non-equilibrium charge carriers (holes and electrons) in the depletion region are immediately separated due to the built-in electric field, thus providing electrical current into the external circuit. It is expressed as the bright spots on the EBIC images (see Figure 7.18 (c) and (d)). Areas that remained dark indicate no electrical current. The latter fact suggests the fast recombination of the electron-hole pairs in these areas. As the SEM and EBIC images were superimposed, the location of the electrically active area was found. In this case, the electrically active area is between the

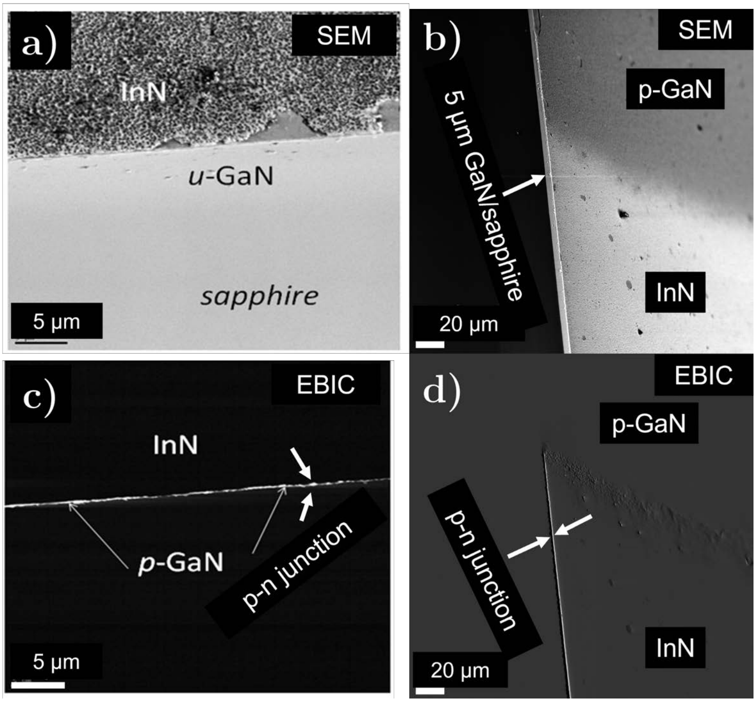

Figure 7.18: Bird's-eye view SEM images under (a) higher and (b) lower magnification of the p-GaN/InN junction. EBIC (c) and (d) images are superposed on the SEM images presented in (a) and (b). The bright line in (c) and (d) indicates the depleted region of the junction. Both SEM and EBIC images were obtained at 5 kV voltage. Based on [**A3**].

p-GaN and InN layers. The depletion region is very shallow (<100 nm) (see Figure 7.18 (d)) and it follows the surface topology.

The depletion region at the p-GaN/InN interface was investigated theoretically by using Nextnano3 software. The software is based on the numerical solving of the Poisson-Shrödinger system coupled with the drift-diffusion equation [205, 206]. Most nanostructures consist of strained materials. Thus Nextnano3 starts by performing a global strain minimization based on a macroscopic elasticity theory. Once the strain field is found, the piezoelectric and the pyroelectric charges are determined (it is especially relevant for the WZ structure materials). Consequently, the electronic structure is calculated within a single-band or multiband $\mathbf{k}\cdot\mathbf{p}$ envelope function approximation. Then, the Poisson, current and Shrödinger equations are solved self-consistently with respect to one another [206]. Nextnano3 includes three models for the carrier transport to simulate structure properties under an applied bias. One is the Wentzel-Kramer-Brillouin type approach. This approach assumes that the carriers are locally in equilibrium and can be characterized by a local Fermi level. The second method is termed the contact block reduction method. It is based on an efficient method to compute the ballistic current through an arbitrarily shaped open system. The third one is termed non-equilibrium Green's function technique. It includes the lesser Green's functions, as well as all relevant scattering processes, in a self-consistent manner [206].

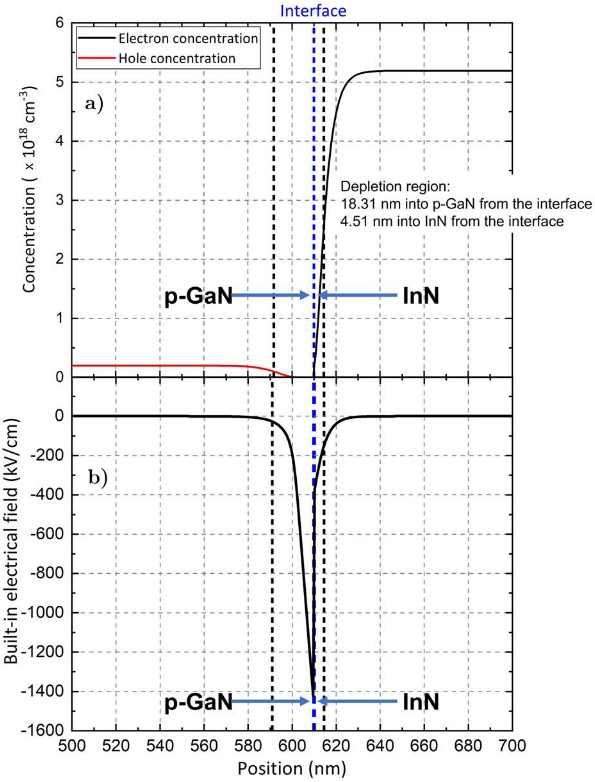

Figure 7.19: (a) Hole and electron concentrations and (b) built-in electrical field as a function of depth at the p-GaN/InN interface. Based on **[A3]**

The built-in electrical field across the p-GaN/InN junction interface is enhanced due to the gradient of spontaneous polarization. Figure 7.19 (a) presents the hole and electron concentration in the vicinity of the p-GaN/InN interface. Figure 7.19 (b) shows the built-in electrical field as a function of depth at the p-GaN/InN interface. The initial conditions for the simulations and doping concentration were evaluated from the equilibrium charge carrier concentrations acquired by Hall measurements. From the simulation, the thickness of the depletion region was found to be about 22.8 nm. The carrier concentration distribution in the depletion region penetrates further into the p-GaN layer (18.3 nm from the interface) than into the InN layer (4.5 nm from the interface). It is worth noting that in this work, the InN layer grown on the p-GaN layers exhibited one of the best electrical parameters reported in the literature amongst the MOVPE and MBE grown InN layers. The measured electron concentration for this work InN was n_e=5.19·10^{18} cm^{-3} and mobility μ_e=980 $cm^2V^{-1}s^{-1}$. The best values reported in the literature are n_e=(3 ÷ 5)·10^{18} cm^{-3}, μ_e=(542 ÷ 980) $cm^2V^{-1}s^{-1}$ [23, 25, 191, 207].

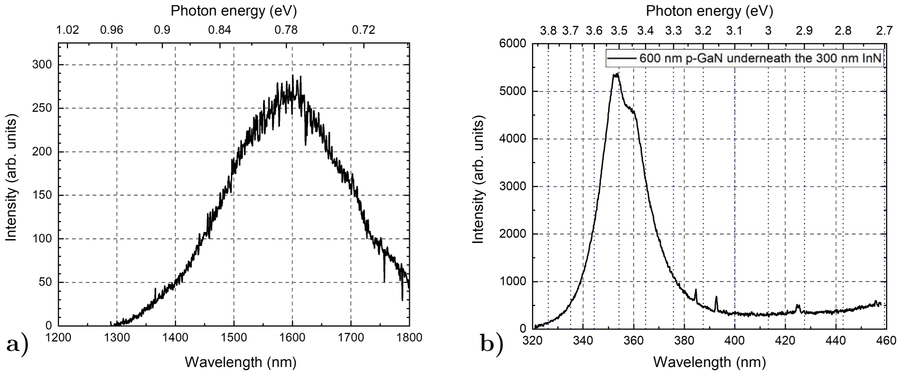

Figure 7.20: Room-temperature PL spectra of (a) InN layer grown by the pulsed MOVPE and (b) 600 nm p-GaN layer. Based on [**A3**].

Furthermore, PL measurements of the p-GaN/InN heterostructure at room temperature were performed. Although InN on the 600 nm p-GaN exhibited improved crystalline quality, its PL spectrum remained unchanged (see Figure 7.20 (a)), as presented in Figure 7.16 (a) (dark-red curve). PL maximum peak was centered at 0.78 eV (1600 nm). The PL spectrum of the p-GaN is a typical GaN room-temperature PL spectrum with near band-edge emission around 3.49 eV (355 nm) [208]. PL spectrum for the p-GaN layer is presented in Figure 7.20 (b).

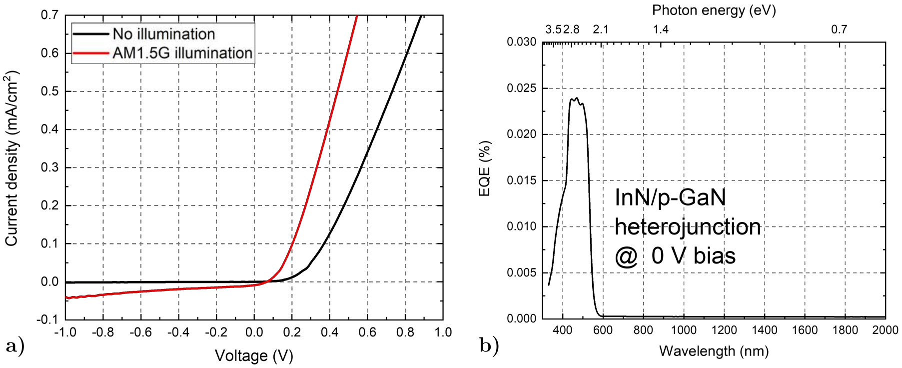

Figure 7.21: (a) Current voltage (J-V) characteristics of the p-GaN/InN heterojunction with no illumination and under AM1.5G illumination. (b) EQE spectra of the unbiased p-GaN/InN heterojunction. Based on [**A3**]

Photovoltaic response and external quantum efficiency (EQE) measurements for the p-GaN/InN heterojunction were performed to study the capability to generate a photo-current. Results are presented in Figure 7.21. AM1.5G standard solar spectra were simulated using Wacom Electric Co. solar simulator (JIS, IEC standard-conforming, CLASS AAA, Tokyo, Japan) calibrated in a manner that gave 100 $mWcm^{-2}$ using two reference solar cells: a-Si and c-Si. The electrical data was recorded by Keithley 2400 source meter (Tektronics, IL USA). The EQE characteristics were measured by CEP-25BXS (Bunkoh-Keiki Co., Ltd., Tokyo, Japan) in the extended spectral region of 300 ÷ 2000 nm.

The current density was measured for the applied bias voltage from -1 V to +1 V. The J-V characteristics present an asymmetrical behavior with a clear diode-like rectification pattern. Within the measured region, near the turn-on voltage of 0.2 V under the dark condition and of 0.06 V under the illumination (see Figure 7.21 (a)), the J-V characteristics follow a power law of $V \sim I^2$; consequently, for single-type carrier injection, the current conduction is expected to be space-charge limited. At larger applied voltages, the J-V does not deviate from the linearity, which could be an indication of low series resistance and low density of interface states. Figure 7.21 (b) presents EQE spectra of the unbiased p-GaN/InN heterojunction. The carrier collection peaked in the region of 400 ÷ 500 nm.

EQE spectra of the p-GaN/InN heterojunction at different reverse bias voltages (0 V, -10 V and -20 V) in the 300 ÷ 600 nm region are presented in Figure 7.22(a). Photo-response in the latter region comes from the absorption in both the p-GaN and InN layers. In general, a rising trend of the full spectrum with the increased reverse bias voltage, where the peak at 511 nm (2.4 eV) is the strongest, was observed. The sub-maximum at around 355 nm (3.49 eV) originates from the band gap transitions in the p-GaN layer and is peaked at the same wavelength of the PL emission in Figure 7.20. It means that conditions are favorable for both charge carriers generated in the p-GaN to reach the contacts. This fact means that electrons are able to get to the n-contact, while holes – p-contact. The same applies to the broad interval at 375 ÷ 500 nm (3.3 ÷ 2.2 eV), which correlates with known multiple transition mechanisms. The first is in the UV range, peaked at 3.2 ÷ 3.26 eV, indicating the Mg doping that introduces shallow acceptors with ionization energy of 200 meV. The second range peaked in the blue region at 2.7 ÷ 2.9 eV could come from the compensating deep donors formed at high p-doping levels and are responsible for the donor-to-band or donor-acceptor-pair transition [208]. Surprisingly, the EQE in the 300 ÷ 600 nm wavelength range is enhanced significantly above 100%. At -20 V reverse bias voltage, a contribution to the EQE in the longer wavelength range (>1500 nm) could be observed. This contribution is presented in Figure 7.22(b). The band peak position for the carrier extraction peaked around 0.7 eV (1780 nm), corresponding to the InN energy band gap. The nonlinear increase of the photocurrent as a function of reverse bias is presented in Figure 7.22(c). This behavior could indicate that

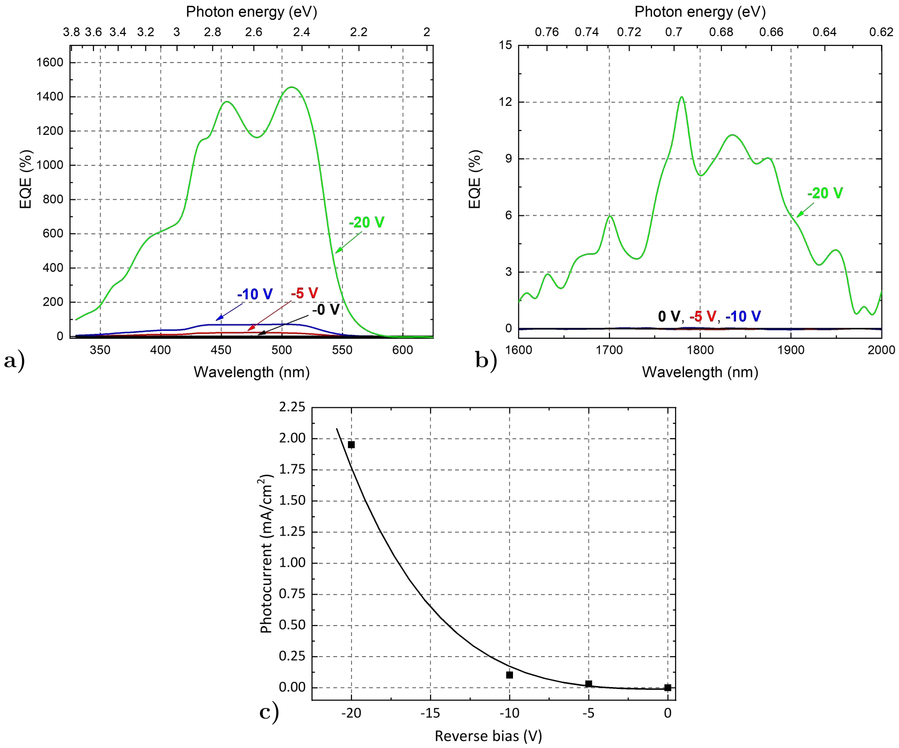

Figure 7.22: (a) EQE of the p-GaN/InN heterojunction at the reverse bias of 0 V, -5 V and -20 V. (b) EQE spectra of the p-GaN/InN heterojunction at the reverse bias of 0 V, -5 V and -20 V in the NIR spectral region. (c) Corresponding photocurrent density as a function of the reverse bias voltage. The line presented in (c) plot is a guide to the eye. Based on **[A3]**

the generated photocurrent increases exponentially with the applied bias due to presence of recombination centers [209].

Theoretical modeling results of the constructed band diagram of the p-GaN/InN heterojunction are presented in Figure 7.23. The calculations were done based on our measurement results. The schematic energy band diagram of the heterojunction under irradiation is illustrated in Figure 7.23(a), which reflects the type-I straddling configuration [210]. The band diagram in Figure 7.23(a) shows the band bending behavior at the p-GaN and InN interface that underlines the heterojunction formation. The photon absorption leads to the formation of excess electrons in the n-side, while holes in the p-side of the heterostructure, thus generating a voltage drop across the junction. The broader depletion region extended in the p-GaN maintains space charge neutrality, which results in efficient collection of the carriers in the UV and blue-visible region (see Figure 7.22). Electrons do not have any offset, while there is a 0.3 eV potential barrier for the holes. Nevertheless, with 1600 ÷ 1800 nm wavelength range and under AM1.5G (1 sun) illumination, electrons and holes are generated in the InN layer, and with sufficient reverse bias voltage applied, holes are able to overcome the interface barrier and generate photocurrent for the NIR region (see Figure 7.23 (b), (c) and Figure 7.22 (b)). The intrinsic concentration is a function of the energy gap of the material. Therefore, a small energy gap in InN semiconductors might exhibit high generation rates [211].

Even though enhancement of the EQE over 100% under different excitation conditions has been reported in the literature [212, 213], the increase up to 1400% in EQE in the p-GaN/InN heterojunction under -20 V reverse bias is not apparent and may be attributed to various factors. The enhancement might come from an enlargement of the depletion region, which contributes to the enhanced absorption and charge collection efficiency at the heterojunction. Due to bias voltage, the ionized donor concentration of GaN increases, and its work function decreases while harvesting photo-generated carriers in a globally larger area for the light in the 300 $\div$ 600 nm region. As well, for carrier multiplication (CM), due to the larger depletion region, a greater amount of the photo-generated carriers are efficiently collected [26, 214].

An important aspect is to extract multiple excitons and hot carriers before the thermalization of the carriers to the band edge and rapid recombination occurs. It could be possible in this particular case when the high-voltage reverse bias is applied. Nevertheless, for the latter effect to occur, InN should be most likely in a cubic phase featuring a wide gap between high-lying optical phonon and low-lying acoustic phonon energies. When the gap is wide enough, Klemens's decay of optical phonons is then prevented [215]. However, a pronounced XRD peak at 31.38° for the InN layer revealed the hexagonal lattice type, thus weakening the expectation for the hot carrier contribution.

This work results showed that the photocurrent increased nonlinearly with the reverse bias voltage (see Figure 7.22 (c)), exhibiting a peak at 2.4 eV (see Figure 7.22 (a)). This value corresponds about to three times the InN band gap. The latter observation might support the version of the contribution from CM, which was demonstrated in bulk InN to occur at photon energy up to three times its band gap [214, 216]. When the reverse bias approaches the breakdown levels, amplification at the electrical level can occur [217]. For a better understanding of what occurs when a reverse bias voltage is applied, calculations of the p-GaN/InN heterojunction at different reverse biases were performed and are presented in Figure 7.23 (b) and Figure 7.23 (c). As the depletion region is thin (in the nm range), electrons can directly tunnel across the depletion region from the p-GaN valence band into the InN conduction band. Under the high reverse bias (>-10 V), photocurrent generation takes place at the breakdown level. It leads to the separation of multiple excitons and efficient electron-hole generation, thus contributing significantly to the EQE of the p-GaN/InN heterojunction. Due to the large conduction band offset of the heterostructure and Mg doping the tunneling and overall photocurrent generation at the p-GaN/InN heterojunction can be improved [218].

In conclusion, in this work we present one of the best MOVPE grown InN layer which is comparable with the electrical parameters presented in the literature. Superior-quality InN layer was grown by employing the pulsed MOVPE method. The improved crystallinity was obtained thanks to pulsed nature and a higher-temperature growth process. Moreover, efficient electron-hole pair generation and extraction in the p-GaN/InN heterojunction were achieved. The heterojunction depletion region was simulated, demonstrating a 22.8 nm width extended by four times more into p-GaN than InN. The good rectifying behavior and photo-carrier extraction were observed without any external electrical field. Under increased reverse bias voltage and enlarged depletion region width, the EQE exceeded more than 100% in the 300 ÷ 550 nm rage, most likely due to carrier multiplication and photoconductivity.

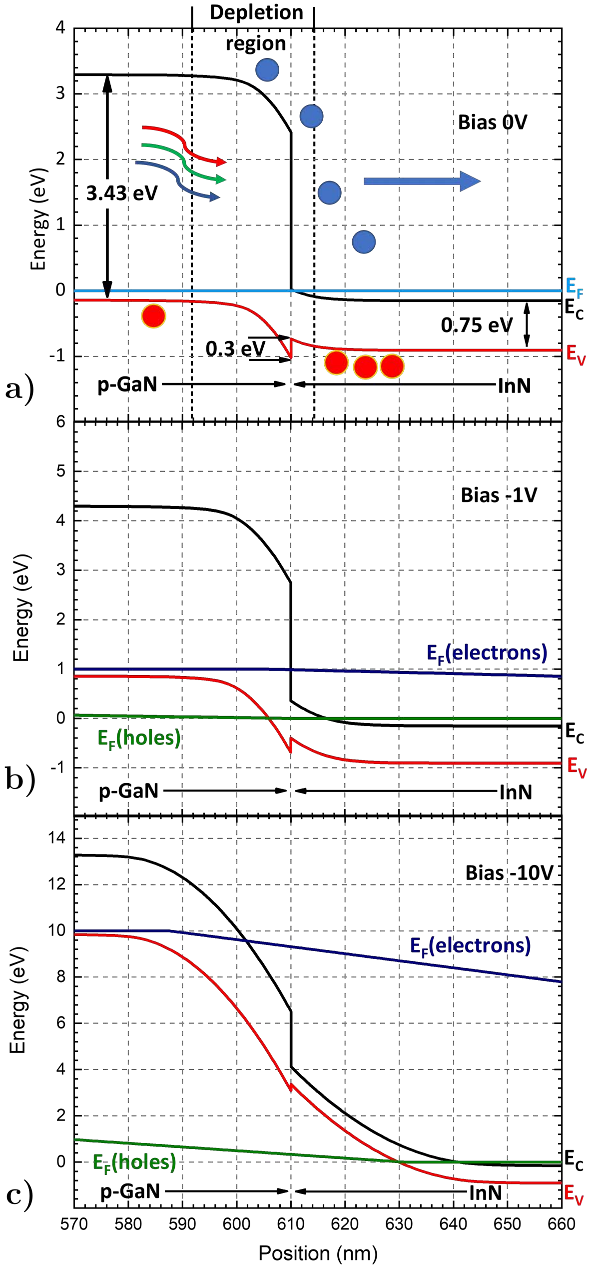

Figure 7.23: (a) Schematic of the unbiased (0V) interface band alignment at room temperature for the p-GaN/InN heterojunction. The irradiation of the junction is indicated with the wavy RGB arrows, blue circles represents electrons, while red circles represents holes. Biased band alignments for the junction (b) at -1 V and (c) -10 V reverse bias voltage are presented respectively. The E$_C$ stands for conduction band, E$_V$ – for valence band and E$_F$ – for Fermi levels of electrons and holes. Based on [**A3**]

CONCLUSIONS

The conclusions of the dissertation work are drawn and presented as follows:

1. It was theoretically found that due to optical mode dispersion in the waveguiding structure N-polarity GaN/ALD-Al_2O_3/Ga-polarity GaN/AlGaN/AlN/sapphire, only higher-order optical modes can generate the second harmonic waves (TM2) in the visible spectrum range. By inverting the polarity of the GaN layers, due to the enhancement of the spatial overlap integral of the fields of the pump and the generated second harmonic higher conversion efficiencies of the second harmonic generation can be achieved.

2. To achieve the (best) optical quality for the AlGaN layer - the important component (cladding layer) of the waveguiding structure, the optimal growth condition for the underneath AlN layer were defined. Good crystal quality and the lowest surface roughness (< 5 nm (AFM RMS roughness 10×10 μm)) of the AlGaN layer was obtained for 645°C nitridation and nucleation temperatures of the AlN layer, which probably effectively relieves the lattice mismatch between the AlGaN and sapphire.

3. GaN layers' polarity switching occurs when ALD-Al_2O_3 exhibit a different crystal configuration than GaN.

4. In the case of a 20 nm ALD-Al_2O_3 layer, the optimized conditions for the nitridation process (2400 s and 1100°C) and homogeneous N-polarity GaN growth in the waveguiding structure N-polarity GaN/ALD-Al_2O_3/Ga-polarity GaN/AlGaN/AlN/sapphire were obtained. If using a thinner ALD-Al_2O_3 layer ($10 \div 15$ nm) shorter nitridation time is necessary, though, the homogeneity of the N-polarity GaN deteriorates.

5. Simultaneous decrease in H_2 and V/III ratio (from 955 to 546) keeping the TMGa flow rate at constant 164 μmol/min value helped to reduce hexagonal shaped hillocks on the N-polarity GaN surface but not the surface roughness. By keeping the V/III ratio at even lower value (338) and reducing the TMGa flow rate (from 164 to 66 μmol/min) N-polarity GaN the surface roughness was reduced to 0.8 nm (AFM RMS roughness 10×10 μm). Reduction in NH_3 decreases the migration barrier for the Ga atoms, while reduction in the TMGa flow reduces Ga atoms quantity on the grown surface thus giving more space for the Ga atoms to migrate.

6. It was found that prolonged nitridation leads to the over-nitrided ALD-Al_2O_3 layers that result in growth of Ga-polarity GaN layers on the ALD-Al_2O_3.

7. Smoother and featureless surface morphology of the GaN layer grown on the ALD-Al_2O_3 layer in the N-polarity GaN/ALD-Al_2O_3/Ga-polarity GaN/AlGaN/AlN/sapphire waveguiding structure can be obtained by using thinner LTB-GaN layers. It may come from the higher surface quality Ga-polarity GaN inclusions, which probably, are a result of LTB-GaN small islands' inability to overgrow the over-nitrided areas of the ALD-Al_2O_3 layer.

8. It was proved that ALD-Al_2O_3 layer terminates the KOH etching process after the N-polarity GaN removal, thus protecting the Ga-polarity GaN layer underneath in the N-polarity GaN/ALD-Al_2O_3/Ga-polarity GaN/AlGaN/AlN/sapphire waveguiding structure.

9. For comparative reasons, N-polarity GaN growth was performed on the 0.3° off-cut sapphire substrates, which confirmed a similar growth pattern obtained on the 20 nm ALD-Al_2O_3 layers with the complex waveguiding structure grown on the sapphire substrate with 0.3° off-cut angle.

10. The pulsed MOVPE method manifested advantages for the growth of the InN layer. The optimized InN layer exhibited a homogeneous structure of high crystalline quality (WZ type) layer without metallic In droplet or InGaN inclusions.

11. The crystal quality of the InN layers was improved by the growth on the 600 nm p-type GaN layer, revealing low residual carrier (electron) concentration 10^{18} cm^{-3} levels and high carrier mobility of 980 $cm^2V^{-1}s^{-1}$. These values are among the best in the literature and comparable with the MBE-grown layers.

12. An efficient p-n junction based on p-GaN/InN heterostructure was fabricated using the developed high-quality InN layer. The device demonstrated an extraordinary photoresponse in the range of 300-600 nm suitable for photovoltaic and photodetector applications. The photoresponse in the NIR region with a maximum at 0.7 eV confirmed the band gap absorption of the InN.

SANTRAUKA LIETUVIŲ KALBA

Įvadas

Šiuolaikinis pasaulis labai stipriai susietas su nanotechnologijomis. Laikui bėgant šis ryšis tampa vis stipresnis ir glaudesnis. Nanotechnologijomis jau naudojasi maisto pramonė bei agrokultūros sektorius [1–3], elektronikos [5] ir medicinos sektoriai [6, 7]. Vis mažesnius dydžius yra bandoma išmatuoti ir užregistruoti, vis mažesnių matmenų technologijos yra reikalingos tiriant mikro- bei nanopasaulį. Šiandien vis daugiau elektroninės technologijos yra bandoma pakeisti fotoniniais dariniais bei komponentais. Šiuo atveju informacijos nešėjais tampa fotonai [8]. Pagrindinis pranašumas prieš elektronus yra tai, kad fotonais informacija gali būti pernešama didesniu dažniu (apie 100 THz). Fotonikos technologijose lazeriai yra pagrindiniai šviesos šaltiniai, kaip elektros generatoriai elektrinėse schemose. Optiniai bangolaidžiai yra elektrinių kabelių analogija, o optiniai detektoriai – elektrinių tranzistorių bei jungiklių analogija. Integravus tuos prietaisus ant vienos platformos arba vieno auginamo padėklo atsivertų galimybės naujiems prietaisams gebantiems charakterizuoti mikro- bei nano-pasaulį.

III grupės nitridiniai puslaidininkiai yra unikalūs, nes iš jų galima konstruoti ir fotonines, ir elektronines struktūras. Populiariausiais šios grupės junginiais laikomi InN, kurio draustinių energijų tarpas yra $0.65 \div 0.75$ eV ($1907 \div 1653$ nm) [12,13], GaN – 3.39 eV (365 nm) [9] ir AlN – 6.2 eV (200 nm) [9]. Maišant šias medžiagas tarpusavyje ir taip keičiant draustinių energijų tarpo vertes galima perkloti spektrą nuo artimos infraraudonosios (NIR) iki ultravioletinės (UV) srities. Svarbu ir tai, kad GaN ir AlN dėl jų plataus energetinių juostų tarpo turi labai platų skaidrumo langą. GaN skaidrumo langas yra nuo 7 μm iki 365 nm, AlN – nuo 6.5 μm iki 200 nm [10]. Taip pat, GaN ir AlN pasižymi reikšmingu lūžio rodiklio kontrastu (GaN 2.3330 [10], AlN 2.1297 [11]). Šios savybės skatina jų naudojimą fotoninėse struktūrose, veikiančiose regimojoje spektro srityje. Tuo tarpu InN, kuris sugeria visą regimos šviesos spektrą iki NIR srities ir yra labai stiprus n-tipo puslaidininkis, demonstruoja geras perspektyvas fotovoltaikoje bei detektoriuose.

Šviesos technologijose GaN ir AlN sluoksniai yra taikomi antros harmonikos generatoriuose [14–17]. III grupės nitridiniai puslaidininkiai kristalizuojasi į viurcito tipo kristalinę gardelę, o tai reiškia, kad jie neturi centro simetrijos. Jų antros eilės netiesinis optinis jautris nėra lygus nuliui. Klasikiniu būdu, panaudojant dvejopą spindulių lūžį, sugeneruoti antrąją harmoniką GaN ir AlN yra sudėtinga. Panaudojus fotonines struktūras galima pasiekti antros harmonikos generavimą, taip pat generuoti superkontinuumą. Šiuo atveju generavimas yra pasiekiamas GaN arba AlN bangolaidžiuose. Neseniai [14], o taip šio darbo skaičiavimo rezultatai parodė, kad antros harmonikos generavimo efektyvumas yra pagerinamas panaudojant GaN bangolaidį sudarytą iš dviejų supriešinto poliariškumo dalių. Tačiau čia iškyla dvi problemos. Pirma, tai GaN poliariškumo vertimas auginant struktūrą ant vieno ir to pačio padėklo. Antra problema tai, N-poliariškumo GaN sluoksnio šiurkšti paviršiaus morfologija [19, 20]. Paviršiaus kokybė ypač svarbi bangolaidinėse struktūrose, nes didelis paviršiaus šiurkštumas įneša didelius optinius nuostolius [14]. Hitės grupė parodė, kad GaN poliariškumą galima keisti iš Ga- į N- panaudojant Al_2O_3 ploną sluoksnį [21]. N-poliariškumo GaN sluoksnio formavimą lemia nitridizacijos procesas, todėl jo valdymas/optimizavimas pradiniame etape yra svarbus žingsnis. Antra, būtina nustatyti tokius N-poliariškumo GaN auginimo parametrus, kad paviršiaus morfologija būtu kuo tolygesnė, o pats sluoksnis būtų kuo homogeniškesnis.

Teoriškai yra paskaičiuota, kad elektronų judrumas InN gali siekti 4400 $cm^2V^{-1}s^{-1}$ vertę kambario temperatūroje [22]. Tačiau kol kas geriausios rezultatų vertės svyruoja tarp $500 \div 900$ $cm^2V^{-1}s^{-1}$ [23–25]. Maksimalioms judrumo vertėms pasiekti reikia užauginti aukštos kristalinės kokybės InN sluoksnius, kas nėra labai lengvai įgyvendinama užduotis [23, 27]. Dėl žemos disociacijos temperatūros ir aukšto pusiausvirojo azoto slėgio virš InN paviršiaus sluoksnis turi būti auginamas žymiai žemesnėje temperatūroje nei GaN. Mažinant auginimo temperatūrą prastėja amoniako (NH_3), kaip azoto pirmtako, skilimo efektyvumas. Rezultate InN auga reaktyvinio azoto trūkume kas lemia metalinio indžio (In) lašelių ant sluoksnio paviršiaus susiformavimą, o pačiame sluoksnyje padaugėja defektų susietų su N, In arba deguonies (O) atomais (vakansijos, intarpai) [23, 28].

Dėl santykinai didelių auginimo greičių MOVPE technologija yra efektyviausias epitaksinių sluoksnių formavimo būdas, todėl ir labiausiai paplitęs optoelektroninių prietaisų gamyboje. Šiame darbe aukštos kokybės InN epitaksinių sluoksnių formavimui buvo panaudotas pažangus ir lankstus impulsinis auginimo būdas.

Darbo tikslas

Darbas susideda iš dviejų dalių, kuriame yra nagrinėjamas skirtingų III-grupės nitridinių puslaidininkių MOVPE auginimas, siekiant jų taikymo specifiniuose prietaisuose. Pirmoje dalyje yra nagrinėjama N-poliariškumo GaN auginimo ypatybes ant Al_2O_3 sluoksnio, nusodinto ant kompleksinės GaN/AlGaN bangolaidinės struktūros. Antroje – aukštos kokybės InN sluoksnio auginimas ant p-tipo GaN, taip sudarant p-n sandūrą. Pagrindinis darbo tikslas yra išvystyti/ištobulinti III-grupės nitridinių puslaidininkinių heterostruktūrų, skirtų prietaisams veikiantiems skirtinguose spektro ruožuose, formavimą.

Sprendžiami uždaviniai

- Teoriškai įvertinti GaN/AlGaN daugiasluoksnės bangolaidinės heterostruktūros, gebančios generuoti antrąją harmoniką, sluoksnių storius.
- Optimizuoti GaN/AlGaN daugiasluoksnio bangolaidžio optinio apvalkalo – Al-poliariškumo AlN ir AlGaN sluoksnių auginimo parametrus.
- Ištobulinti N-poliariškumo GaN ant 2° safyro padėklų auginimo procedūrą ir pritaikyti ją auginimams ant ALD-Al_2O_3 sluoksnių.
- Optimizuoti N-poliariškumo GaN sluoksnio ant Al_2O_3, nusodinto ant GaN/AlGaN bangolaidinės struktūros, auginimo parametrus ir taip užbaigiant planarinio daugiasluoksnio bangolaidžio su skirtingais GaN poliariškumais konstravimą.
- Taikant impulsinį MOVPE auginimo būdą, užauginti aukštos kristalinės kokybės InN sluoksnį, o panaudojus p-GaN suformuoti efektyviai veikiančią p-n sandūrą.

Mokslinis darbo naujumas

- Hitės grupė parodė, kad taikant ALD būdu nusodintą Al_2O_3 sluoksnį yra galimybė apversti GaN sluoksnio poliariškumą iš Ga į N [21]. Tačiau tai buvo padaryta periodiškai polinėje GaN struktūroje užaugintoje ant tūrinio GaN padėklo. Literatūroje nėra informacijos apie GaN poliariškumo keitimą per visą padėklą, taip suformuojant daugiasluoksnę N-poliariškumo GaN/ALD-Al_2O_3/Ga-poliariškumo GaN/AlGaN/AlN bangolaidinę struktūrą ant 0.3° nuopjovos kampo safyro padėklo.
- Literatūroje nėra informacijos apie auginimo parametrų – nitridizacijos ir GaN buferinio sluoksnio (LTB-GaN) įtaką N-poliariškumo GaN auginimui ant ALD būdu nusodinto Al_2O_3.
- Informacija apie aukštos kristalinės kokybės InN sluoksnio auginimą impulsiniu MOVPE būdu yra nauja ir literatūroje nepublikuota. Žema elektronų koncentracija (10^{18} cm^{-3} eilės) bei aukštas elektronų judrumas (980 $cm^2V^{-1}s^{-1}$) InN sluoksnyje yra išskirtiniai pasiekimai. Nauja ir tai, kad pritaikius minėtu būdu užaugintą InN sluoksnį ant p-tipo GaN buvo sudaryta p-n sandūra bei ištirtas jos fotoatsakas.

Ginamieji teiginiai

1. ALD-Al_2O_3 yra tinkamas GaN poliariškumo vertimui daugiasluoksnėje N-poliariškumo GaN/ALD-Al_2O_3/Ga-poliariškumo GaN/AlGaN/AlN bangolaidinėje struktūroje užaugintoje ant standartinio safyro padėklo. Poliškumo vertimui minimalus ALD-Al_2O_3 storis yra 20 nm.

2. Mažinant V/III santykį bei TMGa srautą, taip pat parenkant optimalią nitridizavimo trukmę, sukuriamos sąlygos geresnei Ga atomų migracijai, kas leidžia pasiekti kokybiško N-poliškumo GaN sluoksnio auginimą, tinkamą formuoti daugialsluoksnius optinius bangolaidžius.

3. Ant GaN padėklų impulsiniu MOVPE metodu auginamas InN pasižymi viena viurcito kristaline faze, kurio kristališkumo kokybę galima gerinti auginant ant p-GaN. InN/p-GaN heterostruktūroje dėl InN sugerties yra stebimas fotoelektrinis atsakas artimojoje infraraudonojoje spektro srityje.

N-poliariškumo GaN/ALD-Al_2O_3/Ga-poliariškumo GaN/AlGaN/AlN/safyro bangolaidinės struktūros auginimas bei N-poliariškumo GaN sluoksnių charakterizavimas

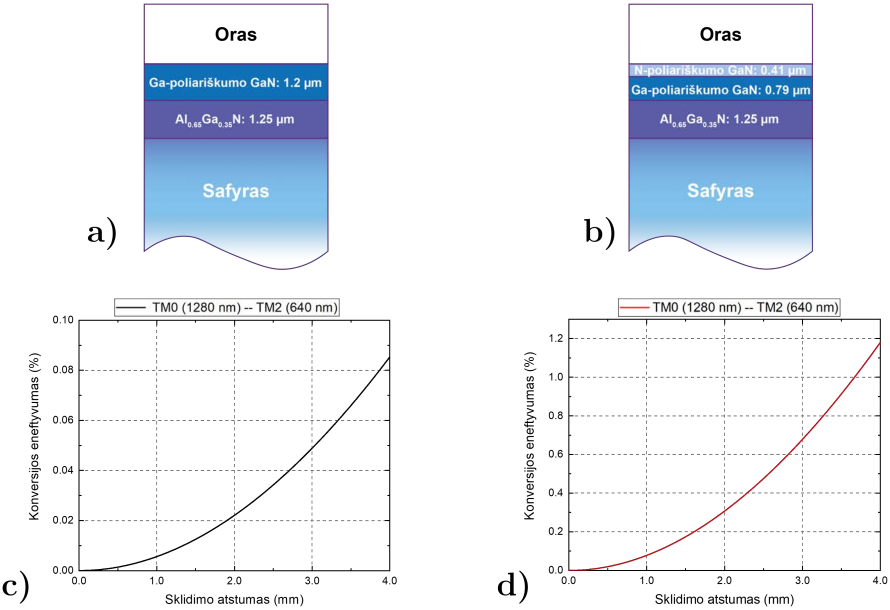

S1 pav.: GaN/AlGaN daugiasluoksnių planarinių bangolaidžių pavyzdžiai: (a) be invertuotos optinės ašies; (b) su invertuota optine ašimi, ir atitinkamai (c), (d) šių struktūrų IIH konversijos efektyvumų priklausomybės nuo sklidimo bangolaidyje atstumo.

Dėl GaN lūžio rodiklio dispersijos nėra įmanoma išpildyti fazių sinchronizmo sąlygos pasitelkiant vien dvejopą spindulių lūžį. Iš literatūroje siūlomų antros harmonikos generavimui GaN būdų, kuriais siekiama išpildyti fazinio sinchronizmo sąlygą, išskirtume du labiausiai priimtinus: fazių kvazisinchronizmą (angl. quasi-phase-matching – QPM) [17] ir modalinį fazių sinchronizmą (angl. modal-dispersion-phase-matching – MDPM) [14]. Pirmas efektas pasiekiamas strukūroje, kurioje antros eilės netiesinis jautris šviesos sklidimo kryptimi per koherentiškumo ilgį yra orientuotas periodiškai. Tokioje struktūroje antros harmonikos fazė per koherentiškumo ilgį yra perstumiama per π atžvilgiu pirmos harmonikos, taip išpildant fazių kvazisinchronizmą. MDPM yra pasiekiamas bangolaidinėse struktūrose. Šiuo atveju, atitinkamai parenkant bangolaidžio parametrus (medžiaga, storis, plotis), galima rasti sąlygą, kad tarp pirmos ir antros harmonikos modų būtų išpildyta fazių sinchronizmo sąlyga. Šiuo atveju IIH konversijos efektyvumas priklauso nuo modų sanklotos integralo, kurį galima padidinti panaudojant polines medžiagas. Jose antros eilės netiesinio jautrio ženklas priklauso nuo kristalo krypties. Keičiant medžiagos poliariškumą taip pat keičiasi ir šis antros eilės netiesinis jautris (invertuojant optinę ašį). Viena iš tokių polinių medžiagų ir yra GaN. Planarinių daugiasluoksnių bangolaidinių struktūrų bei konversijos efektyvumo pavyzdžiai yra pateikti S1 paveiksle.

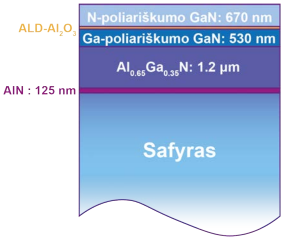

S2 pav.: Darbe formuota ir tirta daugiasluoksnė bangolaidinė struktūra su dviem skirtingais GaN poliariškumais.

Šiame darbe auginta ir tirta struktūra yra pavaizduota S2 paveiksle. Struktūros auginimas buvo pradėtas nuo AlN ir AlGaN su 65% aliumininio (Al) sluoksnių. 65% Al buvo pasirinkta tam, kad gauti reikiamą lūžio rodiklio vertę. AlGaN taip pat buvo naudojamas kaip buferinis sluoksnis Ga-poliariškumo GaN sluoksniui, kad minimizuoti gardelių nesutapimą tarp GaN ir safyro. Tokiu būdu buvo išvengtas Ga-poliariškumo GaN žematemperatūrinis, daug defektų turintis, buferinis sluoksnis, kuris įvestų į bangolaidį papildomai defektų ir padidintų šviesos sklaidą. Optimizuoti AlN auginimo parametrai leido sumažinti AlGaN sluoksnio paviršiaus šiurkštumą iki 3.5 nm. Šio auginimo rezultatai yra pateikti S3 paveiksle.

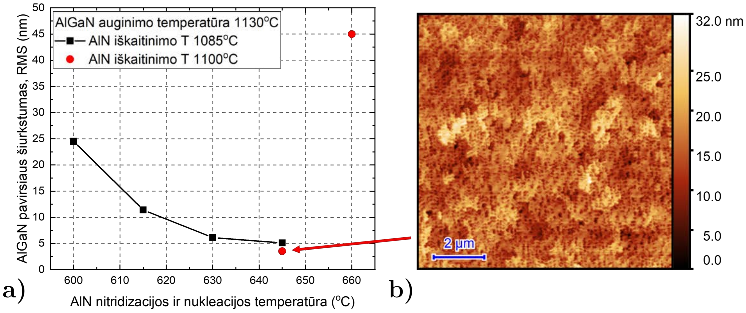

S3 pav.: (a) AlGaN sluoksnio ant AlN 10×10 μm paviršiaus šiurkštumo (RMS, 10×10 μm AFM) priklausomybė nuo AlN nitridizacijos bei nukleacijos temperatūros. (b) Optimizuoto AlGaN sluoksnio paviršiaus 10×10 μm AFM nuotrauka. Juoda kreivė – orientyras akims.

Toliau sekė Ga-poliariškumo GaN sluoksnio auginimas. Šio auginimo re-

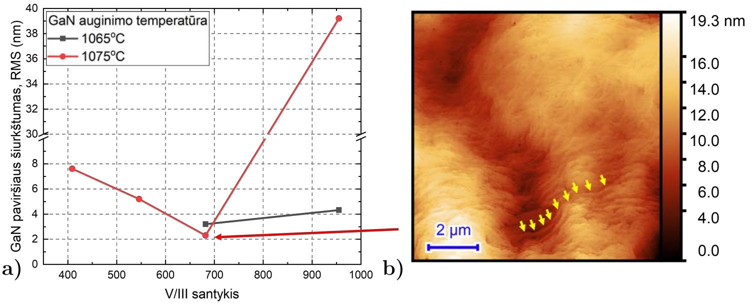

S4 pav.: (a) GaN paviršiaus šiurkštumo (RMS, 10×10 μm AFM) priklausomybė nuo V/III santykio. (b) Optimizuoto GaN sluoksnio paviršiaus AFM nuotrauka. Kreivės grafike yra orientyrai akims.

zultatai yra pateikti S4 paveiksle. Optimizuojant V/III santykį buvo pasiektas sluoksnis-po-sluoksnio (2D) auginimo režimas. 2D auginimo režimo įrodymas yra pateiktas S4 (b) paveiksle, kur aiškiai yra matomos auginimo terasos.

Panaudoję atominių sluoksnių nusodinimo būdu (ALD) užaugintą Al_2O_3 Hite parodė, kad taip yra sudaroma galimybė pakeisti GaN sluoksnio poliariškumą [21]. QPM struktūra su skirtingais GaN poliariškumais buvo suformuota ant tūrinio GaN padėklo. Mūsų darbe GaN poliariškumas buvo keičiamas ant kompleksinės struktūros, kurios pavyzdys yra pateiktas S1 (b) arba S2 paveiksluose. Taip buvo gauta daugiasluoksnė bangolaidinė struktūra su dviem skirtingais GaN poliariškumais. Reikia pabrėžti, kad po Al_2O_3 nusodinimo jo paviršiaus morfologija nepablogėjo, tai yra, paviršius netapo šiurkštesnis.

MOVPE būdu užauginto N-poliariškumo GaN paviršiaus vaizdai yra pateikti S5 paveiksle. Šiame eksperimente buvo panaudoti trys skirtingi ALD-Al_2O_3 storiai: 10 nm, 15 nm bei 20 nm. Auginimo procesas buvo pradėtas

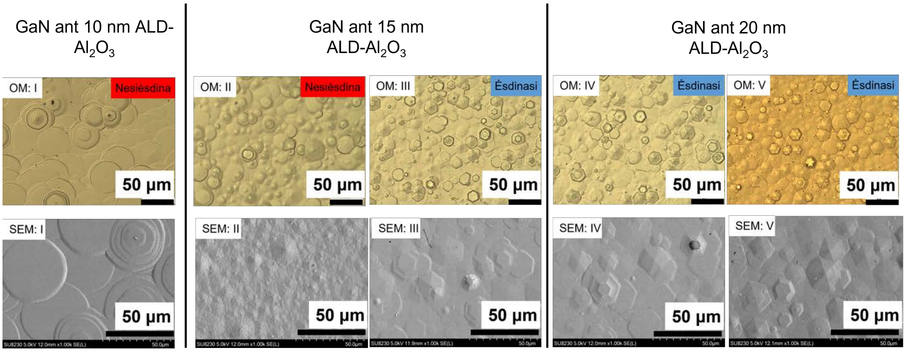

S5 pav.: N-poliariškumo GaN sluoksnių paviršiaus ant skirtingų storių ALD-Al_2O_3 sluoksnių optinės (viršuje) bei SEM (apačioje) nuotraukos.

nuo ilgo, 2400 s trukusio nitridizacijos proceso, kuris perkristalizavo bei paruošė ALD-Al_2O_3 sluoksnį N-poliariškumo GaN auginimui. Yra žinoma, kad N-poliariškumo GaN sluoksnio auginimui ant didesnio (pvz. 2°) nuopjovos kampo safyro padėklo reikalingas pailgintas, aukštos temperatūros (900 ÷ 1000°C) nitridizacijos procesas [19, 143]. Toks procesas priverčia azoto atomus (N) trimis jungtimis prisijungti prie safyro padėklo, taip užduodant N-poliariškumo kryptį. Pilnas N-poliariškumo GaN sluoksnio auginimas buvo atliekamas keturiais žingsniais, tai yra, nitridizacijos, žematemperatūrinio GaN (LTB-GaN) auginimo, iškaitinimo ir aukštatemperatūrinio GaN (HT-GaN) auginimo procesų.

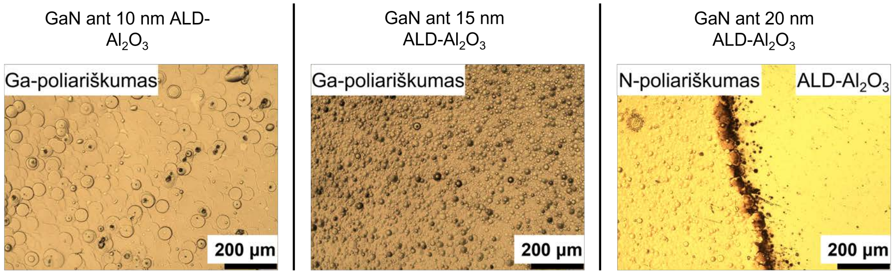

S6 pav.: N-poliariškumo GaN sluoksnių, užaugintų ant skirtingų storių ALD-Al_2O_3 sluoksnių, ėsdinimo rezultatų optinės nuotraukos.

Skirtingiems ALD-Al_2O_3 storių sluoksniams pritaikius minėtą nitridizaciją, N-poliariškumo GaN sluoksnį pavyko gauti tik 20 nm ALD-Al_2O_3 atveju. Vienas N-poliariškumo GaN požymių yra paviršiuje susiformavusios heksagoninės formos piramidės (žr. S5 OM:IV ir OM:V). Kita N-poliariškumo GaN sluoksnio savybė yra jo neatsparumas KOH tirpalui. Tuo tarpu, Ga-poliariškumo GaN yra chemiškai stabilus ir jo paviršių KOH tirplas veikia silpnai. Ėsdinimo rezultatai yra pateikti S6 paveiksle. Jie patvirtino optinių tyrimų išvadą, t.y., kad GaN sluoksnis užaugintas ant 20 nm ALD-Al_2O_3, buvo N-poliariškumo. S6 paveiksle (dešinėje) aiškiai galima stebėti ribą su nuėsdintu N-poliariškumo GaN sluoksniu. Formuluojame išvadą, kad minimalus storis, reikalingas GaN poliariškumo apvertimui, yra 20 nm ALD-Al_2O_3.

Heksagoninės struktūros yra nepageidautinos ant N-poliariškumo GaN paviršiaus. Jos įneštų papildomus optinius nuostolius, dėl šviesos sklaidos bangolaidinėje struktūroje. Kad sumažinti šį heksagoninių struktūrų tankį buvo atliktas auginimo parametrų optimizavimas. Pirmas eksperimentas – mažinant N atomų kiekį (mažinant V/III santykį, bet išlaikant pastovų trimetilgalio (TMGa) 164 μmol/min srautą). Šio eksperimento rezultatai yra parodyti S7 paveiksle. Sumažėjus N atomų kiekiui reaktoriuje, padidėja Ga atomų judrumas auginamo sluoksnio paviršiuje, taip pasiekiamas tolygesnis sluoksnio augimas [90]. N-poliariškumo GaN paviršiuje išnyko heksagoninės struktūros, tačiau, kad paviršius yra netolygus (žr. S7 (c)). Papildomai, buvo eksperimentuojama mažinant ir vandenilio (H_2) bendrą kiekį reaktoriuje, taip siekiant sumažinti GaN garavimą, kuris prisideda prie paviršiaus šiurkštėjimo proceso [146].

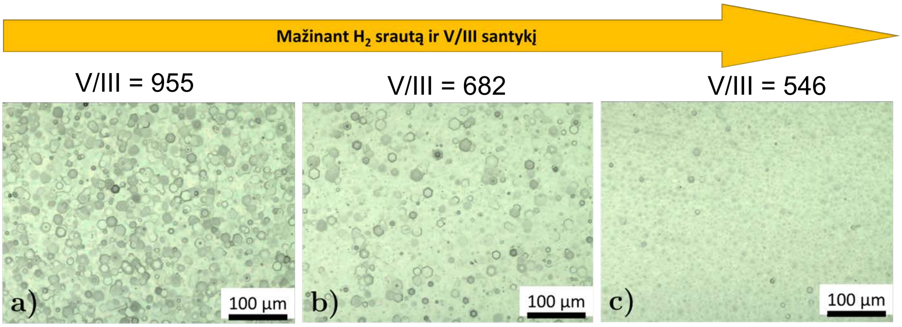

S7 pav.: N-poliariškumo GaN sluoksnių optinės nuotraukos skirtingiems bendro vandenilio kiekiui ir V/III santykiui: (a) 955, (b) 682, (c) 546. TMGa srautas 164 μmol/min.

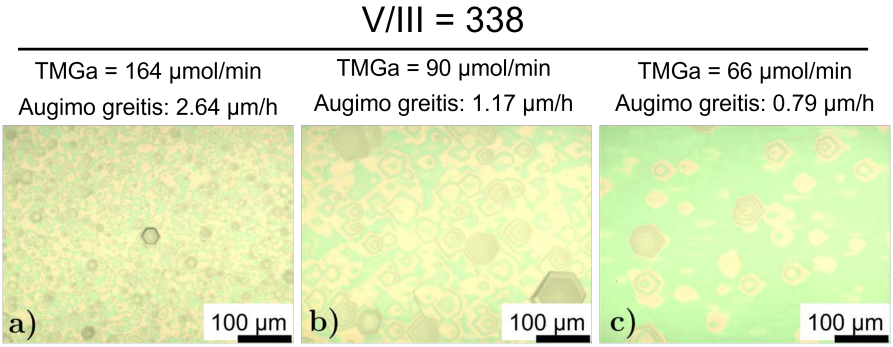

S8 pav.: N-poliariškumo GaN sluoksnių optinės nuotraukos skirtingam TMGa srautui, išlaikant pastovų V/III santykį.

Kitas eksperimentas atliktas mažinant TMGa srautą, bet išlaikant pastovų V/III santykį, t.y. mažinant abu Ga ir N atomų koncentraciją paviršiuje. Eksperimentas buvo atliktas ant safyro padėklų, kuriuose nuopjovos kampas buvo 0.3°. Taip buvo įvertinta TMGa srauto įtaka N-poliariškumo GaN sluoksnio paviršiaus morfologijai. Rezultatai yra pateikti S8 paveiksle. Mažinant TMGa srautą automatiškai mažėja auginimo greitis (mažėja Ga bei N atomų kiekis). Pagal Zywietz'o ir Kanagawa'os skaičiavimus, mažinant N atomų koncentraciją, Ga atomams mažėja migracijos barjeras ir didėja jų judrumas [90, 162]. Taip pat, mažesniam Ga atomų kiekiui paviršiuje (mažinant TMGa srautą) padidėja jų difuzijos ilgiai taip, kad jie gali pasiekti laiptų kraštus ant auginamo padėklo/sluoksnio, taip gaunant sluoksnis-po-sluoksnio auginimą.

Kitas optimizavimo eksperimentas – nitridizacijos trukmės parinkimas. Šio eksperimento rezultatai yra parodyti S9 paveiksle. Nitridizavimo trukmė labai stipriai keičia N-poliariškumo GaN sluoksnio paviršiaus morfologiją. GaN, užauginto ant 3600 s nitridizuoto 20 nm ALD-Al_2O_3, paviršius neturi jokių

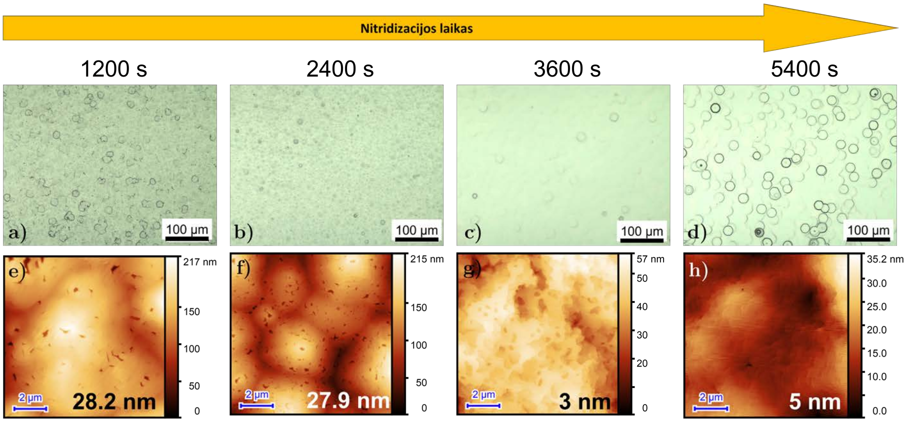

S9 pav.: GaN sluoksnių, užaugintų ant 20 nm ALD-Al_2O_3 su skirtinga nitridizacijos trukme: (a), (e) 1200 s; (b), (f) 2400 s; (c), (g) 3600 s; (d), (h) 5400 s optinės ir 10×10 μm AFM nuotraukos. Skaičiai nanometrais AFM nuotraukoje parodo paviršiaus šiurkštumo vertę (RMS).

heksagoninių struktūrų. Jeigu nitridizacijos trukmė buvo 3600 s ir mažesnė, šie sluoksniai ėsdinosi KOH tirpale, o tai reiškia N-poliariškumo GaN. GaN sluoksnio užauginto ant 20 nm ALD-Al_2O_3 sluoksnio, kurio nitridizacijos trukmė buvo 5400 s paviršiaus morfologija (žr. S9 (d)) yra tokia pati kaip ir GaN užauginto ant 10 nm ALD-Al_2O_3 su trumpesne (2400 s) nitridizacija (žr. S5). Abu bandiniai nesiėsdino KOH tirpale, kas reiškia, kad ant ALD-Al_2O_3 paviršaus užaugo Ga-poliariškumo GaN. Iš to seka, kad per ilga nitridizacijos trukmė gadina ALD-Al_2O_3 sluoksnį ir jis praranda poliariškumo vertimo funkciją.

Dar vienas N-poliariškumo GaN optimizavimo eksperimentas buvo atliktas, kad įvertinti LTB-GaN sluoksnio storio (auginimo laiko) įtaką. Šiuo atveju N-poliariškumo GaN sluoksnis buvo auginamas ant 20 nm ALD-Al_2O_3, po 3600 s trukusios nitridizacijos. Buvo išbandytos 60 s, 90 s, 135 s ir 195 s LTB-GaN auginimo trukmės. Eksperimento rezultatai yra pateikti S10 paveiksle. Visi bandiniai ėsdinosi KOH tirpale (žr. S10 (a)). Pastebėta, kad didinant LTB-GaN auginimo laiką N-poliariškumo GaN šiurkštėja (žr. S10 (b)). Tai galima susieti su N-poliariškumo GaN auginimo dinamika. N-poliariškumo GaN sluoksnio auginimo pradžioje susifromuoja mažos salelės. Kuo tankiau tos salelės yra išsidėsčiusios, bei kuo jos yra tolygesnes tuo labiau lygesnio paviršiaus N-poliariškumo GaN sluoksnį galima užauginti. Viskas yra dėl mažesnės Ga atomų migracijos ant auginamo N-poliariškumo paviršiaus, lyginant su Ga-poliariškumo GaN paviršiumi. Taigi, kuo stambesnės salelės yra suformuojamos auginimo pradžioje, tuo didesnis paviršiaus šiurkštumas bus galutiniame rezultate [92].

Atlikus KOH ėsdinimo eksperimentus buvo pastebėta, kad ant ALD-Al_2O_3 sluoksnių liko neišėsdintos sritys (žr. S10 (a) 60 s ir 90 s). Šių bandinių SEM pa-

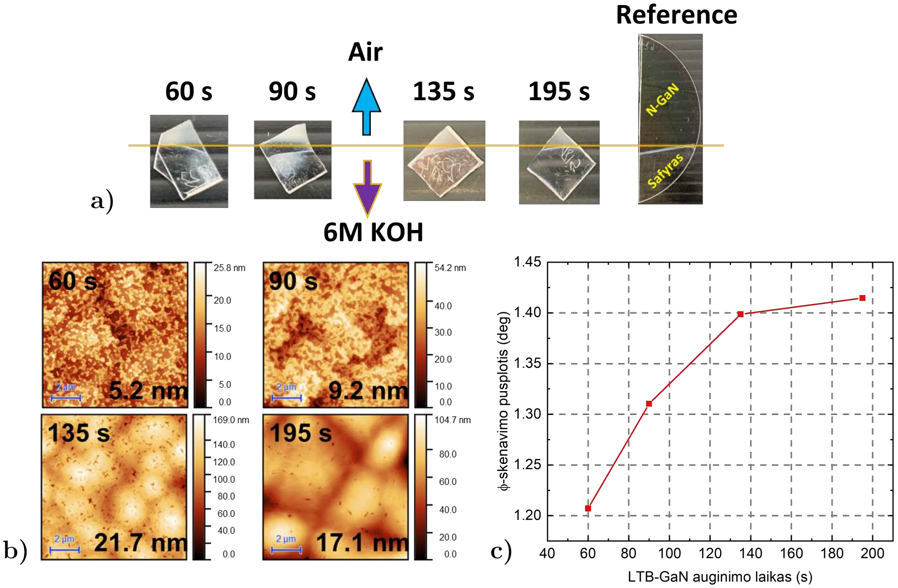

S10 pav.: (a) Bandinių optinės nuotraukos po ėsdinimo eksperimentų ir (b) atitinkami N-poliariškumo GaN paviršiaus AFM vaizdai (skaičiai nanometrais parodo paviršiaus šiurkštumo vertę (RMS, 10×10 μm)). (c) Rentgeno difrakcijos matavimų, φ-skenavimo kreivės puspločio priklausomybės nuo LTB GaN auginimo trumės, rezultatai. Kreivė (c) grafike – orientyras akims.

viršiaus nuotraukos parodė, kad ant sluoksnio paviršiaus liko neišėsdintas GaN sluoksnis, kuris, manoma, yra Ga-poliariškumo fazės fragmentai (žr. S11). Toks rezultatas reiškia, kad tam tikros 20 nm ALD-Al_2O_3 vietos buvo pernitridizuotos ir praradusios poliariškumo vertimo funkciją, todėl tose vietose užaugo Ga-poliariškumo GaN inkliuzai. Kartu buvo įrodyta, kad ALD-Al_2O_3 ant Ga-poliariškumo GaN/AlGaN struktūros, po N-poliariškumo GaN sluoksnio nuėsdinimo, sustabdo ėsdinimo procesą ir apsaugo likusius bangolaidninės struktūros sluoksnius.

Siekiant ištirti kristalografinę sluoksnių kokybę, bandiniams su skirtingu LTB-GaN storiu buvo atlikti Rentgeno difrakcijos matavimai (XRD) (žr. S10 (a)). XRD matavimas buvo atliktas plokštuminėje konfigūracijoje (in-plane), keičiant φ kampą (žr. 4.7, 4.3.1 skyrelis). Tai leido charakterizuoti tik viršutinį N-poliariškumo GaN sluoksnį. φ skenavimo rezultatai yra pateikti S10 (c) paveiksle. Pastebėta, kad N-poliariškumo GaN sluoksnio kristalinė kokybė gerėja auginant ant plonesnių LTB-GaN sluoksnių (60 s ir 90 s). Šis rezultatas patvirtina ėsdinimo rezultatų išvadą apie Ga-poliariškumo GaN inkliuzus N-poliariškumo GaN matricoje, kurie pagerina bendrą sluoksnio kristalinę kokybę.

Aukštos raiškos peršviečiančios elektroninės mikroskopijos (HRTEM) meto-

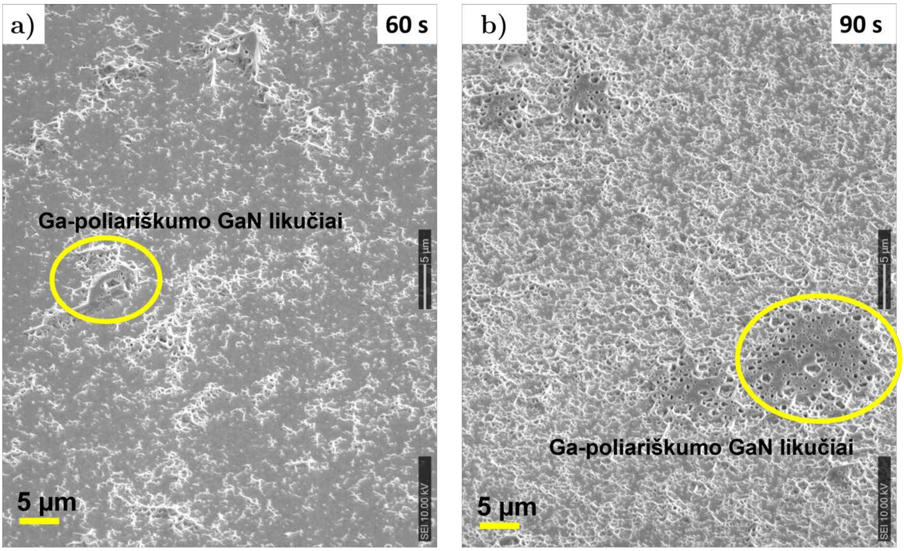

S11 pav.: Ėsdinto N-poliariškumo GaN paviršiaus baltose srityse (žr. S10 (a)) SEM nuotraukos (45° į paviršių kampu): (a) 60 s ir (b) 90 s bandiniams.

du buvo ištirta N-poliariškumo GaN/ALD-Al_2O_3/Ga-poliariškumo GaN sandūrų sritis skirtingų ALD-Al_2O_3 storių bandiniams (10 nm ir 20 nm). Rezultatai yra pateikti S12 paveiksle. Kiekvienam iš HRTEM nuotraukose pažymėtų segmentų buvo atlikta Fourier transformacijos (angl. fast Fourier transformation – FFT) analizė. 10 nm ALD-Al_2O_3 atveju, visų trijų sluoksnių FFT vaizdai nesiskiria (žr. S12 (b, c, d)). Tai reiškia, kad 10 nm ALD-Al_2O_3 sluoksnis po nitridizacijos įgavo ir atkartoja GaN kristalinę konfigūraciją. Tikėtina, kad dėl stiprios Ga bei N atomų difuzijos į 10 nm ALD-Al_2O_3 sluoksnį, pastarasis buvo pažeistas ir kristalizavosi į GaN kristalinę konfigūraciją. 20 nm atveju ALD-Al_2O_3 FFT vaizdas (žr. S12 (g)) yra skirtingas nei GaN srityse (žr. S12 (f), (h)). Tai patvirtina, kad panaudojant optimizuotą nitridizavimą 20 nm ALD-Al_2O_3 sluoksnis yra kristalizuojamas, o taip pat tinkamai paruošiamas N-poliariškumo GaN sluoksnio auginimui. Yra žinoma, kad auginant GaN sluoksnius ant safyro padėklų, GaN kristalo gardelė pasisuka 30° safyro kristalinės gardelės atžvilgiu ir taip sumažina kristalinių gardelių nesutapimą nuo 30% iki 16% [87]. Rezultate GaN ir safyro epitaksinis sąryšis statmenoje auginimo krypčiai plokštumoje yra $[11\bar{2}0]_{\mathrm{GaN}}\|[1\bar{1}00]_{\mathrm{safyras}}$, o auginimo kryptimi – $[0001]_{\mathrm{GaN}}\|[0001]_{\mathrm{safyras}}$. Toks epitaksinis sąryšis ir yra stebimas 20 nm ALD-Al_2O_3 atveju.

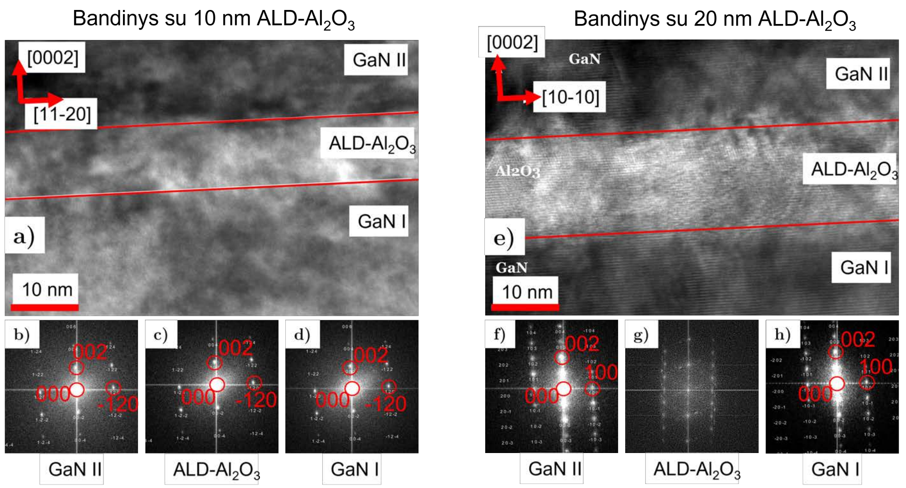

S12 pav.: GaN/ALD-Al_2O_3/GaN sandūrų HRTEM nuotraukos (a) 10 nm (e) 20 nm ALD-Al_2O_3. Skirtingų sričių FFT vaizdai: 10 nm ALD-Al_2O_3 (b), (c) (d) ir 20 nm ALD-Al_2O_3 (f), (g), (h).

InN/p-GaN sandūros formavimas taikant impulsinį MOVPE auginimo metodą bei charakterizavimas

InN, vienas iš sudėtingiausiai auginamų III grupės nitridinių puslaidininkių. Šiame darbe pasiūlytas impulsinis MOVPE auginimo metodas yra viena iš alternatyvų kokybiškam InN gauti. Metodo esmė – NH_3 srauto į reaktorių nepertraukiamas tiekimas, kai trimetilindis (TMIn) yra tiekiamas su pauzėmis. Iš visų III grupės nitridinių puslaidininkių InN auginimo temperatūra yra mažiausia (500 ÷ 600°C), o pusiausvirasis N_2 slėgis – didžiausias [23]. Dėl to reikia užtikrinti pakankamą N atomų kiekį, kad ant paviršiaus nebūtų jų trūkumo ir nesusiformuotų metalinio In lašeliai [192]. 500°C temperatūroje NH_3 skilimas nėra efektyvus, todėl yra tikimybė N trūkumui atsirasti. Keliant temperatūrą, NH_3 skilimas intensyvėja, bet InN garavimo greitis taip pat didėja. Impulsinis auginimo metodas yra atliekamas aukštesnėje temperatūroje (610°C), kai NH_3 skilimas yra efektyvus, o TMIn pauzės leidžia efektyviai padidinti V/III santykį (N kiekį). Aukštesnėse temperatūrose taip pat yra gerinama In atomų migracija ant auginamo sluoksnio paviršiaus [192, 193].

InN recepto optimizavimas buvo atliekamas auginant ant 5 μm nelegiruoto GaN sluoksnio, užauginto ant safyro padėklo. Vienas 27 s trukmės InN auginimo ciklas apėmė 7 s trukmės TMIn impulsą, bei 20 s trukmės pauzę. Optimizavus auginimo receptą, InN impulsiniu MOVPE būdu buvo užaugintas ant 600 nm p-tipo GaN/ 5 μm nelegiruoto GaN/safyro padėklo. Struktūros schematinis vaizdas yra pavaizduotas S13 (a) paveiksle. Nustatyta, kad auginant ant p-GaN InN sluoksnio kristalinė kokybė pagerėjo (žr. S13 (b)). Kristali-

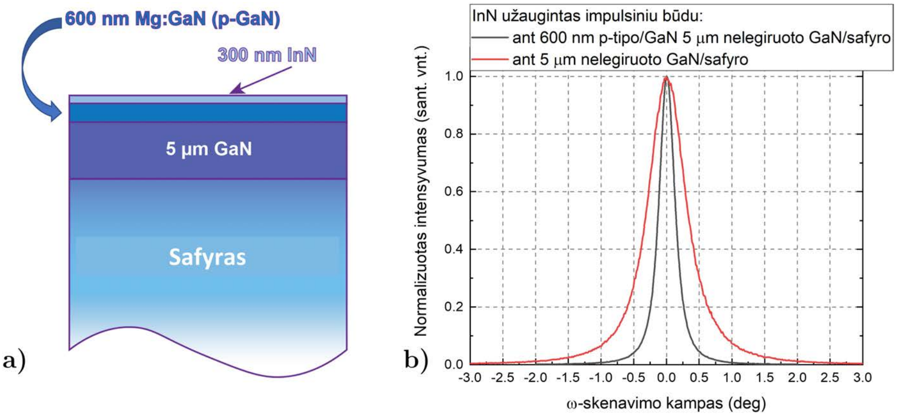

S13 pav.: (a) InN/p-GaN struktūros ant 5 μm nelegiruoto GaN/safyro padėklo schematinis vaizdas. (b) InN sluoksnių, užaugintų impulsiniu MOVPE būdu ant skirtingų GaN sluoksnių, ω-skenavimo kreivės.

nės kokybės pagerėjimą parodo XRD ω-skenavimo (XRC) smailės puspločio sumažėjimas (žr. juodą kreivę S13 (b) paveiksle). Toks kokybės pagerėjimas tikėtinas dėl geresnės InN sluoksnio adhezijos prie p-GaN sluoksnio. Dėl žemesnės auginimo temperatūros p-GaN sluoksnio paviršius yra šiurkštesnis nei nelegiruoto GaN sluoksnio. Atsiranda daugiau nukleacijos vietų nuo kurių InN sluoksnis gali pradėti savo augimą. Taip InN sluoksnio auginimo pradžioje yra suformuojamas tankiai išsidėsčiusių, vienodai orientuotų, geros kristalinės kokybės salelių masyvas [204].

Vienas InN trūkumų – didelė elektronų koncentracija kristaliniuose sluoksniuose, kas dėl Moss-Bursteino sukelto efekto didina InN draustinių energijų tarpą [177]. Šiame darbe impulsiniu MOVPE būdu ant p-GaN užaugintame InN sluoksnyje išmatuota elektronų koncentracija $5.19 \cdot 10^{18}$ cm^{-3} ir judris 980 cm^{2}V^{-1}s^{-1} yra palyginami su molekulinio pluoštelio auginimo (MBE) technologijos rezultatais [23, 25, 191, 207].

Atlikus elektronų pluoštelio indukuotos srovės (EBIC) matavimus buvo patvirtintas p-n sandūros susiformavimas. EBIC rezultatai yra pateikti S14 paveiksle. Šviesi sritis (balta) EBIC nuotraukose parodo p-n sandūros aktyviąją sritį, kurioje dėl susidarusio vidinio elektrinio lauko elektronų pluošteliu sugeneruotos elektron-skylinės poros yra efektyviai išskiriamos, taip generuojant elektros srovę. Iš S14 (d) nuotraukos galima pastebėti, kad p-n sandūra baigiasi ties nuėsdinta InN sluoksnio vieta (žr. S14 (b, d) geltona stėlė). Tai įrodo, kad p-n sandūra susiformavo tarp InN ir p-GaN, o ne tarp nelegiruoto GaN ir p-GaN sluoksnių.

Fotoeletrinio InN/p-GaN sandūros atsako išorinis kvantinis našumas (EQE) esant prijungtoms 0, -5, -10 ir -20 V įtampoms yra pateiktas S15 paveiksle. EQE buvo matuota plačiame 300 ÷ 2000 nm (4.13 ÷ 0.62 eV) spektro ruože.

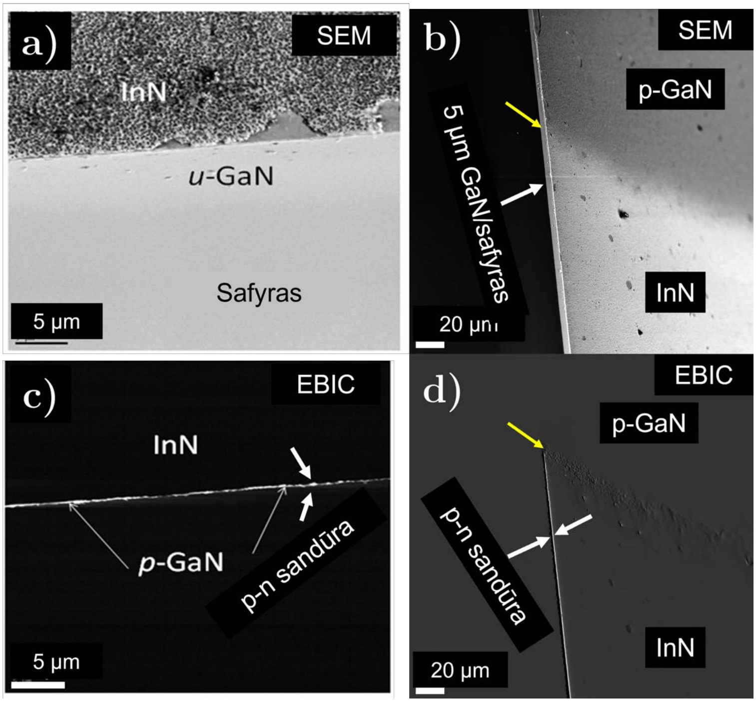

S14 pav.: InN/p-GaN n-p sandūros SEM ir atitinkamai EBIC nuotraukos: (a),(c) vaizdas iš krašto; (b),(d) vaizdas su nuėsdintu InN, atidengiant p-GaN.

Šviesos šaltinis šiame eksperimente buvo Wacom Electric Co. saulės simuliatorius, kuris generavo standartinį AM1.5G saulės spektrą su 100 mWcm^{-2} galios tankiu. Iš abiejų S15 paveiksle pavaizduotų grafikų galima išskirti penkias sritis. Pradedant nuo trumpiausių bangų ruožo, pirmas maksimumas (3.49 eV, 355 nm) (žr. S15 (a) grafiką) yra priskiriamas p-GaN sluoksnio elektronų šuoliams iš valentinės į laidumo juostą, kas atitinka GaN draustinių energijų tarpo vertę [208]. Smailė intervale 3.2 ÷ 3.26 eV (žr. S15 (a) grafiką) yra atsakas, kuris atsiranda dėl elektronų šuolių p-GaN sluoksnyje iš akceptorinių Mg būsenų, kurių jonizacijos energija yra 0.2 eV, į laidumo juostą. Kita smailė intervale 2.7 ÷ 2.9 eV (žr. S15 (a) grafiką) atspindi elektronų šuolius p-GaN sluoksnyje iš valentinės juostos arba akceptorinių Mg būsenų į gilias donorines būsenas, susiformavusias dėl neaktyvuotų Mg kompleksų p-GaN sluoksnyje [208]. Atsakas infraraudonoje srityje (žr. S15 (b) grafiką), kurio maksimumas yra arti 0.7 eV, ir atitinka elektronų šuolius iš valentinės į laidumo juostą InN. Didžiausia EQE vertė nustatyta 2.4 eV energijos fotonams. Ji yra maždaug tris kartus didesnė nei InN draustinių energijų tarpas (0.7 eV). Literatūroje dar pateikiama labai artima vertė (virš 1.7 eV, kai InN draustinių energijų tarpas 0.64 eV), ties kuria buvo stebėtas krūvininkų dauginimosi efektas 500 nm storio InN sluoksniuose, užaugintuose ant GaN [216]. Stebėtas EQE verčių viršijimas 100% neturi

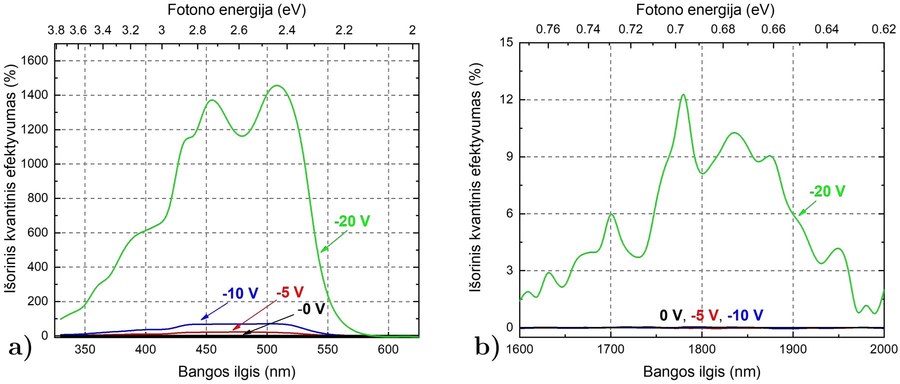

S15 pav.: InN/p-GaN n-p sandūros fotoelektrinio atsako EQE spektras (a) 300 ÷ 650 nm, (b) 1600 ÷ 2000 nm bangos ilgių intervaluose.

vienareikšmio paaiškinimo, nors ir literatūroje aptinkamos vertės viršijančios 100% EQE [212, 213].Toks efektas gali būti interpretuojamas paplatėjusia nuskurdinta sritimi, kuomet yra prijungta aukšta užtvarinė įtampa, taip pat, ir minėtu krūvininkų dauginimosi efektu.

Išvados

1. Skaičiavimo rezultatai parodė, kad dėl optinių modų dispersijos darbe modeliuotoje N-poliariškumo GaN/ALD-Al_2O_3/Ga-poliariškumo GaN/AlGaN/AlN/safyras bangolaidinėje struktūroje tik aukštesnės eilės antros harmonikos optinės modos (TM2) patenka į regimo spektro sritį. Invertuojant GaN sluoksnio poliariškumą, dėl padidėjusio pirmos ir antros harmonikų optinių modų elektrinių laukų sanklotos integralo, padidėja antros harmonikos konversijos efektyvumas.

2. Mažiausio paviršiaus šiurkštumo (< 5 nm RMS, 10×10 μm AFM) AlGaN sluoksnis, tinkamas naudoti bangolaidinėse struktūrose, gautas ant 645°C nitridizavimo ir nukleacijos temperatūroje užauginto AlN. Nitridizavimo bei nukleacijos procesai atlikti toje temperatūroje efektyviai slopina gardelių nesutapimo tarp safyro ir AlGaN sluoksnio pasėkmes.

3. GaN sluoksnio poliariškumo vertimas yra stebimas ant ALD-Al_2O_3 sluoksnių, kuriuose kristalinės gardelės konfiguracija yra skirtinga nei GaN.

4. Optimizavus 20 nm ALD-Al_2O_3 sluoksnio nitridizavimą (2400 s ir 1100°C) pavyko užauginti vienalytį N-poliariškumo GaN sluoksnį. Plonesniems, 10 ir 15 nm, ALD-Al_2O_3 sluoksniams nitridizavimo trukmę reikia trumpinti, tačiau pablogėja N-poliškumo GaN vienalytiškumas.

5. H_2 srauto bei V/III santykio (nuo 955 iki 546) mažinimas, išlaikant pastovų TMGa srautą (164 μmol/min), leido sumažinti heksagoninių piramidžių tankį N-poliariškumo GaN sluoksnio paviršiuje. Mažinant TMGa srautą nuo 164 iki 64 μmol/min ir išlaikant pastovų V/III santykį (388) N-poliariškumo GaN sluoksnio šiurkštumas buvo sumažintas iki 0.8 nm RMS (10×10 μm AFM). Mažėjant N atomų kiekiui reaktoriuje didėja Ga atomų judrumas sluoksnio paviršiuje, o sumažėjęs TMGa srautas didina Ga adatomų difuzijos nuotolį.

6. Nustatyta, kad per ilgai trunkanti nitridizacija sugadina ALD-Al_2O_3 sluoksnį, taip prarandama poliariškumo inversijos funkcija.

7. Daugiasluoksnėje N-poliariškumo GaN/ALD-Al_2O_3/Ga-poliariškumo GaN/AlGaN/AlN/safyras bangolaidinėje struktūroje panaudojant plonesnius LTB-GaN sluoksnius ant 20 nm ALD-Al_2O_3 sluoksnių pavyko užauginti santykinai mažo šiurkštumo vienalyčius N-poliškumo GaN sluoksnius. Vis tik N-poliariškumo GaN sluoksnyje neišvengta Ga-poliariškumo GaN inkliuzų, kurių atsiradimą galėjo lemti pernitridizuotos ALD-Al_2O_3 sritys bei mažų LTB-GaN salelių nesugebėjimas apaugti šių vietų.

8. Įrodyta, kad ALD-Al_2O_3 sluoksnis atlieka ėsdinimo procesą izoliuojantį/stabdantį vaidmenį, taip apsaugodamas kompleksinę ALD-Al_2O_3/Ga-poliariškumo GaN/AlGaN/AlN/safyro bangolaidinę struktūrą.

9. Palyginimui atlikus N-poliariškumo GaN auginimo eksperimentus ant 0.3° safyro padėklų, nustatyta panaši N-poliariškumo GaN auginimo dinamika, kaip ir 20 nm ALD-Al_2O_3 sluoksnio atveju, kai visa daugiasluoksnė struktūra auginta ant 0.3° safyro padėklų.

10. Išbandytas alternatyvus impulsinis MOVPE auginimo būdas leido užauginti vienos fazės (viurcito tipo) ir aukštos kokybės InN kristalinį sluoksnį, be susiformavusių In metalinių lašelių.

11. InN kristalinė kokybė buvo pagerinta auginant ant p-GaN sluoksnio. Sluoksnių kokybę patvirtino išmatuota maža elektronų koncentracija 10^{18} cm^{-3} eilės ir santykinai didelis judris – 980 $cm^2V^{-1}s^{-1}$. Šios elektrinių parametrų vertės yra palyginamos su literatūroje pateikiamomis, MBE būdu augintų InN sluoksnių vertėmis.

12. Sėkmingai buvo suformuota InN/p-GaN heterosandūra, kurios fotoelektrinio atsako išorinis kvantinis našumas 300 ÷ 600 nm ilgio bangų srityje viršijo 100%. Tokia sandūra yra perspektyvi fotovoltikos arba detektavimo taikyme. Nustatytas fotoelektrinis atsakas infraraudonoje spektro srityje su smaile ties 0.7 eV energija įrodo efektyvią savąją sugertį InN sluoksnyje.

BIBLIOGRAPHY

[1] Z. Ali, R. Ahmad, Nanotechnology for water treatment, Enviromental Nanotechnology, Vol 3 **27**, 143 – 163 (2020).

[2] P. L. Kashyap, S. Kumar, P. Jasrotia, D. P. Singh, G. P. Singh, Nanotechnology in wheat production and protection, Enviromental Nanotechnology, Vol 4 **32**, 165 – 194 (2021).

[3] D. M. Salama, M. E. Abd El-Aziz, F. A. Rizk, M. S. A. Abd Elwahed, Applications of nanotechnology on vegetable crops, Chemosphere **266** (2021).

[4] A. Alderson, Apple unveils the A14 Bionic, the world's first 5 nm chipset with 11.8 billion transistors and sizeable performance gains over the A13 bionic (2020).

[5] Y. P. Pundir, R. Saha, P. K. Pal, Effect of gate length on performance of 5nm node N-channel nano-sheet transistors for analog circuits, Semicond. Sci. Technol. **36**(015010) (2020).

[6] S. Gibney, J. M. Hicks, A. Robinson, A. Jain, P. Sanjuan-Alberte, F. J. Rawson, Toward nanobioelectronic medicine: Unlocking new applications using nanotechnology, WIREs Nanomed. Nanobiotechnol. **13**(e1693) (2021).

[7] S. Sindhwani, W. C. W. Chan, Nanotechnology for modern medicine: next step towards clinical translation (review), J. Intern. Med. **290**, 486 – 489 (2021).

[8] M. Gritan, Is photonics the new electronics?, Mater. Today **17**(3) (2014).

[9] E. F. Schubert, *Light-Emitting Diodes* (2006), 2nd edition.

[10] S. R. Bowman, C. G. Brown, M. Brindza, G. Beadie, J. K. Hite, J. A. Freitas, C. R. E. Jr., J. R. Meyer, I. Vurgaftman, Broadband measurements of the refractive indices of bulk gallium nitride, Opt. Mater. Express **4**(7), 1288 (2014).

[11] J. Pastrnak, L. Roskovcova, Refraction index measurements on aln single crystals, Phys. Stat. Sol. **14**, K5–K8 (1966).

[12] I. M. Watson, Metal organic vapour phase epitaxy of AlN, GaN, InN and their alloys: A key chemical technology for advanced device applications, Coord. Chem. Rev. **257**, 2120 – 2141 (2013).

[13] C. E. Reilly, S. Keller, S. Nakamura, S. P. DenBaars, Metalorganic chemical vapor deposition of InN quantum dots and nanostructures, Light Sci. Appl. **10**(150) (2021).

[14] M. Gromovyi, J. Brault, A. Courville, S. Rennesson, F. Semond, G. Feuillet, P. Baldi, P. Boucaud, J. Y. Duboz, M. P. de Micheli, Efficient second harmonic generation in low-loss planar GaN waveguides, Opt. Express **25**, 23035 – 23044 (2017).

[15] D. Alden, W. Guo, R. Kirste, F. Kaess, I. Bryan, T. Troha, A. Bagal, P. Reddy, L. H. Hernandez-Balderrama, A. Franke, S. Mita, C.-H. Chang, A. Hoffmann, M. Zgonik, R. Collazo, Z. Sitar, Fabrication and structural properties of AlN submicron periodic lateral polar structures and waveguides for UV-C applications, Appl. Phys. Lett. **108**(26), 261106 (2016).

[16] D. Alden, T. Troha, R. Kirste, S. Mita, Q. Guo, A. Hoffmann, M. Zgonik, R. Collazo, Z. Sitar, Quasi-phase-matched second harmonic generation of UV light using AlN waveguides, Appl. Phys. Lett. **114**, 103504 (2019).

[17] A. Chowdhury, H. M. Ng, M. Bhardwaj, N. G. Weimann, Second-harmonic generation in periodically poled GaN, Appl. Phys. Lett. **83**, 1077 (2003).

[18] W. H. P. Pernice, C. Xiong, C. Schuck, H. X. Tang, Second harmonic generation in phase matched aluminum nitride waveguides and micro-ring resonators, Appl. Phys. Lett. **100**, 223501 (2012).

[19] J. Song, J. Han, Nitrogen-polar (000-1) GaN grown on c-plane sapphire with a high-temperature AlN buffer, Materials **10**, 252 (2017).

[20] S. Keller, H. Li, M. Laurent, Y. Hu, N. Pfaff, J. Lu, D. F. Brown, N. A. Fichtenbaum, J. S. Speck, S. P. DenBaars, U. K. Mishra, Recent progress in metal-organic chemical vapor deposition of $(000\bar{1})$ N-polar group-III nitrides, Semicond. Sci. Technol. **29**, 113001 (2014).

[21] J. K. Hite, N. Y. Garces, R. Goswami, M. A. Mastro, F. J. Kub, C. R. Eddy Jr., Selective switching of GaN polarity on Ga-polar GaN using atomic layer deposited Al_2O_3, Appl. Phys. Expr. **7**, 025502 (2014).

[22] V. W. L. Chin, T. L. Tansley, T. Osotchan, Electron mobilities in gallium, indium, and aluminum nitrides, J. Appl. Phys. **75**, 7365 (1994).

[23] A. G. Bhuiyan, A. Hashimoto, A. Yamamoto, Indium nitride (InN): A review on growth, characterization, and properties, J. Appl. Phys. **94**(5), 2779 – 2808 (2003).

[24] A. Yamamoto, Y. Murakami, K. Koide, M. Adachi, A. Hashimoto, Growth temperature dependences of MOVPE InN on sapphire substrates, Phys. Stat. Sol. B **228**, 5 – 8 (2001).

[25] C. Lund, M. Catalano, L. Wang, C. Wurm, T. Mates, M. Kim, S. Nakamura, S. DenBaars, U. Mishra, S. Keller, Metal-organic chemical vapor deposition of N-polar InN quantum dots and thin films on vicinal GaN, J. Appl. Phys. **123**, 055702 (2018).

[26] G. Conibeer, S. Shrestha, S. Huang, R. Patterson, H. Xia, Y. Feng, P. Zhang, N. Gupta, M. Tayebjee, S. Smyth, Y. Liao, L. P. Wang, X. Dai, S. Chung, Hot carrier solar cell absorber prerequisites and candidate material systems, Sol. Energy Mater. Sol. Cells **135**, 124 – 129 (2015).

[27] E. Dimakis, K. Tsagaraki, E. Iliopoulos, P. Komninou, T. Kehagias, A. Delimitis, A. Georgakilas, Correlation between nucleation, morphology and residual strain of InN grown on Ga-face GaN (0001), J. Cryst. Growth **278**, 367 – 372 (2005).

[28] M. Lozac'h, Y. Nakano, L. Sang, K. Sakoda, M. Sumiya, Study of defect levels in the band gap for a thick InGaN film, Jpn. J. Appl. Phys. **51**, 121001 (2012).

[29] J. Li, J. Wang, X. Yi, Z. Liu, T. Wei, J. Yan, B. B. X. Xue, *III-Nitrides Light Emitting Diodes: Technology and Applications* (2020), 2nd edition.

[30] M. Suzuki, T. Uenoyama, A. Yanase, First-principles calculations of effective-mass parameters of AlN and GaN, Phys. Rev. B **52**, 8132 – 8139 (1995).

[31] M. Levinshtein, S. Rumyantsev, M. Shur, *Properties of Advanced Semiconductor Materials: GaN, AlN, InN, BN, SiC, SiGe* (2001).

[32] A. R. Acharya, Group III – Nitride semiconductors: Preeminent materials for modern electronic and optoelectronic applications, Himalayan Physics **5**, 22 – 26 (2015).

[33] R. Quay, *Gallium Nitride Electronics* (2008).

[34] H. Morkoç, *Handbook of Nitride Semiconductors and Devices: Materials Properties, Physics and Growth*, volume 1 (2008).

[35] S. Nakamura, S. Pearton, G. Fasol, *The Blue Laser Diode: the Complete Story*, volume 1 (2000).

[36] F. Bernardini, V. Fiorentini, D. Vanderbilt, Spontaneous polarization and piezoelectric constants of III-V nitrides, Phys. Rev. B **56** (1997).

[37] M. Leszczynski, H. Teisseyre, T. Suski, I. Grzegory, M. Bockowski, J. Jun, S. Porowski, K. Pakula, J. M. Baranowski, C. T. Foxon, T. S. Cheng, Lattice parameters of gallium nitride, Appl. Phys. Lett. **69** (1996).

[38] E. T. Yu, X. Z. Dang, P. M. Asbeck, S. S. Lau, G. J. Sullivan, Spontaneous and piezoelectric polarization effects in III–V nitride heterostructures, J. Vac. Sci. Technol. B **17**, 1742 (1999).

[39] T. Zahedi, Z. H. Firouzeh, Efficient third-harmonic generation in asymmetric $In_xGa_{1-x}N$/InN double quantum wells, J. Appl. Phys. **130**, 093104 (2021).

[40] S. R. Bowman, C. G. Brown, B. Taczak, Optical dispersion and phase matching in gallium nitride and aluminum nitride, Opt. Mater. Express **8**(4), 1091 (2018).

[41] M. Welna, R. Kudrawiec, M. Motyka, R. Kucharski, M. Zając, M. Rudziński, J. Misiewicz, R. Doradziński, R. Dwiliński, Transparency of gan substrates in the mid-infrared spectral range, Cryst. Res. Technol. **47**(3), 347 – 350 (2012).

[42] N. A. Sanford, A. V. Davydov, D. V. Tsvetkov, A. V. Dmitriev, S. Keller, U. K. Mishra, S. P. DenBaars, S. S. Park, J. Y. Han, R. J. Molnar, Measurement of second order susceptibilities of GaN and AlGaN, J. Appl. Phys. **97**, 053512 (2005).

[43] A. Majkić, A. Franke, R. Kirste, R. Schlesser, R. Collazo, Z. Sitar, M. Zgonik, Optical nonlinear and electro-optical coefficients in bulk aluminium nitride single crystals, Phys. Status Solidi B **254**, 1700077 (2017).

[44] Y. Zheng, C. Sun, B. Xiong, L. Wang, Z. Hao, J. Wang, Y. Han, H. Li, J. Yu, Y. Luo, Optical nonlinear and electro-optical coefficients in bulk aluminium nitride single crystals, Laser Photonics Rev. **16**, 2100071 (2022).

[45] D. Passeri, M. Larciprete, A. Belardini, S. Paoloni, A. Passaseo, C. Sibilia, F. Michelotti, Second harmonic generation in AlGaN, GaN and $\mathrm{Al_xGa_{1-x}N}$/GaN multiple quantum well structures, Appl. Phys. B **79**, 611 – 615 (2004).

[46] Y. Zheng, C. Sun, B. Xiong, L. Wang, Z. Hao, J. Wang, Y. Han, H. Li, J. Yu, Y. Luo, Integrated gallium nitride nonlinear photonics, Laser Photonics Rev. **16**, 2100071 (2021).

[47] N. Li, C. Ho, Z. Pei, F. Shiyang, Y. H., Y. Zhu, L. Y. T. Lee, Aluminium nitride integrated photonics: a review, Nanophotonics **10**(9), 2347 – 2387 (2021).

[48] S. Pezzagna, J. Brault, M. P. de Micheli, P. Vennegues, A. D. Wieck, J. Massies, GaN, a new material for integrated nonlinear optics, Proc. ECIO 25 – 27 (2007).

[49] R. W. Boyd, *Nonlinear Optics* (2007), 3rd edition.

[50] J. A. Armstrong, N. Bloembergen, J. Ducuing, P. S. Pershan, Interactions between light waves in a nonlinear dielectric, Phys. Rev. **127**, 1918 – 1939 (1962).

[51] P. N. Butcher, D. Cotter, *The Elements of Nonlinear Optics.* (1990).

[52] F. Träger, *Springer Handbook of Lasers and Optics* (2012).

[53] R. G. Hunsperger, *Integrated Optics: Theory and Technology* (2009), 6th edition.

[54] R. Dändliker, The concept of modes in optics and photonics, Education and Training in Optics and Photonics Conference (2021).

[55] A. Yariv, Coupled-mode theory for guided-wave optics, IEEE J. Quantum Electron. **9**, 919 – 933 (1973).

[56] T. Troha, M. Rigler, D. Alden, I. Bryan, W. Guo, R. Kirste, S. Mita, M. D. Gerhold, R. Collazo, Z. Sitar, M. Zgonik, UV second harmonic generation in AlN waveguides with modal phase matching, Opt. Mater. Express **6**, 2014 – 2023 (2016).

[57] D. N. Hahn, G. T. Kiehne, J. B. Ketterson, G. K. L. Wong, P. Kung, A. Saxler, M. Razeghi, Phase-matched optical second-harmonic generation in GaN and AlN slab waveguides, J. Appl. Phys. **85**, 2497 – 2501 (1999).

[58] H. Chen, H. Fu, X. Huang, X. Zhang, T. H. Yang, J. A. Montes, I. Baranowski, Y. Zhao, Low loss GaN waveguides at the visible spectral wavelengths for integrated photonics applications, Opt. Express **25**(25), 31758–31773 (2017).

[59] A. Stolz, E. Cho, E. Dogheche, Y. Androussi, D. Troadec, D. Pavlidis, D. Decoster, Optical waveguide loss minimized into gallium nitride based structures grown by metal organic vapor phase epitaxy, Appl. Phys. Lett. **98**(16), 161903 (2011).

[60] X. Guo, C. L. Zou, H. X. Tang, Second-harmonic generation in aluminum nitride microrings with 2500%/W conversion efficiency, Optica **3**, 1126 – 1131 (2016).

[61] A. W. Bruch, X. Liu, X. Guo, J. B. Surya, Z. Gong, L. Zhang, J. Wang, J. Yan, H. X. Tang, Second-harmonic generation in aluminum nitride microrings with 2500%/W conversion efficiency, Appl. Phys. Lett. **113**(13), 131102 (2018).

[62] M. Fejer, G. Magel, D. Jundt, R. Byer, Quasi-phase-matched second harmonic generation: tuning and tolerances, IEEE J. Quantum Electron. **28**(11), 2631 – 2654 (1992).

[63] D. S. Hum, M. M. Fejer, Quasi-phasematching, C. R. Phys. **8**, 180 – 198 (1992).

[64] J. Hite, Progress in periodically oriented III-nitride materials, J. Cryst. Growth **456**, 133 – 136 (2016).

[65] M. Daulelsberg, C. Martin, H. Protzmann, A. R. Boyd, E. J. Thrush, J. Käppeler, M. Heuken, T. R. A., E. V. Yakovlev, A. V. Kondratyev, Modeling and process design of III-nitride MOVPE at near-atmospheric pressure in close coupled showerhead and planetary reactors, J. Cryst. Growth **298**, 418 – 424 (2007).

[66] Aixtron, AIXTRON to support LED and Laser Reasearch at Peking University, `https://www.aixtron.com/en/press/press-releases/AIXTRON%20to%20support%20LED%20and%20Laser%20Research%20at%20Peking%20University_n437` (2013).

[67] K. Sato, Y. Furukawa, K. Nakajima, *Advances in Crystal Growth Research* (2001).

[68] L. Royer, Recherches expérimentales sur l'épitaxie ou orientation mutuelle de cristaux d'espèces differentes, Bull. Soc. franç. Minér. Crist. **51**, 7 –159 (1928).

[69] K. Seshan, *Handbook of Thin Film Deposition Processes and Techniques: Principles, Methods, Equipment and Applications, Second Edition* (2002).

[70] J. Haigh, S. O'Brien, The mechanism of the growth of InP by MOCVD: A flow-tube investigation of the pyrolysis of the indium precursor, J. Cryst. Growth **68**, 550 (1984).

[71] M. Yoshida, H. Watanabe, F. Uesugi, Mass spectrometric study of $Ga(CH_3)_3$ and $Ga(C_2H_5)_3$ decomposition reaction in H_2 and N_2, J. Electrochem. Soc. **132**, 677 (1985).

[72] R. Karlicek, J. A. Long, V. M. Donnelly, Thermal decomposition of metalorganic compounds used in the MOCVD of InP, J. Cryst. Growth **68**, 123 (1984).

[73] J.-H. Park, T. S. Sdarshan, *Cehimcal Vapor Deposition* (2001).

[74] G. B. Stringfellow, *Organometallic Vapor-Phase Epitaxy: Theory and Practice* (1999), 2nd edition.

[75] S. Kasap, P. Capper, *Springer Handbook of Electronic and Photonic Materials* (2017), 2nd edition.

[76] A. C. Jones, M. C. Hitchman, *Chemical Vapour Deposition Precursors, Processes and Applications* (2009).

[77] A. Trampert, O. Brandt, K. H. Ploog, X-ray thin-film measurement techniques: in-plane diffraction measurements, Semicond. Semimet. **50**, 167 – 192 (1997).

[78] H. Amano, N. Sawaki, I. Akasaki, Metalorganic vapor phase epitaxial growth of a high quality GaN film using an AlN buffer layer, Appl. Phys. Lett. **48**, 353 (1986).

[79] I. Akasaki, H. Amano, Y. Koide, K. Hiramatsu, N. Sawaki, Effects of ain buffer layer on crystallographic structure and on electrical and optical properties of GaN and $Ga_{1\text{-}x}Al_xN (0 < x \leqq 0.4)$ films grown on sapphire substrate by MOVPE, J. Cryst. Growth **98**, 209 – 219 (1989).

[80] S. Nakamura, GaN growth using GaN buffer layer, Jpn. J. Appl. Phys. **30**, 1705 – 1707 (1991).

[81] S. Keller, B. P. Keller, Y. Wu, B. Heying, D. Kapolnek, J. S. Speck, U. K. Mishra, S. P. DenBaars, Influence of sapphire nitridation on properties of gallium nitride grown by metalorganic chemical vapor deposition, Appl. Phys. Lett. **68**, 1525 – 1527 (1996).

[82] K. Uchida, A. Watanabe, F. Yano, M. Kouguchi, T. Tanaka, S. Minagawa, Nitridation process of sapphire substrate surface and its effect on the growth of GaN, J. Appl. Phys. **79**, 3487 – 3491 (1996).

[83] N. Grandjean, J. Massies, M. Leroux, Nitridation of sapphire. Effect on the optical properties of GaN epitaxial overlayers, Appl. Phys. Lett. **69**, 2071 – 2073 (1996).

[84] K. Lawniczak-Jablonska, Z. R. Zytkiewicz, S. Gieraltowska, M. Sobanska, P. Kuzmiuk, K. Klosek, Chemical bonding of nitrogen formed by nitridation of crystalline and amorphous aluminum oxide studied by X-ray photoelectron spectroscop, RSC Adv. **10**, 27932 – 27939 (2020).

[85] S. Mohn, N. Stolyarchuk, T. Markurt, R. Kirste, M. P. Hoffmann, R. Collazo, A. Courville, R. Di Felice, Z. Sitar, P. Vennéguès, M. Albrecht, Polarity control in group-iii nitrides beyond pragmatism, Phys. Rev. Appl. **5**, 054004 (2016).

[86] N. Stolyarchuk, T. Markurt, A. Courville, K. March, O. Tottereau, P. Vennéguès, M. Albrecht, Impact of sapphire nitridation on formation of Al-polar inversion domains in N-polar AlN epitaxial layers, J. Appl. Phys. **122**, 155303 (2017).

[87] N. Grandjean, Y. Massies, J. Martinez, P. Vennéguès, M. Leroux, M. Laugt, GaN epitaxial growth on sapphire (0001): the role of the substrate nitridation, J. Cryst. Growth **178**, 220 – 228 (1997).

[88] T. D. Moustakas, The role of extended defects on the performance of optoelectronic devices in nitride semiconductors, Phys. Status Solidi A **210**, 169 – 174 (2013).

[89] S. Keller, N. A. Fichtenbaum, F. Wu, D. Brown, A. Rosales, S. P. DenBaars, J. S. Speck, U. K. Mishra, Influence of the substrate misorientation on the properties of N-polar GaN films grown by metal organic chemical vapor deposition, J. Appl. Phys. **102**, 083546 (2007).

[90] T. Zywietz, J. Neugebauer, M. Scheffler, Adatom diffusion at GaN (0001) and $(000\bar{1})$ surfaces, Appl. Phys. Lett. **73**(4) (1998).

[91] S. A. Kukushkin, V. N. Bessolov, A. V. Osipov, A. V. Luk'yanov, Mechanism and kinetics of early growth stages of a GaN film, Phys. Solid State **44**(7), 1399 – 1405 (1998).

[92] Q. Sun, Y. S. Cho, I. H. Lee, J. Han, K. B. H., H. Cho, Nitrogen-polar GaN growth evolution on c-plane sapphire, Appl. Phys. Lett. **93**, 131912 (2008).

[93] M. Sumiya, K. Yoshimura, T. Ito, K. Ohtsuka, S. Fuke, K. Mizuno, M. Yoshimoto, H. Koinuma, A. Ohtomo, M. Kawasaki, Growth mode and surface morphology of a GaN film deposited along the n-face polar direction on c-plane sapphire substrate, J. Appl. Phys. **88**, 1158 – 1165 (2000).

[94] J. T. Zettler, K. Haberland, M. Zorn, M. Pristovsek, W. Richter, P. Kurpas, M. Weyers, Real-time monitoring of MOVPE device growth by reflectance anisotropy spectroscopy and related optical techniques, J. Cryst. Growth **195**, 151 – 161 (1998).

[95] K. Haberland, *Optical in-situ Studies during MOVPE with respect to III-V device production*, PhD thesis (2002).

[96] N. E. Kaluza, *MOVPE Growth and Characterization of* $Al_xGa_{1-x}N/GaN$ *Heterostructures for HEMT Application*, PhD thesis (2003).

[97] H. Lüth, *Surfaces and Interfaces of Solid Materials* (1995), 3rd edition.

[98] G. Binning, C. F. Quante, C. Gerber, Atomic force microscope, Phys. Rev. Lett. **56**(9) (1998).

[99] G. Wielgoszewski, `https://commons.wikimedia.org/wiki/File:AFM_schematic_(EN).svg`.

[100] Q. Zhong, D. Inniss, K. Kjoller, V. B. Elings, Fractured polymer/ silica fiber surface studied by tapping mode atomic force microscopy, Surf. Sci. **290**, L688 – L692 (1993).

[101] A. A. Bunaciu, E. G. Udrişţioiu, H. Y. Aboul-Enein, X-ray diffraction: Instrumentation and applications, Crit. Rev. Anal. Chem. **45**(4), 289 – 299 (2015).

[102] T. Mitsunaga, X-ray thin-film measurement techniques: out-of-plane diffraction measurements, The Rigaku Journal **25**(1) (2009).

[103] S. Kobayashi, X-ray thin-film measurement techniques: in-plane diffraction measurements, The Rigaku Journal **26**(1) (2010).

[104] P. Batson, N. Dellby, O. Krivanek, Sub-ångstrom resolution using aberration corrected electron optics, Nature **418**, 617 – 620 (2002).

[105] M. Haider, P. Hartel, H. Muller, S. Uhlemann, J. Zach, Information transfer in a TEM corrected for spherical and chromatic aberration, Micron **43**, 504 – 508 (2012).

[106] D. J. Smith, Progress and problems for atomic-resolution electron microscopy, Micron **43**, 504 – 508 (2012).

[107] S. Sadamatsu, M. Tanaka, K. Higashida, S. Matsumura, Transmission electron microscopy of bulk specimens over 10μm in thickness, Ultramicroscopy **162**, 10 – 16 (2016).

[108] B. Flutz, J. M. Howe, *Transmission Electron Microscopy and Diffractometry of Materials* (2008), 3rd edition.

[109] J. I. Hanoka, R. O. Bell, Electron-beam induced currents in semiconductors, Ann. Rev. Mater. Sci. **11**, 353 – 380 (1981).

[110] A. Roshko, M. D. Brubaker, P. T. Blanchard, K. A. Bertness, T. E. Harvey, R. H. Geiss, I. Levin, Comparison of convergent beam electron diffraction and annular bright field atomic imaging for GaN polarity determination, J. Mater. Res. **32** (2017).

[111] C. Wurm, E. Ahmadi, F. Wu, N. Hatui, S. Keller, J. Speck, U. Mishra, Growth of high-quality N-polar GaN on bulk GaN by plasma-assisted molecular beam epitaxy, Solid State Commun. **305**, 113763 (2020).

[112] K. Xu, N. Yano, A. W. Jia, A. Yoshikawa, K. Takahashi, Kinetic process of polarity selection in GaN growth by RF-MBE, Phys. Stat. Sol. (b) **228**(2), 523 – 527 (2001).

[113] B. J. Rodriguez, A. Gruverman, A. I. Kingon, R. J. Nemanich, O. Ambacher, Piezoresponse force microscopy for polarity imaging of GaN, Appl. Phys. Lett. **80**(22), 4166 – 4168 (2002).

[114] A. Pandey, B. S. Yadav, D. V. S. Rao, D. Kaur, A. K. Kapoor, Dislocation density investigation on mocvd-grown gan epitaxial layers using wet and dry defect selective etching, Appl. Phys. A **122**(614) (2016).

[115] Y. P. Hong, J. H. Park, C. W. Park, H. M. Kim, D. K. Oh, B. G. Choi, S. K. Lee, K. B. Shim, Investigation of defects and surface polarity in AlN and GaN using wet chemical etching technique, J. Korean Cryst. Growth Cryst. Technol. **24**(5) (2014).

[116] D. Li, M. Sumiya, S. Fuke, Y. D., D. Que, Y. Suzuki, Y. Fukuda, Selective etching of GaN polar surface in potassium hydroxide solution studied by x-ray photoelectron spectroscopy, J. Appl. Phys. **90**(8) (2001).

[117] W. Ananda, External quantum efficiency measurement of solar cell, 15th International Conference on Quality in Research (QiR): International Symposium on Electrical and Computer Engineering. (2017).

[118] W. Yang, Z. Ma, X. Tang, C. Feng, W. Zhao, P. Shi, Internal quantum efficiency for solar cells, Sol. Energy **82**, 106 – 110 (2008).

[119] M. Rigler, T. Troha, W. Guo, R. Kirste, I. Bryan, R. Collazo, Z. Sitar, M. Zgonik, Second-harmonic generation of blue light in GaN waveguides, Appl. Sci. **8**, 1218 (2018).

[120] Y. Zhou, D. Wang, R. Chu, C.-W. Tang, Y. Qi, Z. Lu, K. J. Chen, K. M. Lau, Correlation of in-situ reflectance spectra and resistivity of gan/al$_2$o$_3$ interfacial epilayer in metalorganic chemical vapor deposition, J. Electron. Mater. **34**(1), 112–118 (2005).

[121] S. Keller, S. P. DenBaars, Metalorganic chemical vapor deposition of group III nitrides - a discussion of critical issues, J. Cryst. Growth **248**, 479–486 (2003).

[122] B. L. Liu, M. Lachab, A. Jia, A. Yoshikawaa, K. Takahashi, MOCVD growth of device-quality GaN on sapphire using a three-step approach., J. Cryst. Growth **234**, 637–645 (2002).

[123] J. Wang, F. Xu, C. He, L. Zhang, L. Lu, X. Wang, Z. Qin, B. Shen, High quality AlN epilayers grown on nitrided sapphire by metal organic chemical vapor deposition, Sci. Rep. **7**, 42747 (2017).

[124] X.-H. Li, S. Wang, H. Xie, Y. O. Wei, T.-T. Kao, M. M. Satter, S.-C. Shen, P. D. Yoder, T. Detchprohm, R. D. Dupuis, A. M. Fischer, F. A. Ponce, Growth of high-quality AlN epilayers on sapphire substrates at relatively low temperatures by metalorganic chemical vapor deposition, Phys. Stat. Sol. (B) **252**(5), 1089–1095 (2015).

[125] T. Asai, K. Nonaka, K. Ban, K. Nagata, K. Nagamatsu, M. Iwaya, S. Kamiyama, H. Amano, I. Akasaki, Growth of low-dislocation-density AlGaN using Mg-doped AlN underlying layer, phys. stat. sol. (c) **7**(7-8), 2101–2103 (2010).

[126] J. Hakamata, Y. Kawase, L. Dong, S. Iwayama, M. Iwaya, T. Takeuchi, S. Kamiyama, H. Miyake, I. Akasaki, Growth of high-quality AlN and AlGaN films on sputtered AlN/sapphire templates via high-temperature annealing, phys. stat. sol. (b) **255**, 1700506 (2018).

[127] L. T. Tan, P. Chen, S. J. Chua, Impact of V/III flux ratio and Si-doping concentration on GaN grown by metalorganic chemical-vapor deposition on sapphire substrate, ICONIP '02. Proceedings of the 9th International Conference on Neural Information Processing. Computational Intelligence for the E-Age (IEEE Cat. No.02EX575) 172 – 176 (2002).

[128] S. Pezzagna, P. Vennéguès, N. Grandjean, J. Massies, Polarity inversion of GaN(0 0 0 1) by a high Mg doping, J. Cryst. Growth **269**, 249 – 256 (2004).

[129] V. Ramachandran, R. M. Feenstra, W. L. Sarney, L. Salamanca-Riba, J. E. Northrup, L. T. Romano, D. W. Greve, Inversion of wurtzite GaN(0001) by exposure to magnesium, Appl. Phys. Lett. **75**, 808 (1999).

[130] M. H. Wong, F. Wu, J. S. Speck, U. K. Mishra, Polarity inversion of N-face GaN using an aluminum oxide interlayer, J. Appl. Phys. **108**, 123710 (2010).

[131] J. Hite, M. Twigg, M. Mastro, C. J. Eddy, F. Kub, Initiating polarity inversion in GaN growth using an AlN interlayer, Phys. Status Solidi A **208**, 1504 – 1506 (2011).

[132] N. Stolyarchuk, T. Markurt, A. Courville, K. March, J. Zúñiga Pérez, P. Vennegues, M. Albrecht, Intentional polarity conversion of AlN epitaxial layers by oxygen, Sci. Rep. **8**, 14111 (2018).

[133] M. Takeuchi, H. Shimizu, R. Kajitani, K. Kawasaki, T. Kinoshita, K. Takada, H. Murakami, Y. Kumagai, A. Koukitu, T. Koyama, S. Chichibu, Y. Aoyagi, Al- and N-polar AlN layers grown on c-plane sapphire substrates by modified flow-modulation MOCVD, J. Cryst. Growth **305**(2), 360 – 365 (2007).

[134] T. Isono, T. Ito, R. Sakamoto, Y. Yao, Y. Ishikawa, N. Okada, K. Tadatomo, Growth of N-polar aluminum nitride on vicinal sapphire substrates and aluminum nitride bulk substrates, Phys. Status Solidi B **257**, 1900588 (2020).

[135] J. Lemettinen, H. Okumura, T. Palacios, S. Suihkonen, Growth of N-polar aluminum nitride on vicinal sapphire substrates and aluminum nitride bulk substrates, Appl. Phys. Express **11**, 101002 (2018).

[136] C. Li, H. Wang, H. Liu, S. J. Chua, Structural and strain anisotropies of N-polar GaN epilayers on offcut sapphire substrates, J. Vac. Sci. Technol. A **34**, 051501 (2016).

[137] C. Li, K. Zhang, Q. Z., X. Yin, X. Ge, J. Wang, Q. Wang, C. He, W. Zhao, Z. Chen, High quality N-polar GaN films grown with varied V/III ratios by metal–organic vapor phase epitaxy, RSC Adv. **10**, 43187 – 43192 (2020).

[138] X. R. Huang, J. Bai, M. Dudley, B. Wagner, R. F. Davis, Y. Zhu, Step-controlled strain relaxation in the vicinal surface epitaxy of nitrides, Phys. Rev. Lett. **95**, 086101 (2005).

[139] K. Kuze, N. Osumi, Y. Fujita, Y. Inoue, T. Nakano, Analysis of interface formation mechanism in GaN double-polarity selective-area growth by metalorganic vapor phase epitaxyn, Jpn. J. Appl. Phys. **55**, 05FA05 (2016).

[140] J. Zúñiga Pérez, V. Consonni, L. Lymperakis, X. Kong, A. Trampert, S. Fernández-Garrido, O. Brandt, H. Renevier, S. Keller, K. Hestroffer, M. R. Wagner, J. S. Reparaz, F. Akyol, S. Rajan, S. Rennesson, T. Palacios, G. Feuillet, Polarity in GaN and ZnO: Theory, measurement, growth, and devices, Appl. Phys. Rev. **3**, 041303 (2016).

[141] J. Yoo, K. Shojiki, T. Tanikawa, S. Kuboya, T. Hanada, R. Katayama, T. Matsuoka, Polarity control of GaN grown on pulsed-laser-deposited AlN/GaN template by metalorganic vapor phase epitaxy, Jpn. J. Appl. Phys. **55**, 05FA04 (2016).

[142] G. Deng, Y. Zhang, Y. Yu, L. Yan, P. Li, X. Han, L. Chen, D. Zhao, G. Du, Significantly improved surface morphology of N-polar GaN film grown on SiC substrate by the optimization of V/III ratio, Appl. Phys. Lett. **112**, 151607 (2018).

[143] Q. Sun, Y. S. Cho, B. H. Kong, H. K. Cho, T. S. Ko, C. D. Yerino, I.-H. Lee, J. Han, N-face GaN growth on c-plane sapphire by metalorganic chemical vapor deposition, J. Cryst. Growth **311**, 2948–2952 (2009).

[144] B. Miljević, *Characterization of growth and real structure of nitride based semiconductor devices by use of synchrotron radiation*, PhD thesis (2012).

[145] Y.-H. Yeh, K.-M. Chen, Y.-H. Wu, Y.-C. Hsu, W.-I. Lee, Hydrogen etching on the surface of gan for producing patterned structures, J. Cryst. Growth **314**, 9 – 12 (2011).

[146] S. Faraji, E. Meissner, R. Weingärtner, S. Besendörfer, J. Friedrich, In-Situ preparation of GaN sacrificial layers on sapphire substrate in MOVPE reactor for self-separation of the overgrown GaN crystal, Crystals **10**(12) (2020).

[147] P.-M. Coulon, P. Feng, B. Damilano, S. Vézian, T. Wang, P. A. Shields, Influence of the reactor environment on the selective area thermal etching of GaN nanohole arrays, Sci. Rep. **10**, 5642 (2020).

[148] Y. Y. Lai, S. C. Hsu, H. S. Chang, Y. S. W, C. H. Chen, L. Y. Chen, Y. J. Cheng, The study of wet etching on Gan surface by potassium hydroxide solution, Res. Chem. Intermed. **43**, 3563–3572 (2017).

[149] W. Guo, R. Kriste, KOH based selective wet chemical etching of AlN, $\mathrm{Al_xGa_{1\text{-}x}N}$ crystals: A way towards substrate removal in deep ultraviolet-light emitting diode, Appl. Phys. Lett. **106**(082110) (2015).

[150] T. Fujii, Y. Gao, R. Sharma, E. L. Hu, S. P. DenBaars, S. Nakamura, Increase in the extraction efficiency of gan-based light-emitting diodes via surface roughnening, Appl. Phys. Lett. **84**(6) (2004).

[151] M. Tautz, M. T. Kuchenbrod, J. Hertkorn, R. Weinberger, M. Welzel, A. Pfitzner, D. D. Diaz, Influence of the epitaxial composition on N-face GaN KoH etch kinetics determined by ICP-OES, Beilstein J. Nanotechnol. **11**, 41 – 50 (2020).

[152] M. Tautz, A. Weimar, C. Graßl, M. Welzel, D. D. Diaz, Anisotropy and mechanistic elucidation of wet-chemical gallium nitride etching at the atomic level, Phys. Status Solidi A **1217**, 2000221 (2020).

[153] M. Bickermann, S. Schmidt, B. M. Epelbaum, P. Heimann, S. Nagata, A. Winnacker, Wet KOH etching of freestanding AlN single crystals, J. Cryst. Growth **300**, 299–307 (2007).

[154] V. S. Harutyunyan, A. P. Aivazyan, E. R. Weber, Y. Kim, Y. Park, S. G. Subramanya, High-resolution x-ray diffraction strain-stress analysis of GaN/sapphire heterostructures, J. Phys. D: Appl. Phys. **34**(A35 – A39) (2001).

[155] P. Hacke, T. Detchprohm, K. Hiramatsu, N. Sawaki, Schottky barrier on n-type GaN grown by hydride vapor phase epitaxy, Appl. Phys. Lett. **63**(19), 2676 (1993).

[156] T. Zywietz, J. Neugebauer, M. Scheffler, The adsorption of oxygen at gan surfaces, Appl. Phys. Lett. **74**, 1695 – 1697 (1999).

[157] M. Sumiya, K. Yoshimura, K. Ohtsuka, S. Fuke, Dependence of impurity incorporation on the polar direction of GaN film growth, Appl. Phys. Lett. **76**(15), 2098 – 2100 (2000).

[158] C. G. Van de Walle, C. Stampfl, J. Neugebauer, Theory of doping and defects in III—V nitrides, J. Cryst. Growth **189/190**, 505 – 510 (1998).

[159] R. Korotkov, B. Wessels, Electrical properties of oxygen doped GaN grown by metalorganic vapor phase epitaxy, MRS Internet J. Nitride Semicond. Res. **5**, 301 – 307 (2000).

[160] R. Kriste, R. Collazo, G. Callsen, M. R. WAgner, T. Kure, R. J.S., S. Mita, J. Xie, A. Rice, J. Tweedie, Z. Sitar, A. Hoffmann, Temperature dependent photoluminescence of lateral polarity junctions of metal organic chemical vapor deposition grown GaN, Appl. Phys. Lett. **110**(093503) (2011).

[161] X. Houqiang, J. Jiang, Y. Dai, M. Cui, K. Li, X. Ge, J. Hoo, L. Yan, J. Guo, S. Ning, H. Sun, B. Sarkar, W. Guo, J. Ye, Polarity control and nanoscale optical characterization of AlGaN-based multiple-quantum-wells for ultraviolet C emitters, ACS Appl. Nano Mater. **3**(6), 5335 – 5342 (2020).

[162] Y. Kanagawa, T. Akiyama, T. Ito, K. Shiraishi, T. Nakayama, Surface stability and growth kinetics of compound semiconductors: An ab initio-based approach, Materials **6**, 3309 – 3360 (2013).

[163] A. R. Smith, R. M. Feenstra, D. W. Greve, M. S. Shin, M. Skowronski, J. Neugebauer, J. E. Nothrup, Reconstructions of GaN(0001) and $(000\overline{1})$ surfaces: Ga-rich metallic structures, J. Vac. Sci. Technol. B **16**, 2242 (1998).

[164] X. Q. Shen, T. Ide, S. H. Cho, M. Shimizu, S. Hara, H. Okumura, Stability of N- and Ga-polarity GaN surfaces during the growth interruption studied by reflection high-energy electron diffraction, Appl. Phys. Lett. **77**, 4013 (2000).

[165] J. Wu, When group-III nitrides go infrared: New properties and perspectives, J. Appl. Phys. **106**(011101) (2009).

[166] V. Davydov, A. Klochikhin, R. Seisyan, V. Emtsev, S. Ivanov, F. Bechstedt, J. Furthmüller, H. Harima, A. Mudryi, J. Aderhold, O. Semchinova, J. Graul, Absorption and emission of hexagonal InN. evidence of narrow fundamental band gap, Phys. Stat. Sol. B **229**(r1 – r3) (2002).

[167] T. Matsuoka, H. Okamoto, M. Nakao, Growth of wurtzite InN using MOVPE and its optical characteristics, Phys. Stat. Sol. C **0**, 2806 – 2809 (2003).

[168] O. Briot, B. Maleyre, S. Clur-Ruffenach, B. Gil, C. Pinquier, F. Demangeot, J. Frandon, The value of the direct bandgap of InN: a re-examination, Phys. Stat. Sol. C **1**, 1425 – 1428 (2004).

[169] X. H. Ji, S. P. Lau, H. Y. Yang, Q. Y. Zhang, Structural and optical properties of wurtzite InN grown on Si(111), Thin Solid Films **515**, 4619 – 4623 (2007).

[170] M. Yoshimoto, Y. Yamamoto, J. Saraie, Fabrication of InN/Si heterojunctions with rectifying characteristics, Phys. Stat. Sol. C **0**, 2794 – 2797 (2003).

[171] D. Alexandrov, K. S. A. Butcher, M. Wintrebert-Fouquet, Absorption and photoluminescence features caused by defects in InN, J. Cryst. Growth **269**, 77 – 86 (2004).

[172] X. Xu, P. Specht, R. Armitage, J. C. Ho, E. R. Weber, C. Kisielowski, Characterization of oxide precipitates in epitaxial InN by transmission electron microscopy, Appl. Phys. Lett. **87**(9), 092102 (2005).

[173] K. S. A. Butcher, T. L. Tansley, InN, latest development and a review of the band-gap controversy, Superlattices Microstruct. **38**, 1 – 37 (2005).

[174] C. Stampfl, C. G. Van de Walle, D. Vogel, P. Krüger, J. Pollmann, Native defects and impurities in InN: First-principles studies using the local-density approximation and self-interaction and relaxation-corrected pseudopotentials, Phys. Rev. B **61**, R7846 – R7849 (2000).

[175] S. Zhao, B. H. Le, D. P. Liu, X. D. Liu, M. G. Kibria, T. Szkopek, H. Guo, Z. Mi, p-type InN nanowires, Nano Lett. **13**(11), 5509 – 5513 (2013).

[176] M. A. Mayer, S. Choi, O. Bierwagen, H. M. Smith, E. E. Haller, J. S. Speck, W. Walukiewicz, Electrical and optical properties of p-type InN, J. Appl. Phys. **110**(12), 123707 (2011).

[177] K. S. A. Butcher, H. Hirshy, P. R. M., M. Wintrebert-Fouquet, P. P.-T. Chen, Stoichiometry effects and the Moss–Burstein effect for InN, Phys. Stat. Sol. A **203**, 66 – 74 (2006).

[178] W. Walukiewicz, S. Li, J. Wu, K. Yu, J. Ager, H. E.E., H. Lu, W. J. Schaff, Optical properties and electronic structure of InN and In-rich group III-nitride alloys, J. Appl. Phys. **269**, 119 – 127 (2004).

[179] V. Cimalla, C. Förster, G. Kittler, I. Cimalla, R. Kosiba, G. Ecke, O. Ambacher, R. Goldhahn, S. Shokhovets, A. Georgakilas, H. Lu, W. Schaff, Correlation between strain, optical and electrical properties of InN grown by MBE, Phys. Stat. Sol. C **0**, 2818 – 2821 (2003).

[180] K. S. A. Butcher, A. J. Fernandes, P. P.-T. Chen, M. Wintrebert-Fouquet, H. Timmers, S. K. Shrestha, H. Hirshy, R. M. Perks, B. F. Usher, The nature of nitrogen related point defects in common forms of InN, J. Appl. Phys. **101**(12), 123702 (2007).

[181] H. Timmers, S. K. Shresth, A. P. Byrne, The potential of ion beam techniques for the development of indium nitride, J. Cryst. Growth **269**, 50 – 58 (2004).

[182] P. Specht, R. Armitage, J. Ho, E. Gunawan, Q. Yang, X. Xu, C. Kisielowski, E. Weber, The influence of structural properties on conductivity and luminescence of MBE grown InN, J. Cryst. Growth **269**, 111 – 118 (2004).

[183] O. Ambacher, M. S. Brandt, R. Dimitrov, T. Metzger, M. Stutzmann, R. A. Fischer, A. Miehr, A. Bergmaier, G. Dollinger, Thermal stability and desorption of group III nitrides prepared by metal organic chemical vapor deposition, J. Vac. Sci. Technol. B **14**(6), 3532 – 3542 (1996).

[184] A. Koukitu, N. Takahashi, H. Seki, Thermodynamic study on metalorganic vapor-phase epitaxial growth of group III nitrides, Jpn. J. Appl. Phys. **36**, L1136 (1997).

[185] A. Koukitu, T. Taki, N. Takahashi, H. Seki, Thermodynamic study on the role of hydrogen during the MOVPE growth of group III nitrides, J. Cryst. Growth **197**, 99 – 105 (1999).

[186] S. Keller, I. Ben-yaacov, S. P. Denvers, M. U. K., Proceedings of the International Workshop on Nitride Semiconductors (IWN 2000), Nagoya, Japan, 2000. 09. 24 – 27. p233 (2000).

[187] M. Adachi, Y. Murakami, A. Hashimoto, A. Yamamoto, Proceedings of the International Workshop on Nitride Semiconductors (IWN 2000), Nagoya, Japan, 2000. 09. 24 – 27. p339 (2000).

[188] O. Tuna, H. Behmenburg, C. Giesen, H. Kalisch, R. Jansen, G. Yablonskii, M. Heuken, Dependence of InN properties on MOCVD growth parameters, Phys. Status Solidi C **8**, 2044 – 2046 (2011).

[189] A. Kadir, T. Ganguli, M. Gokhale, A. Shah, S. Chandvankar, B. Arora, A. Bhattacharya, Growth and characterization of InN layers by metal-organic vapour phase epitaxy in a close-coupled showerhead reactor, J. Cryst. Growth **298**, 403 – 408 (2007).

[190] B. Zhao, X. Han, F. Yang, X. Dong, Y. Zhang, Studies on growth of N-polar InN films by pulsed metal-organic vapor phase epitaxy, Chem. Res. Chin. Univ. **232**, 669 – 673 (2016).

[191] M. Jamil, , H. Zhao, J. B. Higgins, N. Tansu, MOVPE and photoluminescence of narrow band gap (0.77 eV) InN on GaN/sapphire by pulsed growth mode, Phys. Stat. Sol. A **205**, 2886 – 2891 (2008).

[192] A. Kraus, , H. Bremers, U. Rossow, A. Hangleiter, Double-pulsed growth of InN by RF-MBE, J. Electron. Mater. **42**, 849 – 853 (2013).

[193] M. C. Johnson, S. Konsek, A. Zettl, E. Bourret-Courchesne, Nucleation and growth of InN thin films using conventional and pulsed MOVPE, J. Cryst. Growth **272**, 400 – 406 (2004).

[194] G. Feuillet, B. Daudin, F. Widmann, J. Rouvière, M. Arléry, Plastic versus elastic misfit relaxation in III-nitrides grown by molecular beam epitaxy, J. Cryst. Growth **189** – **190**, 142 – 146 (1998).

[195] J. Mickevičius, D. Dobrovolskas, T. Steponavičius, T. Malinauskas, M. Kolenda, A. Kadys, G. Tamulaitis, Engineering of InN epilayers by repeated deposition of ultrathin layers in pulsed MOCVD growth, Appl. Surf. Sci. **427**, 1027 – 1032 (2018).

[196] S. Yamaguchi, M. Kariya, S. Nitta, T. Takeuchi, C. Wetzel, H. Amano, I. Akasaki, Structural properties of InN on GaN grown by metalorganic vapor-phase epitaxy, J. Appl. Phys. **85**(11), 7682 – 7688 (1999).

[197] A. Kadys, T. Malinauskas, T. Grinys, M. Dmukauskas, J. Mickevičius, J. Aleknavičius, R. Tomašiūnas, A. Selskis, R. Kondrotas, S. Stanionytė, H. Lugauer, M. Strassburg, Growth of InN and In-rich InGaN layers on GaN templates by pulsed metalorganic chemical vapor deposition, J. Electron. Mater. **44**, 188 – 193 (2015).

[198] B. Paszkiewicz, R. Paszkiewicz, A. Szyszka, M. Wosko, W. Macherzynski, M. Tlaczala, R. Kudrawiec, M. Syperek, J. Misiewicz, E. Dumiszewska, W. Strupinski, Study of the activation process of Mg dopant in GaN:Mg layers, Phys. Status Solidi C **3**, 579 – 584 (2006).

[199] D.-H. Youn, M. Lachab, M. Hao, T. Sugahara, H. Takenaka, Y. Naoi, S. Sakai, Investigation on the p-type activation mechanism in Mg-doped GaN films grown by metalorganic chemical vapor deposition, Jpn. J. Appl. Phys. **38**, 631 (1999).

[200] G. Miceli, A. Pasquarello, Self-compensation due to point defects in Mg-doped GaN, Phys. Rev. B **93**, 165207 (2016).

[201] C. T. Kuo, L. H. Hsua, Y. Y. Lai, S. Y. Cheng, H. C. Kuo, C. C. Lin, Y. J. Cheng, Dominant near infrared light-emitting diodes based on p-NiO/n-InN heterostructure on SiC substrate, Appl. Surf. Sci. **405**, 449 – 454 (2017).

[202] B. K. Barick, K. R. Saroj, N. Prasad, D. S. Sutar, S. Dhar, Identifying threading dislocation types in ammonothermally grown bulk α-GaN by confocal Raman 3-D imaging of volumetric stress distribution, J. Cryst. Growth **490**, 104 (2018).

[203] M. Kučera, S. Hasenőhrl, E. Dbročka, A. Rosová, P. Eliáš, F. Gucmann, J. Kuzmík, Morphology, crystalline quality, and optical properties of MOCVD-grown InN/InAlN, heterostructures, 13th International Conference on Advanced Semiconductor Devices And Microsystems (ASDAM) (2020).

[204] M. Higashiwaki, T. Matsui, High-quality InN film grown on a low-temperature-grown GaN intermediate layer by plasma-assisted molecular-beam epitaxy, Jpn. J. Appl. Phys. **41**, L540 – L542 (2002).

[205] D. Munteanu, J. L. Autran, *Nanowires: A 2-D/3-D Schrödinger-Poisson Drift-Diffusion Numerical Simulation of Radially-Symmetric Nanowire MOSFETs* (2012).

[206] S. Birner, T. Zibold, T. Andlauer, T. Kubis, M. Sabathil, A. Trellakis, P. Vogl, Nextnano: General purpose 3-D simulations, IEEE Trans. Electron. Devices **54**, 2137 – 2142 (2007).

[207] A. Adikimenakis, P. Chatzopoulou, G. P. Dimitrakopulos, T. Kehagias, K. Tsagaraki, M. Androulidaki, G. Doundoulakis, J. Kuzmik, A. Georgakilas, Correlation of threading dislocations with the electron concentration and mobility in InN heteroepitaxial layers grown by MBE, ECS J. Solid State Sci. Technol. **9**, 015006 (2020).

[208] M. A. Reshchikov, Luminescence properties of defects in GaN, J. Appl. Phys. **97**, 061301 (2005).

[209] C. T. Dervos, P. D. Skafidas, J. A. Mergos, P. Vassiliou, P-n junction photocurrent modelling evaluation under optical and electrical excitation, Sensors **4**, 58 – 70 (2004).

[210] P. D. C. King, T. D. Veal, C. E. Kendrick, L. R. Bailey, S. M. Durbin, C. F. McConvill, InN/GaNvalence band offset: High-resolution X-ray photoemission spectroscopy measurements, Phys. Rev. B **78**, 033308 (2008).

[211] S. Sze, *Physics of Semiconductor Devices* (1981), 2nd edition.

[212] Y. Yang, X. Peng, S. Hyatt, D. Yu, Broadband quantum efficiency enhancement in high index nanowire resonators, Nano Lett. **15**, 3541 – 3546 (2015).

[213] F. Liu, C. Yan, K. Sun, F. Zhou, X. Hao, M. A. Green, Light-bias-dependent external quantum efficiency of Kesterite Cu_2ZnSns_4 solar cells, ACS Photonics **4**, 1684 – 1690 (2017).

[214] P. Aliberti, Y. Feng, S. K. Shrestha, M. A. Green, G. Conibeer, L. W. Tu, P. H. Tseng, R. Clady, Effects of non-ideal energy selective contacts and experimental carrier cooling rate on the performance of an indium nitride based hot carrier solar cell, Appl. Phys. Lett. **99**, 223507 (2011).

[215] P. Klemens, Anharmonic decay of optical phonons, Phys. Rev. **148**, 845 (1966).

[216] S. Jensen, J. Versluis, E. Canovas, J. J. H. Pijpers, I. R. Sellers, M. Bonn, Carrier multiplication in bulk indium nitride, Appl. Phys. Lett. **101**, 222113 (2012).

[217] S. Feng, Y. Chen, C. Lai, L. Tu, J. Han, Anisotropic strain relaxation and the resulting degree of polarization by one-and two-step growth in nonpolar a-plane GaN grown on r-sapphire substrate, J. Appl. Phys. **114**, 233103 – 233109 (2013).

[218] S. Krishnamoorthy, F. Akyol, P. S. Park, S. Rajan, Low resistance GaN/InGaN/GaN tunnel junctions, Appl. Phys. Lett. **102**, 11350 (2013).

CURRICULUM VITAE

Name:	Marek
Surname:	Kolenda
Date of birth:	1992-09-23
Place of birth:	Vilnius, Lithuania
E-mail:	mkolendaus@gmail.com

Education:

1999–2011	Secondary school. J. I. Kraševskio vid. mokykla (dabar J. I. Kraševskio gimnazija). Rugiagėlių g. 15, LT-11109, Vilnius
2011–2015	Vilnius University, Faculty of Physics. Saulėtekio al. 9, III rūmai, LT-10222, Vilnius. *Bachelor degree* in Physics.
2015–2017	Vilnius University, Faculty of Physics. Saulėtekio al. 9, III rūmai, LT-10222, Vilnius. *Master degree, Magna Cum Laude* in Materials Sciences.
2017–2022	Photonics and Nanotechnology Institute, Vilnius University. Saulėtekio al. 3, LT-10257, Vilnius. *Ph.D. studies* in Technological Sciences, Materials Engineering.

Internship:

2019-11-10–23	Institute of High Pressure Physics, Polish Academy of Sciences. Unipress, prof. Mike Leszczyński, Sokołowksa 29/37; 01-142, Warsaw, Poland.

Work experience:

2012 summer	Engineer. UAB EKSPLA, Savanorių pr. 237, LT-02300, Vilnius.
2013 summer	Engineer. UAB EKSPLA, Savanorių pr. 237, LT-02300, Vilnius.
2014–2018	Engineer. Institute of Applied Research, Vilnius University. Saulėtekio al. 3, LT-10257, Vilnius.
2018–2019	Engineer. Photonics and Nanotechnology Institute, Vilnius University. Saulėtekio al. 3, LT-10257, Vilnius.
2019–now	Junior research fellow. Photonics and Nanotechnology Institute, Vilnius University. Saulėtekio al. 3, LT-10257, Vilnius.

TRUMPOS ŽINIOS APIE AUTORIŲ

Vardas:	Marek
Pavardė:	Kolenda
Gimimo data:	1992-09-23
Gimimo vieta:	Vilnius, Lietuva
El. paštas:	mkolendaus@gmail.com

Išsilavinimas:

1999–2011	Vidurinis išsilavinimas. J. I. Kraševskio vid. mokykla (dabar J. I. Kraševskio gimnazija). Rugiagėlių g. 15, LT-11109, Vilnius
2011–2015	Vilniaus universitetas, Fizikos fakultetas Saulėtekio al. 9, III rūmai, LT-10222, Vilnius. *Bakalauro kvalifikacinis laipsnis.*
2015–2017	Vilniaus universitetas, Fizikos fakultetas Saulėtekio al. 9, III rūmai, LT-10222, Vilnius. *Magistro kvalifikacinis laipsnis, Magna Cum Laude.* Medžiagų technologijų magistras.
2017–2022	Vilniaus universitetas, Fotonikos ir Nanotechnologijų Institutas, Saulėtekio al. 3, LT-10257, Vilnius. *Doktorantūra.* Technologijos Mokslai, Medžiagų inžinerija.

Stažuotė:

2019-11-10–23	Aukštų Slėgių Institutas prie Lenkijos Mokslų Akademijos, Unipress, prof. Mike Leszczyński, Sokołowksa 29/37; 01-142, Varšuva, Lenkija.

Profesinė veikla:

2012 vasara	Inžinierius-stažuotojas. UAB EKSPLA, Savanorių pr. 237, LT-02300, Vilnius.
2013 vasara	Inžinierius-stažuotojas. UAB EKSPLA, Savanorių pr. 237, LT-02300, Vilnius.
2014–2018	Inžinierius. Taikomųjų Mokslų Institutas, Vilniaus Universitetas. Saulėtekio al. 3, LT-10257, Vilnius.
2018–2019	Inžinierius. Fotonikos ir Nanotechnologijų Institutas, Vilniaus Universitetas. Saulėtekio al. 3, LT-10257, Vilnius.
2019–dabar	Jaunesnysis mokslo darbuotojas. Fotonikos ir Nanotechnologijų Institutas, Vilniaus Universitetas. Saulėtekio al. 3, LT-10257, Vilnius.

NOTES

NOTES

Vilnius University Press
Saulėtekio av. 9, III bld., LT-10222 Vilnius
e-mail: info@leidykla.vu.lt, www.leidykla.vu.lt
bookshop.vu.lt, journals.vu.lt
Print run copies 20